Scalable Architectures for High Frequency and Very High Frequency Wireless Power Transfer

by

Xin Zan

A dissertation submitted in partial fulfillment
of the requirements for the degree of
Doctor of Philosophy
(Electrical and Computer Engineering)
in the University of Michigan
2022

Doctoral Committee:

Assistant Professor Al-Thaddeus Avestruz, Chair
Professor Ehsan Afshari
Associate Professor Juan Manuel Rivas Davila
Professor Heath Hofmann
Associate Professor Alanson Sample

Xin Zan
xinzan@umich.edu
ORCID ID: 0000-0003-1797-9764

ACKNOWLEDGMENTS

First, I would like to thank my advisor Prof. Al-Thaddeus Avestruz. It is destiny and fortune to meet with you. You are more than an advisor to me. I admire and respect you. We have joy and fun. We also have hardships together. All make me what I am today. I feel appreciated to have you along the journey. I would also like to thank my colleagues in PEERS. It is like building a start-up company with the first-generation employees, Dr. Akshay Sarin, Dr. Sung Yul Chu, Xiaofan Cui, and Alireza Ramyar.

I would like to thank my committee members Prof. Alanson Sample, Prof. Ehasan Afshari, Prof. Heath Hofmann, and Prof. Juan Manuel Rivas Davila. I want to say thanks for your strong support including letters, suggestions, courses, and questions. I would also like to thank professors and staff in the ECE department. They ignite my curiosity, fulfill my unknown, and help logistics. They are Prof. Anthony Grbic, Prof. Becky Peterson, Prof. Ehasan Afshari, Prof. Kamal Sarabandi, Prof. Amir Mortazawi, Kristen Thornton, Anne Rhoades, and Judi Jones.

I would like to also thank my collaborators, Prof. Fei Lu, Dr. Sung Yul Chu, Reza Kheirollahi, Zizhen Guo, Dr. Sheng Zheng, Prof. Xiaonan Lu, Prof. Zheyu Zhang, Yanqiao Li, Yingying Fan, Can Deng, Yue Yang, Michelle Gehner, Daniel Roman, and Jack Rademacher.

I would like to thank Handong Gui. He is my mentor and friend. I often remind the happy memories with him. I will always remember him. Handong, I miss you very much. I would like to thank my best friend Qicang Shen. He is the closest to me although we have many arguments. I would like to thank Xiaofan Cui and Dr. Lei Gu. Without them, it will be harder for me to walk through the Ph.D. journey. I would also like to thank Yali Yang. We had most trips together these years.

I would like to thank my friends Jin Li, Xiaozhi Yu, and Xiao Zhu. I also would like to thank my friends Yichen Wang, Yumeng Ma, Yiyu Pan, Yifei Ma, Ruoyu Zhang, Liang Yao, Wendi Ding, Duo Yang, Lu Wen, Chaowei Xiao, Tianshu Dong, Jiajia Fan, Xun Xu, Jing Peng, Dandan Shan, Haokui Xu, Hongmei Tang, Menglou Rao, Zhuo Chen, Jiayue Qin, Yuguo Zhong, Yuqing Huang, Yuanying Wang, Jun Hou, Ping Wang, Shuoting Zhang, Yue Ma, Li Xu, Boyi Zheng, Zichao Ye, and Zitao Liao. I also would like to thank Omar, Noyan, and Hossein for their help in my study. I would like to thank all my friends from China, Michigan, Tennessee, and California.

I would like to thank my dear parents. You are always strongly supporting me and all my

decisions even though we have disagreements. I would also like to thank my grandparents. I feel sorry for not accompanying you these days and breaking promises of going back home. I wish you good health forever. I would also like to thank my aunts, uncles, and cousins. My family is all my backup force. Last but not least, I would like to thank myself for not giving up my dream during the Ph.D. journey.

I feel grateful and delighted for what I have, who I meet, and what happens around me.

TABLE OF CONTENTS

LIST OF FIGURES

LIST OF TABLES

LIST OF ABBREVIATIONS

HF high frequency

VHF very high frequency

CMCD current-mode class D

DPT double pulse test

WPT wireless power transfer

PCB printed circuit boards

PAPR peak-to-average power ratio

SAR specific absorption rate

PR-WPT piecewise resonant wireless power transfer

PR piecewise resonant

ZVS zero voltage switching

SR sine-wave resonance

ABSTRACT

Wireless charging is already taking hold with abundant commercial products that operate at around a hundred kHz. Currently, high frequency (high frequency (HF), 30 MHz) and very high frequency (very high frequency (VHF), 30-300 MHz) wireless power transfer (WPT) stand out because of better passive components, faster transient response, better combination with communications, and higher receiver input voltages. However, current wireless power transfer (WPT) systems are not fully scalable for different applications with different power levels and transfer distances in the wireless power world.

The thesis investigates scalable architectures for HF and VHF WPT, which can scale the power level and transfer distance while maintaining the efficiency with an application range from watts for biomedical and consumer electronics to tens of watts for robots and drones, breaking the trade-offs among devices, power, frequency, and transfer distance. The vision is to provide energy anytime and everywhere for electronic devices in the wireless power world.

To fully utilize the fast switching speed of Gallium nitride (GaN) at HF-VHF, an ultrafast and isolated gate driver is investigated with variable frequencies, variable duty cycles, and arbitrarily long on- and off- times. It can be scaled for different active devices with the ultimate speed of below 270 ps rise and fall times.

To mitigate the EMI (electromagnetic interference) and EMC (electromagnetic compatibility) problems at HF-VHF, a magnetic field cancellation method is presented for the encircled circuits inside WPT coils to make miniaturized devices operate properly under strong magnetic fields. The fundamental magnetic field for the encircled circuits can be reduced to 1 % compared to that without cancellation.

To design robust and resilient WPT systems, a classic circuit topology CMCD is brought back to the renaissance, which can work as both inverter and rectifier. It can absorb parasitics and be modeled as a purely second-order system, which does not require multi-resonant tuning in the higher-order ZVS resonant converters. The straightforward design reveals the advantages of a wide load range and small input current ripple at the same time.

With CMCD as a building block, the vision of a wireless power world can be possible. A single CMCD inverter coupled with a CMCD rectifier, i.e. a singleton system, fulfills the low power

and short transfer distance applications. A segmented CMCD inverter coupled with a segmented CMCD rectifier, i.e. a segmentation system, fulfills the high power and long transfer distance applications. The segmented CMCD power converters aggregate the magnetic flux and corresponding power together from each identical and synchronous module by electrically connecting the resonance, which also physically increases the coil size at HF-VHF and extends the transfer distance and power level but maintains the efficiency of the optimized singleton system.

In the end, the thesis concludes the contributions and illustrates the future directions of HF and VHF power conversion and transmission.

CHAPTER 1

Introduction

1.1 Vision of Wireless Power Transfer (WPT)

Wireless charging technology is quickly taking hold in our world with abundant commercial products available that operate at low frequencies of around 100 kilohertz (kHz) following the "Qi" standard. Current commercial markets focus on consumer electronics, mainly cellphones. Instead of putting the easily worn-out cords into the devices, people can simply put the devices on charging pads. In 2016, Samsung resumed this technology into the market. In 2018, Huawei brought bi-directional wireless charging, i.e. peer-to-peer charging, to general "Qi" standard cellphones. To be charged, these phones must be aligned closely to pads or another phone, which limits what is known as "transfer distance". Besides consumer electronics, the future of WPT needs to provide energy anytime and everywhere. In 2021, Xiaomi used phased array to charge electronics inside a room in a concept advertisement. Another idea of a resonant cavity can also be used to wirelessly power devices inside a room [1]. Definitely, there is no end to explore the potential of wireless powering technology.

Similar to the Internet of Things (IoT), in the vision of the wireless power world, devices can not only share information, but also share energy and power. In the vision of the wireless power world, trillion devices will be penetrated into our lives by 2025 [2] to make our world a more energy-efficient, environmentally-friendly, safer, healthier, and better-connected place. Energy harvesting has a sweet spot for 1 μW to 300 μW applications [2]. For power-hungry applications that desire more power, efficient RF power sources need to supply these devices. Besides consumer electronics, multiple types of WPT transceivers are needed to mitigate battery usage and lifetime, which helps improve major economic and environmental concerns related to the manufacture and disposal of hundreds of millions of batteries every single day [2]. As shown in Fig. 1.1, there are central power stations and local devices. Energy exchanges among central power stations and local devices. In the wireless power world, different applications desire different power levels and transfer distances, shown in Fig. 1.2. For implementable medical devices, which save lives and

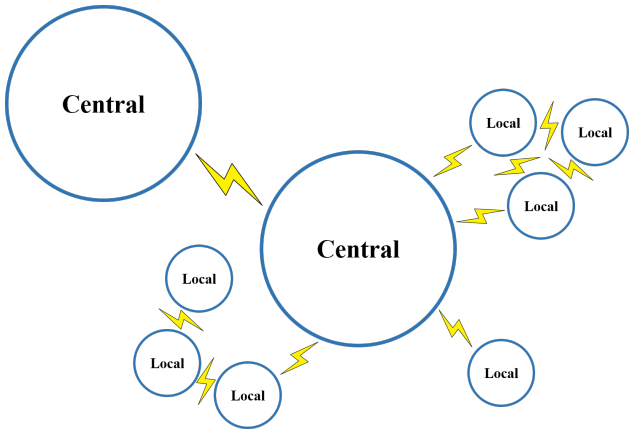

Figure 1.1: A vision of wireless power transfer.

improve health, WPT eliminates cords that pierce into the skin or regular surgeries for maintenance. But special care needs to be focused on the in-vivo receivers. For UAVs and robots, which charge frequently and intensively, connector wear and unreliability are unacceptable; WPT can eliminate cabling and power quickly, reliably, and resiliently. For electric vehicles, which make a green planet, WPT and dynamic WPT can cooperate with autonomous driving.

The wireless power world may be hard to imagine but if one recalls the early days of communications that were based on wired devices, such as the corded telephone, it is possible to understand the potential impact of WPT. With the explosion in cellphones used by people all over the world, we now live in a world of telephones without wires. The technology of WPT is similarly "scalable" and will expand quickly, becoming ubiquitous throughout a broad range of applications.

1.2 Motivations of High Frequency (HF) and Very High Frequency (VHF) Power Conversion

1.2.1 Passive Components

High frequency (HF, 3-30 MHz) and very high frequency (VHF, 30-300 MHz) power conversion bring high efficiency, miniaturization, and integration of passive components, especially in miniaturized devices and systems.

Firstly, air-core inductors can replace the magnetic core ones, which are lighter and smaller. As shown in Fig. 1.3 [5]. The volume of magnetic-core inductors increases with frequency once hits the limit of frequency while the volume of air-core inductors keeps decreasing along with the increased frequency, which makes air-core inductors stand out at higher frequencies, especially

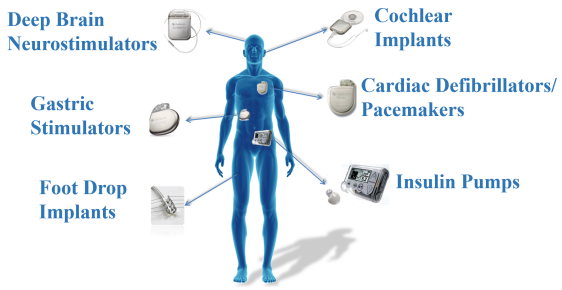

(a) Implantable medical devices. Imagine from: http://groups.csail.mit.edu/netmit/IMDShield/.

(b) Consumer electronics.

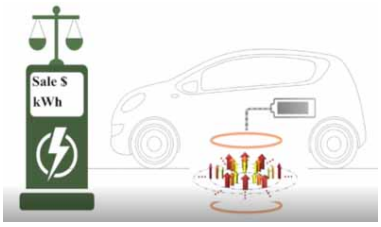

(c) Electric vehicle [3].

(d) UAV [4].

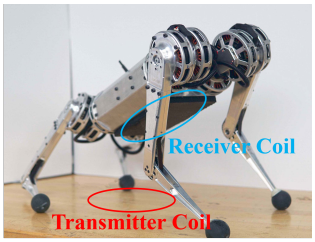

(e) Robot [4].

Figure 1.2: Typical applications using wireless power transfer.

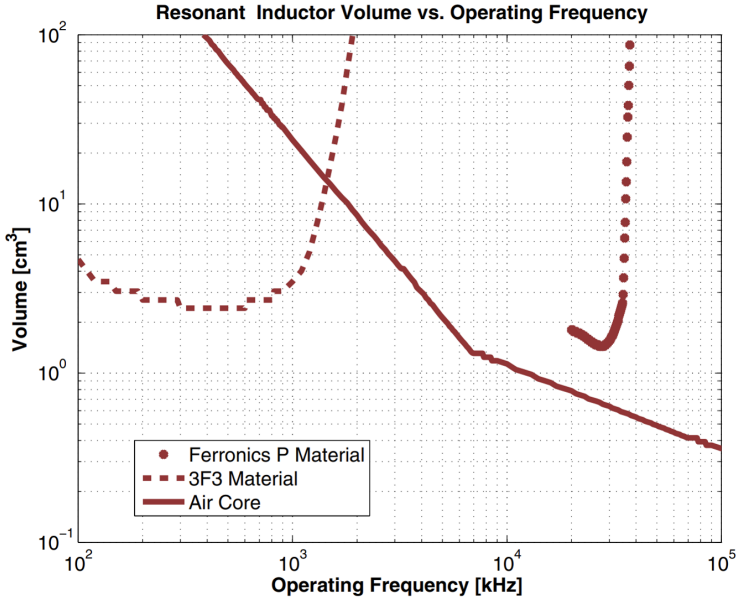

Figure 1.3: Comparison between conventional magnetic material (3F3), RF material (P) and air-core inductor volume [5].

in miniaturized devices and systems. HF and VHF WPT adopt air-core inductors as WPT coils, improving the figure of merit $Q \cdot k$ when increasing frequency.

Secondly, the quality factor of air-core inductors is proportional to the square root of frequency for single turn inductors as $Q_{\mathrm{L}} = \frac{2\pi f L}{R_{\mathrm{ac}}} \propto \sqrt{f}$ [5]. At higher frequencies, these inductors can have less loss and higher efficiency, which is better for thermal dissipation, especially in miniaturized devices and systems.

Thirdly, higher operating frequency means smaller passive components in the number of counts and in volumes, which is promising in miniaturization and integration, saving more space and volume of power management for other powerful functions, especially in miniaturized devices and systems.

1.2.2 Transient Response

Increasing the operating frequency is the fundamental method to accelerate the transient response. For a given quality factor Q of a second-order system, settling time is reduced at higher frequencies, which is needed in applications that need a fast response in voltage or current dynamics, including envelope tracking [6, 7] in 5G communications and GPU and CPU cores in AI and datacenters. When $Q = 5$, the settling time is 50 μs for 100 kHz operation while it will be 0.1 % as 50 ns if boosting the operating frequency to 1000 times as 100 MHz.

1.2.3 Combination with Communications

Increasing the operating frequency is attractive to combine power conversion and information transfer together. If power converters operate around 1 MHz with the phase-shift key and frequency-shift key, the data rate for communications is only 200 kbps [8], which takes more than 10 hours to download a 1 GB file. A significant data rate can be achieved if increasing the frequency of power conversion.

1.2.4 Receiver Input Voltages

For a fixed or a given receiver coil, increasing the operating frequency is a method to increase the receiver input voltages. Higher voltages mean smaller currents and less conduction loss for the same amount of power. For miniaturized receivers that are small or far away from the transmitter, it is important to increase the receiver input voltage, which determines the load power and efficiency for passive rectifiers with a fixed diode voltage drop. The receiver input voltage is also the open-circuit voltage on the receiver side [9]. For a given magnetic flux produced by the transmitter

coil, the higher operating frequency, the higher receiver input voltages from Faraday's law of electromagnetic induction.

1.3 State-of-the-Art HF and VHF WPT

Techniques used for HF and VHF dc–dc power conversion apply to wireless power transfer; although, WPT efficiencies from dc to dc for identical topologies are lower because of the needed higher reactive power for the WPT link. VHF power conversion requires the appropriate choices of active devices, passive components, gate drivers, circuit topologies, integrated circuits, and RF design techniques [5, 10, 11]. Parasitics of printed circuit boards (PCB), active devices, passive components, and prototype layout become significant at higher frequencies and can affect system performace. In addition, another considerable challenge in WPT is the wide load range or load independency, either from variable loads, different coupling coefficients, and voltage levels. The WPT transmitter needs to be insensitive to unloading because a practical WPT receiver needs to be removed from the charging pad frequently and freely. For battery charging applications, constant output current with small current ripple is the preferred mode of operation for the receiver.

HF and VHF power conversion can be realized using discrete devices and gate drivers. For devices, commercial and custom high-performance RF lateral double-diffused MOSFETs (LDMOSFETs) [12–14] had been historically used because of acceptably low parasitic capacitance and gate resistance before the prevalence of better performing GaN (gallium nitride) HEMTs. VHF gate drivers require ultrafast slew rate, isolation, variable frequency, variable duty cycle, arbitrary long on- and off-times, flexible control inputs, and small gating loss [15]. Self-oscillating resonant gate drivers [12–14, 16] and conventional multi-resonant gate drivers [17] have been employed to mitigate gating loss but have a slower slew rate and operate at a single switching frequency and fixed duty cycle; the gate voltage waveforms are typically sinusoidal or trapezoidal. Logic inverter banks can be used to drive GaN HEMTs directly to better customize the gate drive [18]. Reference [15] investigated an ultrafast gate driver using logic CMOS inverters with transformer isolation that operates at VHF with different duty cycles and arbitrary long pulses.

For power converters, resonant topologies typically operate at zero-voltage-switching (ZVS) and absorb circuit parasitics into the topology. Class E resonant converters [14] along with variations like resonant boost converters [13] and class Φ_2 [12, 18] have been widely investigated at VHF. Conventional class E operation is typically sensitive to loading conditions for zero-voltage-switching (ZVS) and zero-voltage-derivative-switching (ZVDS), which can limit the operation over a wide load range.

There has been plenty of research investigating resonant converters that operate over a wide load range. Some had reduced the choke inductances and sacrificed the input and output current

ripple to attain a wide load range [19–21]. The symmetric class EF system [19], transformed class E inverters [20], and transformed class Φ_2 inverters [20] absorb the much smaller chokes into part of the resonant network, resulting in large input or output current ripple. Reference [21] compensated the tuning where the impedance is flat together with the reduced choke inductance to extend the load range. With additional lossy components, greater complexity, or more complex control strategies [12, 18, 22–28], a wide load range together with small input and output current ripple can be achieved. References [12, 22] used resistance compression networks with class E inverters to extend the load range but sacrificed the efficiency from the additional components. Reference [18] used a bandpass matching network with a symmetric class Φ_2 system to extend the load range by a factor of 7 at 64 MHz, achieving 73 % efficiency at 11 W peak power. Reference [23] investigated a push-pull Φ_2 inverter with a T network, which can achieve load-independent characteristics while reducing the input ripple and reactive power loss for 6.78 MHz WPT applications [24, 25]; however, the circuit topology can be difficult to extend to higher frequencies. References [26–28] used a variable equivalent capacitor from phase-switched impedance modulation to achieve a wide load range with active control.

Currently, GaN devices have been used to push the switching frequency of dc–dc converters to 64 MHz [18] in class Φ_2^2, 75 MHz [7] in multi-level buck using discretes, and 1 GHz [29] in a microstrip circuit class E^2 with greater than 70 % efficiency at greater than 5 W power. LDMOSFETs had been used in 100 MHz class E^2 dc–dc converters, which deliver 1.7 W at 55 % efficiency [14]. Most symmetric systems at MHz power conversion are designed for constant output voltage, including class E, class EF, and class Φ_2, while constant output current with small ripple is needed for direct battery charging.

Another approach to VHF power conversion has been investigated through circuit integration. Silicon integrated circuits (IC) with multi-phase buck converters achieved a load power of 0.44 W at 83.2 % efficiency at 233 MHz [30]. 140 MHz multi-phase buck regulators were fully integrated and featured up to 80 MHz unity gain bandwidth [31]. Another custom IC using a GaN half-bridge with an integrated gate driver [32] had enabled fertile research in 100 MHz power conversion, including 100 MHz capacitive wireless power transfer [33] delivering 2.5 W from dc to ac with no rectifier to a resistive load with approximately 90 % efficiency. DC-DC efficiencies are typically lower than DC-AC efficiencies for WPT because of rectifier losses. 100 MHz inductive WPT was used for a high-density IC chip with 34 % power transfer efficiency [34].

Achieving high efficiency and high power in VHF WPT is still an ongoing challenge whether using discrete components or circuit integration. Current WPT systems are considered “not fully scalable”, which is hard to expand to broad usage to achieve the vision of WPT in Fig. 1.1, especially for different power levels and transfer distances.

1.4 Two Fundamental Limitations

Besides the above design challenges regarding HF and VHF power conversion, two main fundamental limitations exist in HF-VHF WPT.

1. **Power and Frequency Trade-off** because of semiconductor devices, making it hard to achieve high power at HF and VHF power conversion. To make devices operate at higher frequencies, the junction capacitance needs to be small, correspondingly, the current rating of a single device is small. Then the power rating is also small, which means higher frequencies, less power rating. For example, in GaN HEMTs GS665XX series from GaN Systems [35], the drain current I_{max}, which is commensurate with power level, is nearly inversely proportional to the reciprocal of parasitic capacitances C_{oss}, which corresponds to the operating frequency, as shown in Fig. 1.4 where the parasitic capacitance and maximum current are normalized to the values of GS66502's. This can be also represented in applications. Fig. 1.5 shows the system power rating decreases with the system operating frequency.

2. **Transfer Distance and Frequency Trade-off** because of limited WPT coil inductance, making it hard to achieve far transfer distance at HF-VHF WPT. For HF-VHF WPT, usually resonant converters dominate. The most basic equation for resonant converters is $\omega = 1/\sqrt{L\,C}$, where ω is the frequency, L and C are the resonant inductance and capacitance, respectively. Thus, L is limited at HF-VHF. If simply using circular single-turn filament coils from $L = \mu_0 \pi a$ [36], where a is the radius, and calculating the mutual inductance M using [37], then the relationship between the inductance value and transfer distance is shown in Fig. 1.6 with coupling coefficient $k = 0.2$.

To achieve a higher power level at HF-VHF, a prevailing choice is to increase the voltage level but it requires high voltage rating components and high isolation safety requirements. The specific on-state resistance of the ideal drift region is proportional to the square of the voltage, as $R_{\text{on-ideal}} = 4\text{BV}^2/(\epsilon_{\text{s}}\mu_{\text{n}}E_{\text{C}}^3)$ [39], where $\epsilon_{\text{s}}\mu_{\text{n}}E_{\text{C}}^3$ is referred as Baliga's figure of merit for power devices, increasing conduction loss; their C_{oss} loss is proportional to the power function of voltage [40], increasing the switching loss. Thus, high voltage semiconductor devices to drive the big coils drop the efficiency while increasing the power level. Another prevailing approach is to have power combiners [22, 41–43] at HF-VHF, like resistance compression networks [22]. However, most power combiner circuits [22, 43] add extra losses because of additional active or passive components, dropping the efficiency. The prevailing methods cannot maintain the efficiency while increasing the power at HF-VHF power conversion.

To enlarge the transfer distance at HF-VHF, a bigger physical dimension coil can be used. Big coils require high terminal voltage with high voltage semiconductor devices to drive for a given

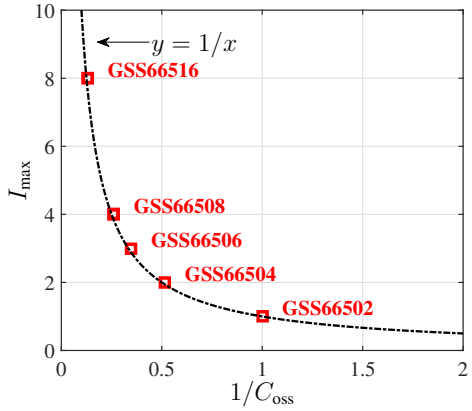

Figure 1.4: Drain current $I_{\max}$, which is commensurate with power level,is nearly inversely proportional to the reciprocal of parasitic capacitances C_{oss}, which corresponds to the operating frequency, among GaN HEMTs GS665XX series from GaN Systems [35] where the parasitic capacitance and maximum current are normalized to the values of GS66502's.

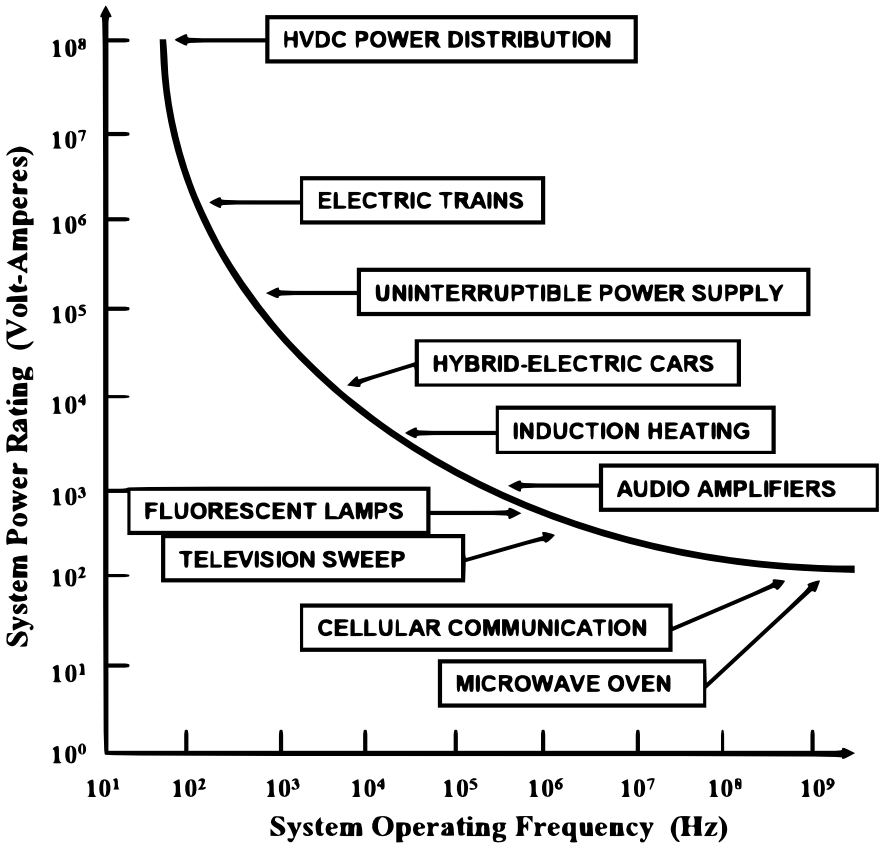

Figure 1.5: Power rating decreases with the operating frequency of power semiconductor devices, which manifests in applications [38].

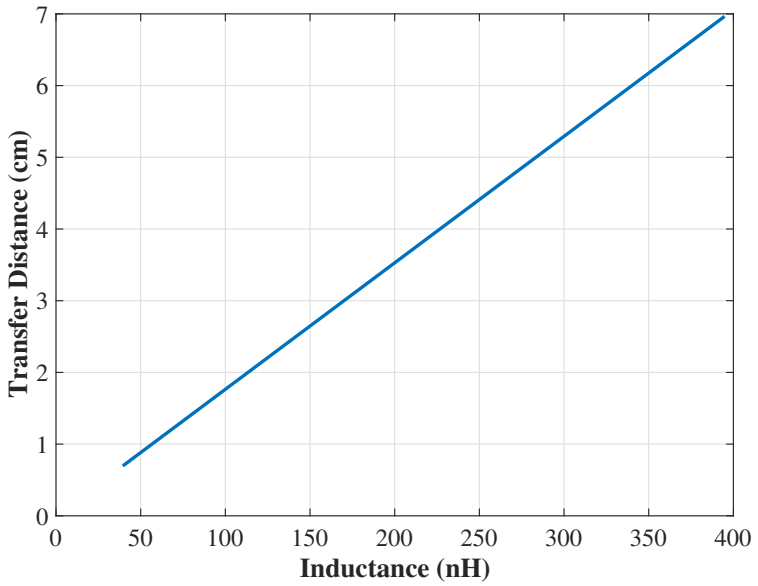

Figure 1.6: The relationship between transfer distance between the two identical circular coupled single-turn filaments coils and their self-inductance values with coupling coefficient $k = 0.2$.

coil current. Similarly, high voltage semiconductor devices have more conduction loss [39] and C_{oss} loss [40] to have big coils. Thus, having big coils together with high voltage semiconductor devices drops the efficiency while increasing the transfer distance. Segmented coils can enlarge the transfer distance while maintaining small driving voltages by segmenting the coils with discrete and distributed capacitors [44, 45]. However, the prevailing segmented coils [44, 45] are driven by a single power amplifier or power converter. Thus, the power is limited.

1.5 Thesis Contributions and Organizations

To overcome the design challenges in Section 1.3 and the two fundamental trade-offs in Section 1.4, I investigate scalable architectures for HF and VHF WPT systems, which are suitable for different applications of wireless power transfer systems with different power levels and transfer distances, as shown in Fig. 1.7.

Big circular WPT coils are segmented evenly with capacitance. They are fed with evenly distributed power sources. The number of segments n starts from 1 to a maximum number of N. In the near-field WPT region, a higher n means nP for the power and approximate nd for the transfer distance, where P and d are the transfer power and distance when $n = 1$. A higher n means n power sources are needed with corresponding circuits and control. All the power sources operate identically and synchronously, the switch utilization, passive components rating,

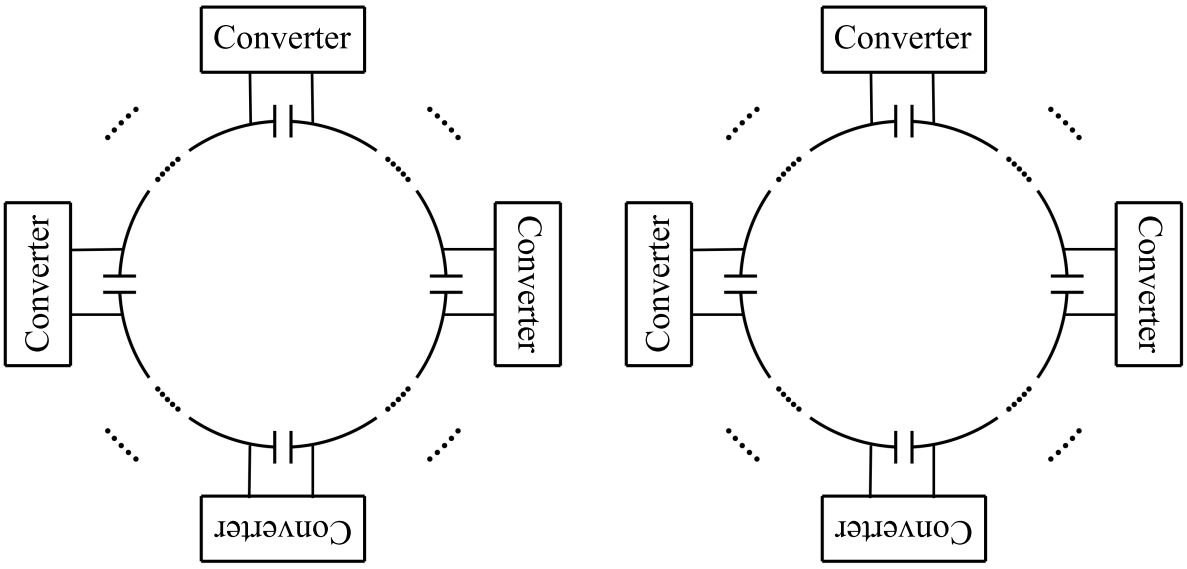

(a) HF-VHF Transmitter. (b) HF-VHF Receiver.

Figure 1.7: Scalable architectures.

and system efficiency remain unchanged while varying n.

Compared with other counterparts and alternatives that can only break either **Power and Frequency Trade-off** or **Transfer Distance and Frequency Trade-off** with sacrifices in efficiency as mentioned before, the contributions of the scalable architectures are

1. Compared with other power combiner circuits [22, 43], for example, resistance compression networks [22], the scalable architectures do not add extra components which bring loss and decrease the overall efficiency;

2. Compared with a single big dimension coil that enlarges the transfer distance, the scalable architectures do not increase the voltage levels or require high voltage rating semiconductor devices;

3. Compared with conventional segmented coils [44, 45], the scalable architecture partitions the power conversion among modular converters instead of a single higher-power one, which brings more reliability, flexibility, and a better selection of components and design tradeoffs.

Three system scenes investigated in the thesis are shown in Fig. 1.8.

1. Fig. 1.8(a) shows the application scene where the power and transfer distance are relatively low with sinusoidal waveforms. It simply uses one converter for each side with $n = 1$;

2. Fig. 1.8(c) shows the application scene where the power and transfer distance are relatively high with sinusoidal waveforms. It uses four converters for each side with $n = 4$; While in reality, the number of segments can be different;

3. Fig. 1.8(b) shows the application scene where the power and transfer distance are relatively low with multi-resonant waveforms. It simply uses one converter for each side with $n = 1$.

The converters adopted in the above architectures are current-mode class D (CMCD). In this thesis, 100 MHz singleton systems with $n = 1$ and 100 MHz segmentation systems with $n = 4$ are presented, which refer to Fig. 1.8(a) and 1.8(c), respectively. These two systems only transfer power at the fundamental frequency with purely sinusoidal waveforms. Another piecewise resonant system with $n = 1$ transfers power at 6.78 MHz fundamental frequency and its third harmonic 20.34 MHz is also presented, which can also be scaled to a higher n for a higher power level or longer transfer distance, which refers to Fig. 1.8(b).

The reminder of this thesis is structured as follows.

In Chapter 2, an isolated ultrafast gate driver for pulse and VHF power electronics is investigated. Ultrafast and isolated gate drivers advance the development of pulse and VHF power electronics for applications that include LiDAR, space systems, miniaturized hardware, and testing of emerging ultrafast devices. The isolated ultrafast gate driver in this paper achieves a gate voltage slew rate above 12 GV/s with rise and fall times below 270 ps with the proper choice of components. Magnetic isolation provides transient immunity and positive feedback enables dynamic DC restoration to allow arbitrarily long on- and off-times and preserve variable duty cycles. With the isolated ultrafast gate driver, an EPC 2038 GaN FET achieves a drain voltage slew rate of over 37 GV/s when hard-switching and improves total efficiency by 8 % (including gating loss) with a careful choice of logic inverters in a symmetric 100 MHz CMCD wireless power transfer system. The ultrafast gate driver with isolation and positive feedback was implemented with a commercial RF signal transformer and discrete logic inverters and validated in a hard-switching double pulse test (DPT), a narrow pulse test repeating at 165 MHz, and a 100 MHz soft-switching CMCD resonant converter.

In Chapter 3, a magnetic field cancellation and manipulation method is investigated. Components and circuits encircled by WPT coils allow miniaturization but require field cancellation for components and circuits that are sensitive to magnetic fields. Very high frequency (VHF) operation reduces the volume and number of components, which makes encirclement within WPT coils easier. A field cancellation method was investigated to minimize the magnetic field for the encircled circuits in WPT coils using a two-coil structure. The WPT and cancelling coils are driven together by a single CMCD power converter with opposite-phase currents to optimize the field cancellation within the coils. Using this cancelling method, the magnetic field for the encircled circuits was

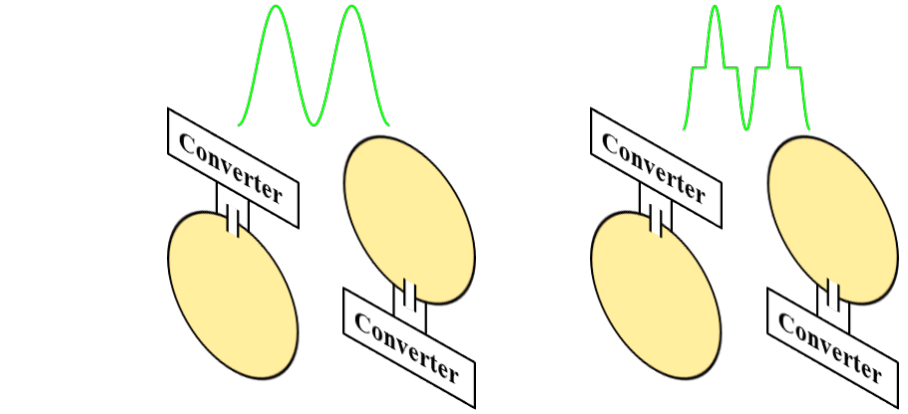

(a) Singleton.

(b) PAPR.

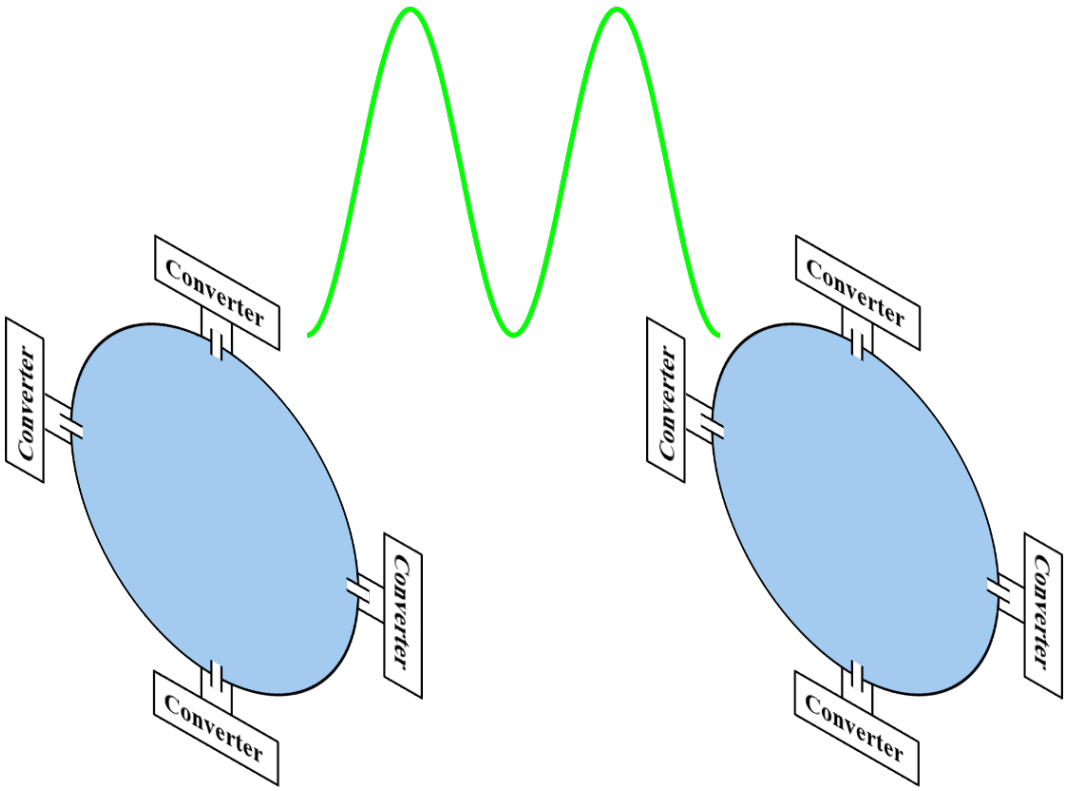

(c) Segmentation.

Figure 1.8: Different scenes in the scalable architectures.

reduced by 99 % in hardware compared to that without cancellation.

In Chapter 4, a design methodology of a WPT system using a CMCD inverter as the transmitter and a CMCD rectifier as the receiver, i.e. a singleton CMCD WPT system, is investigated. Power conversion for wireless power transfer (WPT) at 100 MHz is important for miniaturization and integration, which is critical for charging wearable consumer electronics, and devices for the Internet of Things (IoT). Design and implementation at this frequency are challenging in the selection of components and circuit configurations for operation over a wide load range. The optimization of the tuned compensation networks together with a step-by-step guide for a systematic and rigorous optimal design is derived in this paper from fundamental circuit models for symmetric CMCD WPT systems. Symmetric CMCD WPT systems can have inherently constant output current for a wide load range with small current ripples for the optimal design, which is useful in direct battery charging applications. Both uncontrolled and synchronous rectifiers are analyzed, demonstrated, and compared in hardware with the optimal designs. A 100 MHz prototype with an output peak power of 6.9 W has a power circuit dc–dc efficiency of 81.9 % despite only natural convection cooling of miniaturized GaN devices. The prototype maintains nearly constant power circuit efficiency above 80.5 % with a peak of 83.2 % over a wide power range that spans from 1.7 W to 6.9 W.

In Chapters 5 and 6, a methodology of scaling WPT power level and transfer distance while maintaining the efficiency is investigated using a segmented CMCD inverter as the transmitter and a segmented CMCD rectifier as the receiver, i.e. a segmentation CMCD WPT system. The segmented CMCD power converters aggregate the magnetic flux and corresponding power together from each identical and synchronous module by electrically connecting the resonance, which also physically increases the coil size at HF-VHF and extends the transfer distance and power level but maintains the efficiency of the optimized singleton system.

In Chapter 7, a piecewise resonant wireless power transfer (PR-WPT) system is investigated to achieve the high efficiency, simplicity, and reliability for the in-vivo receivers as wireless power transfer is emerging as the preeminent powering technology for implantable medical devices. A high peak-to-average power ratio (PAPR) waveform is generated by a current-mode class D amplifier operating at 6.78 MHz. A 4^{th}-order passive filter is matched to the fundamental and third harmonic voltages of the transmitter, using harmonic elimination for the waveform and closed-form impedance analysis. A full-bridge Schottky rectifier converts the matched voltage into dc. Experiment demonstrates the proof of principle and simulation results show that the piecewise resonant methods can increase the dc output voltage by up to 30 %, hence improving the rectifier efficiency. Potential applications for PR-WPT systems are discussed.

In Chapter 8, contributions of the dissertations are illustrated and future research directions of HF and VHF power conversion and transmission are proposed with research questions and

engineering applications.

CHAPTER 2

Isolated Ultrafast Gate Driver

2.1 Introduction

Ultrafast gate drivers are needed in LiDAR for range accuracy and resolution [46, 47], in VHF (very-high-frequency) for minimizing loss and expanding the range of operation [10, 17], in space applications for increasing reliability through isolation [48], and in the double pulse test of emerging ultrafast devices including new generations of GaN [49, 50]. The specific requirements and challenges in isolated ultrafast gate driver design include:

(1) *Ultrafast slew rate* to ensure fast switching transitions that are needed for narrow pulses and very high frequency so that the transitions do not excessively limit the minimum on- and off-times and dominate the switching periods. Fast switching transitions also reduce switching losses in PWM converters [7, 32, 51] and in the turn-off of resonant converters like current-mode class D converters [4, 52].

(2) *Isolation* to separate the control signal from the gate, so that the gate drive voltage can be referenced to the same potential as the source terminal of the power device, which is particularly a concern in high-side switches. In addition to the isolation of the gate driver control signal, high-side drivers require isolated power supplies, which is challenging at VHF because of coupling capacitance. A 75 MHz high-side gate driver had been demonstrated in [7] using isolated power supplies. Even in ground-referenced power switches, isolation provides immunity from the source inductance combined with high di/dt (from high currents and/or fast transitions), which can cause power device mistriggering when the transients exceed the threshold voltage; this can be especially problematic in devices where the on-state and off-state gate drive voltages are adversely limited by low gate breakdown voltages. Compared to other isolation methods, transformer coupling typically provides better common-mode immunity at high speeds.

(3) *Variable frequency, duty cycle, and arbitrarily long on- and off-times* to adjust frequency, pulse width, ZVS timing, dead time, or overlap for voltage/current modulation or because of parasitics and component tolerance, temperature variation, and nonlinearity in both pulse

[46, 47, 49, 50], PWM [7, 32, 48], and resonant converters [4, 10, 13, 17, 52]. During start-up or closed-loop control conditions, arbitrary duration pulses are often necessary to drive the gate when the converter deviates from steady-state operation. To preserve duty cycle and arbitrarily long on- and off-times, high-speed isolation methods (e.g. capacitive or transformer coupling) will require a method for dynamic DC restoration.

(4) *Flexible control inputs* to interface with ultrahigh speed controllers and logic that operate at lower voltages, require impedance matching, render differential signaling, or are susceptible to loading conditions.

(5) *Small gating loss* to mitigate the escalating losses from switching devices at very high frequency, where gating loss can be as much as 40 % of the loss budget at 30 MHz [17].

In contrast to the new isolated ultrafast gate driver described in this paper, prevailing state-of-the-art gate drivers meet some, but not all of these requirements. In particular, as transition times approach 100 ps and as switching frequencies reach deeper into VHF, isolation together with arbitrarily long on- and off-times, to our knowledge had not been achieved. Methods using transformer isolation can transmit fast pulses at very high frequencies with small propagation delay but cannot sustain arbitrarily long pulses [53]. Commercial gate drivers like the TI LMG1020 can operate at switching frequencies up to 60 MHz with 400 ps typical rise and fall times. A resonant gate driver is a prevailing choice for reducing the gating loss at VHF [13, 17], but usually exacerbates the time interval in the "linear region" of the power device [10, 17] and can result in higher loss regardless of whether the gate waveform is sinusoidal [13] or trapezoidal [13, 17]. Also, resonant gate drivers usually have a fixed frequency and duty cycle for a particular configuration and set of components. Sinusoidal, trapezoidal, and hard-switching gate drivers have been demonstrated at 100 MHz and above [10, 13, 32], but at lower slew rates and without isolation. Commercial digital isolators have been used at 27.12 MHz [52] and 75 MHz [7]; because of low slew rates, they cannot transmit very short pulses and have a limited maximum operational frequency with relatively large propagation delay.

In this chapter, we present an architecture for an isolated ultrafast gate driver and hardware examples that allows arbitrarily long on- and off-times yet capable of 1) below 260 ps rise and fall times; 2) isolation with dynamic DC restoration; and 3) variable frequency and duty cycle preservation. We perform a DPT (double pulse test) with hard-switching and investigate operation in a CMCD (current-mode class D) resonant converter operating at 100 MHz with an EPC 2038. In addition, hardware results show a pulse repetition rate at 165 MHz is possible and that a design driving a higher power GaN FET at 100 MHz with 16X higher gate charge than the EPC 2038 with rise and fall times below 270 ps is implementable.

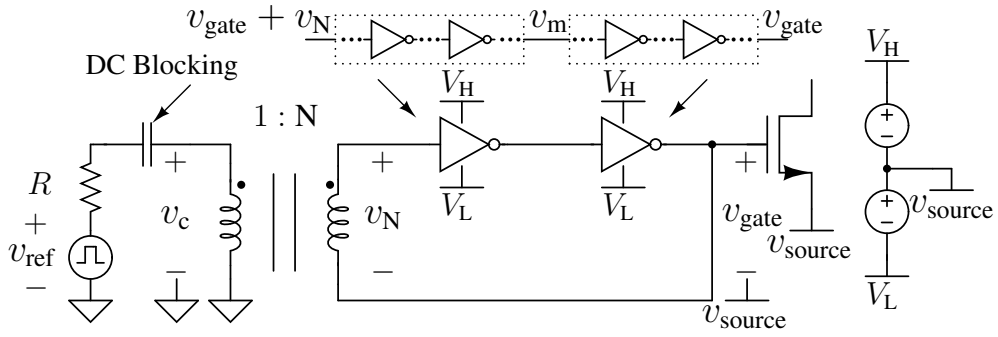

Figure 2.1: Isolated ultrafast gate driver architecture uses a transformer and logic inverters with positive feedback. Inverters could be a composite of cascaded and scaled inverters. In the hardware implementation, the turns ratio of the transformer is 1:2 and the logic inverter pair has one logic inverter per stage with a single-ended control signal.

2.2 Operation

2.2.1 Isolated Ultrafast Gate Driver Architecture

The isolated ultrafast gate driver in this paper is shown in Fig. 2.1, which consists of a broadband signal transformer and composite logic inverters with an even number of stages. The transformer provides isolation, boosts the control signal v_c by the turns ratio $1:N$, and matches impedance if necessary. The control voltage v_c could be either single-ended or differential (single-ended in Fig. 2.1). The composite logic inverters have input voltage ($v_N + v_{gate}$), intermediate voltage v_m between the pair, and output voltage v_{gate}, which drives the power device and is also connected to the secondary winding of the transformer to provide positive feedback for *dynamic DC restoration*, where the offset dc voltage to the transformer secondary depends on the output state. This results in the gate driver output state being held despite the inevitable voltage decay or *droop* in the secondary winding. Volt-second balance of the transformer and charge balance of the DC blocking capacitor eventually causes droop.

The aggregate propagation delay from v_{in} to v_{gate} in the forward path is T_{pd}, which is the sum of the propagation delays of the logic inverters. Each logic inverter is powered by V_H and V_L. The inputs to the logic inverters are clamped with the restrictions on clamp voltages enforced to be $V_{clampL} < V_L$ and $V_{clampH} > V_H$ for proper operation.

Each composite logic inverter can be implemented, for example in an integrated circuit, as a composite of cascaded inverters each with scaled devices to minimize aggregate propagation delay for a particular current drive required by a power device. In discrete implementations, parallel inverters can be used to increase the current drive.

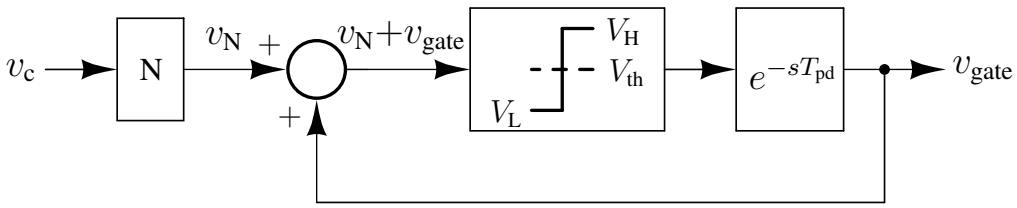

Figure 2.2: Block diagram of the positive feedback mechanism in the isolated ultrafast gate driver architecture.

2.2.2 Waveforms

Some simplifying assumptions are used to assist with analysis:

1. the transformer maintains the voltage relationship from the turns ratio instantaneously across the primary and secondary windings because leakage inductance is negligible so that $v_{\mathrm{N}}(t) = \mathrm{N}\, v_{\mathrm{c}}(t)$;

2. the logic inverter threshold is $V_{\mathrm{th}} = \frac{1}{2}\left(V_{\mathrm{H}} + V_{\mathrm{L}}\right)$;

3. successful triggering of the first logic inverter input with $(v_{\mathrm{N}} + v_{\mathrm{gate}})$ exceeding the threshold V_{th} results in positive feedback after a delay of T_{pd} as shown in Fig. 2.2.

The effect of leakage inductance is described in Section 2.3.1.

2.2.2.1 Periodic Short-Pulse Operation

We define periodic short-pulse operation as the periodic steady-state regime where on- and off-times are sufficiently short so that the voltage droop on the transformer secondary is negligible.

The following analysis assumes that the logic inverters are unclamped for ease of explanation; this simplification can be justified by the fact that the timing of the edges is unchanged for the clamped case. Assuming a midpoint threshold voltage V_{th} helps illustrate the operating principles through a straightforward analysis; in reality, the threshold voltages may be different for low-to-high and high-to-low transitions, which can be accounted by a change in on-time and off-time durations and an asymmetry in rise and fall propagation delays. Figure 2.3 represents the steady-state waveforms of the periodic short-pulse regime of the isolated ultrafast gate driver when the duty cycle is equal to or below 50 % in Fig. 3(a) and when the duty cycle is above 50 % in Fig. 3(b).

The input voltage for the composite of cascaded logic inverters ($v_{\mathrm{N}} + v_{\mathrm{gate}}$) is crucial in determining the behavior; this consists of a periodic waveform usually with four voltage levels: a plateau, a valley, ledge A on the rise, and ledge B on the fall. The voltage quantities that are

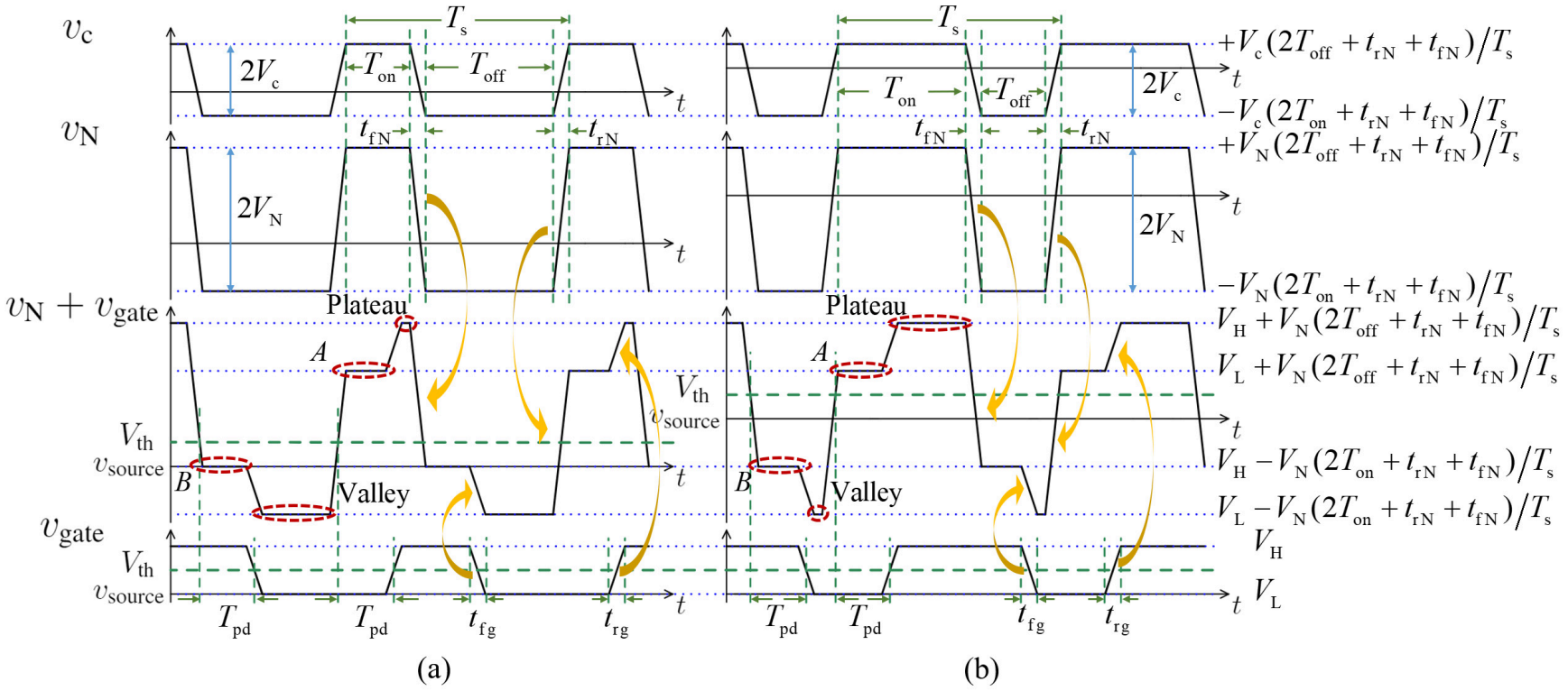

Figure 2.3: Steady-state waveforms of the isolated ultrafast gate driver operating in the periodic short-pulse regime at: (a) equal to or below 50 % duty cycle and (b) above 50 % duty cycle.

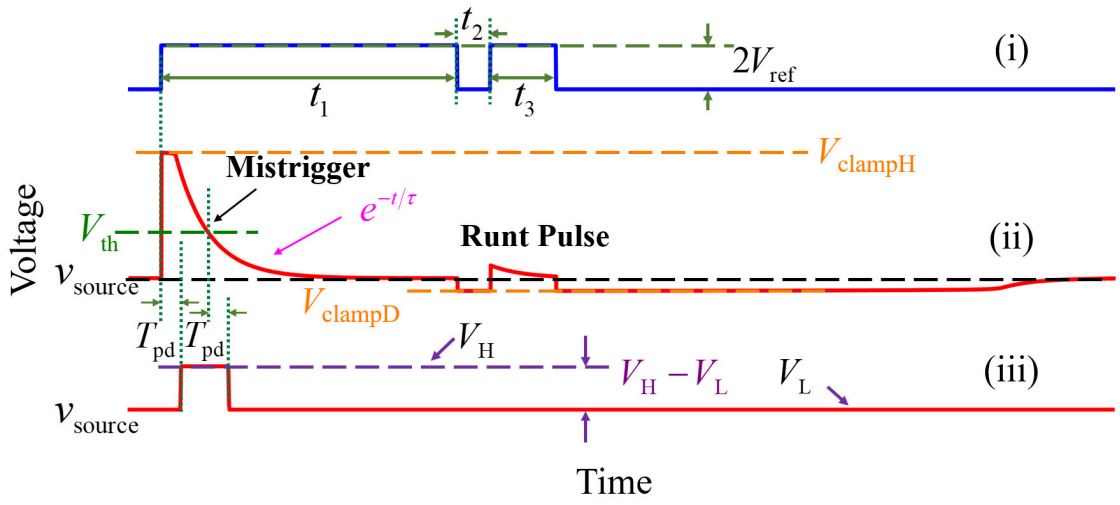

(a) Waveforms. (i) Reference Signal v_{ref}; (ii) Logic Inverter Input Voltage ($v_N + v_{gate}$); (iii) Gate Driver Output Voltage v_{gate}.

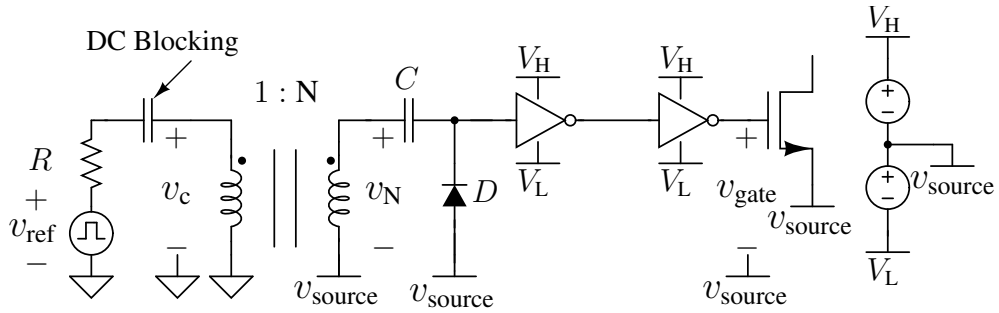

(b) Circuit.

Figure 2.4: Time-domain waveforms illustrate arbitrary long-pulse behavior for the well-known circuit on p. 32 in [54]. Voltage droop causes the gate driver output to not sustain for the duration of the long reference signal pulse, which also causes mistriggering in subsequent pulses.

labeled in Fig. 2.3 are referenced to the source voltage v_{source} and are a function of on-time T_{on}, off-time T_{off}, rise time t_{rN}, and fall time t_{fN}. The peak-to-peak values of v_c and v_N are $2V_c$ and $2V_N$, respectively. Ledge A on the rise of ($v_N + v_{gate}$) results from the combination of the rise of v_N and from the positive feedback of the subsequent rise of v_{gate}. Similarly, ledge B results from the combination of the fall of v_N and the fall of v_{gate}.

2.2.2.2 Arbitrary Long-Pulse Operation

We define arbitrary long-pulse operation as the regime where arbitrarily long on- or off-times have resulted in the decay of the transformer secondary voltage to nearly zero. Volt-second balance of the transformer and charge balance of the DC blocking capacitor eventually causes the decay. A well-known gate driver circuit [54] without dynamic DC restoration from positive feedback is

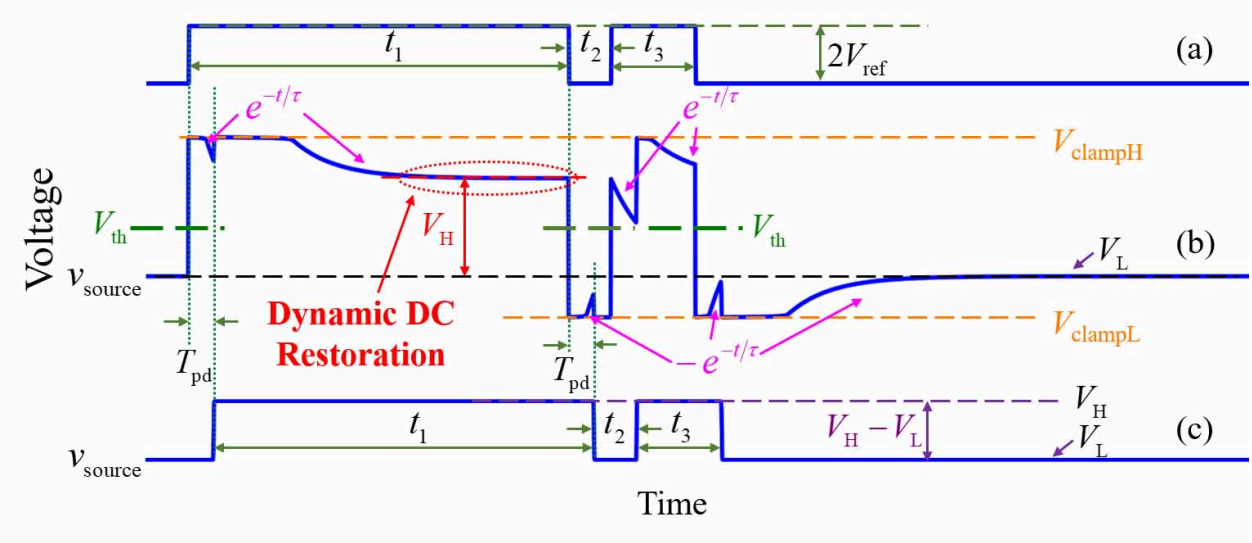

Figure 2.5: Time domain diagrams of the isolated ultrafast gate driver illustrate behavior from a combination of a long pulse and an intermediate duration before a second pulse. (a) Reference Signal v_{ref}; (b) Logic Inverter Input Voltage ($v_N + v_{gate}$); (c) Gate Driver Output Voltage v_{gate}. Note that in this figure $V_L = v_{source}$.

shown in Fig. 2.4(b); droop eventually results in a mistrigger and the output voltage does not hold its state as shown in Fig. 2.4(a).

The isolated ultrafast gate driver with positive feedback allows dynamic DC restoration, which preserves the arbitrarily long on- and off- times of t_1, t_2, and t_3 in Fig. 2.5 using the same reference signal as Fig. 2.4(a). To simplify the description of the operation with dynamic DC restoration, we assume the pulse starts with the initial voltage in the transformer having had decayed to zero and that the voltage at the logic inverter is at a valid logic voltage state (V_L in Fig. 2.5). A rising edge from the reference signal v_{ref} manifests as a rising on the logic inverter input voltage ($v_N + v_{gate}$), which subsequently decays with time constant τ. A second rising edge at the input of the logic inverter manifests from the positive feedback from the gate driver output after the composite propagation delay T_{pd}. This positive feedback creates an offset to the transformer secondary voltage that remains even after the voltage across the secondary winding voltage v_N has drooped to zero, hence holding the input to the logic inverter at a valid logic state (V_H in Fig. 2.5). This valid input V_H holds a valid V_H at the gate driver output indefinitely until a falling edge from the reference signal. The behavior is similar for a V_H to V_L pulse.

2.2.3 Design Criteria for the Isolated Ultrafast Gate Driver

In this section, we discuss the sufficient conditions for the proper operation of this gate driver. Transformer isolation in Fig. 2.1 requires zero average voltage at the primary, which is ensured by

a dc blocking capacitor.

2.2.3.1 Periodic Short-Pulse Operation

The sufficient condition for the upper bound on the aggregate propagation delay is

$$T_{\text{pd}} < \min\{T_{\text{on}}, T_{\text{off}}\} - 0.5 \max\{t_{\text{rg}}, t_{\text{fg}}\}, \tag{2.1}$$

where t_{rg} and t_{fg} are the rise and fall times of v_{gate}, which ensures non-zero durations for the plateaus and valleys in Fig. 2.3. In addition, ledge B must be below the threshold V_{th} and ledge A must be above to ensure that the first logic inverter will be triggered, which requires

$$V_{\text{N}} > \frac{T_{\text{s}}}{2\,(2 \cdot \min\{T_{\text{on}}, T_{\text{off}}\} + t_{\text{rN}} + t_{\text{fN}})}(V_{\text{H}} - V_{\text{L}}), \tag{2.2}$$

where t_{rN} and t_{fN} are the rise and fall times of v_{N} shown in Fig. 2.3. As long as conditions (2.1) and (2.2) are maintained, voltage clamping the input of the logic inverter does not change the trigger points, even though the waveforms are modified. In choosing V_{c}, it important to note that in practice, the transformer coupling coefficient k should be included with turns ratio N so that $V_{\text{c}} = V_{\text{N}}/k\,\text{N}$.

2.2.3.2 Arbitrary Long-Pulse Operation

For proper operation, the pulse widths need to satisfy $\min\{t_1, t_2, t_3\} > T_{\text{pd}}$ from (2.1). There is a condition on the minimum value of the peak-to-peak open-circuit voltage at the transformer secondary

$$2V_{\text{N}} \geq V_{\text{clampH}} - V_{\text{clampL}}. \tag{2.3}$$

Additional conditions for arbitrary long-pulse operation are minimum and maximum limits on the droop time constant τ. The droop time constant, which can be considered a design variable, is determined by the magnetizing inductance of the transformer and the resistance represented by R for a large dc blocking capacitor in Fig. 2.1. The maximum value of τ is determined by the minimum design requirement for t_1 and t_2 and the technology limitations on T_{pd} and V_{th}, but can be adjusted by choice of logic levels V_{H} and V_{L}, and clamp voltages V_{clampH} and V_{clampL} if allowed by technology choice (e.g. IC design/process or discrete logic inverter),

$$\tau < \min\left\{\frac{V_{\text{clampH}} - V_{\text{H}}}{V_{\text{H}} - V_{\text{th}}}\,t_1 + \frac{V_{\text{H}} - V_{\text{L}}}{V_{\text{H}} - V_{\text{th}}}\,T_{\text{pd}}\,,\ \frac{V_{\text{L}} - V_{\text{clampL}}}{V_{\text{th}} - V_{\text{L}}}\,t_2 + \frac{V_{\text{H}} - V_{\text{L}}}{V_{\text{th}} - V_{\text{L}}}\,T_{\text{pd}}\right\}. \tag{2.4}$$

The minimum value of τ is only determined by technology limitations and voltage level choices

$$\tau > \max\left\{\frac{T_{\text{pd}}}{\ln\left(\frac{V_{\text{clampH}}-V_{\text{L}}}{V_{\text{th}}-V_{\text{L}}}\right)}, \frac{T_{\text{pd}}}{\ln\left(\frac{V_{\text{H}}-V_{\text{clampL}}}{V_{\text{H}}-V_{\text{th}}}\right)}\right\}. \tag{2.5}$$

Equations (2.4) and (2.5) can be combined to calculate lower bounds on t_1 and t_2 that may supersede the limit from (2.1),

$$t_1 > \frac{V_{\text{H}}-V_{\text{th}}}{V_{\text{clampH}}-V_{\text{H}}}T_{\text{pd}} \times \left[\frac{1}{\ln\left(\frac{V_{\text{clampH}}-V_{\text{L}}}{V_{\text{th}}-V_{\text{L}}}\right)} - \frac{V_{\text{H}}-V_{\text{L}}}{V_{\text{H}}-V_{\text{th}}}\right]; \tag{2.6}$$

$$t_2 > \frac{V_{\text{th}}-V_{\text{L}}}{V_{\text{L}}-V_{\text{clampL}}}T_{\text{pd}} \times \left[\frac{1}{\ln\left(\frac{V_{\text{H}}-V_{\text{clampL}}}{V_{\text{H}}-V_{\text{th}}}\right)} - \frac{V_{\text{H}}-V_{\text{L}}}{V_{\text{th}}-V_{\text{L}}}\right]. \tag{2.7}$$

Together, (2.1) and (2.3)–(2.7) are a set of sufficient conditions for operation in combined long-pulse and short-pulse regimes as exemplified by Fig. 2.5, which is similar to a double pulse test. If t_1 is a long pulse, which means the current in the transformer primary converges to V_{ref}/R, then the minimum requirement on t_2 is that the transformer has sufficiently reset before the leading edge of t_3 so that the logic inverter input voltage reaches the threshold V_{th} on this edge; it is worth noting that τ can also be considered as the transformer reset time constant. Condition (2.5) ensures that the input voltage of the logic inverter remains correctly asserted after the reference signal assertion at the leading edge of t_2 through the duration of the propagation delay T_{pd} so that the positive feedback affirmatively returns the valid value asserted by the reference signal. Similarly, the additive term in (2.4), which involves T_{pd}, is derived from the fact that the input voltage to the logic inverter, after the reference signal assertion at the leading edge of t_3, must remain correctly asserted above the threshold voltage V_{th} at the logic inverter input through the duration of the propagation delay T_{pd} so that the positive feedback affirmatively returns the valid value asserted by the reference signal. The behavior of all subsequent pulses can be inferred from this same analysis.

2.3 Implementation and Validation

2.3.1 Signal Transformer Design

Dynamic DC restoration using positive feedback eases the signal transformer design requirements because of droop tolerance and potentially improves isolation. Droop tolerance allows lower magnetizing inductance within the limits given by (eq:tau1) and (eq:tau2). Together with fewer required turns, intrawinding (turn-to-turn) capacitance is decreased and higher self-resonant fre-

quency is possible. Leakage inductance trades off with interwinding (primary-secondary coupling) capacitance. For example, bifilar windings have low leakage inductance, but high interwinding capacitance whereas $180°$ sector windings have the opposite; a sector wound transformer can be used to trade off leakage inductance with interwinding capacitance [55]. The maximum tolerable interwinding capacitance is application dependent; it depends on the dv/dt of v_{source} relative to control voltage ground. Two factors limit the tolerable leakage inductance:

1. the resonance formed by the secondary-referred leakage inductance and the input capacitance at the logic inverter must have a frequency whose period T_{lc} is much smaller than the minimum on- or off-time

$$T_{\text{lc}} \ll \min\left\{T_{\text{on}},\, T_{\text{off}}\right\};$$

2. the attenuated V_{c} from the voltage divider formed by the primary magnetizing inductance L_μ and leakage inductance L_{l1} must satisfy the maximum among voltages specified in (2.2) and (2.3)

$$\frac{L_\mu}{L_{\text{l1}} + L_\mu}\text{N}V_{\text{c}} > V_{\text{N}}.$$

   This attenuation can be accommodated by higher control voltage V_{c}.

Dynamic DC restoration prevents droop from encroaching on the logic inverter input noise margins by maintaining a valid input state; this enables better tolerance to ringing and thus may allow higher leakage inductance, which subsequently can mean lower interwinding/coupling capacitance.

2.3.2 Component Selection

The core of the isolated ultrafast gate driver is composed of an RF signal transformer and high-speed logic inverters. WBC4-14L from Coilcraft has a turns ratio of $1:2$ and a bandwidth from 1.5 MHz to 1.2 GHz. Six different logic inverters were tested as shown in Table 2.1 and Fig. 2.6; these inverters included buffered (*suffix xxx04*) and unbuffered (*suffix xxxU04*) variants from three companies: TI, NXP, and OnSemi.

We drive an EPC 2038 GaN FET because it can be employed in pulsed lasers for LiDAR and is useful for VHF power electronics because of its small output capacitance C_{oss}. The gate charge of the EPC 2038 ($Q_{\text{g}} = 44\,\text{pC}$) requires an average driving current at switching frequency f_{s} of $I_{\text{avg}} = Q_{\text{g}}\, f_{\text{s}}$, which is $4.4\,\text{mA}$ at 100 MHz, which means that any of the individual logic inverters in Table 2.1 has the driving capability.

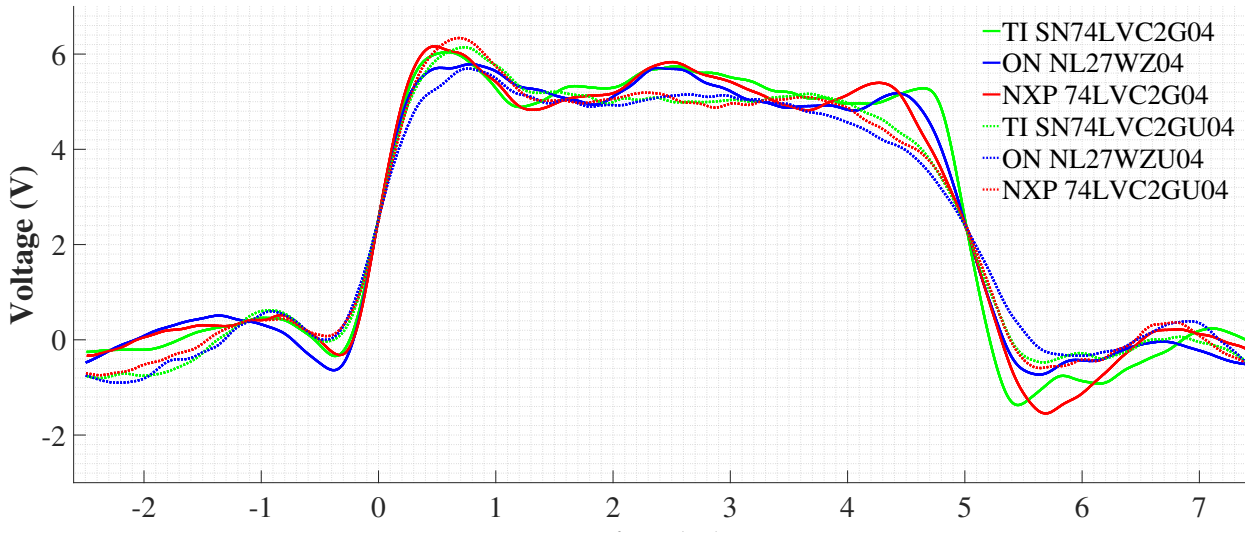

Figure 2.6: Single-cycle gate voltage comparison among different dual logic inverters. The experimental data were collected with a 4 GHz measurement system with 1 TS/s sampling rate and re-plotted in Matlab.

Each of the logic inverters in Table 2.1 are contained in a dual package and were tested under identical conditions ($V_{\mathrm{H}} = 5\,\mathrm{V}$ and $V_{\mathrm{L}} = 0\,\mathrm{V}$) using the same double pulse test circuit. The superimposed gate voltages are shown in Fig. 2.6 at a duty cycle that is approximately 50 %. Table 2.1 shows each rise time t_{r} and fall time t_{f}, which are calculated over the 20 % to 80 % amplitude interval along with the corresponding gating loss P_{loss} at 100 MHz.

Gate voltages and timing intervals were measured using a 4 GHz TAP4000 active probe and a 4 GHz 6-series mixed-signal oscilloscope with a 1 TS/s sampling rate, both from Tektronix. The TAP4000 is a 10X active voltage probe with an 8 V dynamic range and less than 0.8 pF of probe capacitance, which represents minimal loading for measurements on the equivalent 8 pF

Table 2.1: Experimental Comparison Using Dual Logic Inverters for Ultrafast Gate Drivers at 100 MHz Switching

Component (Manufacturer)	t_{r} (ps)	t_{f} (ps)	P_{loss} (mW)
SN74LVC2G04 (TI)	259	245	108
NL27WZ04 (On Semi)	255	462	120
74LVC2G04 (NXP)	228	496	146
SN74LVC2GU04 (TI)	301	686	183
NL27WZU04 (On Semi)	345	928	189
74LVC2GU04 (NXP)	273	911	220

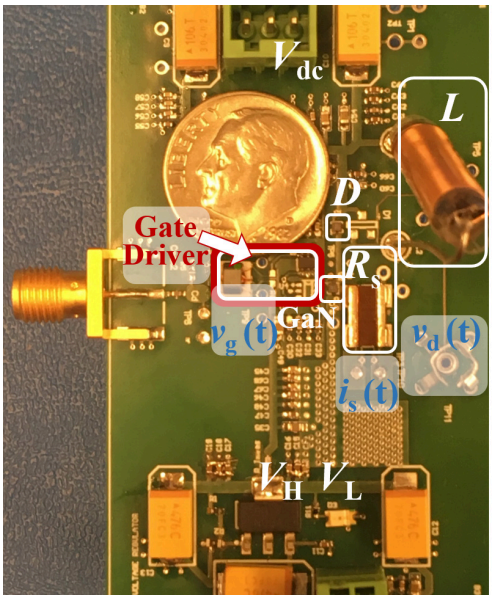

Figure 2.7: PCB of the double pulse test circuit with the miniaturized isolated ultrafast gate driver for EPC 2038 with WBC4-14L and SN74LVC2G04.

EPC 2038 gate capacitance. Gating loss was measured using two 6.5-digit 34465A multimeters from Keysight.

In practice, several factors influence the propagation delay of the logic inverters and so the worst-case value should be used from the datasheet that corresponds to the expected operating range. Higher die temperature increases the propagation delay, but higher power supply voltage decreases it.

The input and output of logic inverters have clamp diodes to protect against over- and under-voltages. These clamps are rated for a specific current; for example, the SN74LVC2G04 has an absolute maximum allowable clamp current of 50 mA. The maximum current at the transformer secondary is typically limited by the surge impedance, which corresponds to the reflected characteristic impedance across the RF signal transformer; also, an explicit resistor (e.g. for matching) will also limit this current.

The SN74LVC2G04 from Texas Instruments, which has a buffered output, has the best overall performance in t_r, t_f, and P_{loss}; rise and fall slew rates are 12.0 GV/s and 12.7 GV/s, respectively.

2.3.3 Double Pulse Test Circuit

The double pulse test (DPT) is one of the critical methods to evaluate the performance of a gate driver under hard-switching conditions [56] and arbitrary long-pulse operation. We evaluate the EPC 2038 in the isolated ultrafast gate driver at 45 V and 0.3 A drain voltage and current. The DPT

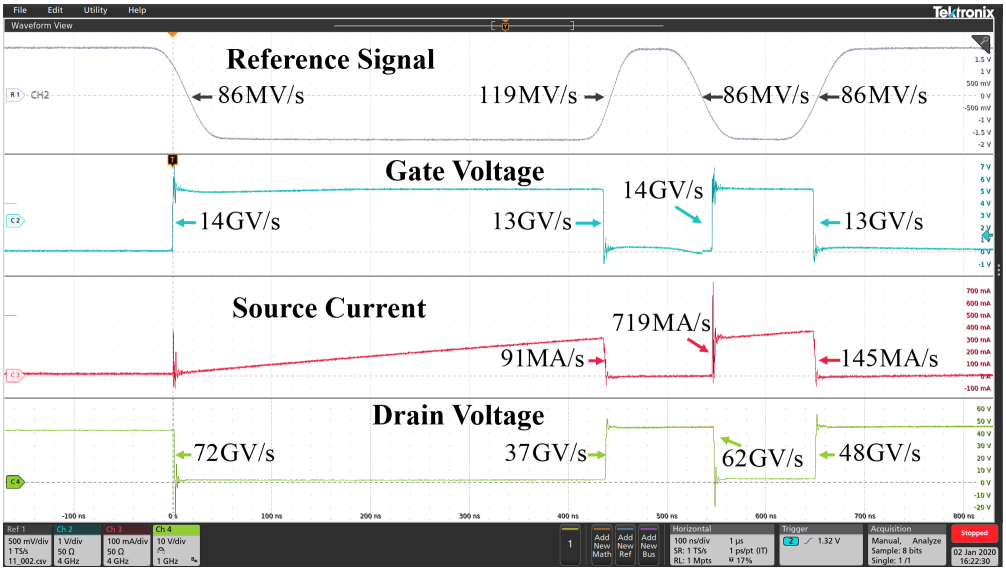

Figure 2.8: Typical waveforms of DPT. The gate voltage $v_{\mathrm{g}}(t)$ was measured with a 4 GHz TAP4000 active probe, the source current $i_{\mathrm{s}}(t)$ was measured with a 4 GHz TDP7704 probe in differential mode and a sense resistor, and the drain voltage $v_{\mathrm{d}}(t)$ was measured with a 1 GHz TPP1000 passive probe. The test points on the PCB are marked in Fig. 2.7.

circuit was implemented using a diode-connected EPC 2038 with the gate shorted to the source (which conducts as a freewheeling diode with the current in the reverse direction), a 56 μH inductor (EPCOS B8211E series) as the inductive load, and a 5 Ω shunt resistor (Vishay VCS1625ZP) as the current sensor.

There are several considerations for printed circuit board layout. These include maintaining adequate clearance between the ground planes on the control side and the power side to minimize the stray coupling capacitance. For power devices with high di/dt, using Kelvin connections to the source for gate driving results in a smaller voltage transient on v_{source} in Fig. 2.1. Fig. 2.7 shows the PCB and Fig. 2.8 shows typical DPT waveforms with corresponding slew rates labeled.

A continuous 100 MHz control signal with 40 % duty cycle was also evaluated using the same circuit for DPT. Figure 2.9 shows the time-domain waveforms: v_c, v_{N}, v_{gate}, and $v_{\mathrm{N}} + v_{\mathrm{gate}}$, which is similar to Fig. 2.3; although the maximum and minimum voltages of $v_{\mathrm{N}}\,(t) + v_{\mathrm{gate}}\,(t)$ are clamped, the timing validates the approximations in Section 2.2.

A continuous 165 MHz control signal with narrow pulses was also evaluated using the same circuit for DPT. Figure 2.10 shows the time-domain waveform of v_{gate}. The gate voltage has rise and fall times of 280 ps and 263 ps, respectively, and corresponding slew rates of 10.94 GV/s and 11.65 GV/s. The pulse width is narrow at 1.237 ns when measuring at 80 % of the driving voltages $V_{\mathrm{H}} = 5\,V$ and $V_{\mathrm{L}} = 0\,V$. The gating loss is 183 mW.

The strategies employed in this gate driver topology could possibly be used for isolated control

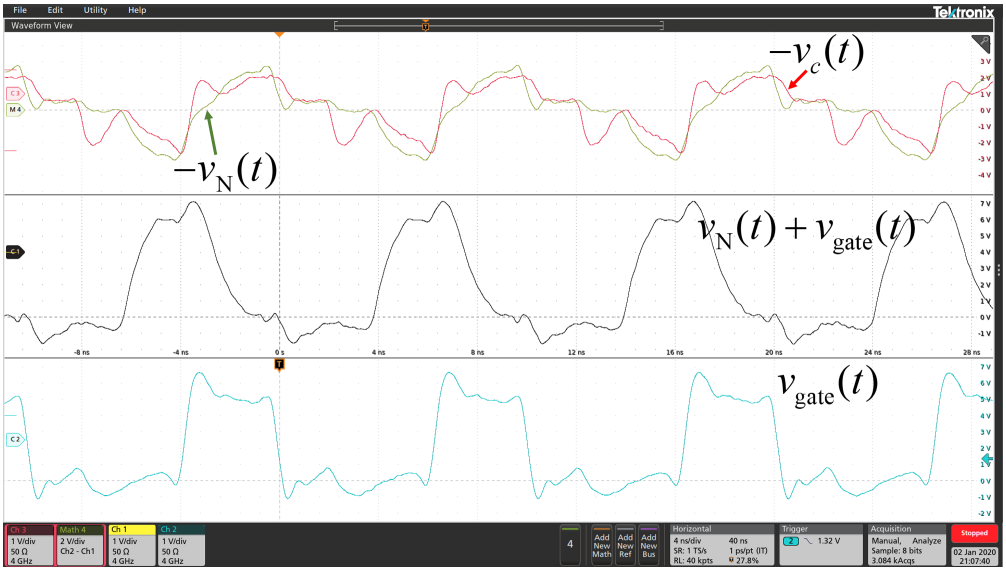

Figure 2.9: A demonstration of the gate voltage with a duty cycle of 40 %. $v_{gate}(t)$ and $v_N(t) + v_{gate}(t)$ were measured with 4 GHz TAP4000 active probes while $v_c(t)$ was measured with a 4 GHz TDP7704 probe in differential mode. Four voltage levels: plateau, valley, ledge A, and ledge B from Section 2.2, can be observed in $v_N(t) + v_{gate}(t)$, which are clamped by the logic inverter input diodes. The discrepancy between the scope traces for $v_c(t)$ and $v_N(t)$ and the idealized waveforms in Fig. 2.3 can be attributed to the resonance between the transformer leakage inductance and the input capacitance of the logic inverter gate. In addition, impedance mismatches occur in the signal path from the input cable, PCB traces, and component parasitics.

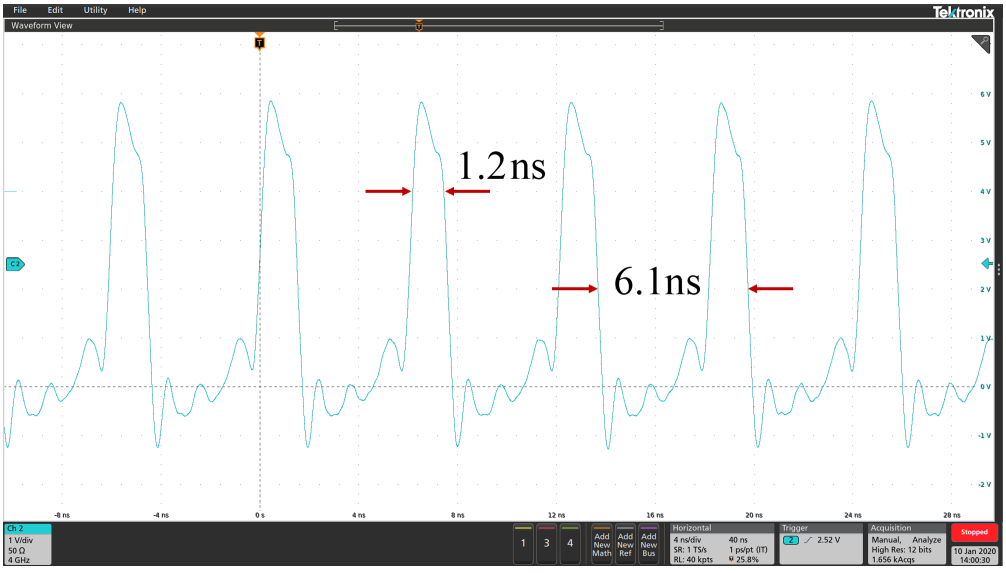

Figure 2.10: A demonstration of the gate voltage with a narrow pulse of 1.237 ns at 164.6 MHz repetition rate. $v_{gate}(t)$ was measured with a 4 GHz TAP4000 active probe. The rise and fall times are 280 ps and 263 ps, respectively, with corresponding slew rates of 10.94 GV/s and 11.65 GV/s.

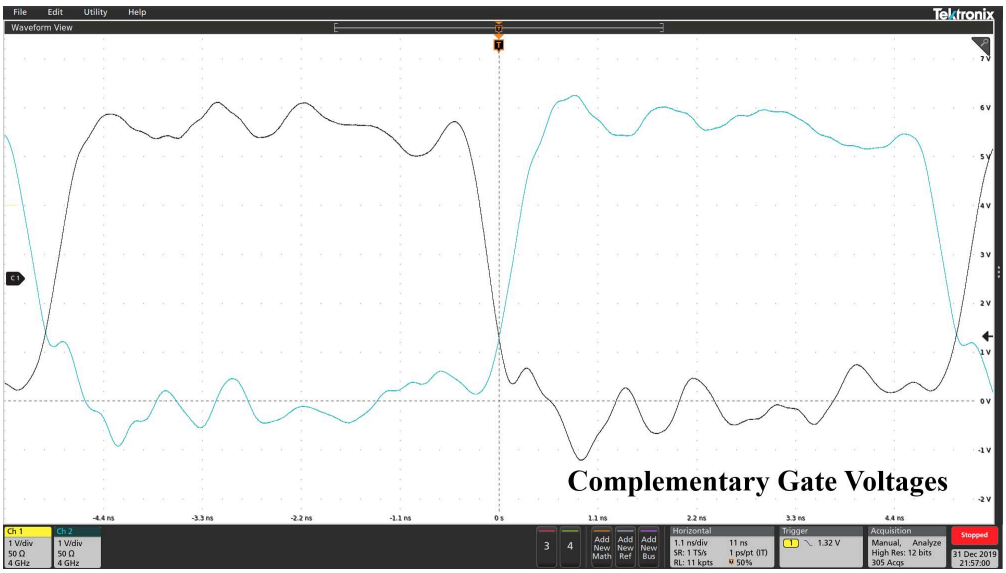

Figure 2.11: Complementary gate voltages in the current-mode class D power converter with a TI SN74LVC2G04 as the logic inverters using 4 GHz TAP4000 active probes and 1 TS/s sampling rate.

feedback loops in VHF converters as it provides fast response and pulse preservation.

2.3.4 Symmetric CMCD WPT System

The isolated ultrafast gate driver was used in a symmetric CMCD WPT system operating at 100 MHz, whose design and implementation details can be found in [4]. With the gate driver using a dual inverter gate SN74LVC2G04, the gating loss P_{gate} is 0.26 W, which is a 57 % improvement from the previous 0.61 W in [4] using the same driving voltages $V_{\text{H}} = 5.5\,\text{V}$ and $V_{\text{L}} = 0\,\text{V}$. The gate voltages are shown in Fig. 2.11, which are required to have greater than 50 % duty cycle for proper switch overlap. The rise and fall times are below 300 ps with a slew rate above 10 GV/s. The system achieves an output power P_{o} of 2.6 W, dc-dc efficiency η (without P_{gate}) of 71 %, and a total efficiency (including gating loss) η_{total} of 66 %, as shown in Table 2.2. The hardware is shown in Fig. 2.12.

Implementation with a different logic inverter NL27WZU04 under the same gate driver conditions resulted in a slower rise and fall time, as observed in Fig. 2.6 and Table 2.1. Maintaining the same input power P_{in} at 3.6 W and identical set-ups [4], the WPT system using the NL27WZU04 has significantly lower output power P_{o}, dc-dc efficiency η without P_{gate}, and η_{total}, along with higher gating loss P_{gate}, as shown in Table 2.2.

Based on these comparisons of the effect of gate driver speeds on resonant converter efficiencies, a properly designed isolated ultrafast gate driver results in a significant improvement.

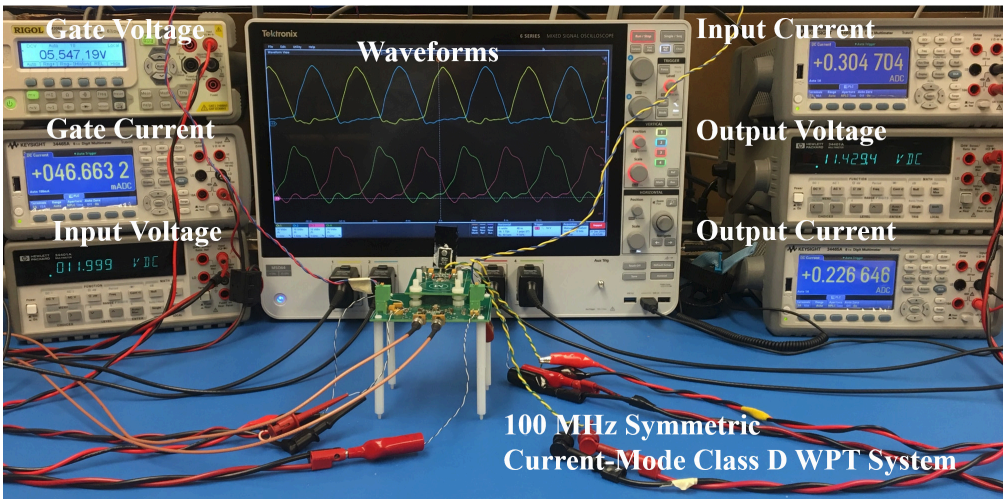

Figure 2.12: Hardware test and measurement of the ultrafast gate driver in a 100 MHz symmetric CMCD WPT system. $P_{\text{in}} = 3.656$ W, $P_{\text{o}} = 2.590$ W, $P_{\text{gate}} = 0.259$ W, η (without P_{gate}) = 70.8 %, and $\eta_{\text{total}} = 66.2$ %.

Table 2.2: End-to-End Experimental WPT Performance of the Gate Drivers

Gate Driver Type	P_{o} (W)	P_{gate} (W)	η w/o P_{gate} (%)	η_{total} (%)
SN74LVC2G04	2.59	0.259	70.8	66.2
NL27WZU04	2.35	0.404	64.4	58.0

2.3.5 Higher Power GaN FET

An isolated ultrafast gate driver for larger power devices requires higher current capability. Fig. 2.13 shows the results for the GS-065-004-1-L from GaN Systems with a voltage rating of 650 V and a current rating of 3.5 A. It requires a gate drive average current of 70 mA at 100 MHz, which is approximately 16 times that of the EPC 2038 and needs parallel logic inverter gates to provide the output current capability. A single logic inverter SN74LVC1G04 is used for the first stage and six dual logic inverters SN74LVC2G04 are used in parallel for a total of twelve for the second stage. The rise and fall times are 206 ps and 268 ps, respectively, with corresponding slew rates of 16.01 GV/s and 12.31 GV/s. The gating loss is 1.436 W at $V_{\text{H}} = 5.5\,V$ and $V_{\text{L}} = 0\,V$.

2.4 Summary

An isolated, variable duty cycle, ultrafast gate driver capable of arbitrarily long on- and off- times has been presented, analyzed, and evaluated. The ultrafast gate driver can operate at 100 MHz with a noteworthy slew rate of above 12 GV/s and gating loss of 108 mW per switch at a driving voltage

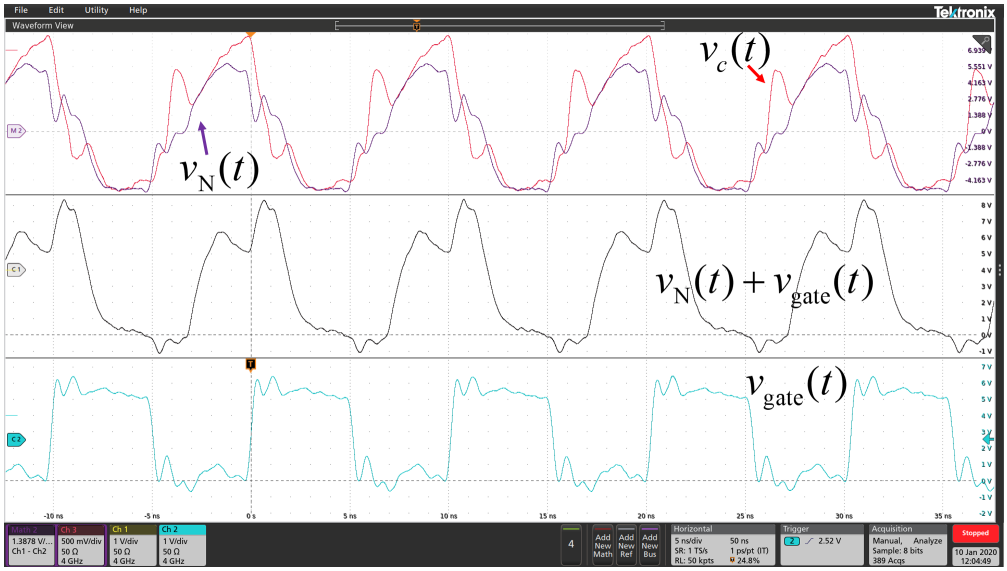

Figure 2.13: A higher power GaN FET GS-065-004-1-L from GaN Systems is used to test the capability of the isolated ultrafast gate driver. The duty cycle is 55 %. $v_{gate}(t)$ and $v_N(t) + v_{gate}(t)$ were measured with 4 GHz TAP4000 active probes while $v_c(t)$ was measured with a 4 GHz TDP7704 probe in differential mode. The rise and fall times are 206 ps and 268 ps, respectively, with corresponding slew rates of 16.01 GV/s and 12.31 GV/s.

of 5 V, and deliver narrow 1.2 ns pulses at 165 MHz. It can drive a pulse power device with a drain slew rate of more than 37 GV/s.

CHAPTER 3

Field Cancellation and Manipulation

3.1 Introduction

Wireless power transfer (WPT) is an enabling and supportive technology for implantable and wearable medical devices [57, 58], wearable and portable consumer electronics [59], and Internet of Things (IoT) devices [9, 60]. The size of WPT coils are the physical dimension boundary for these applications. There is a trend in these applications for circuits to be encircled by WPT coils [59, 61, 62] for compactness and miniaturization. However, sensors, transceivers, measurement circuits, and some integrated circuits encircled by the WPT coils are sensitive to magnetic field, especially at higher frequencies, where voltage and current can be more easily induced; these applications need field cancellation to maintain proper function.

Very high frequency (VHF) achieves miniaturization by reducing the size and count of inductors and capacitors, which can be easily encircled by WPT coils in compact and miniaturized devices. VHF operation also facilitates high quality factor for air-core inductors, requiring less space and volume. VHF WPT can increase the receiver voltage for a single-turn receiver coil and given magnetic flux, improving the miniaturized passive rectifier [9, 52] efficiency and power.

The goal of field cancellation is to achieve the best cancellation performance and require the least number of components for compactness, miniaturization, practical construction, and lowest cost. There has been research on achieving these in wireless power transfer at lower frequencies. Using additional cancelling coils carrying opposite-phase currents is a prevalent method. The cancelling coil currents can be actively fed [63] or generated by an induced voltage [64–67]. Resonant reactive shielding uses series LC resonant cancelling coils to cancel the field with the induced voltage [64–67]. However, in practice, the current amplitude cannot be adequately controlled. Thus, the magnetic field cannot be adequately cancelled. Actively-driven methods can control the cancelling current level to optimize field cancellation, but usually need two separate power electronics circuits that have to be synchronized and separately controlled [63], which is poor for miniaturization, compactness, and cost. Using a single source driving the two coils with multiple turns

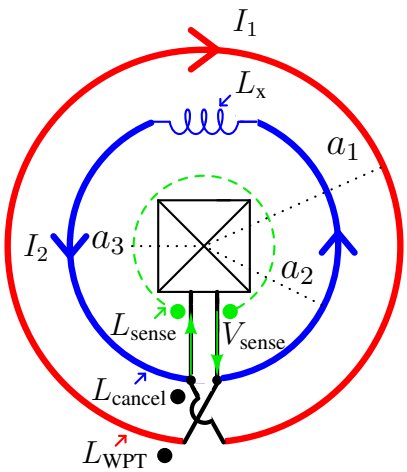

Figure 3.1: The field cancellation method for VHF wireless power transfer.

or windings is possible in simulation [62], but it is typically difficult to implement at higher frequencies because of intrawinding (turn-to-turn) capacitance and with more space and cost. Other shielding methods including passive shielding [60, 68] and Halbach windings [69] are also used, but cannot achieve the goal as well.

In this chapter, we introduce a field cancellation method for VHF WPT systems, which can achieve excellent cancellation performance for encircled circuits, requiring only an additional air-core inductor in series with the cancelling coil, as shown in Fig. 3.1. The field cancelling coil is concentric and wired in parallel with the WPT coil with opposite current flow. Both coils are fabricated with PCB traces, which are consistent and inexpensive. The two coils are driven by a single power electronics inverter, i.e. current-mode class D (CMCD) inverter, which has been demonstrated to be robust and resilient even at 100 MHz [9, 15]. The current amplitude of the cancelling coil is independently determined to optimize the field cancellation even when using the same driver for the WPT coil. For validation, an open-circuit sensing coil, which is fabricated with a thin PCB trace, encircles the circuits including the CMCD to measure the remaining magnetic flux. With the field cancellation method, the magnetic flux is decreased by 99 % at the fundamental frequency from hardware data.

3.2 Field Cancellation Method

A two-coil structure driven by a single power converter, generating two opposite-phase currents with independently determined amplitudes, minimizes the magnetic field for the electronics circumscribed by the WPT coils at low cost. The field cancellation method can be used in transmitters

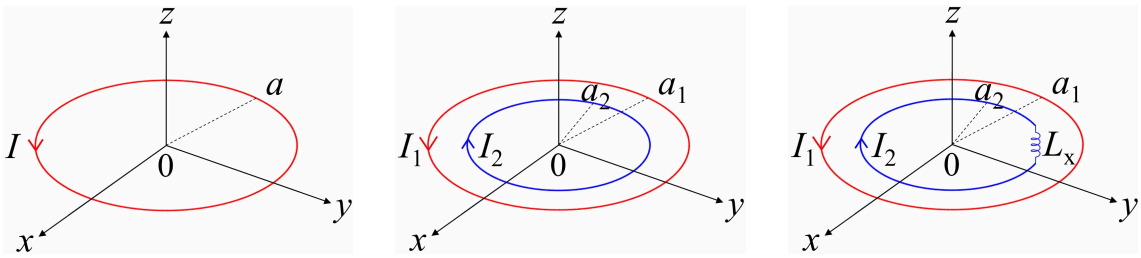

(a) A single coil. (b) Two coils. (c) Two coils with L_x.

Figure 3.2: Different coil configurations.

and receivers. The inner coil is L_{cancel} with radius a_2, the outer coil is L_{WPT} with radius a_1, and the encircled circuits are within a 2D circular area with radius a_3, as shown in Fig. 3.1.

3.2.1 Analysis of Magnetic Field of a Circular Current Coil

The filament circular coil carrying a current I with radius a is located on the $z = 0$ plane and centered at the origin as shown in Fig. 3.2(a). From the vector potential $\boldsymbol{A}$ of the coil, we can derive the magnetic field $\boldsymbol{B}$ [70, 71] and

$$B_z = \frac{\mu_0 I}{2\pi\alpha^2\beta}\left[\left(a^2 - \rho^2 - z^2\right)E(m) + \alpha^2 K(m)\right], \tag{3.1}$$

where $\alpha^2 = (a-\rho)^2 + z^2$, $\beta^2 = (a+\rho)^2 + z^2$, $\rho^2 = x^2 + y^2$, and $m = 1 - \alpha^2/\beta^2$. $E(m)$ and $K(m)$ are complete elliptic integral of the 1st and 2nd kinds, respectively.

Along the center axis, $B_\rho = 0$ and

$$B_z(\rho = 0, z) = \frac{\mu_0 I a^2}{2\left(a^2 + z^2\right)^{\frac{3}{2}}}, \tag{3.2}$$

where $\alpha^2 = \beta^2 = a^2 + z^2$ and $m = 0$.

At the origin, $B_\rho = 0$ and

$$B_z(\rho = 0,\ z = 0) = \frac{\mu_0 I}{2a}, \tag{3.3}$$

where $\alpha^2 = \beta^2 = a^2$ and $m = 0$.

On the $z = 0$ plane, $B_\rho = 0$ and

$$B_z(\rho,\ z = 0) = \frac{\mu_0 I}{2\pi}\left[\frac{E(m)}{a-\rho} + \frac{K(m)}{a+\rho}\right], \tag{3.4}$$

where $m = 4a\rho/(a+\rho)^2$.

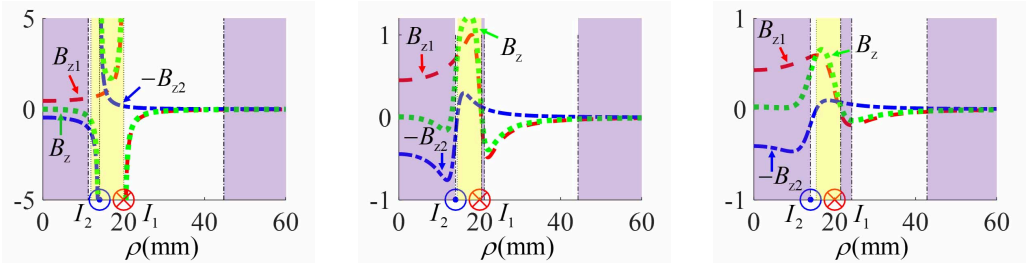

(a) z =0 mm. (b) z =2 mm. (c) z =4 mm.

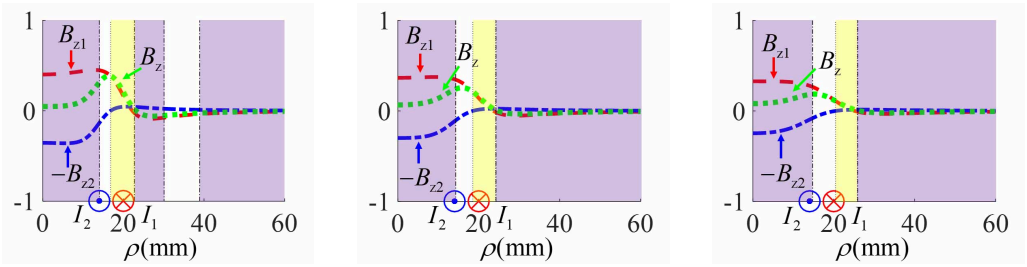

(d) z =6 mm. (e) z =8 mm. (f) z =10 mm.

Figure 3.3: Normalized magnetic fields at different heights from the two coils as shown in Fig. 3.2(b), which satisfies (3.6). B_{z1} and $-B_{z2}$ are the magnetic fields generated by I_1 and $-I_2$, respectively, while B_z is derived from superposition. All the fields are normalized to $|B_{z1}|_{max}$ when z =2 mm. $|B_z|$ is lower by at least 30 % compared to $|B_{z1}|$ in the purple region while $|B_z|$ is larger than $|B_{z1}|$ in the yellow region.

In this chapter, we only analyze B_z for simplicity.

3.2.2 Magnetic Field Cancellation

If two filament circular coils carrying two opposite-phase currents I_1 and $-I_2$ with radius a_1 and a_2 are located on the $z = 0$ plane and centered at the origin as shown in Fig. 3.2(b), the field can be decreased for $\rho < a_2$ and $\rho > a_1$ but increased for $a_2 < \rho < a_1$ on the $z = 0$ plane. The total magnetic field is calculated by superposition of the fields from each coil

$$B_z(\rho,\, z) = B_{z1}(\rho,\, z) - B_{z2}(\rho,\, z), \tag{3.5}$$

where $B_{z1}(\rho,\, z)$ and $B_{z2}(\rho,\, z)$ can be calculated in (3.1) for the two coils.

$B_z(\rho = 0,\, z = 0) = 0$ is the most straightforward optimization goal for field cancellation at the origin with the optimal solution of

$$\left|\frac{I_1}{I_2}\right| = \frac{a_1}{a_2}. \tag{3.6}$$

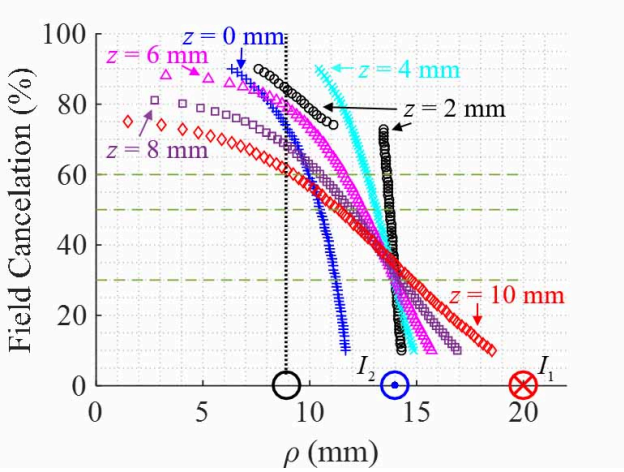

Figure 3.4: Field cancellation performance at different heights and radii with the field cancellation condition (3.6).

The field cancellation performance at each single point can be defined by

$$\left.\frac{\Delta B_z}{B_z}\right|_{\rho,\,z} = \frac{\big||B_z(\rho,\,z)| - |B_{z1}(\rho,\,z)|\big|}{|B_{z1}(\rho,\,z)|} \times 100\,\%, \tag{3.7}$$

where $B_{z1}(\rho,\,z)$ is the field without cancellation as shown in Fig. 3.2(a) and $B_z(\rho,\,z)$ is the total field with cancellation as shown in Fig. 3.2(b). An example of two-coil field cancellation satisfying (3.6) is shown in Fig. 3.3 where $a_1 = 20\,\text{mm}$ and $a_2 = 14\,\text{mm}$. All the fields are normalized to $|B_{z1}|_{\text{max}}$ at z =2 mm. The purple region represents the magnetic field of Fig. 3.2(b) decreasing by more than 30 % compared to that in Fig. 3.2(a) at each point, i.e. $\Delta B_z/B_z|_{\rho,\,z} \geq 30\,\%$. The yellow region represents the magnetic field increasing in the region, i.e., $|B_z| > |B_{z1}|$.

With one cancelling coil, the portion of the magnetic field that can be cancelled depends on the size of the encircled circuit, i.e. a_3. Fig. 3.4 shows the relationship between $\Delta B_z/B_z$ and maximum radius ρ that maintains a specific $\Delta B_z/B_z$ at different heights. If a minimum of 60 % cancellation is desired for every point in the encircled region, the circuits must be within a radius of 8.89 mm for component heights within 0 mm to 10 mm. $\rho \leq 8.89\,\text{mm}$ and $z \leq \pm 10\,\text{mm}$ is the field cancellation volume for the hardware; larger volume can be achieved at lower cancellation.

3.2.3 Magnetic Field Cancellation Optimization

Magnetic field can also be optimized over a 2D area or a 3D volume. The variables that determine the cancellation are the radius of the inner coil a_2 and amplitude of its current $|I_2|$. V_{sense} is proportional to magnetic field [72] and hence can be used to indicate cancellation. For example, for a 2D area on the $z = 0$ plane, the optimization problem becomes

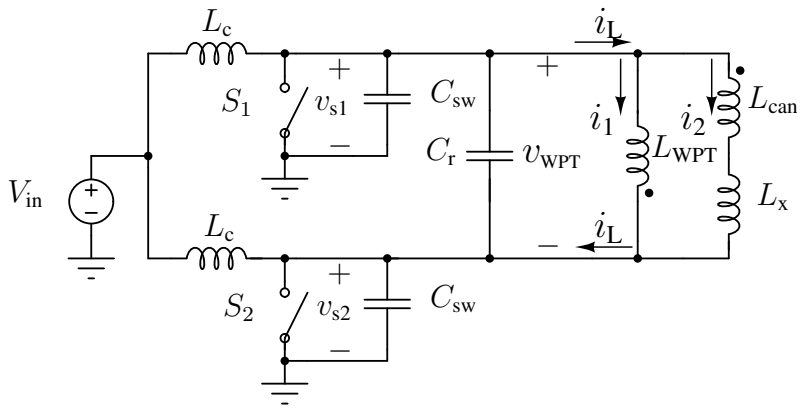

Figure 3.5: Current-mode class D (CMCD) power converter with field cancellation.

$$\begin{aligned} \min_{a_2,\,|I_2|} \quad & V_{\text{sense}} \\ \text{s.t.} \quad & a_3 < a_2 < a_1 \\ & |I_2| < |I_1| \end{aligned} \tag{3.8}$$

where $V_{\text{sense}} = -d\phi/dt$ from Faraday's law of induction. ϕ is the flux over the encircled circuits that are within a circular area with radius a_3, i.e., $\phi = 2\pi \int_0^{a_3} B(\rho,\, z=0)\rho\, d\rho$. $B_{\text{z}}(\rho,\, z=0) = B_{\text{z1}}(\rho,\, z=0) - B_{\text{z2}}(\rho,\, z=0)$, where $B_{\text{z1}}(\rho,\, z=0)$ and $B_{\text{z2}}(\rho,\, z=0)$ can be calculated through (3.4). A stack of or concentric multiple coils can be used to further manipulate the magnetic field distribution profile, but is an additional investigation outside the scope of this chapter.

In this paper, $a_2 = (a_1 + a_3)/2$ was selected for simplicity. The optimization variable is $|I_2|$ with the opposite phase of I_1. Because $a_2 < a_1$, we observe $L_{\text{cancel}} < L_{\text{WPT}}$. If the two coils are driven by a single source, an extra inductor L_{x} is needed in series with L_{cancel} to maintain the constraint $|I_2| < |I_1|$ for the same voltage. For a given a_1/a_2, different sets of $|I_1|/|I_2|$ have different field cancellation performance within a_3 for the encircled circuits. There is an optimal $|I_2|$ for a given a_2 that has the best field cancellation performance, i.e., a minimum V_{sense}.

3.2.4 Equivalent WPT Coil and its Driver

A robust and resilient current-mode class D (CMCD) inverter is selected to drive the two coils at VHF because CMCD absorbs device and circuit parasitics, tolerates component mismatch, and has ground-referenced switches [9, 15], as shown in Fig. 3.5. The design and implementation of a CMCD power converter with its gate driver at VHF can be found in [9, 15].

Because of L_{cancel}, L_{x}, and coupling coefficient k between L_{cancel} and L_{WPT}, the equivalent

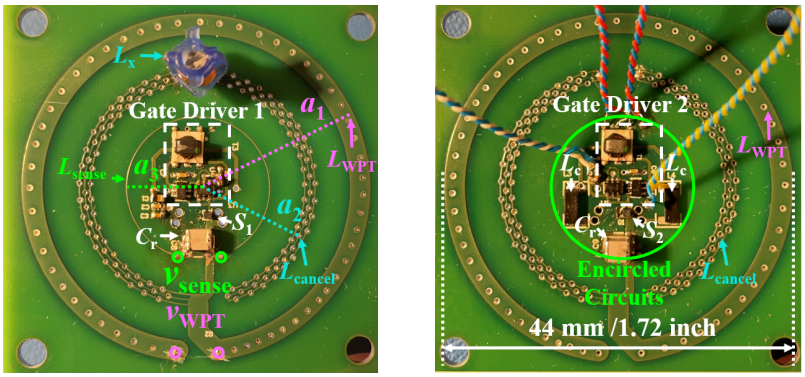

(a) Front side. (b) Back side.

Figure 3.6: Miniaturized hardware with the field cancellation method.

resonant inductor in the CMCD inverter becomes

$$L_{\text{eq,r}} = \frac{V_{\text{WPT}}}{j\omega(I_1 + I_2)} = \frac{L_{\text{WPT}}\left(L_{\text{cancel}} + L_{\text{x}}\right) - M^2}{L_{\text{WPT}} + \left(L_{\text{cancel}} + L_{\text{x}}\right) + 2M}, \tag{3.9}$$

where $M = k\sqrt{L_{\text{WPT}}L_{\text{cancel}}}$ and $L_{\text{eq,r}}$ behaves as the self-inductance of an equivalent WPT coil. With the coupling, the currents that flow through L_{cancel}, L_{x}, and L_{WPT} are

$$I_1 = \frac{V_{\text{WPT}}}{j\omega} \frac{L_{\text{cancel}} + L_{\text{x}} + M}{L_{\text{WPT}}\left(L_{\text{cancel}} + L_{\text{x}}\right) - M^2} \tag{3.10}$$

and

$$I_2 = \frac{V_{\text{WPT}}}{j\omega} \frac{L_{\text{WPT}} + M}{L_{\text{WPT}}\left(L_{\text{cancel}} + L_{\text{x}}\right) - M^2}. \tag{3.11}$$

L_{x} can be calculated from (3.6)

$$L_{\text{x}} = \left(L_{\text{WPT}} + M\right)\frac{a_1}{a_2} - L_{\text{cancel}} - M. \tag{3.12}$$

or other optimal solution of $|I_2|$ from (3.8).

3.3 Hardware Implementation and Results

3.3.1 Implementation

The WPT and cancelling coils, L_{WPT} and L_{cancel} respectively, are implemented as 4-layer, 1-oz PCB traces, which are consistent, low cost, and easy to manufacture. L_{x} can be a small surface-mount inductor (tens of nH). The voltage V_{sense} of the open-circuit PCB coil L_{sense} measures the

Table 3.1: Implementation of the Field Cancellation Method

Components & Parameters	Values
Operating Frequency	62.5 MHz
WPT Coil L_{WPT} & a_1	65 nH & 20 mm
Cancellation Coil L_{cancel} & a_2	44.7 nH & 14 mm
Sensing Coil L_{sense} & Radius	46.5 nH & 9 mm
L_{x}	(a) Open (b) 164-06A06L
k between L_{WPT} and L_{cancel}	0.38
Explicit Resonant Capacitors C_{r}	(a) 77.1 pF (b) 142.8 pF

encircled magnetic flux. L_{x} is optimized with $|I_2|$ to minimize the magnetic field. C_{r} is chosen for zero-voltage-switching (ZVS) operation of the CMCD inverter. An open-load CMCD inverter, as shown in Fig. 3.5, was constructed to verify the field cancellation performance. Fig. 3.6 shows the miniaturized hardware of this field cancellation method with components and values shown in Table 3.1.

3.3.2 Measurement and Comparison of Field Cancellation Performance

Field cancellation performance was verified with an optimal I_2 and compared to that with zero I_2. Magnetic field cancellation can be observed from the voltage V_{sense} of the open-circuit sensing coil, which encircles the circuits. A figure of merit for cancellation performance is the percentage of the magnetic field that couples to the sense coil

$$k' = \frac{V_{\text{sense}}}{V_{\text{WPT}}}\sqrt{\frac{L_{\text{WPT}}}{L_{\text{sense}}}}. \tag{3.13}$$

The comparative improvement in cancellation is

$$\frac{\Delta B_{\text{z}}}{B_{\text{z}}} = \frac{|k' - k'_1|}{k'_1} \times 100\,\%, \tag{3.14}$$

where k'_1 =13.6 % relates to no field cancellation with only L_{WPT} as shown in Fig. 3.2(a) and k' relates to field cancellation as shown in Fig. 3.2(c). The best field cancellation $\Delta B/B_{\text{z}} = 99\,\%$. The fundamental-frequency components of V_{sense} and V_{WPT}, notated in Fig. 3.6, are obtained from the fast Fourier transform (FFT) of the time-domain waveforms as shown in Fig. 3.7. The additional harmonics are from scope probes pickup of capactive coupling.

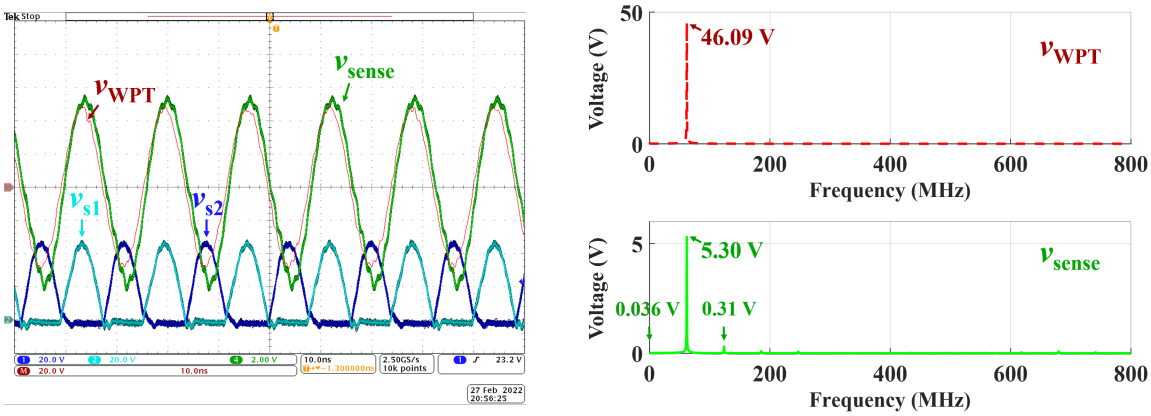

(a) Without cancellation, $k_1' = 13.6\,\%$, $\Delta B_z/B_z = 0\,\%$. Time-domain and frequency-domain signals of v_{WPT} and v_{sense}.

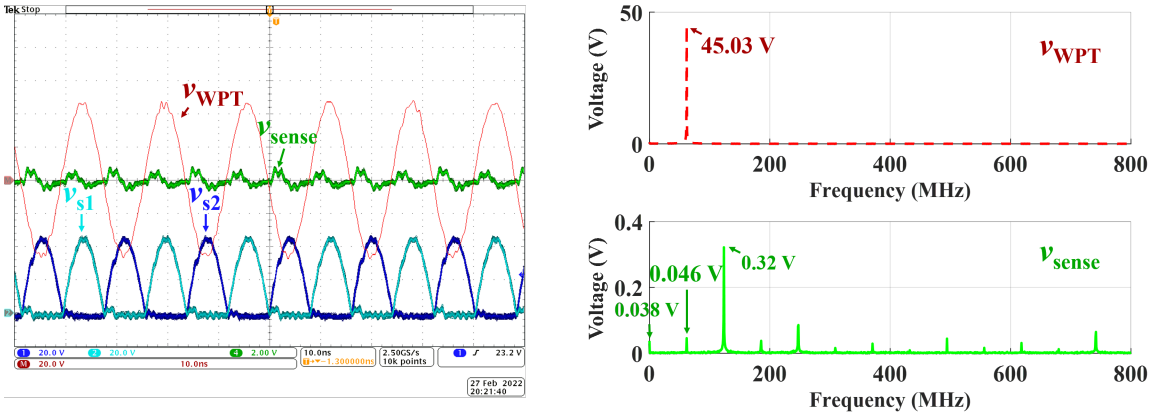

(b) With cancellation, $k' = 0.1\,\%$, $\Delta B_z/B_z = 99\,\%$. Time-domain and frequency-domain signals of v_{WPT} and v_{sense}.

Figure 3.7: Comparison of field cancellation performance.

3.4 Summary

Field cancellation using an additional cancelling coil and L_x was demonstrated to have decreased the magnetic field for the encircled components and circuits by 99 %, which achieves excellent field cancellation performance and requires the fewest number of components for compactness, miniaturization, and lowest cost. Both the WPT and cancellation coils were driven by the same current-mode class D power converter.

CHAPTER 4

Singleton CMCD WPT System

4.1 Introduction

Very-high-frequency (30 MHz - 300 MHz, VHF) power conversion enables miniaturization by reducing the size of passive components [5, 10–13]. Increasing switching frequency facilitates circuit integration [13, 30–33] and delivers fast transient response [5, 12, 13, 31, 73]. For miniaturized wireless power transfer (WPT) systems, inductors that are used as chokes, resonant inductors, and WPT coils are one of the considerable sources of thermal dissipation. Increasing the operating frequency is one of the methods that create high quality factor for the air-core inductors [5, 74], thus improving the WPT figure of merit $Q \cdot k$ and reducing loss dissipation, which supports miniaturization and integration. Much of the VHF research had been focused on dc–dc converters [5,7,10–14,18,22,30–32,73], but few on VHF wireless power transfer [4,33,34,75,76], which are needed in implantable medical devices, RFID, infrastructure sensors, robots and drones, consumer electronics, and the Internet of Things (IoT). This paper presents a 100 MHz inductive wireless power transfer system using current-mode class D (CMCD) converters [4, 52, 77] on both the transmitter and receiver, which we term a *symmetric CMCD WPT system*, shown in Fig. 4.1,

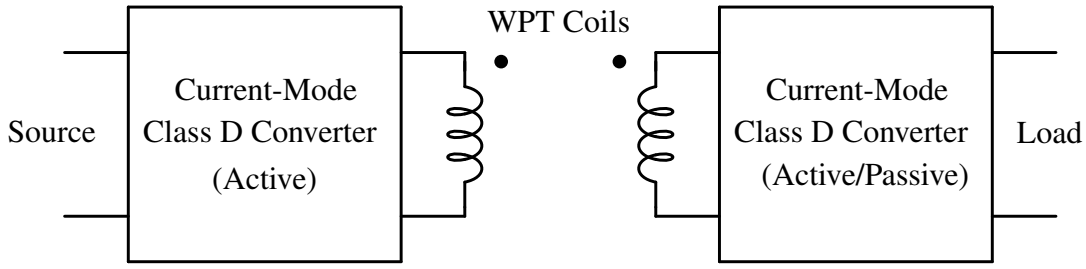

Figure 4.1: Symmetric CMCD WPT system with an active CMCD inverter as the transmitter, and either an uncontrolled/passive or synchronous CMCD rectifier as the receiver. The load can be either resistive or a voltage source.

with discrete components that include commercially available GaN devices.

Techniques used for VHF dc–dc power conversion apply to wireless power transfer; although, WPT efficiencies from dc to dc for identical topologies are lower because of the needed higher reactive power for the WPT link. VHF power conversion requires the appropriate choices of active devices, passive components, gate drivers, circuit topologies, integrated circuits, and RF design techniques [5, 10, 11]. In addition, another considerable challenge in wireless power transfer is the wide load range, either from variable loads or from different input voltages, which means the compensation networks need to be carefully designed, yet easily implemented and resilient. The WPT transmitter needs to be insensitive to unloading because a practical WPT receiver needs to be removed from the charging pad frequently and freely. For battery charging applications, constant output current with small current ripple is the preferred mode of operation for the receiver.

VHF power conversion can be realized using discrete devices and gate drivers. For devices, commercial and custom high-performance RF lateral double-diffused MOSFETs (LD-MOSFETs) [12–14] had been historically used because of acceptably low parasitic capacitance and gate resistance before the prevalence of better performing GaN (gallium nitride) HEMTs. VHF gate drivers require ultrafast slew rate, isolation, variable frequency, variable duty cycle, arbitrary long on- and off-times, flexible control inputs, and small gating loss [15]. Self-oscillating resonant gate drivers [12–14, 16] and conventional multi-resonant gate drivers [17] have been employed to mitigate gating loss but have a slower slew rate and operate at a single switching frequency and fixed duty cycle; the gate voltage waveforms are typically sinusoidal or trapezoidal. Logic inverter banks can be used to drive GaN HEMTs directly to better customize the gate drive [18]. Reference [15] investigated an ultrafast gate driver using logic CMOS inverters with transformer isolation that operates at VHF with different duty cycles and arbitrary long pulses.

For power converters, resonant topologies typically operate at zero-voltage-switching (ZVS) and absorb circuit parasitics into the topology. Class E resonant converters [14] along with variations like resonant boost converters [13] and class Φ_2 [12, 18] have been widely investigated at VHF. Conventional class E operation is typically sensitive to loading conditions for zero-voltage-switching (ZVS) and zero-voltage-derivative-switching (ZVDS), which can limit the operation over a wide load range.

There has been plenty of research investigating resonant converters that operate over a wide load range. Some had reduced the choke inductances and sacrificed the input and output current ripple to attain a wide load range [19–21]. The symmetric class EF system [19], transformed class E inverters [20], and transformed class Φ_2 inverters [20] absorb the much smaller chokes into part of the resonant network, resulting in large input or output current ripple. Reference [21] compensated the tuning where the impedance is flat together with the reduced choke inductance to extend the load range. With additional lossy components, greater complexity, or more complex control

Table 4.1: Performance Comparison in State-of-the-Art 100 MHz Power Conversion

References	[12]	[33]	[32]	[4]	[76]	[15]	This work
f_s	100 MHz	100 MHz	100 MHz	100 MHz	100 MHz	100 MHz	100 MHz
Publication	2006 PESC	2015 COMPEL	2016 TPEL	2019 ECCE	2020 APEC	2020 TPEL	This paper
Topology	Class E Resonant Rectifier	Half-Bridge -	Half-Bridge Half-Bridge	CMCD CMCD	CMCD CMCD	CMCD CMCD	CMCD CMCD
Application	DC - DC	WPT	DC - DC	WPT	WPT	WPT	WPT
Peak Efficiency with Gating Loss	75 % (dc–dc)	≈ 90 % (dc-ac, ac-ac)	≈ 88 % (dc–dc)	59 % (dc–dc)	59 % (dc–dc)	66 % (dc–dc)	79 % (dc–dc)
Output Power at Peak Efficiency	10 W	2.5 W	5 W	2.8 W	8.9 W	2.6 W	6.9 W
Semiconductor Tech.	Si	GaN	GaN	GaN	GaN	GaN	GaN
Discrete or IC	Discrete	IC	IC	Discrete	Discrete	Discrete	Discrete

strategies [12, 18, 22–28], a wide load range together with small input and output current ripple can be achieved. References [12, 22] used resistance compression networks with class E inverters to extend the load range but sacrificed the efficiency from the additional components. Reference [18] used a bandpass matching network with a symmetric class Φ_2 system to extend the load range by a factor of 7 at 64 MHz, achieving 73 % efficiency at 11 W peak power. Reference [23] investigated a push-pull Φ_2 inverter with a T network, which can achieve load-independent characteristics while reducing the input ripple and reactive power loss for 6.78 MHz WPT applications [24, 25]; however, the circuit topology can be difficult to extend to higher frequencies. References [26–28] used a variable equivalent capacitor from phase-switched impedance modulation to achieve a wide load range with active control.

Currently, GaN devices have been used to push the switching frequency of dc–dc converters to 64 MHz [18] in class Φ_2^2, 75 MHz [7] in multi-level buck using discretes, and 1 GHz [29] in a microstrip circuit class E^2 with greater than 70 % efficiency at greater than 5 W power. LDMOSFETs had been used in 100 MHz class E^2 dc–dc converters, which deliver 1.7 W at 55 % efficiency [14]. Most symmetric systems at MHz power conversion are designed for constant output voltage, including class E, class EF, and class Φ_2, while constant output current with small ripple is needed for direct battery charging.

Another approach to VHF power conversion has been investigated through circuit integration. Silicon integrated circuits (IC) with multi-phase buck converters achieved a load power of 0.44 W at 83.2 % efficiency at 233 MHz [30]. 140 MHz multi-phase buck regulators were fully integrated and featured up to 80 MHz unity gain bandwidth [31]. Another custom IC using a GaN half-bridge with an integrated gate driver [32] had enabled fertile research in 100 MHz power conversion, including 100 MHz capacitive wireless power transfer [33] delivering 2.5 W from dc to ac with no rectifier to a resistive load with approximately 90 % efficiency. DC-DC efficiencies are typically lower than DC-AC efficiencies for WPT because of rectifier losses. 100 MHz inductive WPT was used for a high-density IC chip with 34 % power transfer efficiency [34]. Table 4.1 illustrates a comparison of some of the recent progress in 100 MHz power conversion with our work in 100 MHz symmetric CMCD WPT systems. Achieving high efficiency and high power in very-high-frequency wireless power transfer is still an ongoing challenge whether using discrete components or circuit integration.

The symmetric CMCD system [4, 52, 77, 78] is an important class of WPT systems, which with proper design can have the following properties at the same time: (a) Wide Load Range, (b) Constant Output Current, and (c) Small Input and Output Current Ripple. Compared to other higher-order symmetric counterparts, including class E, class EF, and class Φ_2 systems at MHz power conversion, the symmetric CMCD system is the lowest order consisting of two loosely-coupled, second-order systems while also absorbing the parasitics of the active devices. The needed multi-

resonant tuning in the higher-order counterparts is not required for the CMCD inverter and rectifier. Among the advantages, the CMCD inverter is inherently insensitive to unloading, which typically occurs in WPT transmitters. The ground-referenced switches also reduce the complexity of gate driver design. Despite the valuable properties of the symmetric CMCD system, it is not often used. One of the reasons is the lack of a rigorous design method for symmetric CMCD systems.

The contribution and novelty in this paper is that we present a globally optimal design method for the symmetric CMCD system. The uniqueness of the optimal solution can be guaranteed and parameter sensitivity can be analyzed. Inherently, with proper design, symmetric CMCD WPT systems have a wide load range and constant output current together with small input and output current ripple at the same time, without additional lossy components, greater complexity, and more complex control techniques. The rigorous and straightforward step-by-step practical design procedure that we present ensures that the converter operates at ZVS with high efficiencies over a wide load and input voltage range with constant output current, and small input and output current ripple. Several 100 MHz hardware prototypes from this design strategy in different configurations are demonstrated to be physically compact and efficient. The prototype with a passive CMCD rectifier maintains nearly constant power circuit efficiency above 80.5 % with a peak of 83.2 % over a wide power range that spans from 1.7 W to 6.9 W. The bipolar capability of the receiver output voltage is analyzed. Comparisons between synchronous and passive rectifiers are also presented for the optimal designs of symmetric CMCD WPT systems.

4.2 Operation of Current-Mode Class D: Inverters, Rectifiers, and Symmetric WPT Systems

Current-mode class D (CMCD) converters are a family of DC-AC (Fig. 4.2) and AC-DC (Fig. 4.5) power converters. They are based on a push-pull structure with an LCR parallel resonant tank. The operation of CMCD power converters can typically be modeled as an equivalent square-wave current source feeding a parallel resonant tank, which is a purely second-order system.

A wireless power transfer system with a CMCD inverter coupled with a CMCD rectifier as shown in Fig. 4.1 is symmetric in its input and output circuit topologies, i.e. a *symmetric CMCD WPT system*. The switches in the inverter are necessarily active, but the switches in the rectifier can be either active or passive.

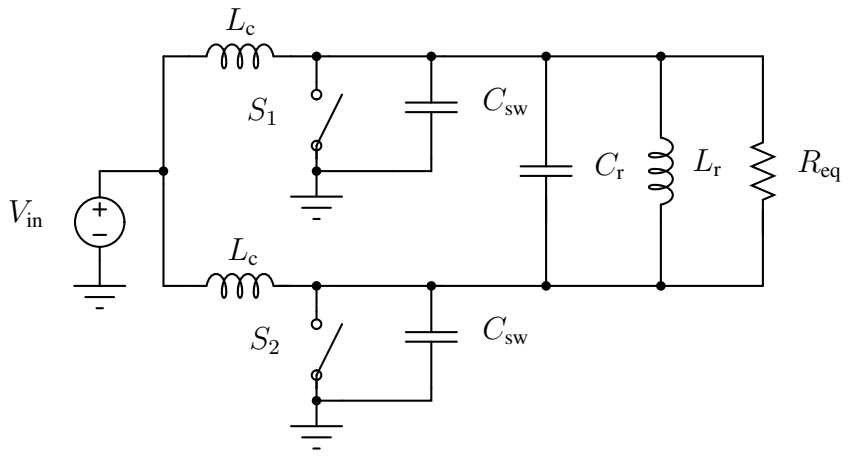

Figure 4.2: Current-mode class D (CMCD) inverter.

4.2.1 Current-Mode Class D Inverter

The current-mode class D converter is the lowest-order and most straightforward topology with a purely second-order parallel resonance and ground-referenced complementary switching, which is in comparison to other higher-order RF switch-mode power amplifiers, including class E, class E/F (class EF), and similar variations. In the CMCD converter, the dominant parasitics can be absorbed into the parallel resonant network to retain the second-order. A pure second-order circuit is more straightforward to design and implement with potentially lower cost and higher power density, making it an attractive option for miniaturization and integration at 100 MHz, or even at higher operating frequencies.

In most applications, current-mode class D converters [57, 79–83] can employ two crucial approximations for analysis:

1. resonant tank with a very high quality factor Q, where loading does not affect the dynamics;
2. choke inductors which can be considered infinite, making the choke current ripple and the effect on tank resonance negligible.

In every complementary operation of a switch, one of the switch capacitances C_{sw} is in parallel with the resonant capacitor C_{r} and the other is shorted to ground, which can be observed in Fig. 4.3. This means that C_{sw} can be absorbed into the resonance as a parallel combination with C_{r}. It is worth noting that there is a current divider between C_{r} and C_{sw}, which increases the rms current flowing through the switch that is on, which can be observed in Fig. 4.4.

The operational frequency

$$f_s = \frac{1}{2\pi\sqrt{L_{\text{r}}\ (C_{\text{r}} + C_{\text{sw}})}}, \tag{4.1}$$

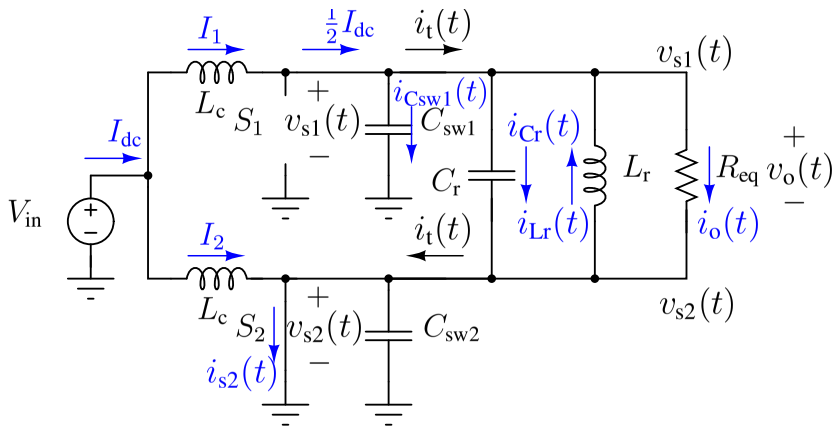

(a) $t_0 \sim t_1$.

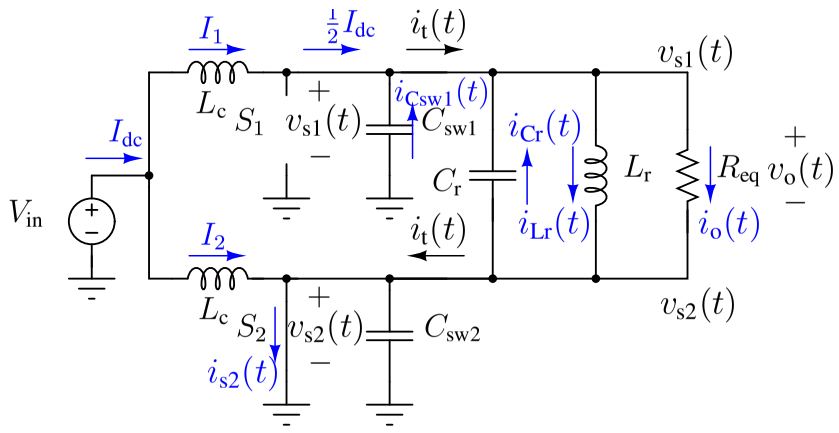

(b) $t_1 \sim t_2$.

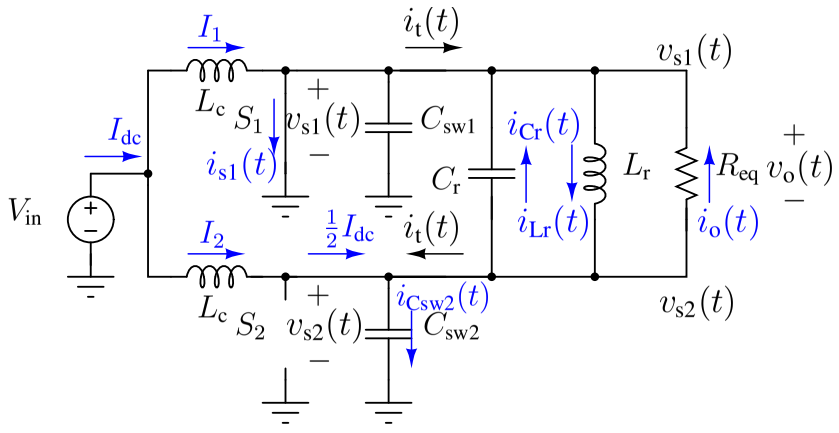

(c) $t_2 \sim t_3$.

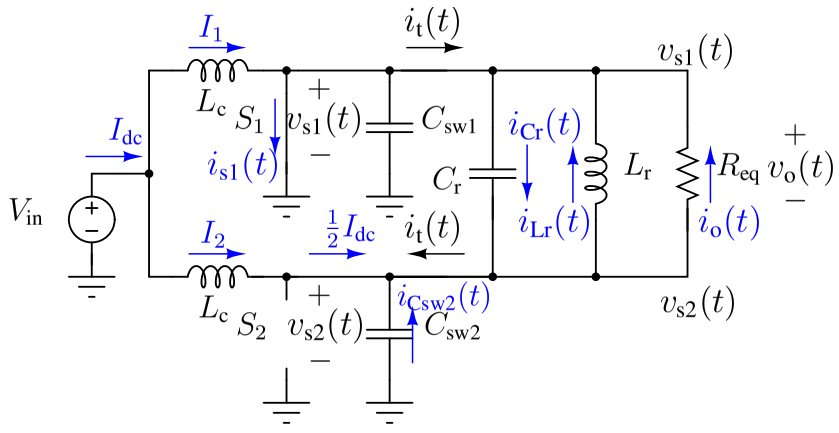

(d) $t_3 \sim t_4$.

Figure 4.3: The intervals of circuit operation in CMCD inverters. The blue arrows represent the actual current flow while the reference polarities are indicated by v_{s1}, v_{s2}, v_o, and i_t with passive sign convention. The corresponding typical waveforms are shown in Fig. 4.4.

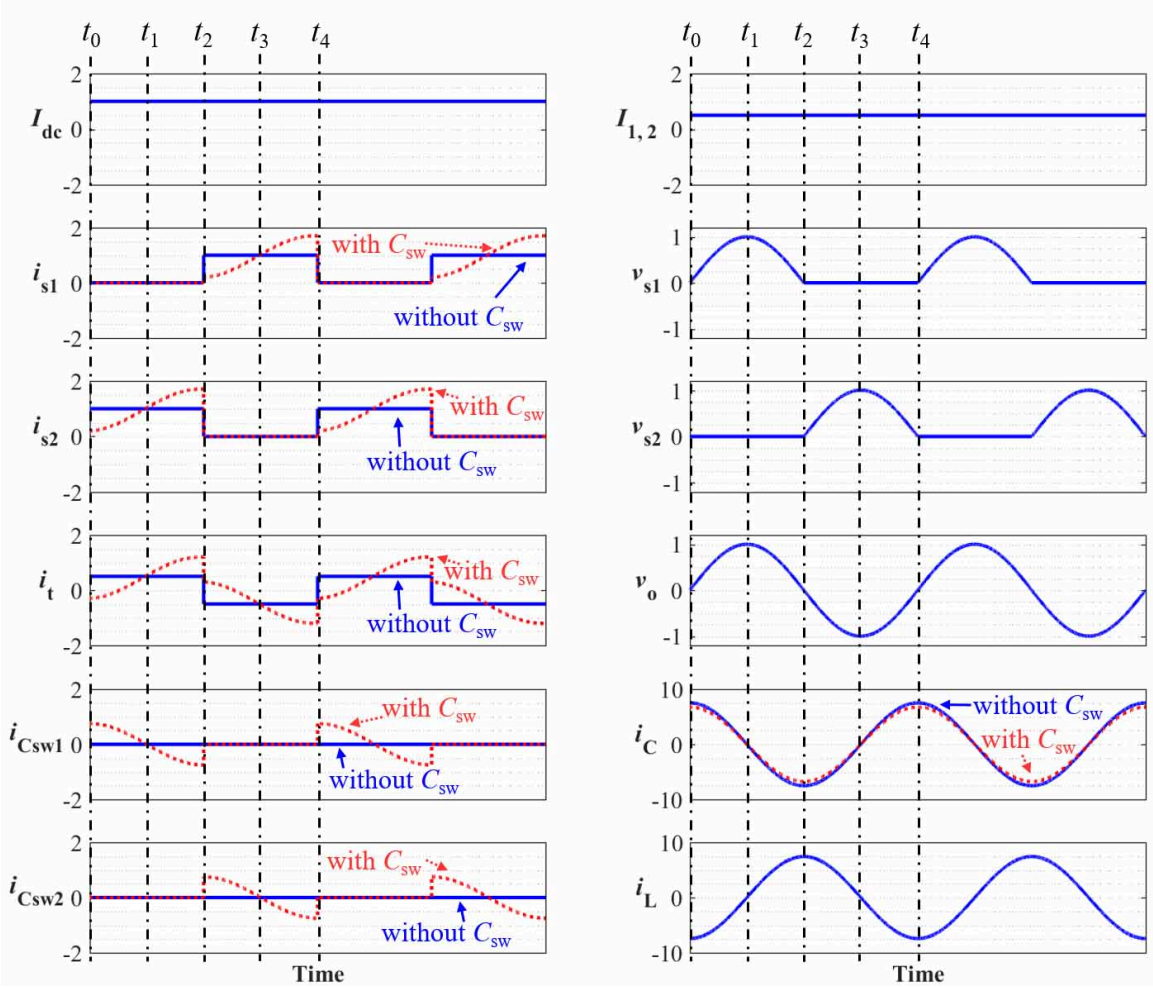

Figure 4.4: Typical waveforms of well-tuned current-mode class D inverters with very high quality factor Q and very large choke inductors L_c, where the currents are normalized to the input dc current I_{dc} and the voltages are normalized to the peak switch voltage $V_{o,pk}$. The corresponding circuits are shown in Fig. 4.3.

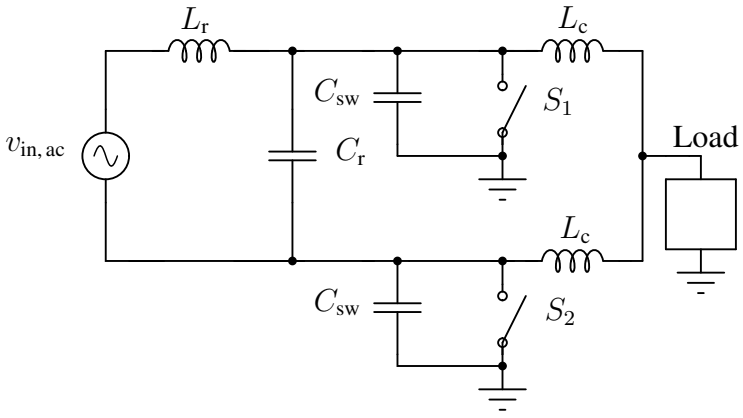

(a) CMCD rectifier with ac input voltage source.

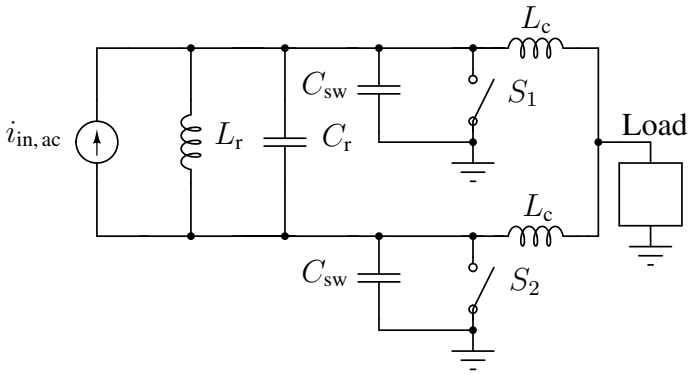

(b) CMCD rectifier with ac input current source.

Figure 4.5: Current-mode class D (CMCD) rectifier.

where C_r represents the capacitance which is in parallel with the differential output and C_sw represents the capacitances that are in parallel with S_1 and S_2, including C_oss.

Because the average voltage across a choke inductor is zero, the average switch voltage, v_s1 or v_s2, must equal V_dc, making the ratio between the peak switch voltage $V_\mathrm{o,\,pk}$ and V_dc be

$$\frac{V_\mathrm{o,\,pk}}{V_\mathrm{dc}} = \pi. \tag{4.2}$$

The ratio of peak drain voltage to the input dc voltage is lower than for conventional class E converters, but higher than for some class E variations.

4.2.2 Current-Mode Class D Rectifier

The CMCD rectifier was first proposed in [52], which is the time-reversal dual [84] of the CMCD inverter. It belongs to full-wave rectifiers but only has a single diode drop, which is different from

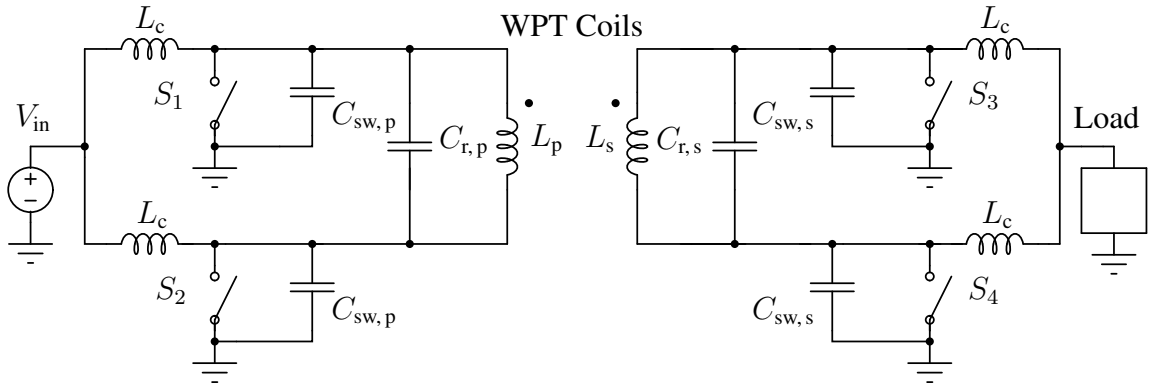

Figure 4.6: Circuit for a symmetric CMCD WPT system.

the full-bridge full-wave rectifier. The derivation and evolution of the CMCD rectifier come from the modeling of a symmetric CMCD WPT system, which will be illustrated in Section 4.3. For a CMCD rectifier, the input can be configured as a voltage source with a series resonant inductor, shown in Fig. 4.5(a), or a current source with a parallel resonant inductor, shown in Fig. 4.5(b). The two circuits in Fig. 4.5 are equivalent through Thévenin and Norton transformations

$$V_{\text{in, ac}} = I_{\text{in, ac}} \cdot j\omega L_{\text{r}}, \tag{4.3}$$

where $V_{\text{in, ac}}$ and $I_{\text{in, ac}}$ are the phasor representations of $v_{\text{in, ac}}(t)$ and $i_{\text{in, ac}}(t)$. The load can be either resistive or a voltage source. The resonant frequency is (4.1).

4.2.3 Symmetric Current-Mode Class D WPT System

The symmetric CMCD WPT system can be implemented as the circuit in Fig. 4.6. The transmitter is necessarily implemented with two active switches S_1 and S_2, while S_3 and S_4 in the receiver can be either active devices or passive diodes.

Both the CMCD inverter and rectifier follow the same principles of operation as discussed above. The phase difference between the control sequences of S_1 and S_3 is θ. If active devices are used on both sides, the phase shift can be actively controlled and bi-directional power transfer, which is useful for peer-to-peer charging [77, 85], becomes possible. For a fixed phase shift, which is the case for a CMCD inverter and a passive CMCD rectifier, power transfer is uni-directional.

With symmetric CMCD WPT systems, different configurations for loads and power transfer directions are possible. There are three symmetric CMCD WPT systems with combinations of resistive and dc voltage loads together with active and passive semiconductor devices, as shown in

Figs. 4.7, 4.8, and 4.9 with corresponding waveforms in Figs. 4.10, 4.11, and 4.12, respectively; these waveforms are normalized to their peak values. In this section, C_{sw} is ignored for simplicity. Figs. 4.7 and 4.8 use resistive loads with positive or negative output voltages, respectively. S_3 and S_4 in the receiver in Figs. 4.7 and 4.8 can be either active semiconductor switches or passive diodes. The current flow in Figs. 4.7 and 4.8 indicate the direction of the diodes when S_3 and S_4 are passive, resulting in the polarity of the output voltage.

Synchronous rectification is possible if S_3 and S_4 are active. The control sequences of S_1, S_2, S_3, and S_4 determine the current flow in S_3 and S_4. For a positive output voltage, v_{s1} leads v_{s3} by 90 degrees, the current is drawn from the ground through S_3 and S_4 as shown in Figs. 4.7 and 4.10. For a negative output voltage, negative v_{s3} leads v_{s1} by 90 degrees, the currents flow toward the ground in S_3 and S_4, as shown in Figs. 4.8 and 4.11. For a four-quadrant switch, a straightforward method to change the polarity of the current flow in S_3 and S_4 is to swap the control signals of S_3 and S_4, making both positive and negative output voltages on a load possible.

For bi-directional power transfer [77], S_3 and S_4 must be active with the terminal dc voltages able to source and sink currents as power inputs and outputs, respectively. The direction of the power flow is determined by the control sequences of S_1, S_2, S_3, and S_4. As with synchronous rectification, if v_{s1} leads v_{s3} by 90 degrees, power is transferred from the primary side (V_1) to the secondary side (V_2) whereas if v_{s3} leads v_{s1} by 90 degrees, the power flow is opposite. The waveforms are shown in Fig. 4.12 when the power is transferred from the secondary to the primary with the intervals of circuit operation in Fig. 4.9. A straightforward way to reverse the power transfer direction is to swap the control signals of S_3 and S_4.

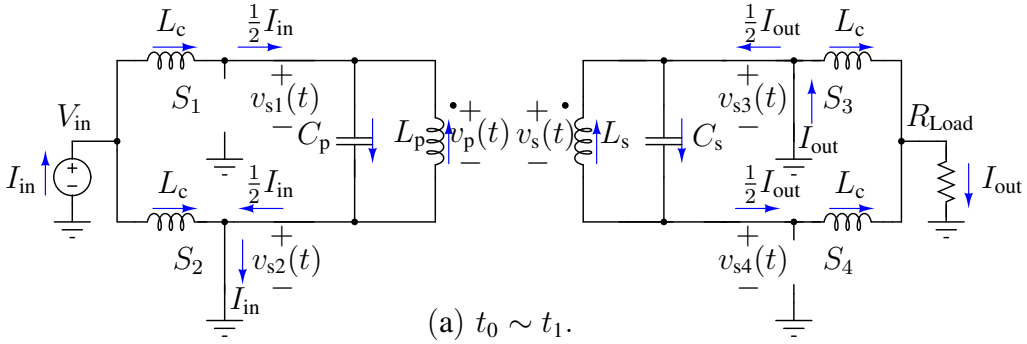

(a) $t_0 \sim t_1$.

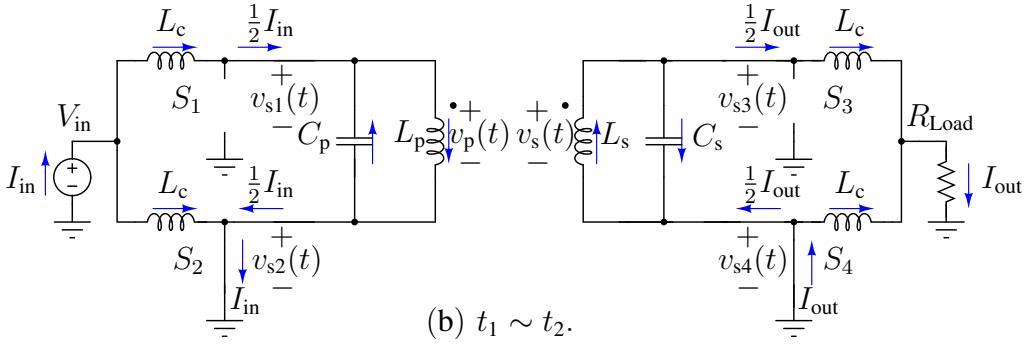

(b) $t_1 \sim t_2$.

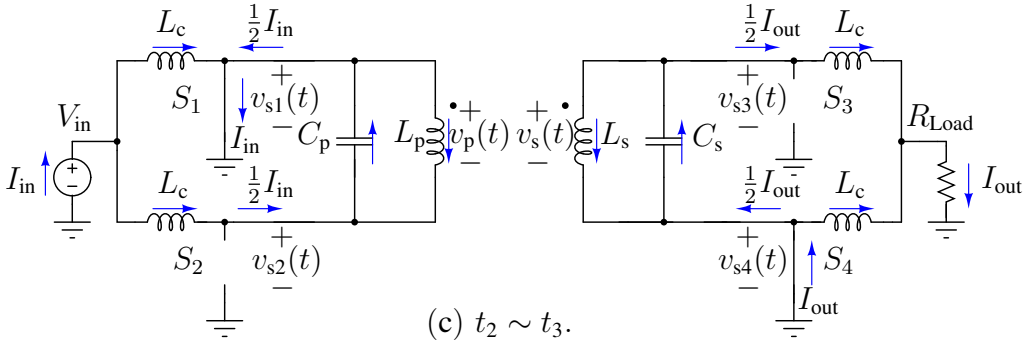

(c) $t_2 \sim t_3$.

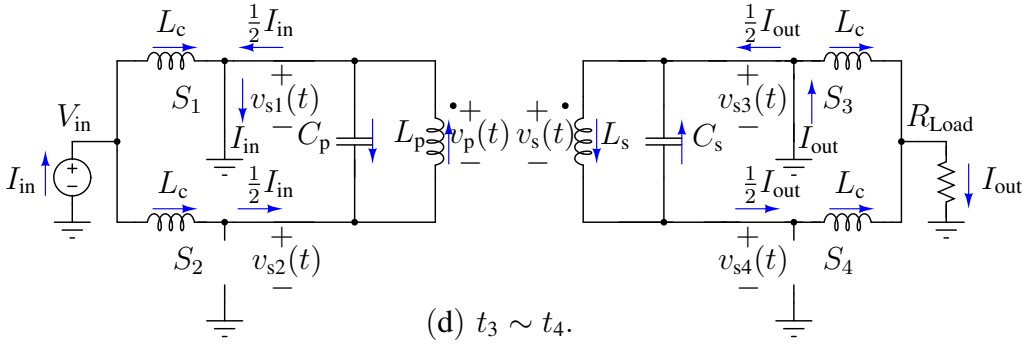

(d) $t_3 \sim t_4$.

Figure 4.7: The intervals of circuit operation in symmetric CMCD WPT systems with POSITIVE output voltage. The transmitter is an active CMCD inverter while the receiver is either a passive or a synchronous CMCD rectifier. The blue arrows represent the actual current flow while the reference polarities are indicated by v_{s1}, v_{s2}, v_{s3}, v_{s4}, v_p, and v_s, all with passive sign convention. The corresponding waveforms are shown in Fig. 4.10. (a) $t_0 \sim t_1$. (b) $t_1 \sim t_2$. (c) $t_2 \sim t_3$. (d) $t_3 \sim t_4$.

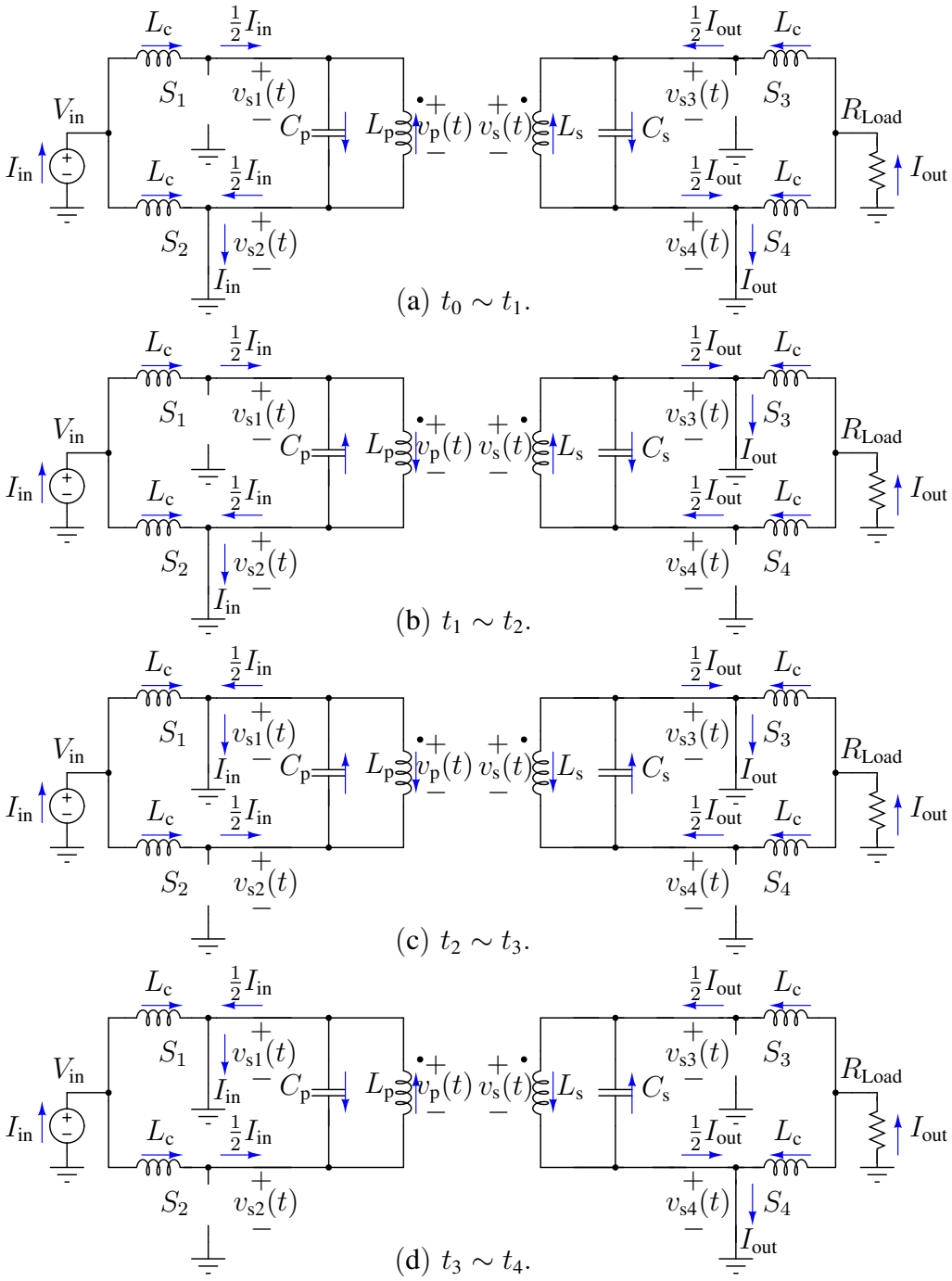

Figure 4.8: The intervals of circuit operation in symmetric CMCD WPT systems with NEGATIVE output voltage. The transmitter is an active CMCD inverter while the receiver is either a passive or a synchronous CMCD rectifier. The blue arrows represent the actual current flow while the reference polarities are indicated by v_{s1}, v_{s2}, v_{s3}, v_{s4}, v_p, and v_s, all with with passive sign convention. The corresponding waveforms are shown in Fig. 4.11.

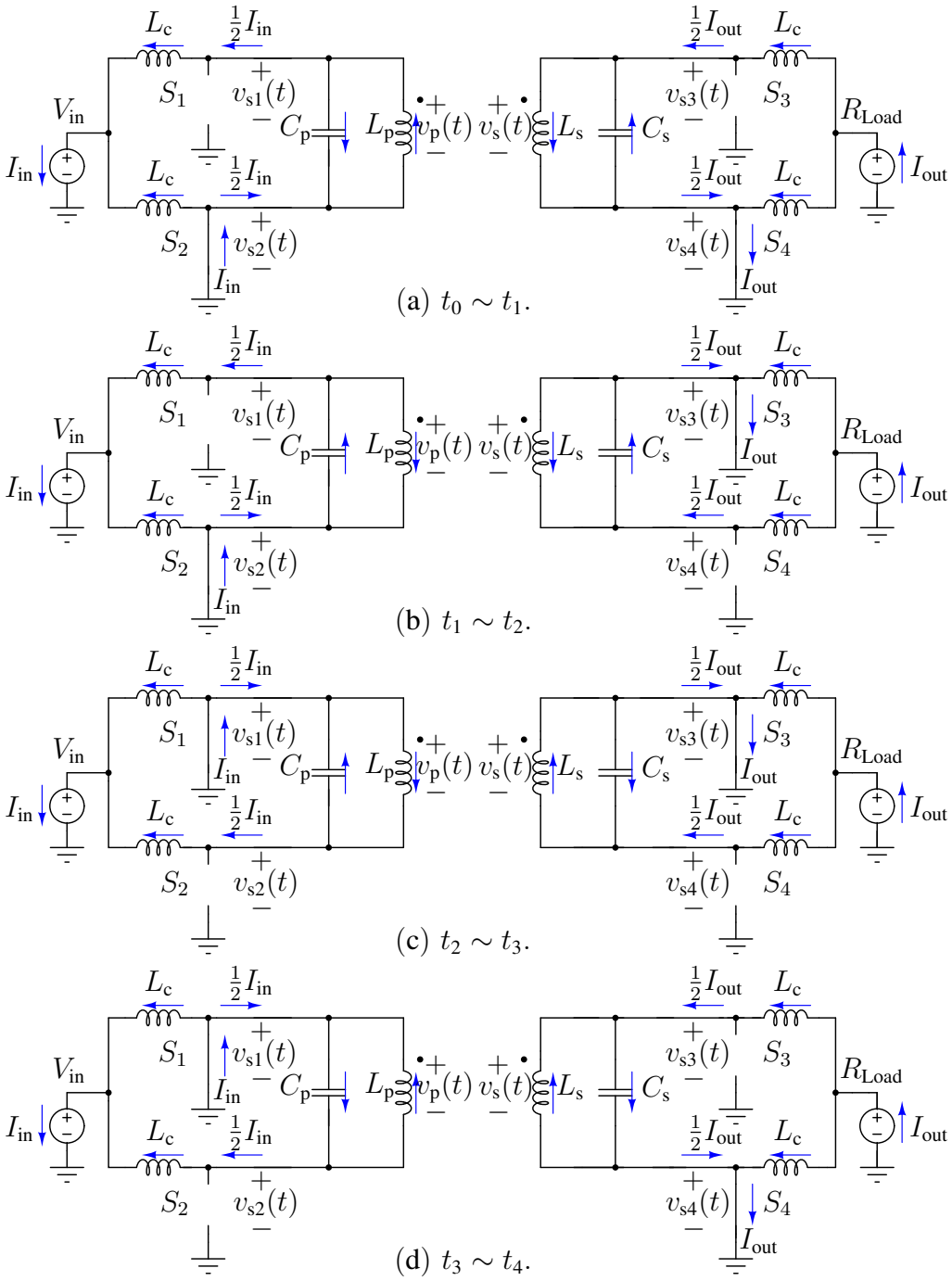

Figure 4.9: The intervals of circuit operation in symmetric CMCD WPT systems with power flow from right (secondary) to left (primary), both with dc voltage sources. Both primary and secondary use active CMCD inverters to achieve bi-directional power transfer. The blue arrows represent the actual current flow while the reference polarities are indicated by v_{s1}, v_{s2}, v_{s3}, v_{s4}, v_p, and v_s, all with passive sign convention. The waveforms are shown in Fig. 4.12.

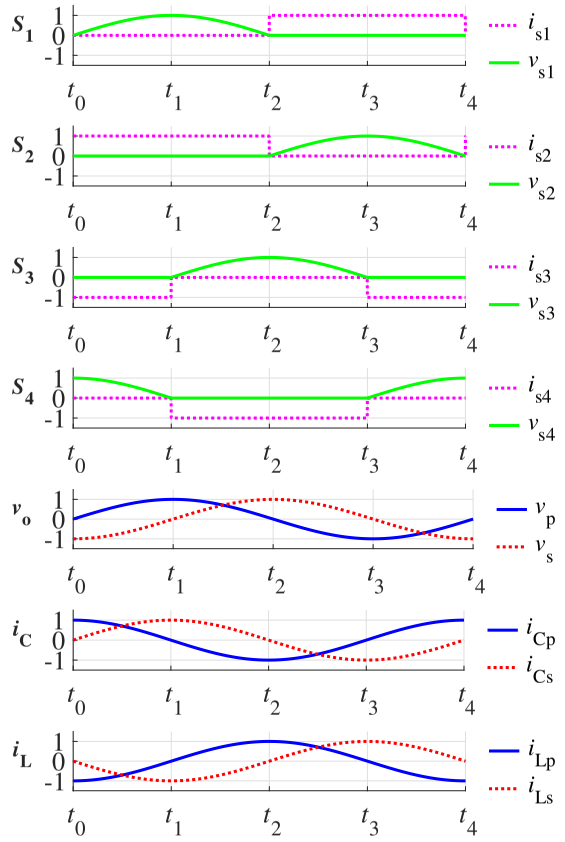

Figure 4.10: Typical waveforms for Fig. 4.7 with resistive load and POSITIVE output dc voltage on the receiver.

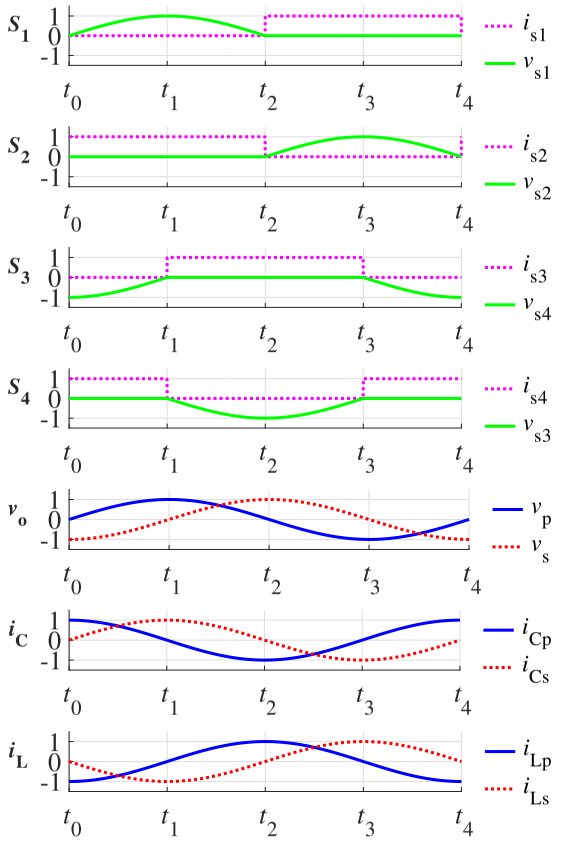

Figure 4.11: Typical waveforms for Fig. 4.8 with resistive load and NEGATIVE dc output voltage on the receiver.

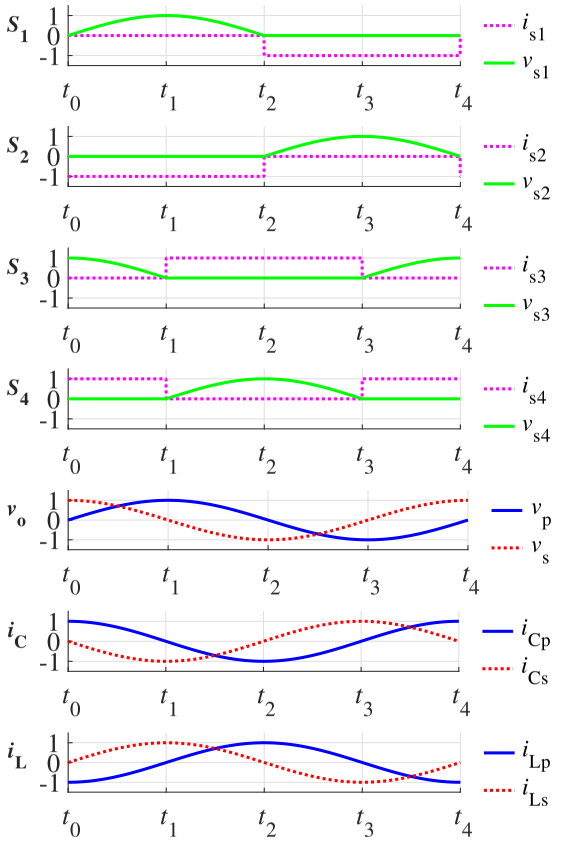

Figure 4.12: Typical waveforms for Fig. 4.9 when power is transferred from secondary to primary, requiring v_s to lead v_p by 90 degrees.

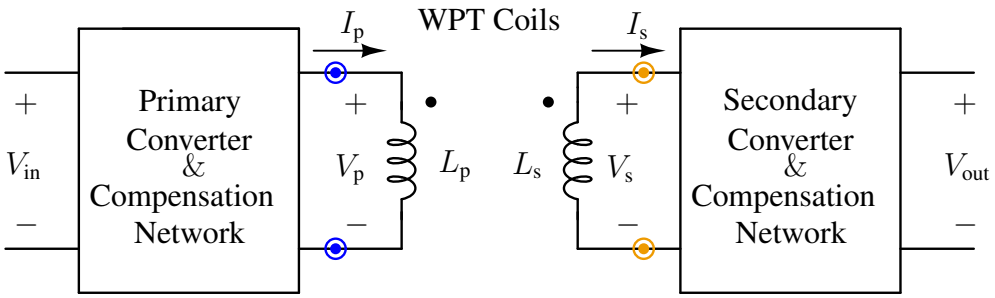

Figure 4.13: A uni-directional near-field magnetically-coupled WPT system.

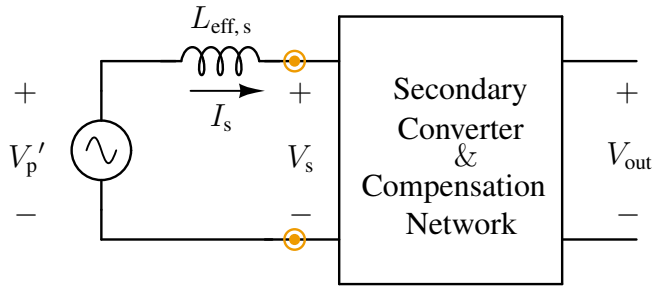

Figure 4.14: Receiver-side model of the uni-directional near-field magnetically-coupled WPT system.

4.3 Modeling of Symmetric CMCD WPT Systems

A uni-directional near-field WPT system that is magnetically coupled can be canonically represented by Fig. 4.13 with a DC-AC inverter coupled to an AC-DC rectifier through WPT coils L_p and L_s with coupling coefficient k. Many wireless power transfer systems are loosely coupled through what is essentially an air-core transformer. For a loosely-coupled system (e.g., $k \approx 0.2$), the primary and secondary resonances in each of the CMCD converters can be well-approximated as decoupled. The resonant inductors L_r in Figs. 4.2 and 4.5 for the primary and secondary are $(1-k^2)\,L_p$ and $(1-k^2)\,L_s$ once coupled, respectively, which we will derive later in this section.

Two modeling methods for symmetric CMCD WPT systems, corresponding to two conventional models for a transformer are investigated. These two models are the current-controlled-voltage-source (CCVS) model and the T-model. The CCVS wireless power transfer (CCVS-WPT) model uses single-sided models with an equivalent voltage source or an equivalent resistor on the secondary. The T wireless power transfer (T-WPT) model is derived from a prevailing method for impedance network analysis. If the quality factors of the primary and secondary parallel resonant tanks are high, which is typical of WPT systems, $v_p(t)$ and $v_s(t)$ can be well-represented by their fundamental frequency components V_p and V_s, respectively. The following analyses in this paper

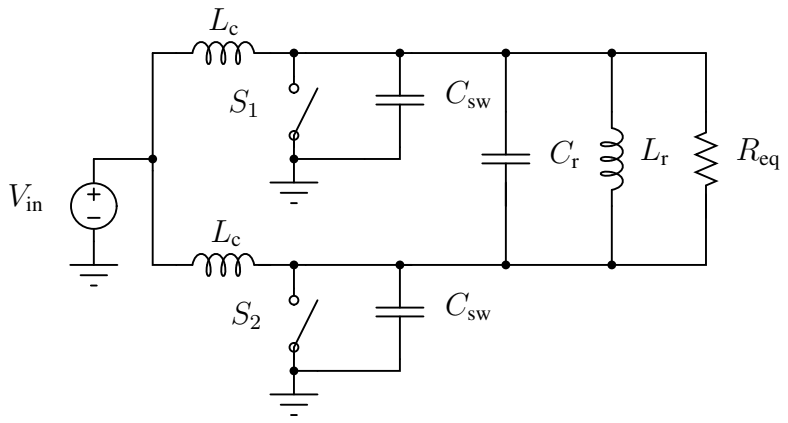

(a) Symmetric CMCD WPT transmitter-side circuit model.

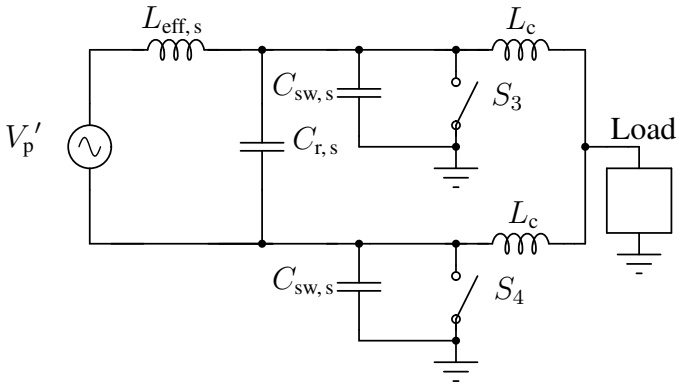

(b) Symmetric CMCD WPT receiver-side circuit model.

Figure 4.15: CCVS-WPT single-sided circuit models of the symmetric CMCD WPT system.

are based on peak-value phasor representations.

4.3.1 Single-Sided Model

The phasor representation of the CCVS-WPT model is derived from the voltage and current relationship of the CCVS coupled inductors with the reference polarities in Fig. 4.13,

$$\begin{pmatrix} V_p \\ V_s \end{pmatrix} = \begin{pmatrix} j\omega L_p & -j\omega M \\ j\omega M & -j\omega L_s \end{pmatrix} \begin{pmatrix} I_p \\ I_s \end{pmatrix}, \tag{4.4}$$

where V_p and V_s are the voltages across the primary and secondary WPT coils, respectively; I_p and I_s are the currents through the primary and secondary WPT coils, respectively. The secondary coil

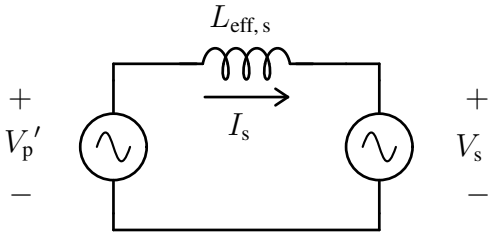

Figure 4.16: Reduced CCVS-WPT single-sided model of symmetric CMCD WPT system using equivalent voltage sources.

voltage

$$\begin{aligned} V_{\text{s}} &= j\omega M I_{\text{p}} - j\omega L_{\text{s}} I_{\text{s}} \\ &= j\omega M \left(\frac{V_{\text{p}}}{j\omega L_{\text{p}}} + \frac{M I_{\text{s}}}{L_{\text{p}}} \right) - j\omega L_{\text{s}} I_{\text{s}} \\ &= k\sqrt{\frac{L_{\text{s}}}{L_{\text{p}}}} V_{\text{p}} - j\omega \left(1 - k^2\right) L_{\text{s}} I_{\text{s}} \end{aligned} \tag{4.5}$$

can be represented by a reflected voltage source

$$V_{\text{p}}' = k\sqrt{\frac{L_{\text{s}}}{L_{\text{p}}}} V_{\text{p}} \tag{4.6}$$

and a voltage drop across an effective inductance on the receiver side

$$L_{\text{eff, s}} = \left(1 - k^2\right) L_{\text{s}}, \tag{4.7}$$

where k is the coupling coefficient between the L_{p} and L_{s}. The equivalent circuit is shown in Fig. 4.14.

The receiver-side model represents the transmitter and WPT coils as an equivalent voltage source V_{p}' coupled to the receiver through an equivalent inductor $L_{\text{eff, s}}$ in Fig. 14. In general, any magnetically-coupled WPT system, which is typically represented as a two-sided model in Fig. 4.13, can be represented by a single-sided model. These single-sided models can be referenced to either the transmitter or receiver, hence a transmitter- or receiver-side model. A typical approach to a transmitter-side model is to represent the receiver and WPT coils as an equivalent resistor R_{eq} and an equivalent inductor $L_{\text{eff, p}}$, as shown in Fig. 4.15(a) for a symmetric CMCD WPT system. The receiver-side model of a symmetric CMCD WPT system is shown in Fig. 4.15(b), which is an example of general receiver-side model in Fig. 4.14.

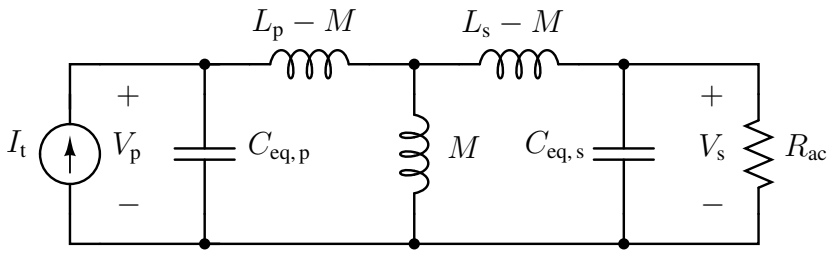

Figure 4.17: T-WPT model of the symmetric CMCD WPT system.

The resonant frequency in the receiver-side is determined by

$$\omega = \frac{1}{L_{\mathrm{eff,\,s}}\, C_{\mathrm{eq,\,s}}} = \frac{1}{(1-k^2)\, L_\mathrm{s}\, C_{\mathrm{eq,\,s}}}, \tag{4.8}$$

where $C_{\mathrm{eq,\,s}} = C_{\mathrm{sw,\,s}} + C_{\mathrm{r,\,s}}$. Because of symmetry, the transmitter resonant frequency is

$$\omega = \frac{1}{L_{\mathrm{eff,\,p}}\, C_{\mathrm{eq,\,p}}} = \frac{1}{(1-k^2)\, L_\mathrm{p}\, C_{\mathrm{eq,\,p}}}, \tag{4.9}$$

where $L_{\mathrm{eff,\,p}} = (1-k^2)\, L_\mathrm{p}$ and $C_{\mathrm{eq,\,p}} = C_{\mathrm{sw,\,p}} + C_{\mathrm{r,\,p}}$.

V_p and V_s often depend on the switching, compensation network, and load in Fig. 4.13 and might not be represented as stiff voltage sources. However, for CMCD inverters and rectifiers, V_p and V_s are stiff for a wide load range. The choke inductors in Fig. 4.15 have a zero average voltage drop, which act to stiffen V_p and V_s by constraining their half-cycle average voltages.

If the primary and secondary are loosely coupled in a WPT system (Fig. 4.13), the secondary offers very little loading to the primary and vice-versa. V_s can then be replaced by a voltage source making the single-sided model simpler, as shown in Fig. 4.16. It is worth noting that for this case, the CMCD operates like a dual active bridge [86] in that power flow is determined by two voltage sources across an equivalent inductor. Phase-shift power modulation can then be used for bi-directional wireless power transfer between the two sides [77, 85].

4.3.2 Impedance Network with the T-Model

Impedance analysis with a T-model representing the coupled WPT coils is a prevalent way to analyze WPT systems. The equivalent impedance at the differential ports of the CMCD WPT system is decomposed as a single-end circuit in Fig. 4.17 with $R_\mathrm{ac} = \frac{\pi^2}{2} R_\mathrm{Load}$ [4, 87]. $C_{\mathrm{eq,\,p}}$ and $C_{\mathrm{eq,\,s}}$ are the equivalent resonant capacitances, which include switch capacitance C_sw and explict resonant capacitor C_r while L_p and L_s are the self-inductances of the WPT coils on the primary

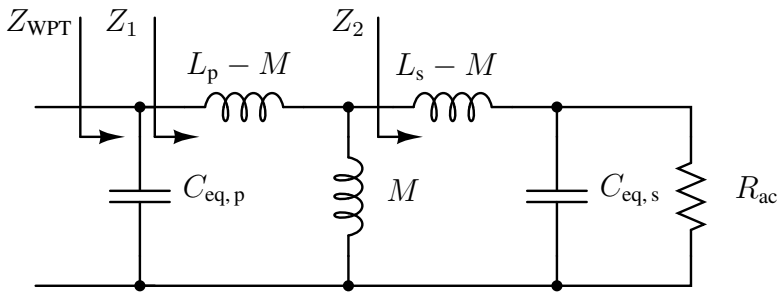

Figure 4.18: Impedance analysis for T-WPT model of the symmetric CMCD WPT model.

and secondary sides. The mutual inductance is

$$M = k\sqrt{L_{\text{p}}\, L_{\text{s}}}, \tag{4.10}$$

with coupling coefficient k.

As shown in Fig. 4.18, the port impedances at each stage Z_2, Z_1, and Z_{WPT} can be found,

$$\begin{aligned} Z_2 &= R_{\text{ac}} \parallel jX_{C_{\text{eq, s}}} + jX_{L_{\text{s}}'} = \frac{R_{\text{ac}} {X_{C_{\text{eq, s}}}}^2}{{R_{\text{ac}}}^2 + {X_{C_{\text{eq, s}}}}^2} \\ &\quad + j\frac{{R_{\text{ac}}}^2(X_{C_{\text{eq, s}}} + X_{L_{\text{s}}'}) + {X_{C_{\text{eq, s}}}}^2 X_{L_{\text{s}}'}}{{R_{\text{ac}}}^2 + {X_{C_{\text{eq, s}}}}^2} \\ &= R_2 + jX_2, \end{aligned} \tag{4.11}$$

where R_2 and X_2 are the real and imaginary parts of Z_2, respectively, $X_{L_{\text{s}}'} = \omega(L_{\text{s}} - M)$, and $X_{C_{\text{eq, s}}} = -1/\omega C_{\text{eq, s}}$;

$$\begin{aligned} Z_1 &= jX_{L_{\text{p}}'} + jX_M \parallel Z_2 = \frac{R_2 {X_M}^2}{{R_2}^2 + (X_2 + X_M)^2} \\ &\quad + j\frac{({R_2}^2 + {X_2}^2)(X_{L_{\text{p}}'} + X_{\text{M}}) + {X_{\text{M}}}^2(X_{L_{\text{p}}'} + X_2)}{{R_2}^2 + (X_2 + X_{\text{M}})^2} \\ &\quad + j\frac{2X_{L_{\text{p}}'} X_2 X_{\text{M}}}{{R_2}^2 + (X_2 + X_{\text{M}})^2} \\ &= R_1 + jX_1, \end{aligned} \tag{4.12}$$

where R_1 and X_1 are the real and imaginary parts of Z_1, respectively, $X_{L_{\text{p}}'} = \omega(L_{\text{p}} - M)$, and

$X_{\mathrm{M}} = \omega M$;

$$\begin{aligned} Z_{\text{WPT}} = Z_1 \parallel jX_{C_{\text{eq,p}}} &= \frac{R_1 {X_{C_{\text{eq,p}}}}^2}{{R_1}^2 + (X_{C_{\text{eq,p}}} + X_1)^2} \\ &+ j\frac{{R_1}^2 X_{C_{\text{eq,p}}} + {X_{C_{\text{eq,p}}}}^2 X_1 + X_{C_{\text{eq,p}}} {X_1}^2}{{R_1}^2 + (X_{C_{\text{eq,p}}} + X_1)^2} \\ &= R_{\text{WPT}} + jX_{\text{WPT}}, \end{aligned} \tag{4.13}$$

where R_{WPT} and X_{WPT} are the real and imaginary parts of Z_{WPT}, respectively, and $X_{C_{\text{eq,p}}} = -1/\omega C_{\text{eq,p}}$.

With L_{p}, L_{s}, and k as the defining parameters of a wireless power transfer system, $C_{\text{eq,p}}$ and $C_{\text{eq,s}}$ need to be chosen in the compensation networks to achieve a real input impedance. However, it is not straightforward to find the solution by directly setting the imaginary part X_{WPT} to zero. Actually, only considering X_{WPT} is not enough. Rather, a substitution method, which we discuss in Section 4.4, can be straightforward and complete.

4.4 Properties of Tuned Symmetric CMCD WPT Systems

Analyzing and understanding the behaviors of symmetric CMCD WPT systems enable us to properly design, operate, and find suitable applications.

4.4.1 Real Input Impedance

A typical objective for the input of a wireless power transfer system is a real impedance for Z_{WPT} in Fig. 18. From (4.8) and (4.9) in the CCVS-WPT model for symmetric CMCD WPT systems,

$$\begin{aligned} C_{\text{eq,p}} &= \frac{1}{\omega^2(1-k^2)L_{\text{p}}}, \\ C_{\text{eq,s}} &= \frac{1}{\omega^2(1-k^2)L_{\text{s}}}. \end{aligned} \tag{4.14}$$

Substituting (4.14) into (4.13), we obtain a purely resistive Z_{WPT}, i.e. $X_{\text{WPT}} = 0$, hence

$$\begin{aligned} Z_{\text{WPT}} = R_{\text{WPT}} = R_{\text{opt}} &= \frac{2}{\pi^2\omega^2 k^2 C_{\text{eq,p}} C_{\text{eq,s}} R_{\text{Load}}} \\ &= \frac{2\,(1-k^2)}{\pi^2 k^2 R_{\text{Load}}} \sqrt{\frac{L_{\text{p}}}{C_{\text{eq,p}}}} \sqrt{\frac{L_{\text{s}}}{C_{\text{eq,s}}}}, \end{aligned} \tag{4.15}$$

where

$$\sqrt{\frac{L_{\mathrm{p}}}{C_{\mathrm{eq,\,s}}}} = \sqrt{\frac{L_{\mathrm{s}}}{C_{\mathrm{eq,\,p}}}}, \tag{4.16}$$

and

$$\sqrt{L_{\mathrm{p}} C_{\mathrm{eq,\,p}}} = \sqrt{L_{\mathrm{s}} C_{\mathrm{eq,\,s}}}. \tag{4.17}$$

Power can then be calculated as

$$\begin{aligned} P_{\mathrm{o}} &= \frac{V_{\mathrm{p}}^2}{2R_{\mathrm{WPT}}} = \frac{\pi^4 \omega^2 k^2 C_{\mathrm{eq,\,p}} C_{\mathrm{eq,\,s}} R_{\mathrm{Load}} V_{\mathrm{in}}^2}{4} \\ &= \frac{\pi^4 k^2 {V_{\mathrm{in}}}^2 R_{\mathrm{Load}}}{4\left(1-k^2\right)} \sqrt{\frac{C_{\mathrm{eq,\,p}}}{L_{\mathrm{p}}}} \sqrt{\frac{C_{\mathrm{eq,\,s}}}{L_{\mathrm{s}}}}. \end{aligned} \tag{4.18}$$

It is worth noting that power increases linearly with R_{Load}.

We observe that for any R_{Load}, when (4.14) is satisfied, the inverter switch-nodes see an input impedance of

$$R_{\mathrm{eq}} = \frac{2\left(1-k^2\right)}{\pi^2 k^2 R_{\mathrm{Load}}} \sqrt{\frac{L_{\mathrm{p}}}{C_{\mathrm{eq,\,p}}}} \sqrt{\frac{L_{\mathrm{s}}}{C_{\mathrm{eq,\,s}}}} \tag{4.19}$$

in Fig. 4.15(a), which is real (i.e, zero imaginary part), so that as long as the Q of the tank remains high, a wide range of R_{eq}, thus R_{Load}, is possible.

4.4.2 Constant Output Current

Inherent constant output current is a property of symmetric CMCD WPT systems that has advantages, for example in battery chargers. The CCVS-WPT model shows that the transmitter and the WPT coils can be modeled as a reflected voltage source ${V_{\mathrm{p}}}'$ and a receiver-side effective inductance $L_{\mathrm{eff,\,s}}$ whose values can be calculated from (4.6) and (4.7). Starting from the CCVS-WPT receiver-side model in Fig. 4.15(b), a Norton equivalent circuit transformation is performed [88] and shown in Fig. 4.19(a) with

$${I_{\mathrm{p}}}' = \frac{{V_{\mathrm{p}}}'}{j\omega L_{\mathrm{eff,\,s}}}. \tag{4.20}$$

Whether the load is a resistor or a voltage source, it is equivalent to a resistor R_{ac} using fundamental frequency analysis [4, 87]. If the load is a resistor R_{Load}, then

$$R_{\mathrm{ac}} = \frac{\pi^2}{2} R_{\mathrm{Load}}, \tag{4.21}$$

as derived in [4].

Finally, a current source with a loaded parallel resonant network consisting of R_{ac}, $L_{\mathrm{eff,\,s}}$, and

$C_{\text{eq, s}}$ is obtained, where $C_{\text{eq, s}} = C_{\text{r, s}} + C_{\text{sw s}}$. When $L_{\text{eff, s}}$ resonates with $C_{\text{eq, s}}$, satisfying (4.9), constant output current is achieved, which is load independent. The ac current through R_{ac} is

$$\begin{aligned} I_{\text{ac}} = I_{\text{p}}{}' &= \frac{V_{\text{p}}{}'}{j\omega L_{\text{eff, s}}} = \frac{k\sqrt{\frac{L_{\text{s}}}{L_{\text{p}}}}V_{\text{p}}}{j\omega\left(1-k^2\right)L_{\text{s}}} \\ &= \frac{kV_{\text{p}}}{j\omega\left(1-k^2\right)\sqrt{L_{\text{p}}L_{\text{s}}}}, \end{aligned} \tag{4.22}$$

with magnitude

$$|I_{\text{ac}}| = kV_{\text{p}}\sqrt{\frac{C_{\text{eq, s}}}{\left(1-k^2\right)L_{\text{p}}}} = kV_{\text{p}}\sqrt{\frac{C_{\text{eq, p}}}{\left(1-k^2\right)L_{\text{s}}}}. \tag{4.23}$$

Also, $|V_{\text{p}}| = \pi V_{\text{in}}$ and $I_{\text{out}} = \frac{\pi}{2}|I_{\text{ac}}|$ from [4], then

$$I_{\text{out}} = \frac{k\pi^2 V_{\text{in}}}{2}\sqrt{\frac{C_{\text{eq, s}}}{\left(1-k^2\right)L_{\text{p}}}} = \frac{k\pi^2 V_{\text{in}}}{2}\sqrt{\frac{C_{\text{eq, p}}}{\left(1-k^2\right)L_{\text{s}}}}. \tag{4.24}$$

The output power is

$$\begin{aligned} P_{\text{o}} = {I_{\text{out}}}^2 R_{\text{Load}} &= \frac{\pi^4 k^2 {V_{\text{in}}}^2 R_{\text{Load}}}{4\left(1-k^2\right)}\frac{C_{\text{eq, s}}}{L_{\text{p}}} \\ &= \frac{\pi^4 k^2 {V_{\text{in}}}^2 R_{\text{Load}}}{4\left(1-k^2\right)}\frac{C_{\text{eq, p}}}{L_{\text{s}}}, \end{aligned} \tag{4.25}$$

which is identical to (4.18).

Under tuned conditions where the CMCD inverter and WPT coils behave as a stiff $V_{\text{p}}{}'$, constant output current over a wide load range can be intrinsically achieved in symmetric CMCD WPT systems.

4.4.3 Uniqueness and Sensitivity of Optimal Compensation Networks

Tuning is critical for compensation networks in WPT systems. Thus, it is important to analyze the optimal solution uniqueness and parameter sensitivity of the tuned compensation network. In addition to the equivalent resistances R_{eq} and R_{ac}, the compensation network consists of the resonant inductances and capacitances on both the transmitter and receiver. In this section, we investigate the sensitivity to the capacitances. It has been shown that with tuned compensation capacitances in (4.14), a real Z_{WPT} is obtained in (4.15). Similar sensitivity analysis can be performed for the coupling coefficients and resonant inductances as well. The analysis results in this section can be used to tune the whole WPT system during implementation. The calculation is based on the design

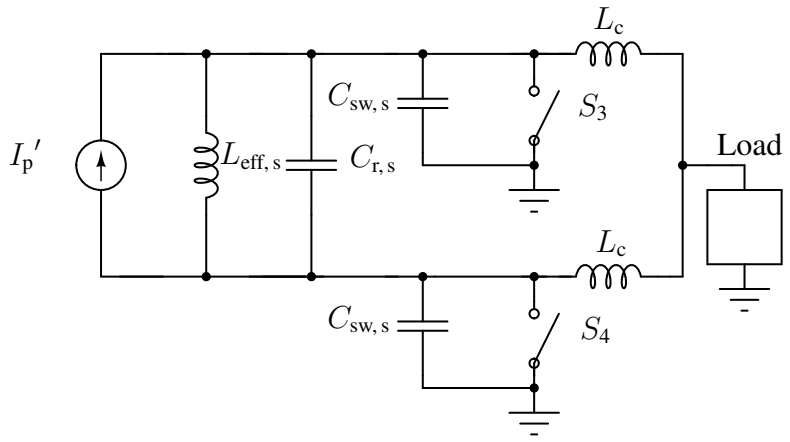

(a) Symmetric CMCD WPT receiver-side circuit model with equivalent ac input current source.

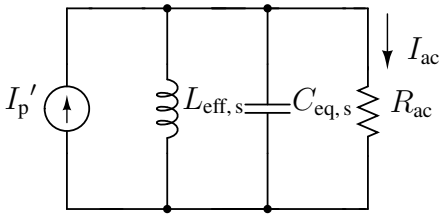

(b) Reduced receiver-side circuit model with 2nd-order parallel resonant tank and ac input current source.

Figure 4.19: CCVS-WPT receiver-side circuit transformations for deriving constant output current.

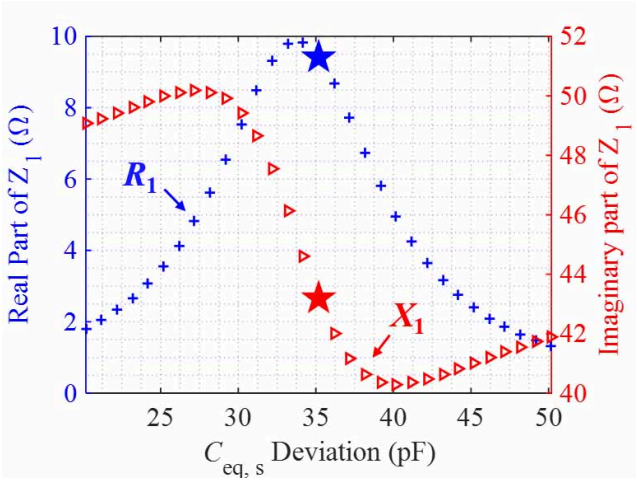

Figure 4.20: Effect of $C_{eq,s}$ deviations on Z_1, which can be regarded as an inductance in series with a resistance. The pentagrams mark the optimal Z_1 for a well-tuned $C_{eq,s} = 1/(\omega^2(1-k^2)L_s)$.

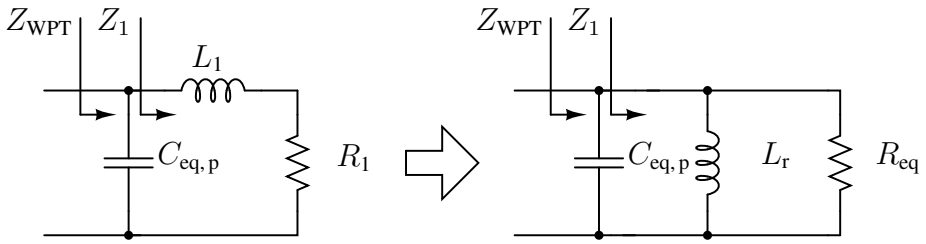

Figure 4.21: Series-to-parallel transformation.

Table 4.2: A Design Case for the Tuned Compensation Network

Components & Parameters	Values
ω	$(2\,\pi \times 100\,\text{M}\,)$ rad/s
R_{Load}	$50\,\Omega$
R_{ac}	$247\,\Omega$
L_{p}, L_{s}	75 nH
k	0.2
$C_{\text{eq, p}}, C_{\text{eq, s}}$	35.2 pF
R_{opt}	$207.36\,\Omega$

case shown in Table 4.2 and the impedance analysis in Fig. 4.18.

As we vary capacitance $C_{\text{eq, s}}$, the real and imaginary parts of Z_1 vary. As shown in Fig. 4.20, the imaginary of Z_1 is always positive, hence Z_1 can be regarded as an inductance $L_1 = X_1/\omega$ with a series resistance R_1. Using a series-to-parallel transformation at ω as shown in Fig. 4.21,

$$\begin{aligned} R_{\text{eq}} &= R_1\left(1+Q^2\right), \\ L_{\text{r}} &= L_1\left(1+\frac{1}{Q^2}\right), \end{aligned} \tag{4.26}$$

where $Q = \omega L_1/R_1 = R_{\text{eq}}/\omega L_{\text{r}}$. The effect of deviations in $C_{\text{eq, s}}$ on R_{eq} and L_{r} is shown in Fig. 4.22. The variations of R_{eq} is axisymmetric with a well-tuned $C_{\text{eq, s}}$ while L_{r} does not have a one-to-one correspondence with $C_{\text{eq, s}}$. $R_{\text{eq}} = R_{\text{opt}}$ when $C_{\text{eq, s}} = 1/\left(\omega^2(1-k^2)L_{\text{s}}\right)$, which is the minimum R_{eq} when varying $C_{\text{eq, s}}$, resulting in the maximum power. The resulting L_{r} can be compensated by $C_{\text{eq, p}}$. The pentagram in Fig. 4.22 is the optimal $R_{\text{eq}} = R_{\text{opt}}$, and $L_{\text{r}} = L_{\text{eff, p}}$ for the well-tuned $C_{\text{eq, s}} = 1/\left(\omega^2(1-k^2)L_{\text{s}}\right)$. If $C_{\text{eq, p}}$ is also well-tuned by satisfying (4.14), $R_{\text{WPT}} = R_{\text{eq}} = R_{\text{opt}}$, $X_{\text{WPT}} = 0$.

Along with $C_{\text{eq, s}}$, $C_{\text{eq, p}}$ can be varied as well. The effects of varying both $C_{\text{eq, p}}$ and $C_{\text{eq, s}}$ on

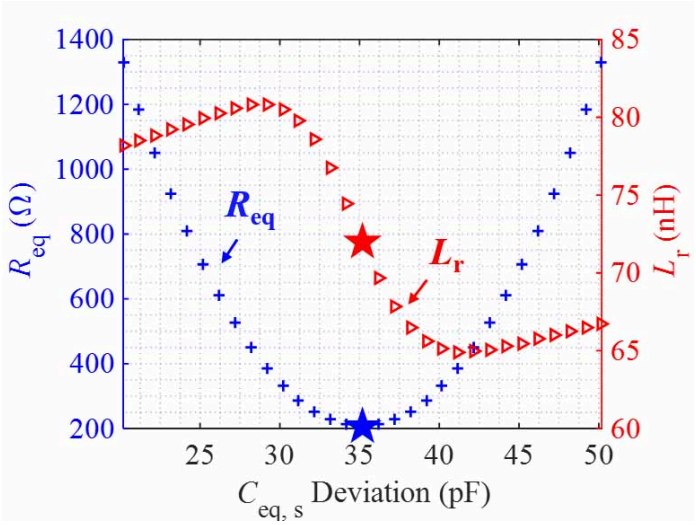

Figure 4.22: Effect of $C_{\text{eq,s}}$ deviations on R_{eq} and L_{r}. The pentagrams mark the optimal $R_{\text{eq}} = R_{\text{opt}}$ and $L_{\text{r}} = L_{\text{eff,p}}$ for well-tuned $C_{\text{eq,s}} = 1/\left(\omega^2(1-k^2)L_{\text{s}}\right)$.

Z_{WPT} are illustrated in Fig. 4.23. We observe that there are several combinations of the tuple $(C_{\text{eq,p}}, C_{\text{eq,s}})$ that each satisfy $R_{\text{WPT}} = R_{\text{opt}}$ or $X_{\text{WPT}} = 0$, which is indicated by the intersections of R_{WPT} and X_{WPT} with the cutting planes of optimal $R_{\text{WPT}} = R_{\text{opt}}$ and $X_{\text{WPT}} = 0$ in Fig. 4.23(a) and Fig. 4.23(b), respectively. However, only one $(C_{\text{eq,p}}, C_{\text{eq,s}})$ satisfies $Z_{\text{WPT}} = R_{\text{WPT}} = R_{\text{opt}}$, as shown in Fig. 4.23(c), which shows that the solution (4.14) is unique.

It is worth noting that for any $C_{\text{eq,s}}$, $R_{\text{WPT}} = R_{\text{opt}}$ is guaranteed for $C_{\text{eq,p}} = 1/\left(\omega^2(1-k^2)L_{\text{p}}\right)$. Thus, we should select $C_{\text{eq,p}}$ first and then vary $C_{\text{eq,s}}$ to make X_{WPT} zero. Larger or smaller $C_{\text{eq,s}}$ will make X_{WPT} deviate from zero, as shown in Fig. 4.24, which causes the loss of ZVS and maximum power transfer because of the displacement from the optimal 90-degree phase shift between the transmitter and receiver voltages.

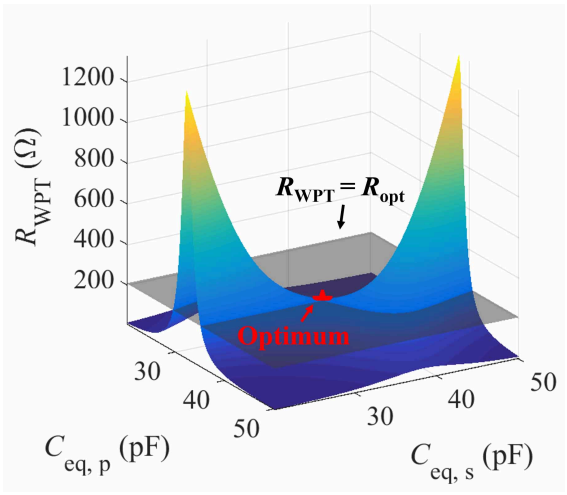

(a) 3D plot: R_{WPT} for different resonant capacitance pairs $(C_{\text{eq,p}}, C_{\text{eq,s}})$ with the cutting plane showing $R_{\text{WPT}} = R_{\text{opt}}$.

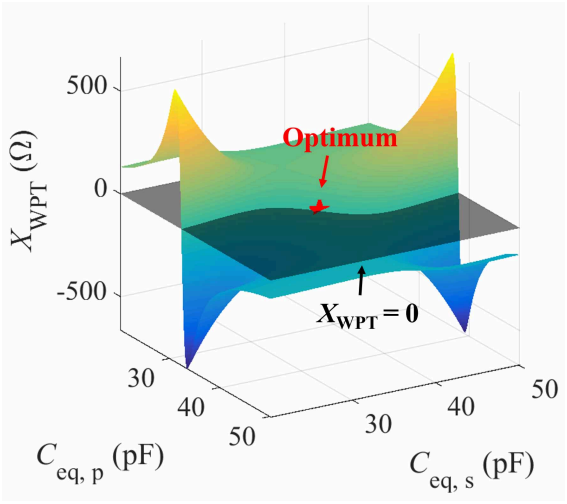

(b) 3D plot: X_{WPT} for different resonant capacitance pairs $(C_{\text{eq,p}}, C_{\text{eq,s}})$ with the cutting plane showing $X_{\text{WPT}} = 0$.

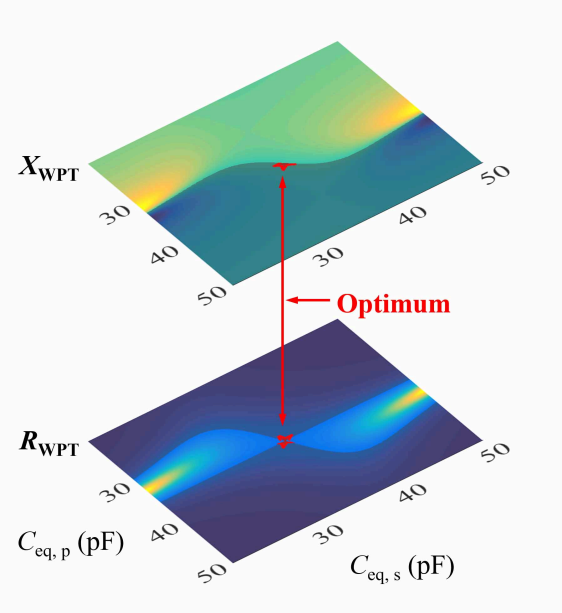

(c) 2D view normal to $R_{\text{WPT}} = R_{\text{opt}}$ and $X_{\text{WPT}} = 0$ planes: $(C_{\text{eq,p}}, C_{\text{eq,s}})$ combinations superimposed. Only a single optimal point $(C_{\text{eq,p}}, C_{\text{eq,s}})$ corresponds to both $R_{\text{WPT}} = R_{\text{opt}}$ and $X_{\text{WPT}} = 0$.

Figure 4.23: WPT impedance $Z_{\text{WPT}} = R_{\text{WPT}} + jX_{\text{WPT}}$ as compensation capacitances $(C_{\text{eq,p}}, C_{\text{eq,s}})$ varies. The WPT system is optimally-tuned when $(C_{\text{eq,p}}, C_{\text{eq,s}})$ satisfies (4.14), having $R_{\text{WPT}} = R_{\text{opt}}$ and $X_{\text{WPT}} = 0$ coincident.

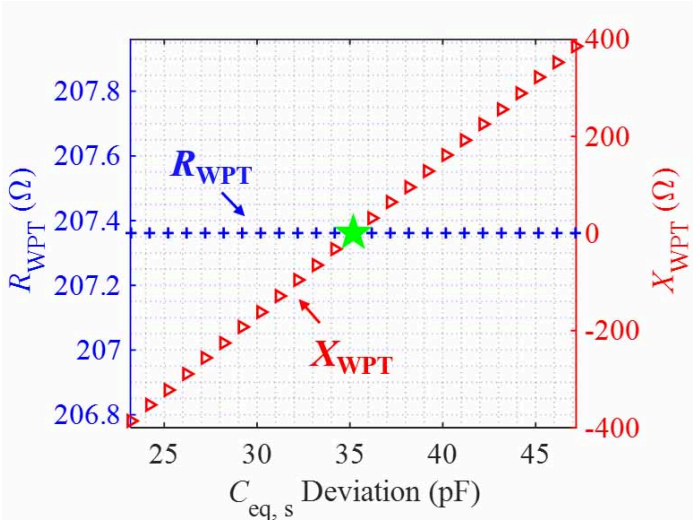

Figure 4.24: After tuning the unloaded transmitter (CMCD inverter) so that $R_{\text{WPT}} = R_{\text{opt}}$ by choosing $C_{\text{eq,p}} = 1/(\omega^2(1-k^2)L_{\text{p}})$, the WPT system can then be tuned in its entirety by choosing $C_{\text{eq,s}}$ so X_{WPT}(▷) equals 0. (+) shows that for optimal $C_{\text{eq,p}}$, R_{WPT} does not vary with $C_{\text{eq,s}}$, which lets us independently choose optimal $C_{\text{eq,s}}$.

4.5 Hardware Implementation and Results

4.5.1 Component Selection

Proper component selection is needed to operate at high frequencies. In the symmetric CMCD WPT hardware, the transmitter uses active devices. The receiver can use either active devices or passive diodes, which correspond to a power flow that is either bi-directional or uni-directional.

In this hardware prototype, active devices are EPC 2037 [89] GaN FETs, which were chosen because of small C_{oss} and gate charge Q_{g}. Compared to the EPC 2038 [90], which had been used previously [4, 15, 75, 76], the EPC 2037 has smaller on-state resistance $R_{\text{ds, on}}$, but larger C_{oss}, corresponding to smaller conduction loss and higher C_{oss} loss. However, the EPC 2037 has smaller total loss. The passive diodes are ZHCS506 [91], which were chosen for small forward voltage drop V_{F} and small diode capacitance C_{D}. The gate drivers provided square waveforms, which were generated by parallel inverters SN74LVC2G04 together with a wideband RF transformer WBC4-14L for signal isolation. The design details of the gate drivers can be found in [15]. The WPT coils, which were identical on both the transmitter and receiver, were fabricated as 4-layer 1 oz FR4 PCB inductors. The choke inductors were the conical BCL-272JL from Coilcraft, which were selected for small stray capacitance and a high impedance over a wide bandwidth. The explicit resonant capacitors were mica capacitors [92] from CDE and VJ HIFREQ Series [93] ceramic capacitors from Vishay, which were selected for high quality factors at 100 MHz and high self-resonant fre-

Table 4.3: Implementation of the Symmetric CMCD WPT System

Components & Parameters	Values
Choke Inductor	BCL-272JL 2.75 μH
GaN HEMT	EPC 2037
Diode	ZHCS506
Gate Driver	SN74LVC2G04 & WBC4-14L
WPT PCB Coils	75 nH ($R = 1.56$ cm)
Transfer Distance	1 cm
Coupling Coefficient	0.2
Explicit Transmitter Capacitance	MICA 30 pF
Explicit Receiver Capacitance	VJ HIFREQ Series 30 pF

quencies well above 100 MHz. The components are listed in Table 4.3. The PCB layouts for the transmitter (active CMCD converter) and receiver (synchronous or uncontrolled/passive CMCD rectifier) are shown in Fig. 4.25.

4.5.2 Tuning

Compensation networks are crucial for WPT hardware systems. A detuned hardware system reduces the efficiency and output power. We present three steps to design the symmetric CMCD WPT hardware, which are especially applicable at 100 MHz where parasitics have a significant effect:

4.5.2.1 Designing the transmitter as an unloaded CMCD inverter

Tuning an unloaded CMCD transmitter is the first step towards complete WPT hardware. An unloaded transmitter is a typical mode of operation in wireless power transfer applications because the receiver is often freely and frequently removed from a charging pad. The strategy is to choose the explicit transmitter resonant capacitance $C_{\mathrm{r,p}}$ first to obtain $R_{\mathrm{WPT}} = R_{\mathrm{opt}}$, which is independent of $C_{\mathrm{r,s}}$ when $C_{\mathrm{eq,p}} = 1/\left(\omega^2(1-k^2)L_{\mathrm{p}}\right)$, as verified in Fig. 4.24. An unloaded transmitter is shown in Fig. 4.26(a) with typical gate and drain voltage waveforms in Fig. 4.26(b), which are similar in quality to the waveforms of lower-frequency CMCD converters [52, 77]. The gating loss is 300 mW and the unloaded transmitter loss is 341 mW both measured with $6\frac{1}{2}$-digit multimeters (Keysight 34465A and HP 34401A) as shown in Fig. 4.26(a). The experimental waveforms in this section are obtained by using four 1 GHz probes (TPP1000 from Tektronix) with 1 GHz, 2.5 GS/s

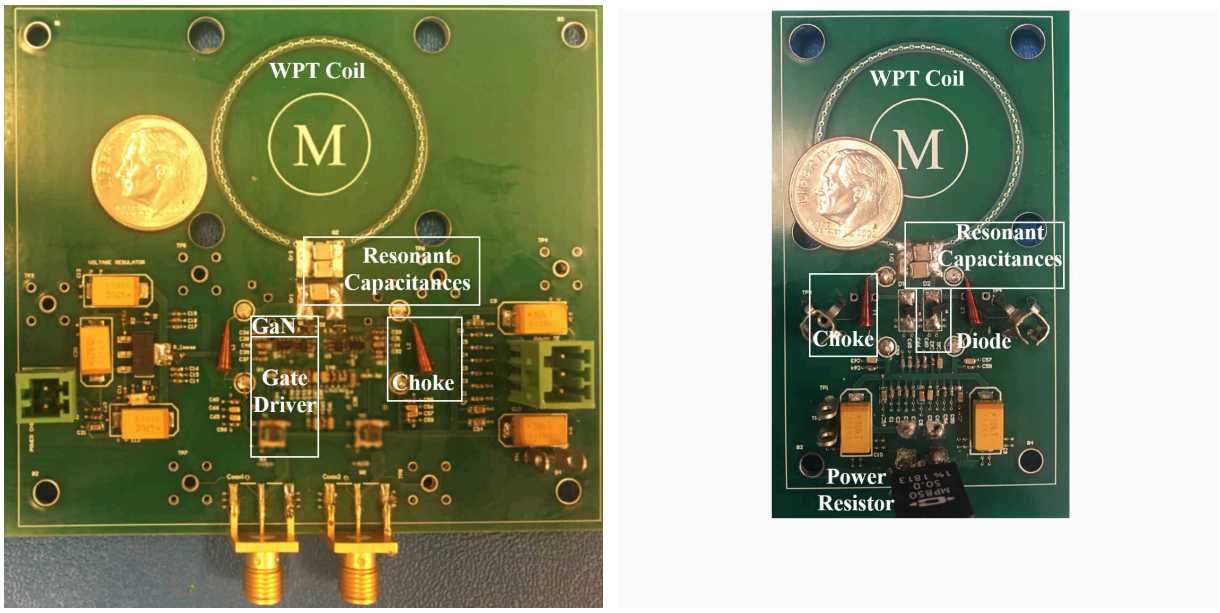

(a) Active CMCD converter.

(b) Passive CMCD converter.

Figure 4.25: Miniaturized 100 MHz CMCD converters relative to US Dime coins.

oscilloscope (MDO4104B-6 from Tektronix).

Together with the maximum output power, the unloaded transmitter loss determines the highest possible efficiency through the lower bound on the loss within symmetric WPT hardware. The goal of Step 1 is to achieve ZVS at the drains of the devices. In practice, a small drain voltage at turn-off or reverse conduction from a decrease in the effective resonant inductance $L_{\text{eff, p}} = (1 - k^2)\, L_{\text{p}}$ when a receiver is coupled, results in only a small and acceptable loss.

4.5.2.2 Determining the coupling coefficient over which the transmitter and receiver coils will operate

Coupling coefficient k varies with the air gap between the transmitter coil and the receiver coil. k is determined by the geometry and physical configuration of the coils. For an isolated receiver coil that is open-circuited, $I_{\text{s}} = 0$ in (4.4), thus,

$$\begin{pmatrix} V_{\text{p}} \\ V_{\text{s}} \end{pmatrix} = \begin{pmatrix} j\omega L_{\text{p}} & -j\omega M \\ j\omega M & -j\omega L_{\text{s}} \end{pmatrix} \begin{pmatrix} I_{\text{p}} \\ 0 \end{pmatrix}, \tag{4.27}$$

then

$$\begin{aligned} V_{\text{p}} &= j\omega L_{\text{p}} I_{\text{p}}, \\ V_{\text{s}} &= j\omega M I_{\text{p}}, \end{aligned} \tag{4.28}$$

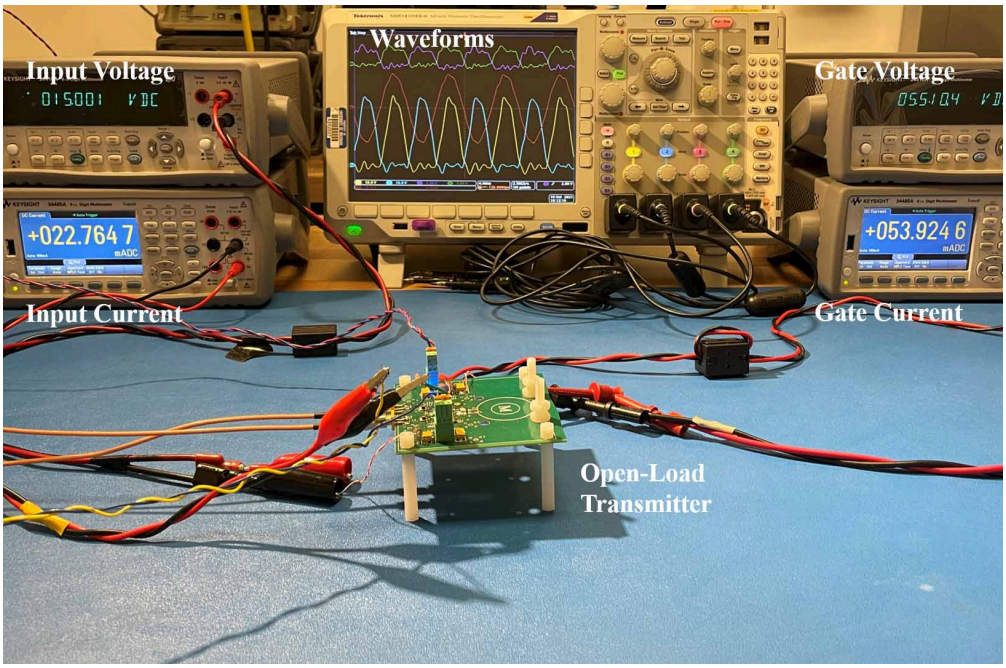

(a) Unloaded symmetric CMCD WPT transmitter (CMCD inverter). Two $6\frac{1}{2}$-digit multimeters measure the total gate drive power. Another two $6\frac{1}{2}$-digit multimeters measure the dc input power. The gating loss is 0.300 W and the unloaded transmitter power circuit loss is 0.341 W.

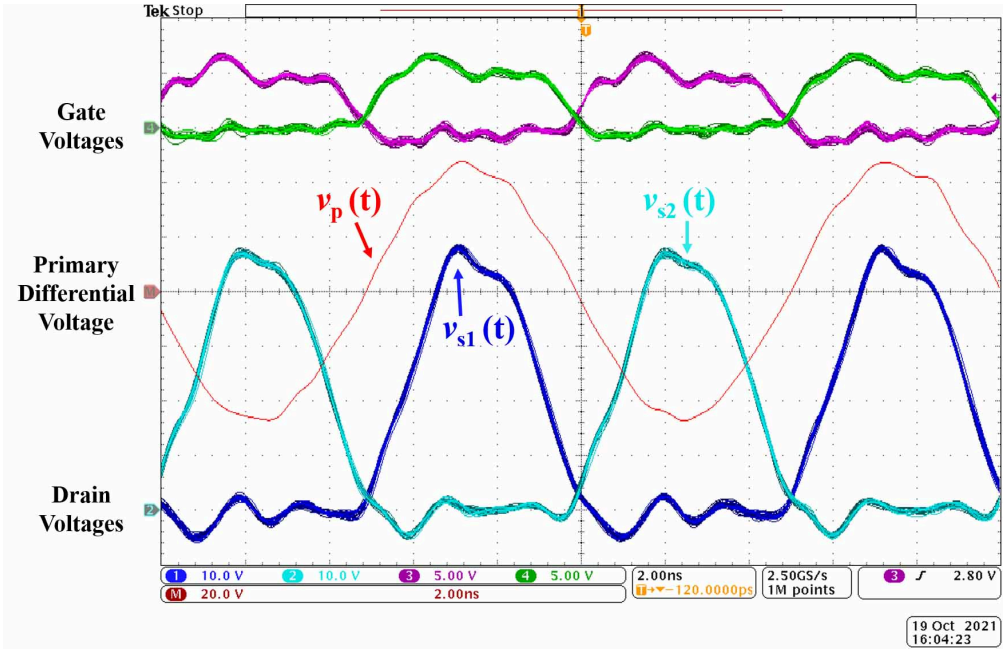

(b) Typical waveforms of the *tuned* 100 MHz unloaded CMCD transmitter when $V_{\text{in}} = 15$ V. The voltage waveforms are obtained using four 1 GHz probes (TPP1000 from Tektronix) with 1 GHz, 2.5 GS/s oscilloscope (MDO4104B-6 from Tektronix).

Figure 4.26: Step 1: Designing the transmitter as an unloaded CMCD inverter.

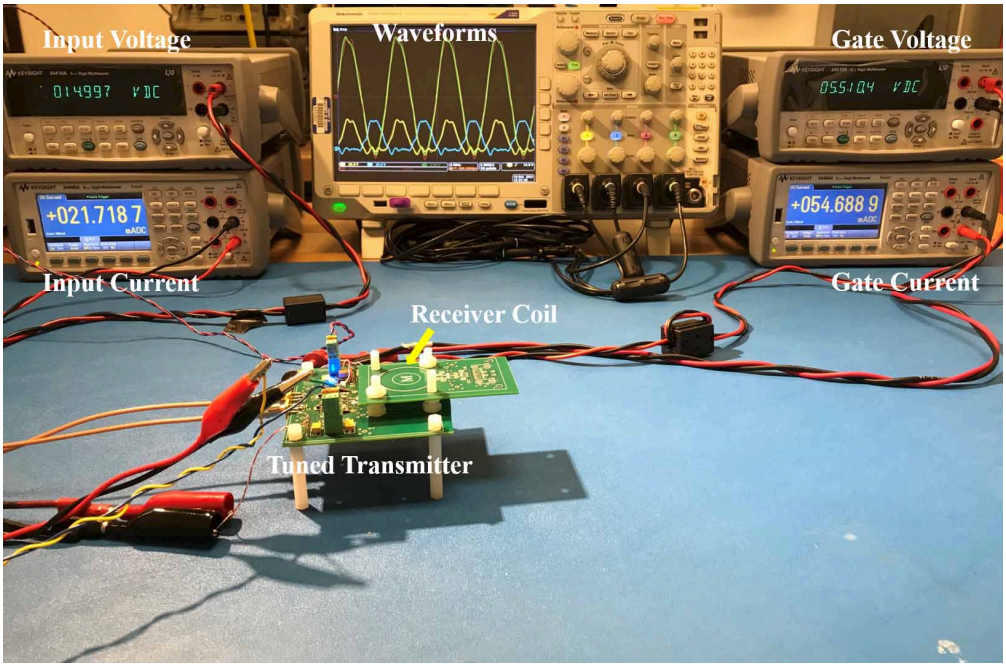

(a) The receiver WPT coil is directly placed on top of the transmitter. The coupling coefficient $k = |V_s|/|V_p| = 0.2$ for identical WPT coils.

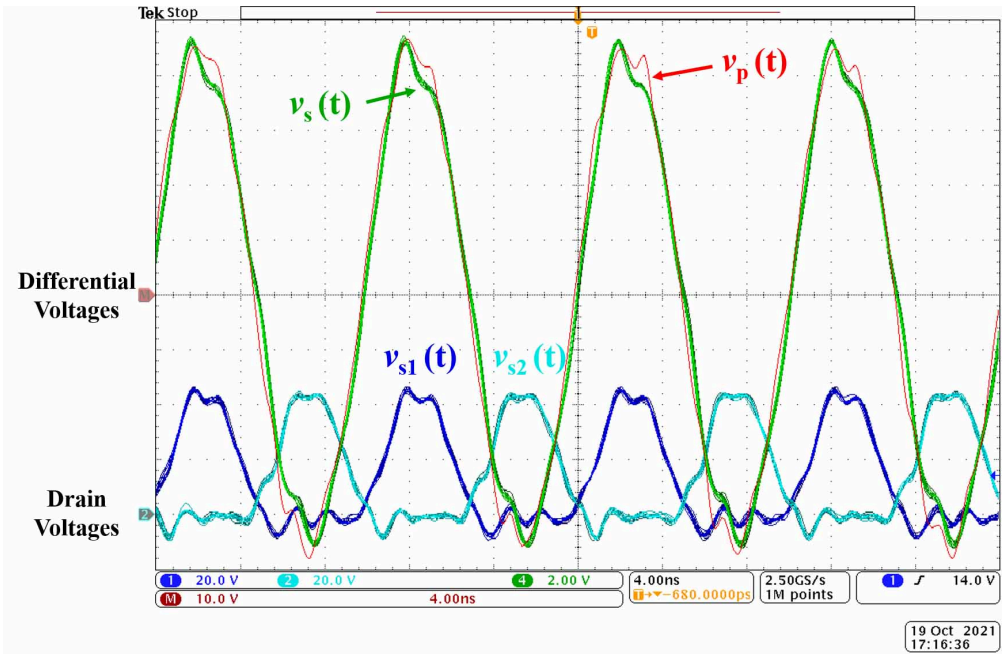

(b) From $v_p(t)$ and $v_s(t)$, the coupling coefficient can be calculated to be approximately 0.2 at 1 cm transfer distance.

Figure 4.27: Step 2: Determining the coupling coefficient over which the transmitter and receiver coils will operate.

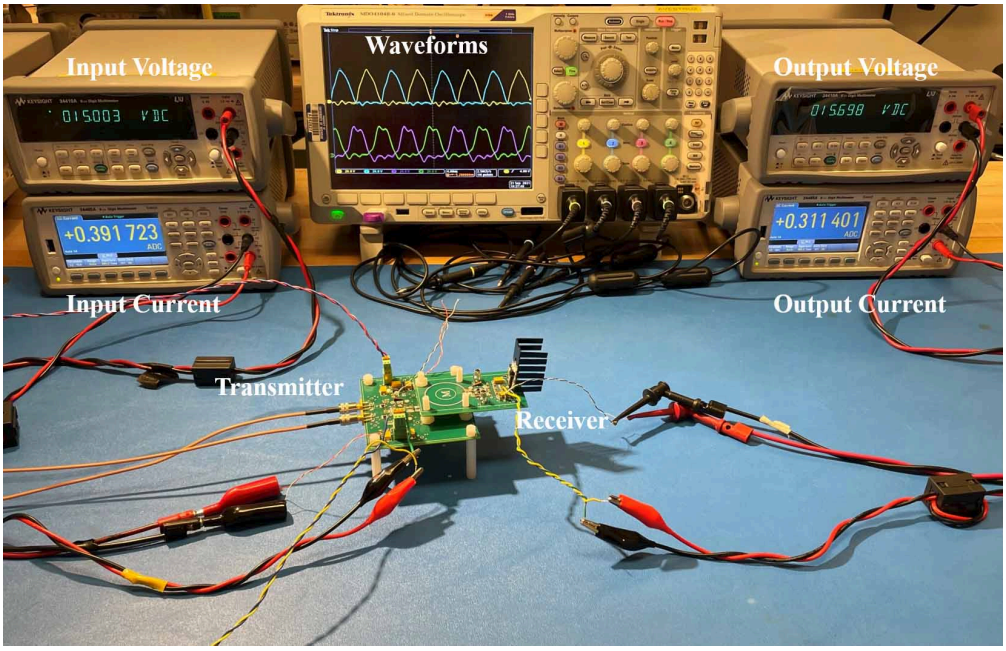

(a) Hardware setup of the tuned symmetric CMCD wireless power transfer system. Power and efficiency are calculated from the input and output voltages and currents by four $6\frac{1}{2}$-digit multimeters (34465A from Keysight and 34401A from HP). The input power is 5.877 W, output power is 4.888 W, and the gating loss is 0.300 W. The dc-dc efficiency without gating loss is 83.2 % while the total efficiency is 79.1 %.

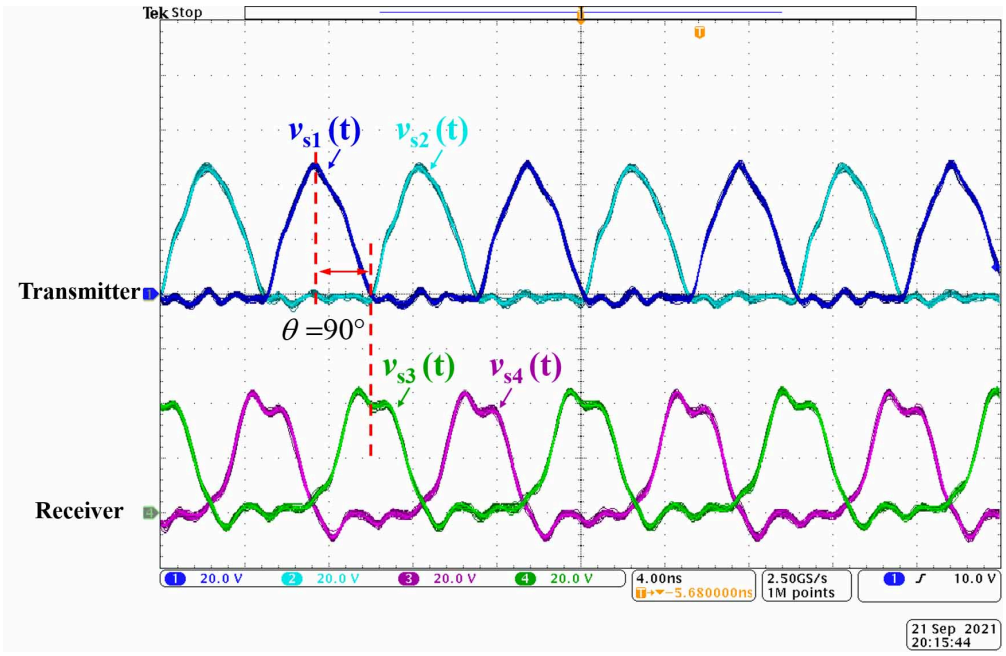

(b) Tuned drain and passive rectifier diode voltage waveforms for the symmetric CMCD WPT system, which corresponds to theoretical predictions in Section 4.2.3. The waveforms are obtained using four 1 GHz probes (TPP1000 from Tektronix) with a 1 GHz, 2.5 GS/s oscilloscope (MDO4104B-6 from Tektronix).

Figure 4.28: Step 3: Tuning the receiver while operating with the transmitter.

where V_{p} and V_{s} are in phase. It is worth noting that

$$k = \frac{|V_{\mathrm{s}}|}{|V_{\mathrm{p}}|}\sqrt{\frac{L_{\mathrm{p}}}{L_{\mathrm{s}}}}. \tag{4.29}$$

The measurement set-up and corresponding waveform are shown in Fig. 4.27, indicating a coupling coefficient of 0.2, which matches with the approximation of using circular filament coils [37] with the parameters in Table 4.3.

4.5.2.3 Tuning the receiver while operating with the transmitter

In the last step, the WPT receiver is coupled to the transmitter. By adjusting $C_{\mathrm{eq,\,s}}$, transmitter drain voltages and receiver drain/diode voltages must achieve the optimal 90-degree phase shift while maintaining the ZVS, which corresponds to theoretical predictions in Section 4.4.3. The explicit transmitter and receiver resonant capacitances are shown in Table 4.3. The tuned symmetric CMCD WPT hardware corresponds to $P_{\mathrm{in}} = 5.877\,\mathrm{W}$, $P_{\mathrm{out}} = 4.888\,\mathrm{W}$, $P_{\mathrm{gate}} = 0.3\,\mathrm{W}$, $\eta_{\text{dc–dc, w/o gating loss}} = 83.2\,\%$, $\eta_{\mathrm{total}} = 79.1\,\%$. The dc input power P_{in}, dc output power P_{out}, and total gating loss P_{gate} are calculated through the measurement of corresponding dc currents and voltages through $6\frac{1}{2}$-digit multimeters in this section.

4.5.3 Calculated Loss Budget

Investigating the loss budget enables the formulation of strategies to decrease loss and increase efficiency. For the case in Fig. 4.28, the loss budget is shown in Fig. 4.29(a). Although C_{oss} loss dominates the budget, higher efficiency can be achieved by operating the GaN FETs at a higher output current and hence power.[1] The limiting factor to running the EPC 2037 devices at higher current is the small packaging, which restricts the amount of heat that can be removed with natural convection cooling.

The gate driver loss is 21 %, which is considerable when using commercially available logic CMOS inverters, in comparison to the 2 % loss from the FET gate charge. The gate driver loss can be better optimized in a customized integrated circuit. Fig. 4.29(b) includes the losses for the symmetric CMCD WPT system using a synchronous rectifier, which will be presented and compared in Section 4.5.5.

[1] C_{oss} loss is largely independent of device current at constant temperature [40].

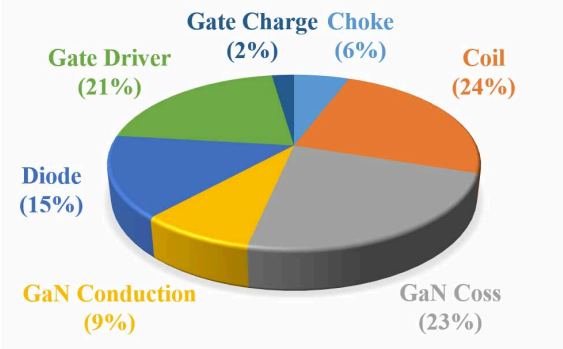

(a) Calculated loss budget when using a passive rectifier with $P_{\text{in}} = 5.877\,\text{W}$, $P_{\text{out}} = 4.888\,\text{W}$, $P_{\text{gate}} = 0.3\,\text{W}$, $\eta_{\text{dc-dc, w/o gating loss}} = 83.2\,\%$, $\eta_{\text{total}} = 79.1\,\%$.

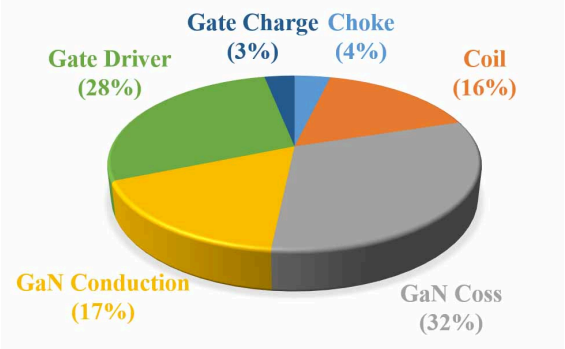

(b) Calculated loss budget when using a synchronous rectifier, which will be discussed in Section 4.5.5. $P_{\text{in}} = 5.835\,\text{W}$, $P_{\text{out}} = 4.390\,\text{W}$, $P_{\text{gate}} = 0.600\,\text{W}$, $\eta_{\text{dc-dc, w/o gating loss}} = 75.2\,\%$, $\eta_{\text{total}} = 68.2\,\%$.

Figure 4.29: Calculated loss budgets of the symmetric CMCD WPT system for passive and synchronous rectifiers when $V_{\text{dc}} = 15\,\text{V}$ and $R_{\text{Load}} = 50\,\Omega$.

4.5.4 Bipolar Receiver Output Voltage

Symmetric CMCD WPT systems can output both positive and negative voltages at the receiver load. As mentioned in Section 4.2.3, by changing the polarity of the diodes in Fig. 4.25(b), as shown in Fig. 4.30(a), the output resistor load will draw current from the negative output dc voltage. It is worth noting that the drain voltages are negative. The waveforms for a CMCD WPT system with negative output voltage are shown in Fig. 4.30(b), which can be compared to Fig. 4.28(b). The result in Fig. 4.30 corresponds to $P_{\text{in}} = 6.090\,\text{W}$, $P_{\text{out}} = 5.016\,\text{W}$, $\eta_{\text{dc–dc, w/o gating loss}} = 82.4\,\%$, $P_{\text{gate}} = 0.3\,\text{W}$, $\eta_{\text{total}} = 78.5\,\%$ when $V_{\text{dc}} = 15\,\text{V}$ and $R_{\text{Load}} = 50\,\Omega$.

Synchronous rectifiers can also support negative output voltage at the receiver resistive load. However, because GaN devices are two-quadrant instead of four-quadrant switches, simply swapping the control signals of S_3 and S_4 will not result in a negative output voltage. Instead, because GaN devices are typically bi-directional, the current-carrying direction of the GaN devices needs to be reversed by referencing the gate driver to the more negative terminal of the channel.

4.5.5 Comparison Between the Synchronous and Passive Rectifiers

Synchronous rectifiers are intended to decrease the conduction loss with a channel resistance instead of a junction voltage drop in diodes for passive/uncontrolled rectifiers [19, 52, 94–96]. It is worth noting that synchronous rectifiers also enable bi-directional wireless power transfer [77]. However, despite the original intent for using synchronous rectifiers, they perform less efficiently than Schottky diodes. Contemporary devices like the EPC 2037 and EPC 2038 that work at 100 MHz have on-state resistances of 3.3 Ω and 0.55 Ω, respectively, with which we compare

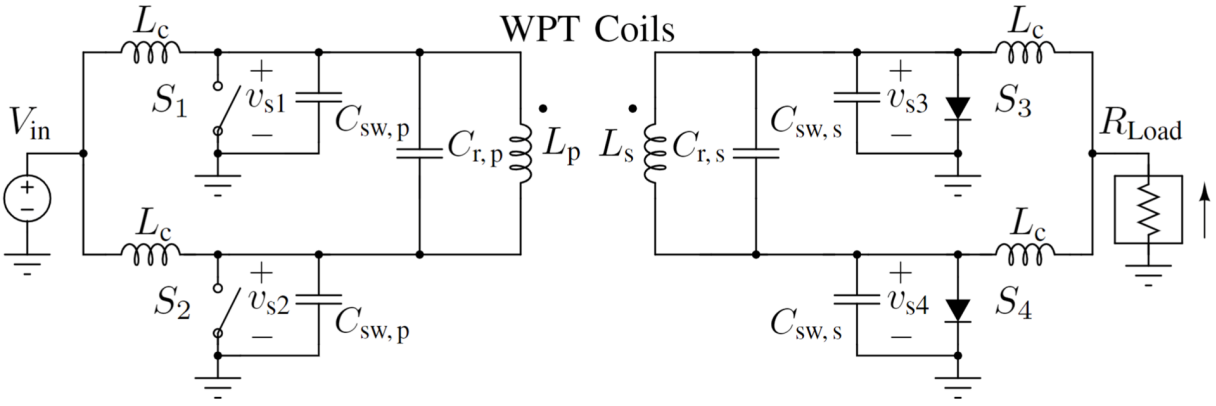

(a) Diode cathodes are connected to ground for a negative dc output voltage.

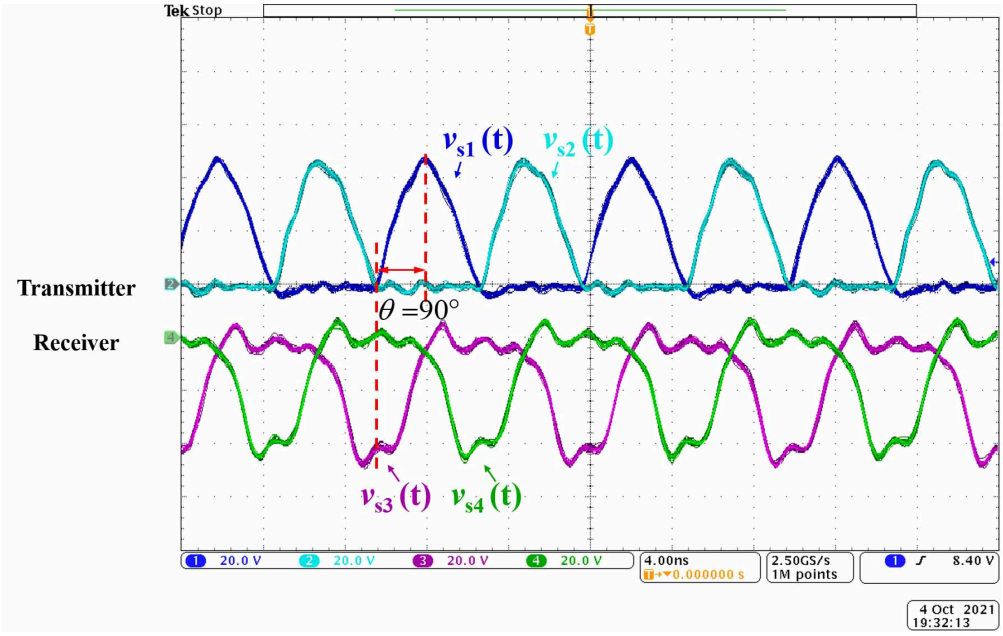

(b) Diode voltages v_{s3} and v_{s4} are both negative and 90 degrees out of phase with the transmitter drain voltages v_{s1} and v_{s2} for negative dc output.

Figure 4.30: Hardware results for a negative dc output voltage correspond to theoretical predictions in Section 4.2.3.

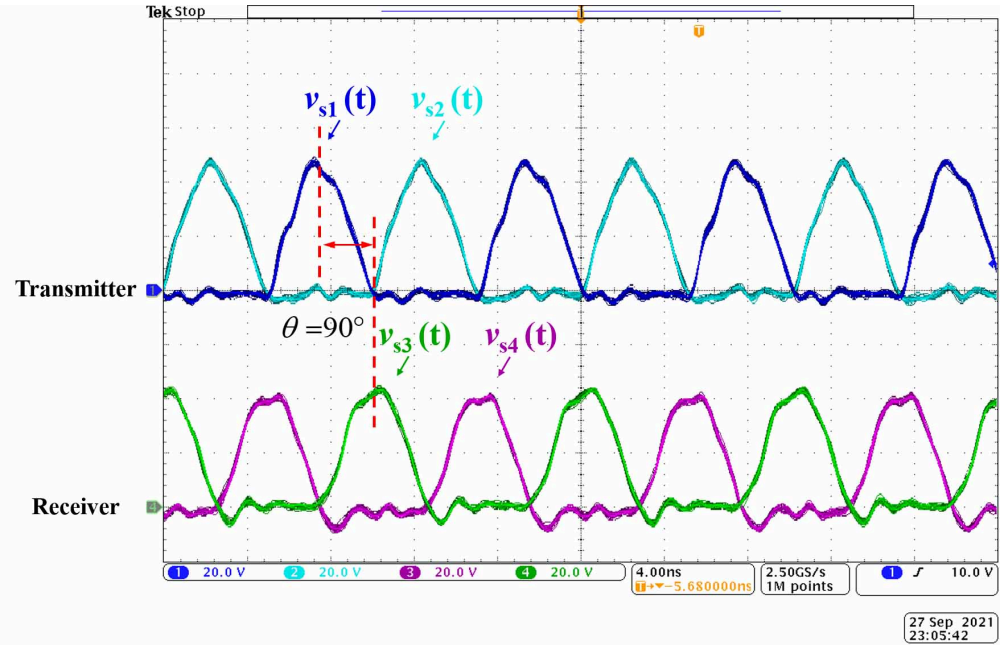

Figure 4.31: Synchronous rectifiers can also be used with resistive loads. Drain waveforms are similar to that using diode rectifiers, as shown in Fig. 4.28(b).

losses to Schottky diode ZHCS506 with a forward voltage of 0.63 V. For the range of the prototype power at 100 MHz, the synchronous rectifier performs more poorly than the passive rectifier because of high C_{oss} loss and twice the gating loss P_{gate}. A loss budget is shown in Fig. 4.29(b), which corresponds to $P_{\text{in}} = 5.835\,\text{W}$, $P_{\text{out}} = 4.390\,\text{W}$, $P_{\text{gate}} = 0.6\,\text{W}$, $\eta_{\text{dc–dc, w/o gating loss}} = 75.2\,\%$, and $\eta_{\text{total}} = 68.2\,\%$ when $V_{\text{dc}} = 15\,\text{V}$ and $R_{\text{Load}} = 50\,\Omega$. The corresponding drain voltages for the synchronous rectifier are shown in Fig. 4.31, which are nearly the same as Fig. 4.28(b) using the passive rectifier. Additional data points for efficiency and power comparison for a $50\,\Omega$ load are shown in Fig. 4.32.

Although the synchronous rectifier may have less efficiency, its salient feature of bi-directional wireless power transfer, for example by using phase-shift modulation [95], makes it important for peer-to-peer (P2P) charging. It is worth noting that bi-directional WPT is also possible for symmetric CMCD wireless power transfer with dc voltage sources that can source and sink power [77]. For example, Fig. 4.33 demonstrates that power can be transferred from the secondary side to the primary side, which is different from all the other cases in this paper. Both CMCD converters are connected to the same DC voltage source $V_{\text{in}} = V_{\text{out}} = 18\,\text{V}$, which is the same configuration with [3, 77, 85]. The result corresponds to $P_{\text{in}} = 8.964\,\text{W}$, $P_{\text{out}} = 6.050\,\text{W}$, $P_{\text{gate}} = 0.6\,\text{W}$, $\eta_{\text{dc–dc, w/o gating loss}} = 67.5\,\%$, and $\eta_{\text{total}} = 63.3\,\%$. Details about phase-shift power modulation for bi-directional WPT using symmetric CMCD WPT systems can be found in [77]. In this section, we focused on the circuit design of the synchronous rectifier in WPT rather than the control strate-

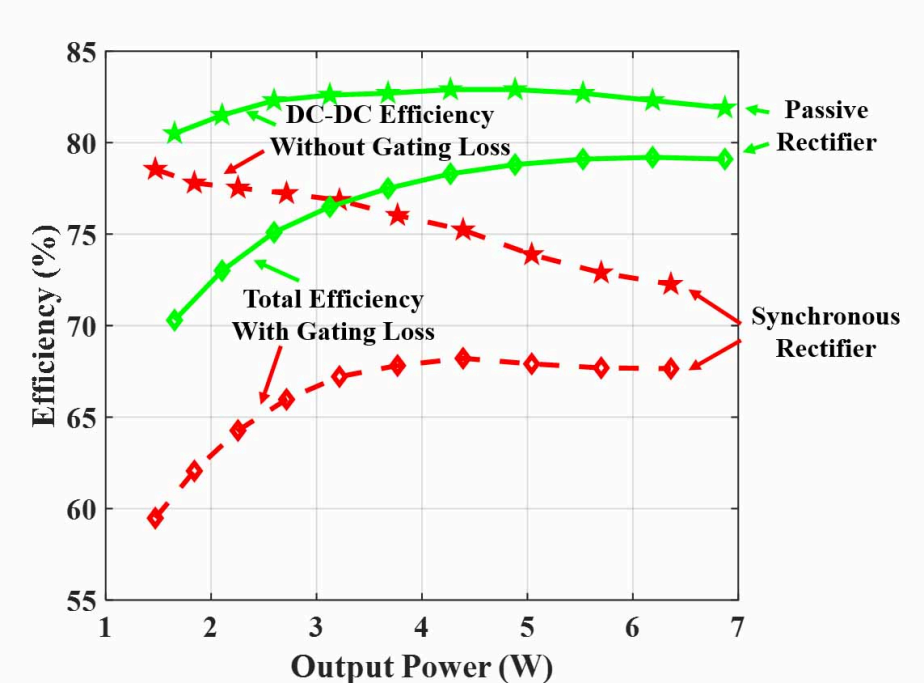

Figure 4.32: Power and efficiency comparison between the synchronous rectifier and passive rectifier when $R_{\text{Load}} = 50\,\Omega$. Passive rectifier outperforms synchronous rectifier in terms of power and efficiency for the same input (different V_{in}) and output (R_{Load}).

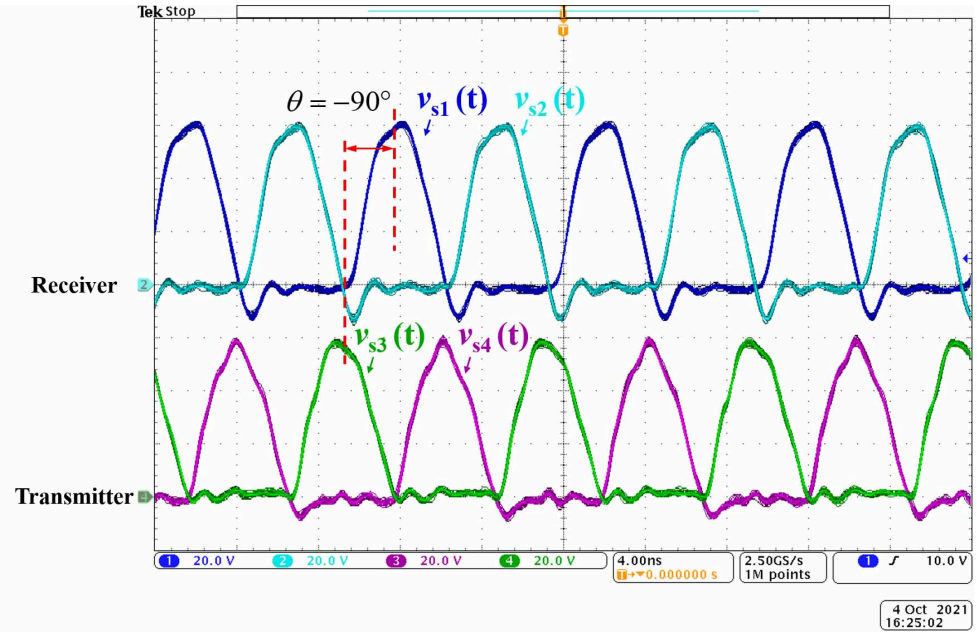

Figure 4.33: Active devices are needed on both sides of the WPT system for bi-directional wireless power. The primary↦receiver behaves as a synchronous rectifier while the secondary↦transmitter behaves as an inverter. The drain waveforms have the opposite polarity of phase, i.e. -90 degrees, for reverse power transfer.

gies such synchronization, which had been addressed in [97–99].

4.5.6 Wide Load Range with Constant Output Current

A wide load range is typically needed for WPT applications with constant output current as a preferred mode of operation for many applications including battery charging. Symmetric CMCD WPT systems intrinsically have a wide load range together with constant output current. In this section, we keep the compensation networks fixed with values shown in Table 4.3, and verify the system characteristics by varying the loads at several different input voltages. Fig. 4.34 shows the drain voltages of the transmitter and the diode voltages for the passive rectifier at $V_{\text{in}} = 15\,\text{V}$ for different loads. One observes that zero or nearly zero voltage switching is maintained both at the transmitter and receiver, with minimal reverse conduction. The transmitter drain voltages nearly overlap with each other, demonstrating the transmitter output voltage V_{p} appears stiff and load-independent within the load range.

For maximum power transfer, the phase shift between the voltages of the transmitter and receiver coil needs to be 90 degrees [77]. This necessarily means that the complementary diode voltages of the receiver S_3 and S_4 need to lag the drain voltages of the transmitter S_1 and S_2 by 90 degrees, respectively. This is demonstrated in Fig. 4.34 when $R_{\text{Load}} = 50\,\Omega$.

The phase shift between the transmitter and receiver coil voltages becomes larger than 90 degrees when the load resistor R_{Load} becomes smaller than $50\,\Omega$, which results in smaller voltages at the receiver, hence making the junction capacitance C_{D} of the passive Schottky rectifiers ZHCS506 [91] larger. As the junction capacitance increases, the parallel resonant tank in Fig. 4.19(b) moves off resonance and appears capacitive at the 100 MHz frequency of $I_{\text{p}}{}'$. The detailed explanation of the greater than 90-degree phase shift can be found in [52].

Constant output current is maintained despite a wide range of resistive loads at a particular dc input voltage, as shown in Fig. 4.35. The deviation in output current is within $\pm 4\,\%$. Smaller deviation can be achieved by either better tuning with more precise explicit capacitors or closed-loop control. The explicit capacitors in the prototype shown in Table 4.3 are 5 % tolerance.

Output power and efficiency over a wide load range are shown in Figs. 4.36(a) and 4.36(b), respectively, with voltage waveforms in Figs. 4.34 and 4.37. We can observe that the output power is linearly increasing with the square of input voltage, which is indicated by the R^2 from linear regression, verifying (4.18) and (4.25). The dc-dc efficiency without the gating loss is above 80 % for different voltages and their corresponding power in Fig. 4.36(a) at 100 % load. One can observe that the efficiency is largely insensitive to the input voltage and nearly constant at a particular loading.

The dc–dc efficiency without gating loss is approximately 80 % or better for loading above

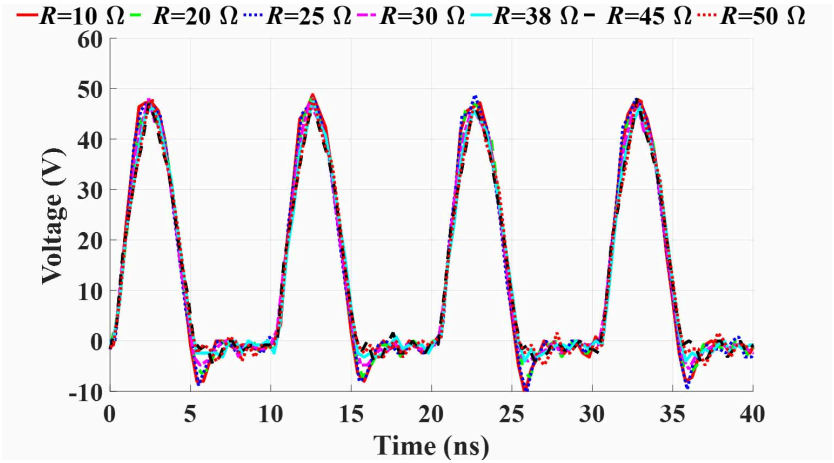

(a) Transmitter odd switch S_1 drain voltages.

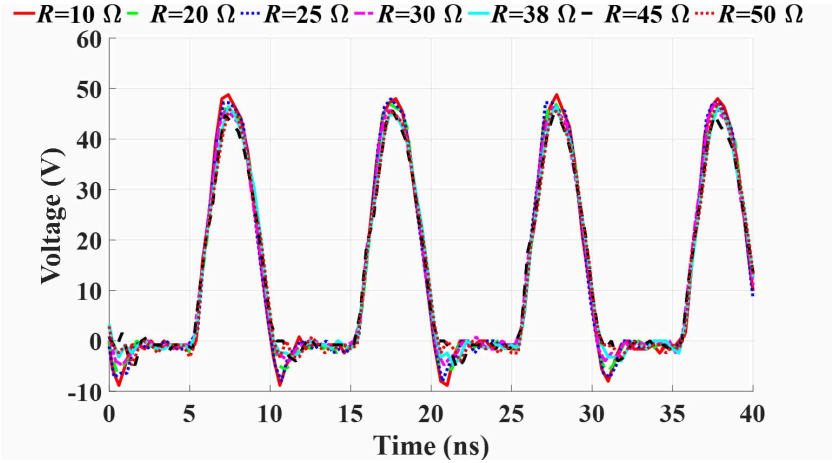

(b) Transmitter even switch S_2 drain voltages.

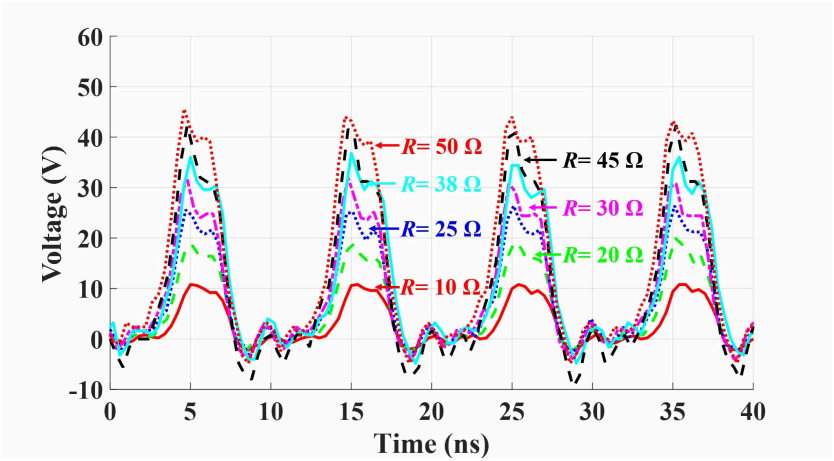

(c) Receiver odd switch S_3 diode voltages.

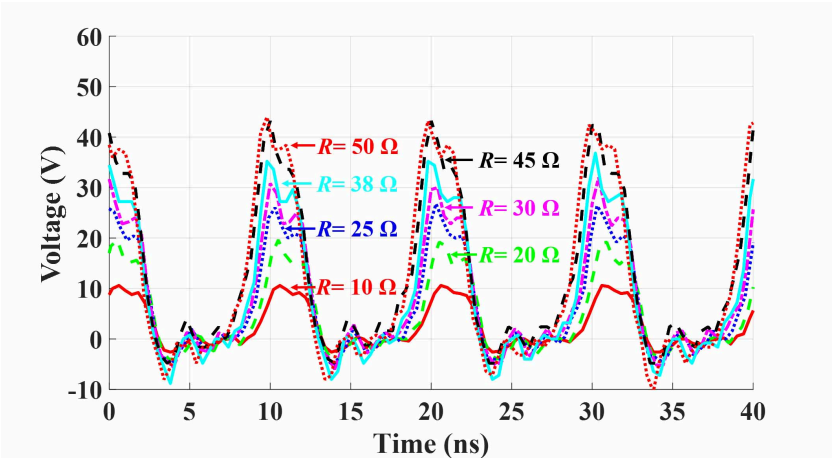

(d) Receiver even switch S_4 diode voltages.

Figure 4.34: In symmetric CMCD WPT hardware, zero voltage switching can be maintained at 100 MHz over a *wide load range*. The transmitter drain and receiver diode voltages show ZVS throughout the $R_{\text{Load}} = 10\,\Omega$ to $50\,\Omega$ load range, with minimal reverse conduction. The transmitter drain voltages nearly overlap with each other within the load range, which appears stiff and load-independent. Input voltage is constant $V_{\text{in}} = 15\,\text{V}$.

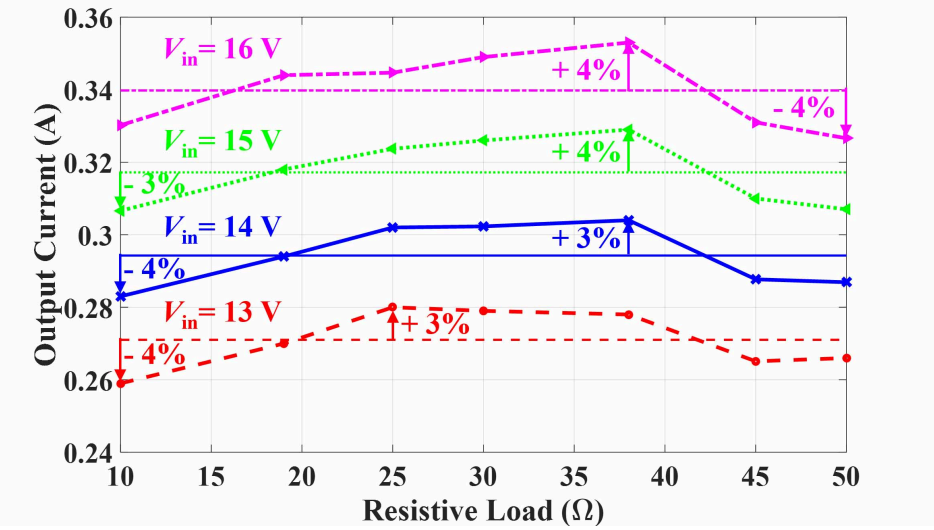

Figure 4.35: Constant output current can be maintained in hardware over a wide load range. The load current is largely determined by the input voltage V_{in}. The maximum current deviation in the WPT prototype was within $\pm$ 4 %.

75 %. The input dc voltage may be used for power modulation as an alternative to phase-shift power modulation [77]. The power and efficiency as a function of input dc voltage for $R_{\text{Load}} = 50\,\Omega$ corresponding to 100 % loading are shown in Fig. 4.38. The WPT system maintains above 80 % efficiency without the gating loss and above 70 % total efficiency for an output power between 1.7 W and 6.9 W using only natural convection cooling of a small device package.

4.6 Summary

Increasing the switching frequency enables miniaturization and offers the opportunity for circuit integration. With optimal design, 100 MHz symmetric CMCD WPT systems can have a wide load range, constant output current, and small input and output current ripple with straightforward design and easily tuned compensation networks. The systematic and rigorous optimal design method for tuning had been developed in this paper from theoretical equivalent circuit models and demonstrated in hardware. With an optimal design, the hardware system with the passive rectifier achieves greater than 80 % efficiency without gating loss and above 70 % total efficiency for a wide power range of 1.7 W to 6.9 W. The peak total efficiency is above 79.1 % for an output power of 4.9 W to 6.9 W. For the optimal designs in hardware, the synchronous rectifier performs less efficiently than the passive rectifier despite synchronous rectifiers allowing bi-directional wireless power transfer. Both rectifiers can have bipolar receiver output voltages.

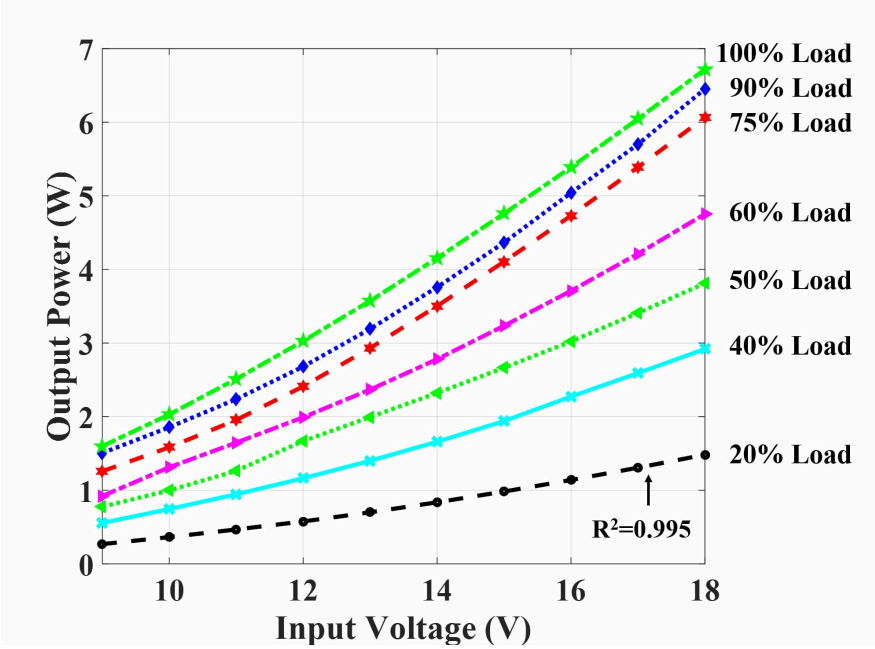

(a) Output power is demonstrated in hardware to be linear with the square of input voltage over a wide load range. The worst-case linear fit has an $R^2 = 0.995$.

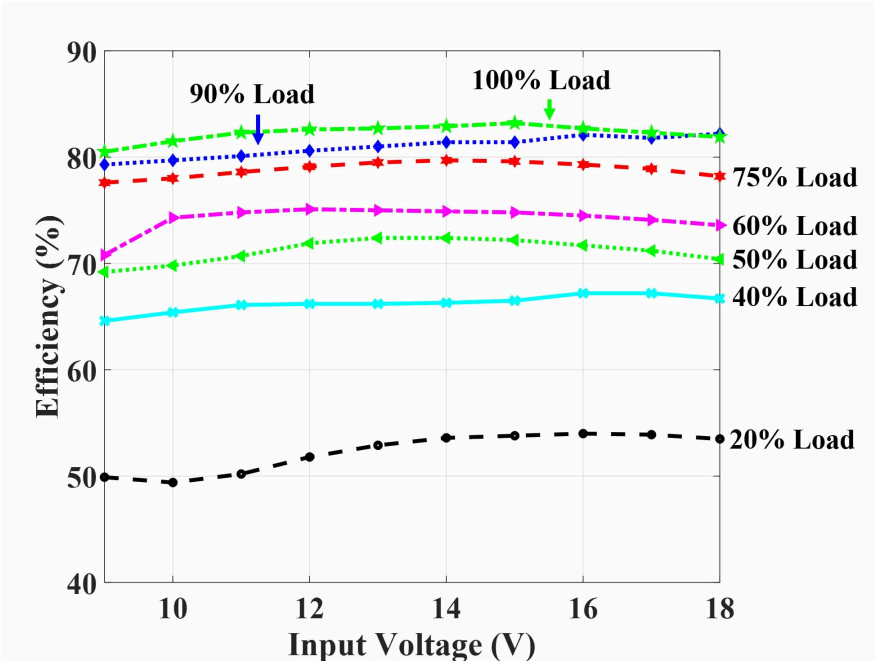

(b) Dc-dc efficiency without gating loss is nearly constant over input voltages for a wide load range. At 100% load, the peak efficiency is 83.2 %.

Figure 4.36: Output power and efficiency of the 100 MHz symmetric CMCD WPT hardware with the passive rectifier over a wide input voltage and load range.

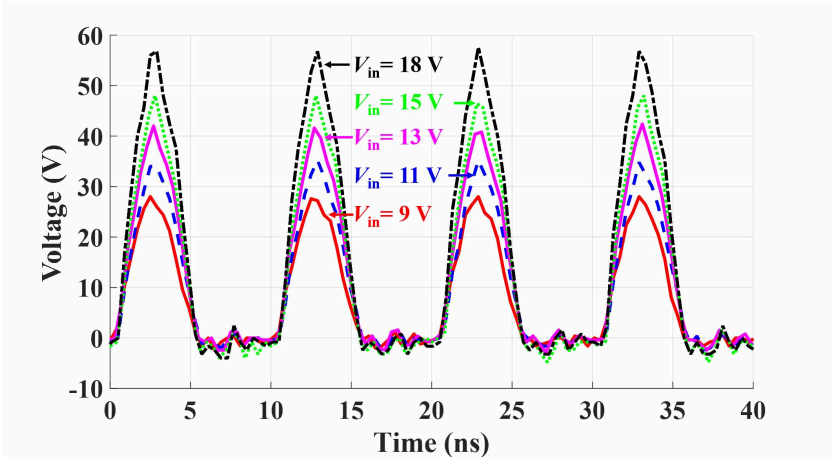

(a) Transmitter odd switch S_1 drain voltages.

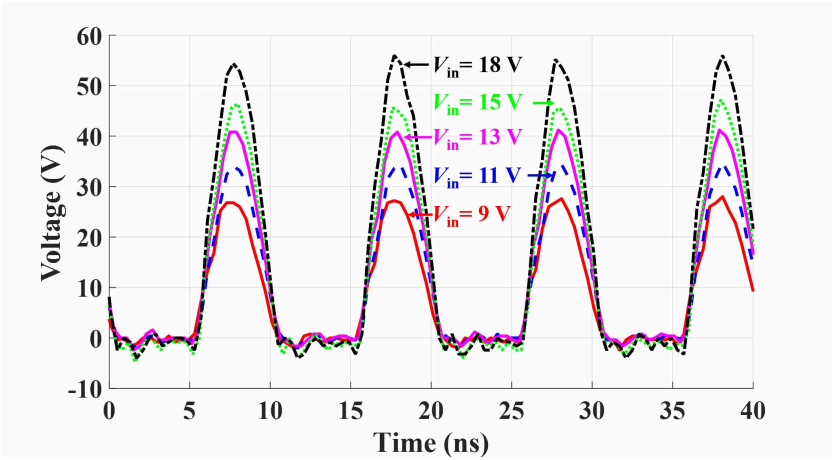

(b) Transmitter even switch S_2 drain voltages.

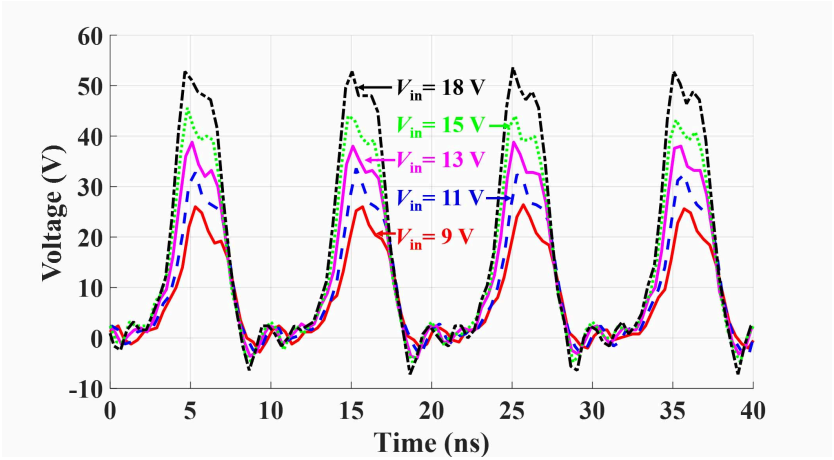

(c) Receiver odd switch S_3 diode voltages.

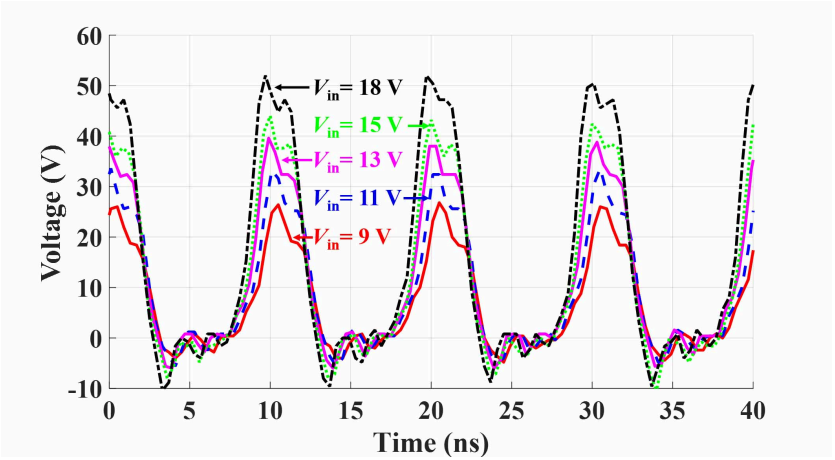

(d) Receiver even switch S_4 diode voltages.

Figure 4.37: In symmetric CMCD WPT hardware, zero voltage switching can be maintained at 100 MHz over a *wide input voltage range*. The transmitter drain and receiver diode voltages show ZVS from $V_{\text{in}} = 9\,\text{V}$ to 18 V, with minimal reverse conduction. Output load is constant $R_{\text{Load}} = 50\,\Omega$.

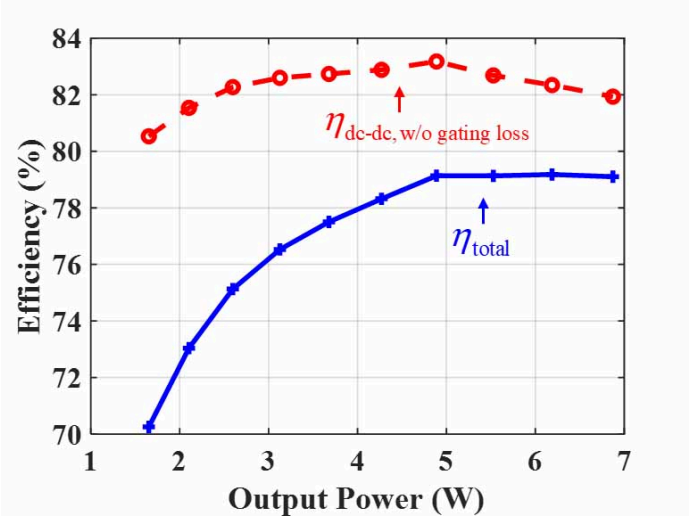

Figure 4.38: Power and efficiency of the symmetric CMCD WPT system with a passive rectifier. Gating loss dominates the efficiency loss at low power, which can be significantly improved with a custom integrated gate drive. The peak output power is 6.9 W with a total efficiency of 79.1 % when $R_{\text{Load}} = 50\,\Omega$.

CHAPTER 5

Segmented CMCD Power Converter

As discussed in Section 1.4, two challenges for HF-VHF WPT systems are the limited power and transfer distance. It is also hard to maintain efficiency while increasing power and transfer distance. A segmented CMCD power converter breaks the trade-off, which can increase the power level and extend the transfer distance while maintaining efficiency. The circuit is shown in Fig. 5.1.

The segmented CMCD power converter consists of n CMCD converters, where $n = 4$ in Fig. 5.1. Each CMCD converter is a primitive and all the primitives operate identically and synchronously. The currents flow through each segment. which is consist of series capacitance and inductance, are in phase. Equivalently, the flux is enlarged because of $n\,L_{\mathrm{r}}$. Flux is aggregated from each inductor segment that is part of a primitive converter. The segment inductances combine and form a large transmitter coil with a larger dimension, extending the transfer distance as suggested in Fig. 1.6. A higher power-frequency product and a lower device current rating are achieved in comparison to conventional segmentation [44], which uses the segmented coil with capacitance but drives at one spot.

5.1 Introduction

The performance of magnetically-coupled wireless power transfer (WPT) systems can be quantified by $Q \cdot k$, the product of the quality factor Q of the coils and the coupling coefficient k, as the figure of merit. This figure of merit determines the maximum system efficiency [100–102] with k determining the power transferred [3, 77]. However, for power transfer at long distances with small receivers, which is prevalent in many applications, $Q \cdot k$ is dramatically decreased because of small k.

The quality factor Q of the coils can be drastically increased by operating at HF-VHF; an air-core inductor has a quality factor that monotonically increases with frequency [5]. Despite the challenges in VHF power conversion [5, 10, 12, 13, 33], which include a power-frequency tradeoff that is endemic in devices shown in Fig. 1.4 and manifested in applications shown in Fig. 1.5 [38],

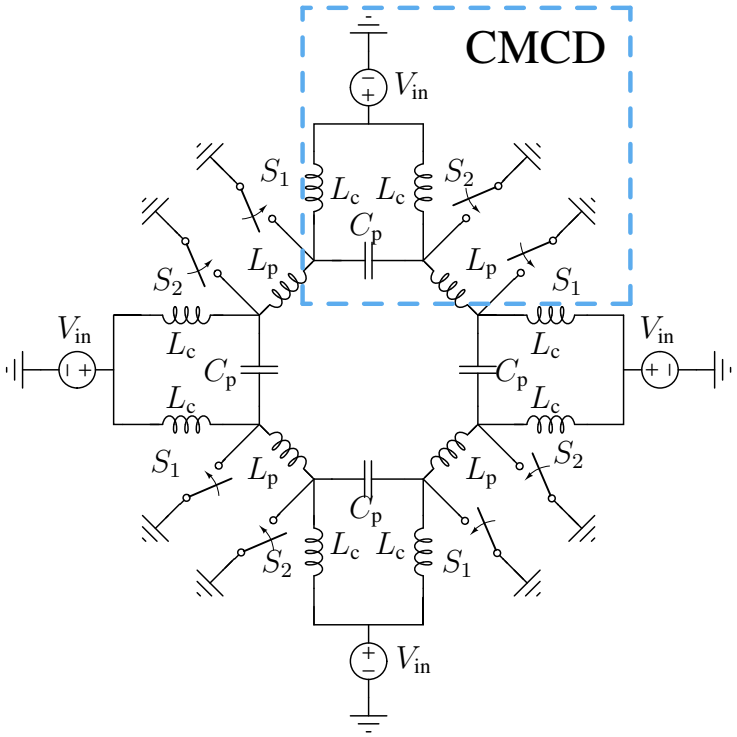

Figure 5.1: Segmented CMCD power converter. The switches S_1 and S_2 can be all active or passive.

an effort persists in wireless power transfer—a capacitive wireless power transfer system operating at 100 MHz was shown to be possible at 2.5 W with nearly 90 % efficiency using a single converter at 0.1 mm transfer distance with two 1.5 mm $\times$ 1.5 mm PCB pads [33].

The coupling coefficient k, which decreases with distance, can be improved by a larger transmitter coil. Small receivers with large transmitter coils as a use case are prevalent in implantable medical devices, RFID, infrastructure sensors, IoT, and consumer devices.

GaN HEMTs lead among choices for VHF power conversion because for a particular device, power capability is higher for a given C_{oss}. For a given inductor, the maximum operating frequency is limited by C_{oss}, the lower bound of the resonant capacitance. As shown in Fig. 1.4, the relationship between the maximum current rating I_{max}, which is an indicator of power capability, and the reciprocal of parasitic drain-to-source capacitance C_{oss} is nearly inversely proportional for devices with identical characteristics, but are scaled differently. This suggests that a single GaN device operating at VHF will be profoundly power-limited.

With VHF operation and GaN HEMTs, we can improve the $Q \cdot k$ product by improving Q, but face limitations in power. This is further exacerbated by the small k from long transfer distances and small receivers. Increasing voltage will increase power, but will incur higher C_{oss} loss [40] and difficulties with safety. Higher voltage devices with small C_{oss} will have higher channel resistance

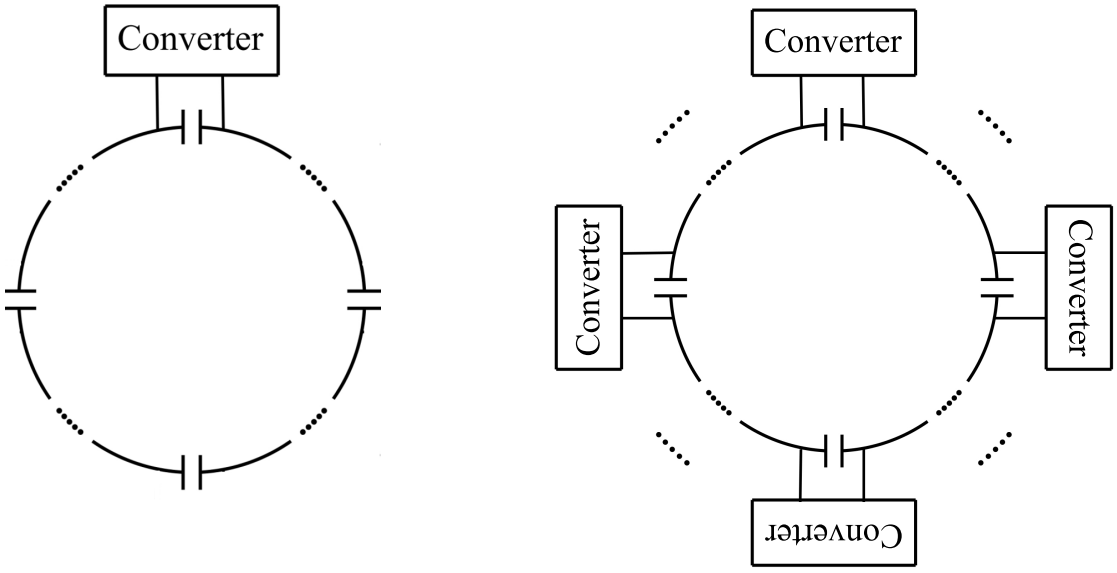

(a) Conventional Segmentation. (b) Novel Segmentation.

Figure 5.2: Segmentation architectures.

and hence lower I_{max} [38]; at higher power, the current rating may be exceeded. Parallel devices may be used to increase the current handling [103], but the higher C_{oss} will decrease the maximum operating frequency.

Combining the output power from smaller but more optimally designed modules can circumvent the device limitations at VHF. Efforts toward this include using multi-stage resistance compression networks [104] for power combining, which in practice may incur additional losses with an increasing number of inductors as power partitioning is increased.

For WPT, segmenting the coils is a way to generate more flux in a physically larger transmitter coil (larger k and hence more power) without an increase in terminal voltage by distributing discrete capacitors [44], illustrated in Fig. 5.2(a). One shortcoming of this conventional segmentation is the potentially high switch current stress at high power. A way to circumvent the difficulties in driving this large transmitter coil is to also segment the power conversion.

In this chapter, we introduce VHF active segmentation, shown in Fig. 5.2(b), which helps with both Q and k in the $Q \cdot k$ product, improving both the power and efficiency of long distance wireless power transfer with small receivers. Compared with conventional segmentation, shown in 5.2(a), where the segmented coil is driven by a single converter or power amplifier, there are multiple converters driving the segmented coil, partitioning the current stress and hence power. The segmented coil and its driving converters can be regarded as an aggregate power converter, which we term *segmented power converter*.

We also demonstrate in hardware the VHF active segmented power converter using four

current-mode class D (CMCD) converters as the *primitive converters*, which is similar to that for cell phone power amplifiers [41]. Singular CMCD converters (*singletons*) have been shown to be good candidates for HF (high-frequency) and VHF (very-high-frequency) power conversion because of ground-referenced switches and straightforward design [52,57,77]. However, the concept of active segmentation is not necessarily limited to VHF power conversion and CMCD converters, but rather can be applied to a broad range of primitives operating at any frequency.

The operation of the active segmented CMCD power converter relies on the primitive converters operating identically and synchronously. Key advantages of this architecture include:

1. increasing the $Q \cdot k$ product through both Q and k by VHF operation and segmentation;
2. increasing the transfer distance with higher power and efficiency through VHF operation and segmentation;
3. increasing the power without increasing the voltage level, which benefits device selection and safety;
4. sharing the power and current stress among primitive converters without increasing device parasitics in contrast to solely parallel switches, resulting in a higher power-frequency product;
5. allowing a design with identical primitive converters, which scales in power and preserves each primitive's efficiency.

In the following sections, the details of the circuit operation are explained, the advantages of active segmentation are compared to other techniques. Finally, a hardware demonstration through a 100 MHz prototype of an inductive wireless power transfer system using a commercial power device EPC 2038 with an approximate efficiency of 74 % and 12 W ac load power including the gating loss.

Ultimately, the best performance for WPT at long distances with small receivers can be attained by combining coil segmentation with primitive converters operating at VHF with parallel switches to increase power and efficiency.

5.2 VHF Active Segmentation

VHF active segmentation increases the $Q \cdot k$ product by increasing both Q and k through VHF operation and enlarging the physical size of the transmitter coil. Flux is aggregated from each inductor segment that is part of a primitive converter, together combining to form a large transmitter

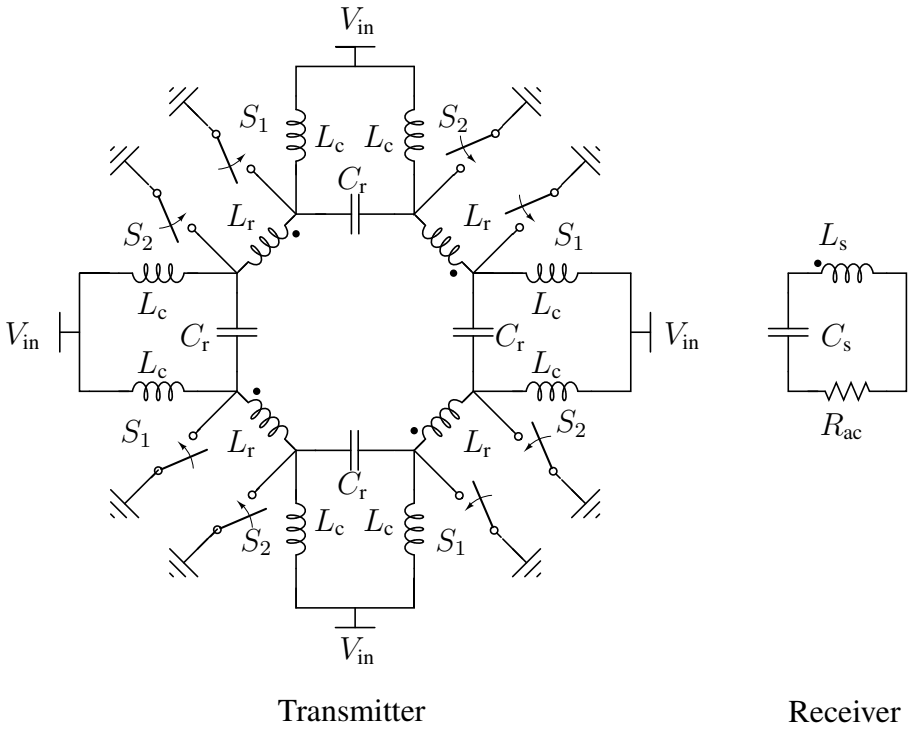

Figure 5.3: Active segmented CMCD WPT system.

coil. Higher power-frequency product and lower device current rating is achieved in comparison to conventional segmentation.

The VHF active segmented wireless power transfer system is shown in Fig. 5.3; the transmitter is an active segmented wireless power transfer coil, which is actively driven by four *primitive* CMCD converters. In this paper, the receiver is simply a series resonant network with the receiver coil coupling uniformly to the transmitter coil.

5.2.1 Primitive Converter

The primitive converter is the basic module of the active segmented power converter. In this proposal, the primitive is a single open-load current-mode class D converter, shown in Fig. 5.4. The primitive is identical to a singleton CMCD transmitter, shown in Fig. 4.3, whose design and operation are delineated in Section 4.2.1. With complementary switching sequences between S_1 and S_2 and dc current enforced by choke L_c, the LCR parallel resonant tank filters out the high-order harmonics of the square-wave current flowing into the resonant tank and keeps the fundamental-frequency current I_L flowing through R_{eq}, which equivalently represents the WPT receiver. The switching strategy and current distribution, which are identical for both the singleton and primitives, are shown in Fig. 4.3. The current flows through the resonant inductor and capacitor

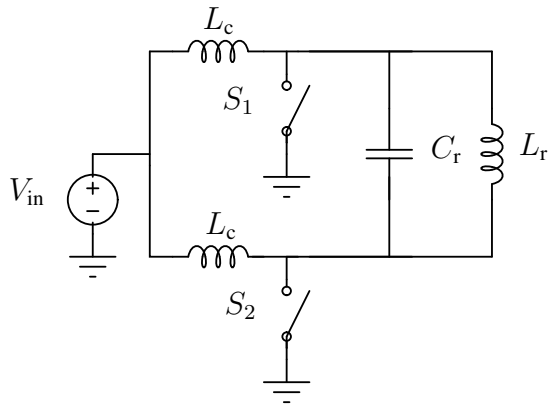

Figure 5.4: The primitive part of the active segmented CMCD transmitter.

is

$$I_{ac} = Q_L I_L = \frac{V_p}{\omega L_r}, \tag{5.1}$$

where Q_L is the quality factor of the tank (L_r, C_r, and R_{eq}) and V_p is the peak value of the switch drain voltages v_{s1} and v_{s2}. The differential voltage across R_{eq} is a sine wave, which is the difference between v_{s1} and v_{s2}. The operating frequency is approximately

$$\omega = \frac{1}{\sqrt{L_r\,(C_{sw} + C_r)}} \tag{5.2}$$

with $L_c \gg L_r$ and high Q_L. C_{sw} is the parallel switch capacitance, explained in [52].

For each primitive converter in Fig. 5.4, the effective switch capacitance C_{sw}, which includes C_{oss}, has been absorbed into the local resonant capacitance C_r. The series and parallel combination of the loop is similar to the segmented coil in [44], but with primitive converters actively driving the resonant components.

5.2.2 Operation Principles

Active segmented power converters rely on primitive converters operating identically and synchronously. There are eight switches in an active segmented CMCD power converter for four *primitive* CMCD converters, shown in Fig. 5.5. The four odd (S_1) and four even (S_2) switches are driven separately by two out-of-phase square waves, which is analogous to S_1 and S_2 in the singleton CMCD converter shown in Fig. 4.3. Thus, similar to Fig. 4.3, the switching strategy and loop current distribution I_{ac} can be regarded as a combination from four primitive converters, shown in Figs. 5.5(a) and 5.5(b) when the four even switches S_2 are ON and alternately in Fig. 5.5(c) and 5.5(d) when the four odd switches S_1 are ON.

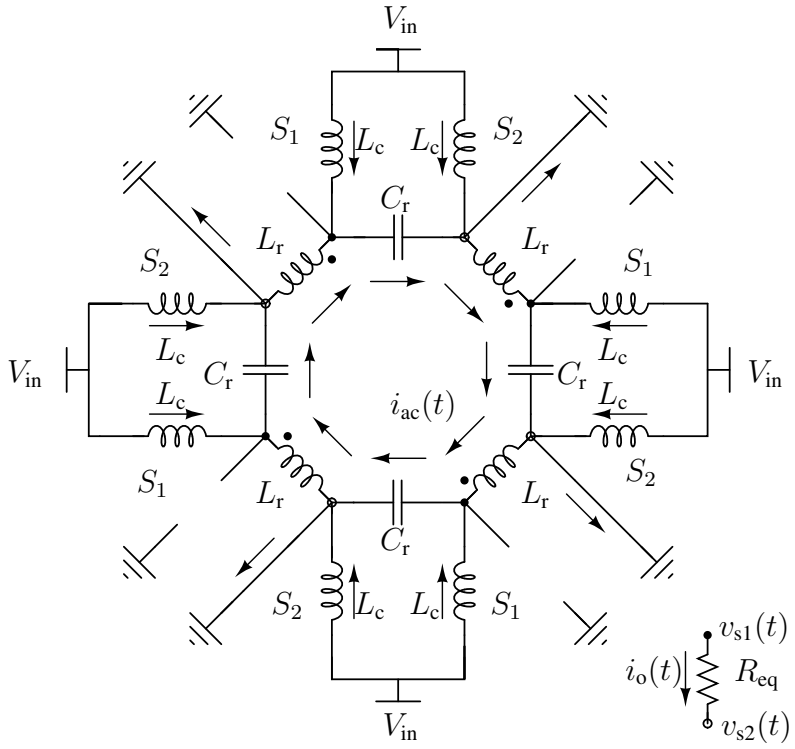

(a) Segmented CMCD converter when S_1 OFF And S_2 ON: $t_0 \sim t_1$.

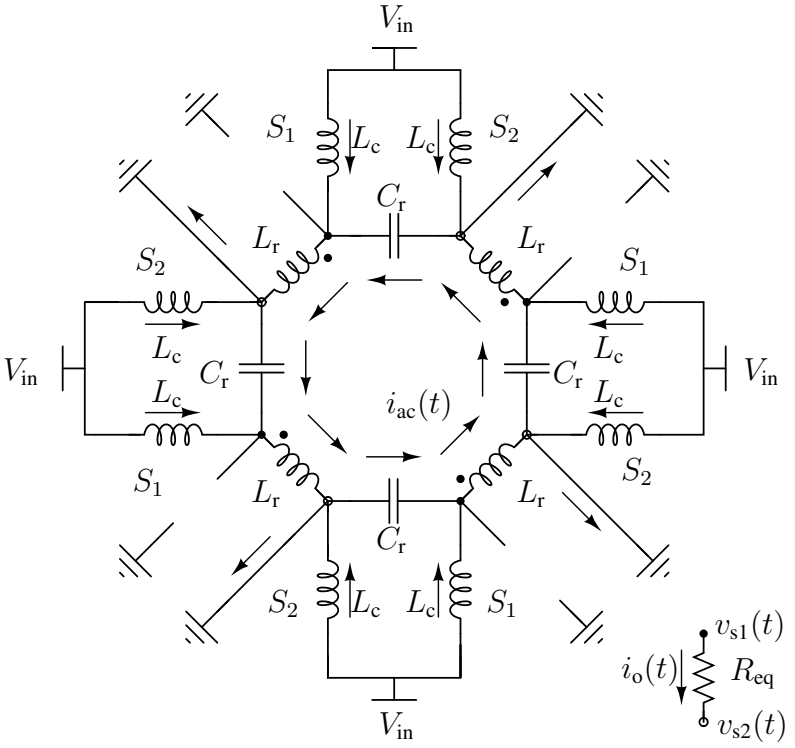

(b) Segmented CMCD converter when S_1 OFF and S_2 ON: $t_1 \sim t_2$.

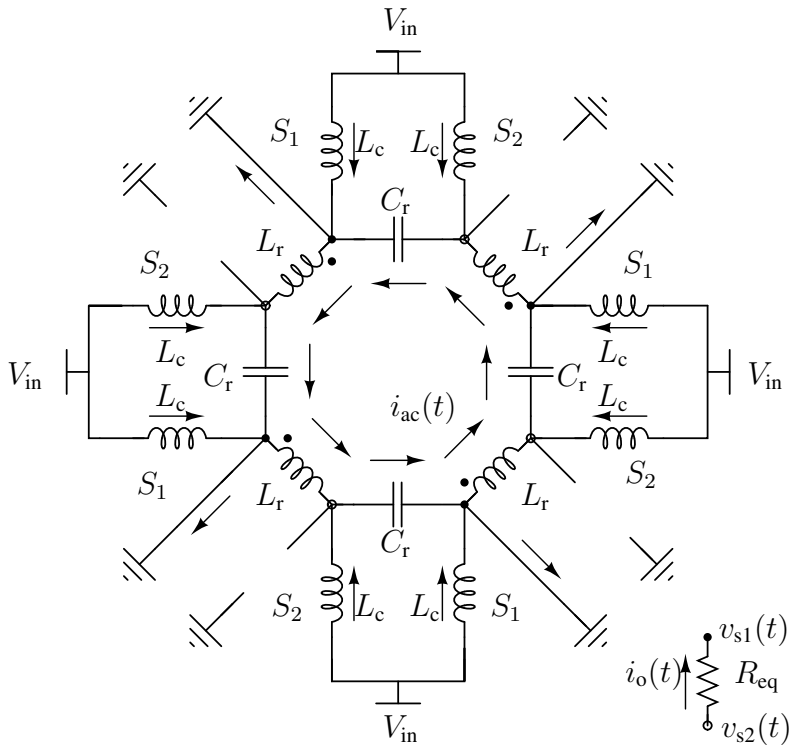

(c) Segmented CMCD converter when S_1 ON And S_2 OFF: $t_2 \sim t_3$.

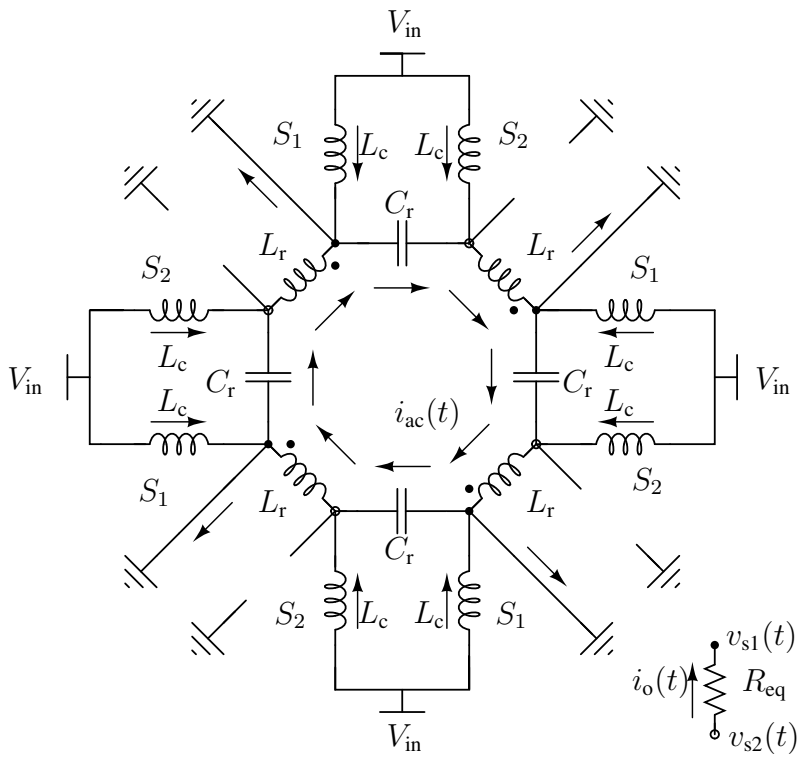

(d) Segmented CMCD converter when S_1 ON and S_2 OFF: $t_3 \sim t_4$.

Figure 5.5: Operation of active segmented CMCD power converter.

Identical in operation to a singleton CMCD converter [52], the switch voltage will be a half sine wave when the switch is OFF; the switch carries all the dc current for its primitive module when it is ON. Thus, the voltages are congruent in magnitude and phase among odd nodes (v_{s1}) and congruent among even nodes (v_{s2}). The loop current I_{ac} is at the operating frequency; in other words, the switching frequency of S_1 and S_2 is the resonant frequency of L_r and C_r

$$\omega = \frac{1}{\sqrt{L_r C_r}}, \tag{5.3}$$

where L_r and C_r have taken the coupling coefficient and switch capacitance into account. The loop current

$$I_{ac} = \frac{V_p}{\omega L_r} = \omega C_r V_p, \tag{5.4}$$

which has the same value as (5.1), generates a magnetic field, where V_p is the peak drain voltage of S_1 and S_2. The flux linkage equals the magnetic flux generated by the loop current

$$\lambda = 1 \cdot \Phi = 4 \times L_r I_{ac} = \frac{4 \times V_p}{\omega}, \tag{5.5}$$

which is a factor of 4 compared with a singleton system' s, where

$$\lambda = 1 \cdot \Phi = L_r I_{ac} = \frac{V_p}{\omega}. \tag{5.6}$$

It is equivalent to having a singleton CMCD WPT system with four times the voltage stress in (5.6) for the same transmitter flux in (5.5).

5.3 Comparison and Benefits

Active segmentation combines features from other methods including a singleton CMCD transmitter, shown in Fig. 4.3, a conventional segmented coil transmitter, shown in Fig. 5.6, and potentially parallel switches. It is worthwhile to examine how these other methods contribute to improving the $Q \cdot k$ figure of merit in wireless power transfer. These comparisons are conducted holding the power and efficiency of the receiver constant. The receiver is a series resonant network L_s, C_s, and R_{ac} with equivalent coupling coefficients to the transmitter coil.

As mentioned before, the switch capacitance C_{sw} explained in [52], can be absorbed into C_r in the singleton CMCD transmitter. Similarly, C_{sw} can be absorbed into the primitive C_r in active segmented transmitter. For the conventional segmented coil converter, the explicit C_r in the driven side should be less than the explicit C_r in other segments because of the additional C_{sw} from the switches in the power converter. Zero voltage switching is guaranteed when the resonant

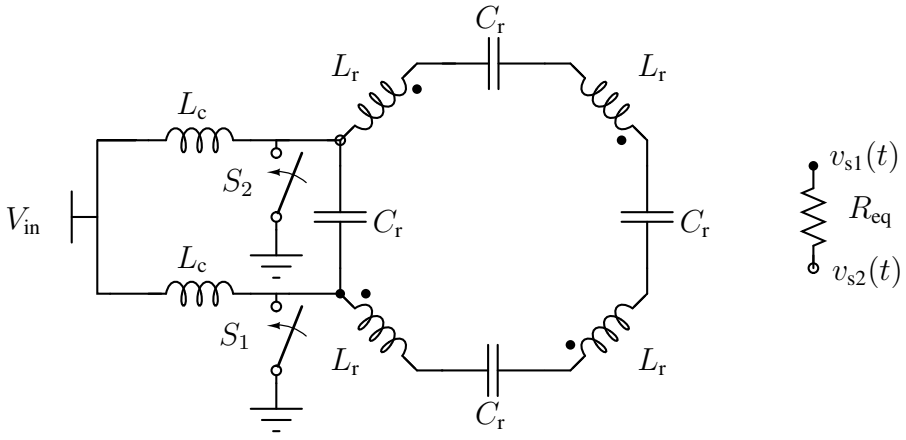

Figure 5.6: Conventional segmented coil converter.

components are chosen according to (5.3).

5.3.1 Comparing Active Segmentation with Singleton and Conventional Segmented Coil Transmitters

For identical receivers, the key is to compare the performance using different transmitters. Transmitter and WPT coils can be represented by a reflected voltage V_{p}' and effective inductance L_{eff} from the perspective of the receiver [52, 77], shown in Fig. 4.5. Here, for the convenience of analysis with uniformly coupled coils, we decompose the receiver inductance L_{s} into four equal parts each with $\frac{1}{4}L_{\text{s}}$; we decompose the singleton transmitter inductance similarly; these are illustrated in Fig. 5.7. Using the equivalent model shown in Fig. 5.8, both the conventional and active segmented coil transmitters have

$$V_{\text{p}}' = 4 \times k\sqrt{\frac{\frac{1}{4}L_{\text{s}}}{L_{\text{r}}}}V_{\text{p}} = 2k\sqrt{\frac{L_{\text{s}}}{L_{\text{r}}}}V_{\text{p}}, \tag{5.7}$$

while for singleton CMCD transmitter

$$V_{\text{p}}' = 4 \times k\sqrt{\frac{\frac{1}{4}L_{\text{s}}}{\frac{1}{4}L_{\text{r}}}}\left(\frac{1}{4}V_{\text{p}}\right) = k\sqrt{\frac{L_{\text{s}}}{L_{\text{r}}}}V_{\text{p}}. \tag{5.8}$$

The effective inductance

$$L_{\text{eff}} = 4 \times \left(1-k^2\right)\frac{1}{4}L_{\text{s}} = \left(1-k^2\right)L_{\text{s}} \tag{5.9}$$

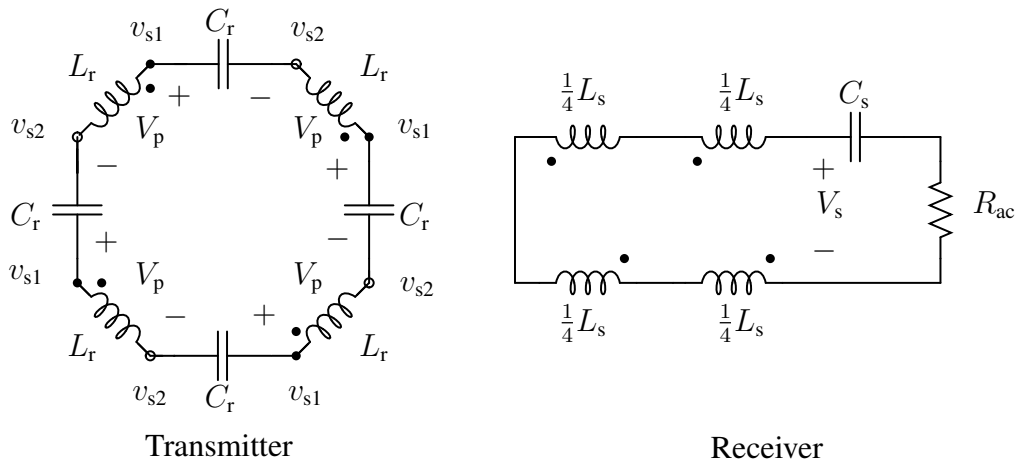

(a) Active segmentation and conventional segmented coil wireless power transfer.

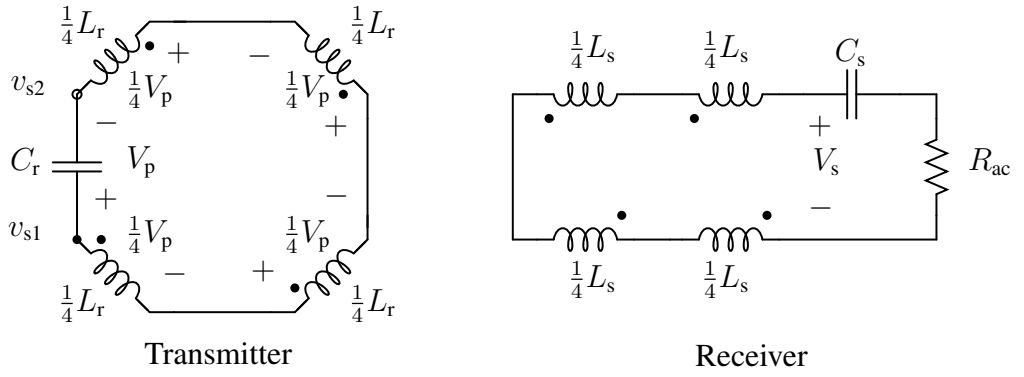

(b) Singleton wireless power transfer.

Figure 5.7: Resonant networks for segmentation and singleton wireless power transfer.

is the same for both segmentation and singleton; L_{eff} resonates with C_s. The output power is

$$P = \frac{{V_p'}^2}{2R_{ac}}. \tag{5.10}$$

Because both conventional and active segmentation have twice the V_p', the receiver will have four times the power in comparison to the singleton for the same switch voltage stress V_p.

For the current stress of the switches, which is represented by $I_{\text{sw, rms}}$, the conventional segmented coil transmitter has four times the stress compared with the switches in the active segmented CMCD transmitter because the same total power is extracted from only two switches instead of four sets of two switches. The device utilization of the active segmented CMCD transmitter is identical to that of the singleton CMCD transmitter. The performance is summarized in Table 5.1.

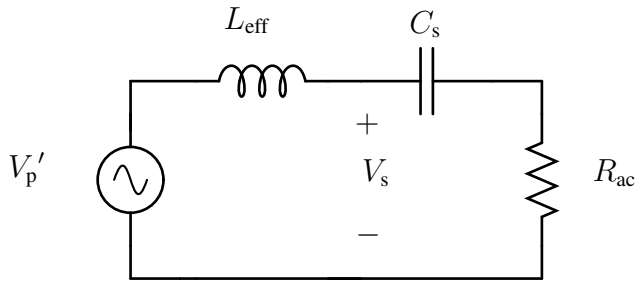

Figure 5.8: Receiver model for WPT systems.

5.3.1.1 Comparing Active Segmentation with Singleton and Conventional Segmented Coil Transmitters with Parallel Switches

Compared to the active segmented CMCD transmitter with power P and switch current stress $I_{\text{sw, rms}}$, the singleton CMCD transmitter, shown in Fig. 4.3, has lower power ($0.25\,P$) for the same device stress V_{p} and $I_{\text{sw, rms}}$ whereas the conventional segmented coil transmitter, shown in Fig. 5.6, has four times the current stress ($4\,I_{\text{sw, rms}}$) in the switches for the same voltage stress V_{p} and power P. Parallel switches can increase the power of a singleton CMCD WPT while maintaining switch current stress and decreasing switch current stress in a conventional segmented coil WPT system while maintaining the power.

For a conventional segmented coil transmitter, we parallel four switches in each of the odd and even sides to share the current; thus, the switch utilization and the power can remain the same compared with the active segmented CMCD transmitter. However, when considering non-ideal switches with switch capacitance C_{sw}, the conventional segmented coil transmitter with parallel switches will have a lower maximum frequency compared to active segmentation. For the active segmented CMCD transmitter, the equivalent resonant capacitance is

$$C_{\text{eq}} = C_{r,\,\text{active segmentation}} + C_{\text{sw}}, \tag{5.11}$$

while for the conventional segmented coil transmitter

$$C_{\text{eq}} = C_{r,\,\text{conventional segmentation parallel}} + 4\,C_{\text{sw}}. \tag{5.12}$$

For the limiting case, where $C_{\text{r}} = 0$, the maximum frequency for active segmentation is

$$\omega_{\text{max, active segmentation}} = \frac{1}{\sqrt{C_{\text{sw}} L_{\text{r}}}}; \tag{5.13}$$

the maximum frequency in a conventional segmented coil transmitter with four parallel switches

is

$$\omega_{\text{max, conventional segmentation parallel}} = \frac{1}{\sqrt{4\,C_{\text{sw}} L_{\text{r}}}}. \tag{5.14}$$

For VHF power conversion, active segmentation is better for the power-frequency product compared to the conventional segmented coil with parallel switches.

For a singleton CMCD transmitter, the drain voltage is doubled for the same power P. The corresponding increased current requires an extra switch to maintain the current stress $I_{\text{sw, rms}}$. In this case, the maximum frequency is

$$\omega_{\text{max, singleton parallel}} = \frac{1}{\sqrt{2\,C_{\text{sw}} L_{\text{r}}}}. \tag{5.15}$$

The maximum frequency for the singleton CMCD transmitter with parallel switches is lower than active segmentation but higher than the conventional segmented coil transmitter with four parallel switches.

One important shortcoming of a singleton CMCD transmitter with parallel switches is that it will drive a smaller transmitter coil than both active and conventional segmentation for the same power. A smaller transmitter coil means a shorter transfer distance for the same k. The performance is summarized in Table 5.1.

5.3.1.2 Loss Comparisons

The active segmented transmitter has numerous advantages but requires more components and control signals, likely increasing the cost and power loss. Among the four methods with identical power and identical receivers, losses from the choke L_{c}, the transmitter coil, switch conduction, and switch C_{oss} are taken into account. The singleton transmitter without parallel switches is also included for comparison. The results are summarized in Table 5.2. Here, for simplicity, we ignore the effect of switch capacitances C_{sw} on $I_{\text{sw, rms}}$ and hence switch conduction loss.

According to the operating principles described above, the chokes share the dc current I_{dc} with power loss

$$P_{\text{choke}} = n_{\text{c}} \times (\frac{1}{n_{\text{c}}} I_{\text{dc}})^2 R_{\text{choke}}, \tag{5.16}$$

where n_{c} is the number of the chokes used in each transmitter. I_{dc} is identical for the active and conventional segmented coil transmitters and independent of parallel switching in segmentation, however halved for the singleton transmitter because the dc voltage is double for the same power.

For the transmitter coil loss, we assume inductance has quality factor of Q making the ESR of

Table 5.1: Active Segmented Transmitter Performance Compared With Conventional Segmented Coil Transmitter, Singleton Transmitter and Their Variations with Paralleling Switches

Methods	Power	Switch Voltage Stress	Switch Current Stress	Maximum Frequency	Transfer Distance
Active Segmented Transmitter	P	V_{p}	$I_{\text{sw, rms}}$	ω_{max}	d
Singleton Transmitter	$0.25\,P$	V_{p}	$I_{\text{sw, rms}}$	ω_{max}	$< d$
Conventional Segmented Coil Transmitter	P	V_{p}	$4I_{\text{sw, rms}}$	ω_{max}	d
Singleton Transmitter with the 2 Parallel Switches	P	$2\,V_{\text{p}}$	$I_{\text{sw, rms}}$	$0.707\,\omega_{\text{max}}$	$< d$
Conventional Segmented Coil Transmitter with the 4 Parallel Switches	P	V_{p}	$I_{\text{sw, rms}}$	$0.5\,\omega_{\text{max}}$	d

Table 5.2: Active Segmented Transmitter Component Loss Compared With Conventional Segmented Coil Transmitter, Singleton Transmitter and Their Variations with Parallel Switches

Methods	Power	Choke Loss	Primary Coil Loss	Switch Conduction Loss	Switch Coss Loss
Active Segmented Transmitter	P	$8 \times \left(\frac{1}{8} I_{\text{dc}}\right)^2 R_{\text{choke}}$	$4 \times \frac{{I_{\text{ac}}}^2}{2} R_{L_{\text{r}}}$	$8 \times {I_{\text{sw, rms}}}^2 R_{\text{ds, on}}$	$8 \times \frac{1}{2} C_{\text{oss}} V_{\text{p}}^2$
Singleton Transmitter	$0.25 \times P$	$2 \times \left(\frac{1}{2} 0.25 I_{\text{dc}}\right)^2 R_{\text{choke}}$	$1 \times \frac{{I_{\text{ac}}}^2}{2} R_{L_{\text{r}}}$	$2 \times {I_{\text{sw, rms}}}^2 R_{\text{ds, on}}$	$2 \times \frac{1}{2} C_{\text{oss}} V_{\text{p}}^2$
Conventional Segmented Coil Transmitter	P	$2 \times \left(\frac{1}{2} I_{\text{dc}}\right)^2 R_{\text{choke}}$	$4 \times \frac{{I_{\text{ac}}}^2}{2} R_{L_{\text{r}}}$	$2 \times (4 I_{\text{sw, rms}})^2 R_{\text{ds, on}}$	$2 \times \frac{1}{2} C_{\text{oss}} V_{\text{p}}^2$
Singleton Transmitter with the 2 Paralleled Switches	P	$2 \times \left(\frac{1}{2} \frac{1}{2} I_{\text{dc}}\right)^2 R_{\text{choke}}$	$1 \times \frac{(2 I_{\text{ac}})^2}{2} R_{L_{\text{r}}}$	$4 \times {I_{\text{sw, rms}}}^2 R_{\text{ds, on}}$	$4 \times \frac{1}{2} C_{\text{oss}} \left(2 V_{\text{p}}\right)^2$
Conventional Segmented Coil Transmitter with the 4 Paralleled Switches	P	$2 \times \left(\frac{1}{2} I_{\text{dc}}\right)^2 R_{\text{choke}}$	$4 \times \frac{{I_{\text{ac}}}^2}{2} R_{L_{\text{r}}}$	$8 \times {I_{\text{sw, rms}}}^2 R_{\text{ds, on}}$	$8 \times \frac{1}{2} C_{\text{oss}} V_{\text{p}}^2$

L_{r} as $R_{L_{\mathrm{r}}} = \omega L_{\mathrm{r}}/Q$. The transmitter coil loss is

$$P_{\mathrm{Tcoil}} = n_{L_{\mathrm{r}}} \times \frac{{I_{\mathrm{ac}}}^2}{2} R_{L_{\mathrm{r}}}, \tag{5.17}$$

where $n_{L_{\mathrm{r}}}$ is the number of segments. The transmitter coil current I_{ac} is calculated in (5.4), which doubles for the singleton transmitter with the same power.

The switch conduction loss is given by

$$P_{\mathrm{sw,\,cond}} = n_{\mathrm{sw}} \times {I_{\mathrm{sw,rms}}}^2 R_{ds,\mathrm{on}}. \tag{5.18}$$

We model the switch C_{oss} as a complete loss

$$P_{\mathrm{sw},\,C_{\mathrm{oss}}} = n_{\mathrm{sw}} \times \frac{1}{2} C_{\mathrm{oss}} {V_{\mathrm{p}}}^2, \tag{5.19}$$

where n_{sw} is the number of switches.

The receiver coil loss is

$$P_{\mathrm{Rcoil}} = \frac{1}{2} \left(\frac{V_{\mathrm{s}}}{\omega L_{\mathrm{s}}} \right)^2 R_{L_{\mathrm{s}}}, \tag{5.20}$$

where V_{s} is the receiver coil peak voltage and $R_{L_{\mathrm{s}}} = \omega L_{\mathrm{s}}/Q$ is identical for identical receiver coils. This loss is identical for the same power P among different transmitters.

The singleton receiver loss will be one fourth of (5.20) because the power is only one fourth at $0.25\,P$ with the same V_{p} at the transmitter. We can see that for the active segmented and singleton transmitters, illustrated in Table 5.2, the power and loss are scaled by a factor of four, which means in comparison with the singleton, active segmented WPT has four times the power for the same efficiency with the same V_{p}.

Among the transmitters that can achieve the same transfer distance, the active segmented and conventional segmented with 4 parallel switches have the same coil loss and switch loss, but the active segmented transmitter has lower choke loss. Neglecting choke loss, there is a trade-off between switch conduction loss and switch C_{oss} loss between an active segmented transmitter and a conventional segmented coil transmitter without parallel switches. Other comparisons can be posited from Table 5.2.

5.3.2 Advantages of VHF Active Segmented Transmitter

Compared to the singleton, the conventional segmented coil transmitters, and their variants with parallel switches, active segmentation is compelling for applications which require high power, high efficiency, and long transfer distance with small receivers. What can be conclude from Table

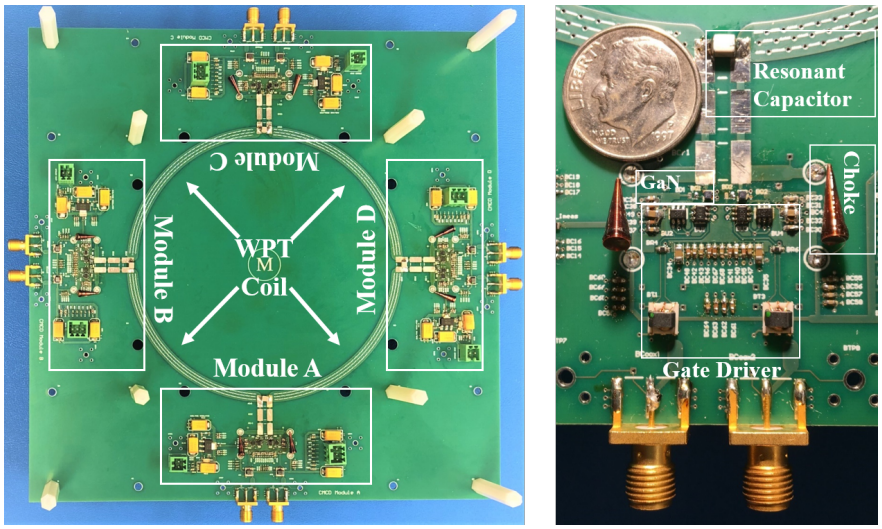

Figure 5.9: PCB layout of active segmented CMCD converter and its primitive module.

5.1 is that among the four methods with identical power, the active segmented transmitter has the least switch stress, maximum operating frequency, and the greatest transfer distance for the same coupling coefficient.

Additionally, compared to a singleton power converter, the loss and power are scalable in the active segmented power converter, which combines power from each primitive converter without changing the device stress; every primitive module shares the load power equally and preserves efficiency.

For implementation, active segmented transmitters can have a symmetric layout and an identical design for the power and control circuits, ensuring matched timing and parasitics. A larger number of components does not necessarily mean loss of efficiency, as observed in Table 5.2.

5.4 Hardware Implementation and Results of VHF Active Segmentation Method

5.4.1 Timing and Sequence of the Eight Switches

It is very difficult to obtain 100 MHz square waves with sharp rising and falling edges from most commercial function generators because of the required bandwidth, especially with enough channels for 8 synchronized control signals for the eight switches. FPGAs typically do not have enough frequency resolution [77]. Instead, we generated the control signal using simple identical circuits. The signal source was a two-channel waveform generator (Keysight 33622A) configured to gen-

Table 5.3: Implementation of Active Segmented CMCD Transmitter.

Items	Components & Parameters
Choke Inductor	BCL-652JL 6.5 μH
Transmitter Resonant Capacitance	QUAD HIFREQ Series 27.6 pF
Receiver Resonant Capacitance	QUAD HIFREQ Series 11 pF
Transmitter PCB Coil	297 nH ($R = 6.3$ cm)
Receiver PCB Coil	180 nH ($R = 3.8$ cm)
Transfer Distance	2.5 cm
DC Input Voltage	18 V

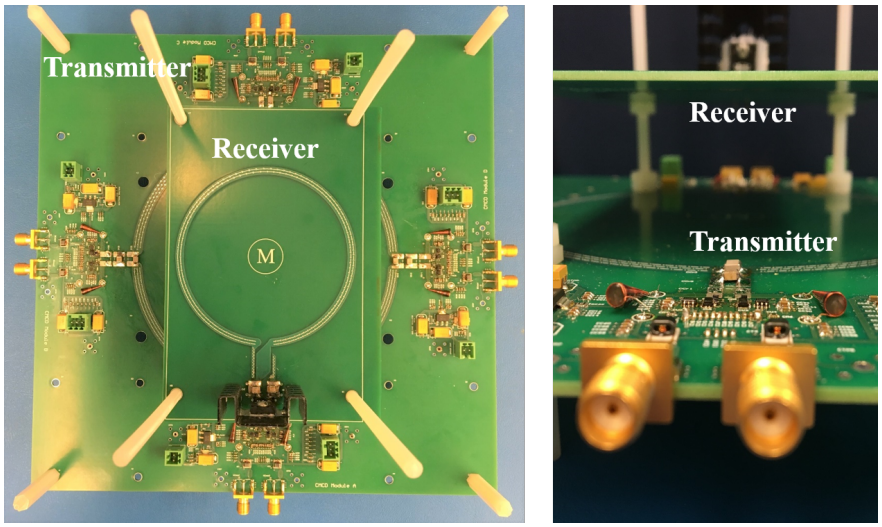

Figure 5.10: Hardware setup of active segmented wireless power transfer.

erate two out-of-phase sine waves. Two 1-to-4 power splitters expanded these channels to eight sinusoidal signals. Schmitt triggers were used to generate square waves with identical duty-ratios from biasing the multi-channel sinusoidal waves. These square waves were used as inputs to gate drives consisting of logic inverters SN74LVC2GU04.

5.4.2 VHF Active Segmentation WPT System Implementation and Results

As previously mentioned, one of the advantages of the VHF active segmented transmitter is the symmetric layout and identical design of the power and control circuits, ensuring matched timing and parasitics. The PCB layout of the active segmented CMCD transmitter and its CMCD primitive module is shown in Fig. 5.9. EPC 2038 was selected for the switches because of its small C_{oss}

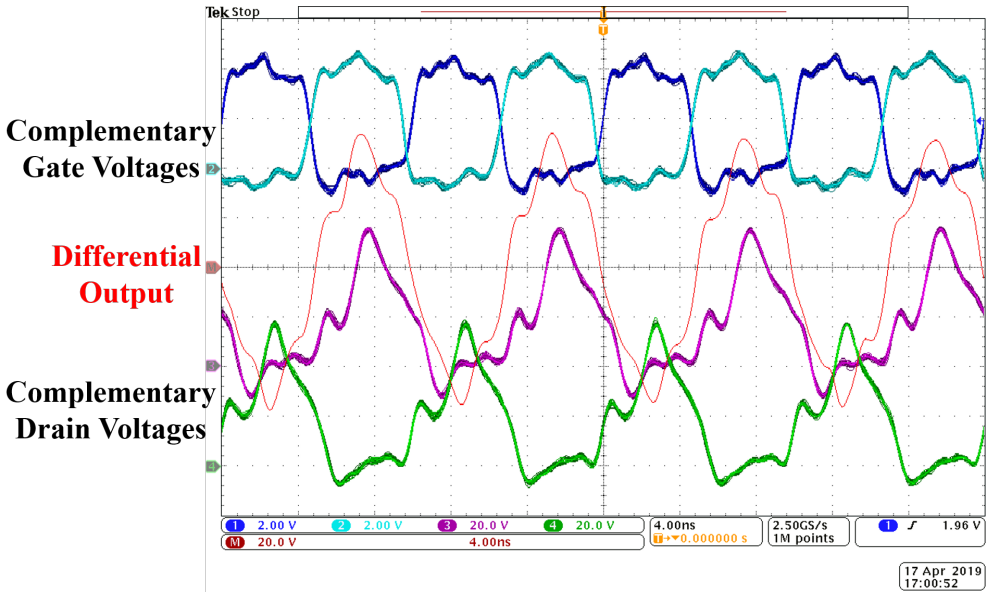

Figure 5.11: Typical waveforms of Module A CMCD primitive module under open-load condition.

(below 5 pF for all voltages) and small gate charge, which is needed for VHF operation. The WPT coils are two 4-layer FR4 PCB inductors. The load is a 20 Ω power resistor. Other components in this WPT implementation are shown in Table 5.3.

For an unloaded active segmented transmitter, the typical gate and drain voltage waveforms for CMCD primitive Module A are shown in Fig. 5.11, which is similar to a singleton CMCD converter [52, 57, 77] in operation. The other three primitives have the identical waveforms to Module A.

When loaded, the four drain voltages across the even switches and output load voltage are shown in Figs. 5.12 and 5.13, respectively. The drain voltages appear synchronized and similar with few variations. The output voltage is a sine wave, which is in phase with V_p for a tuned series resonant network. The output power is 12 W with 81 % efficiency. Considering the gating loss in the gate driver (1.3 W), the efficiency is approximately 74 %.

5.5 Summary

VHF active segmentation has been shown to be a compelling method to increase the transfer distance of a large transmitter with a smaller receiver while preserving power and efficiency. The active segmented power converter operates with identical and synchronized primitive converters. A transmitter prototype and a series resonant receiver demonstrated active segmentation in hardware for 100 MHz wireless power transfer at 12 W and 74 % efficiency.

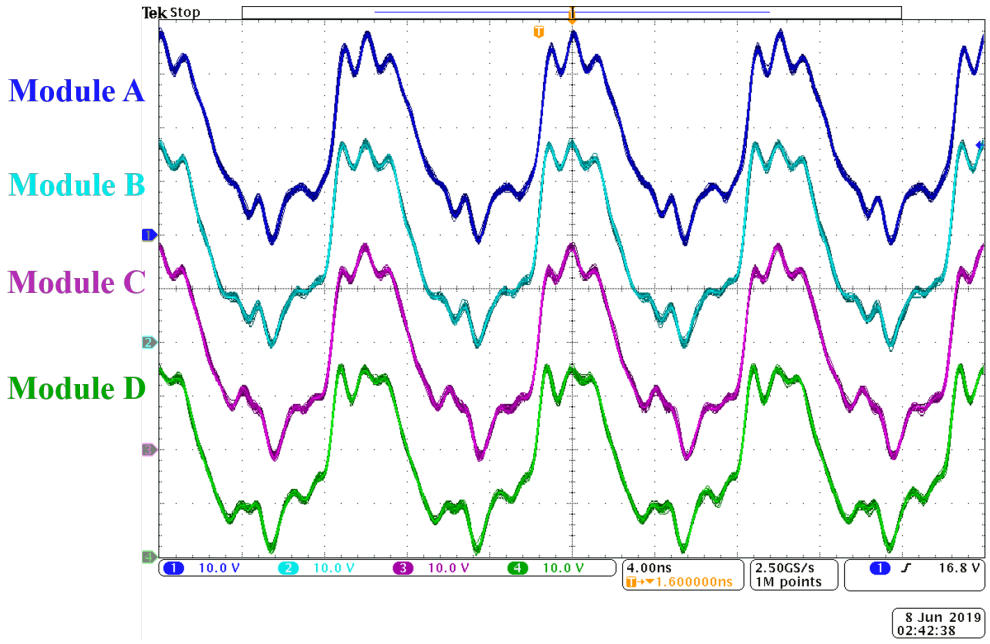

Figure 5.12: Drain voltages of even switches of the four active segmented CMCD primitive modules with a 20 Ω load.

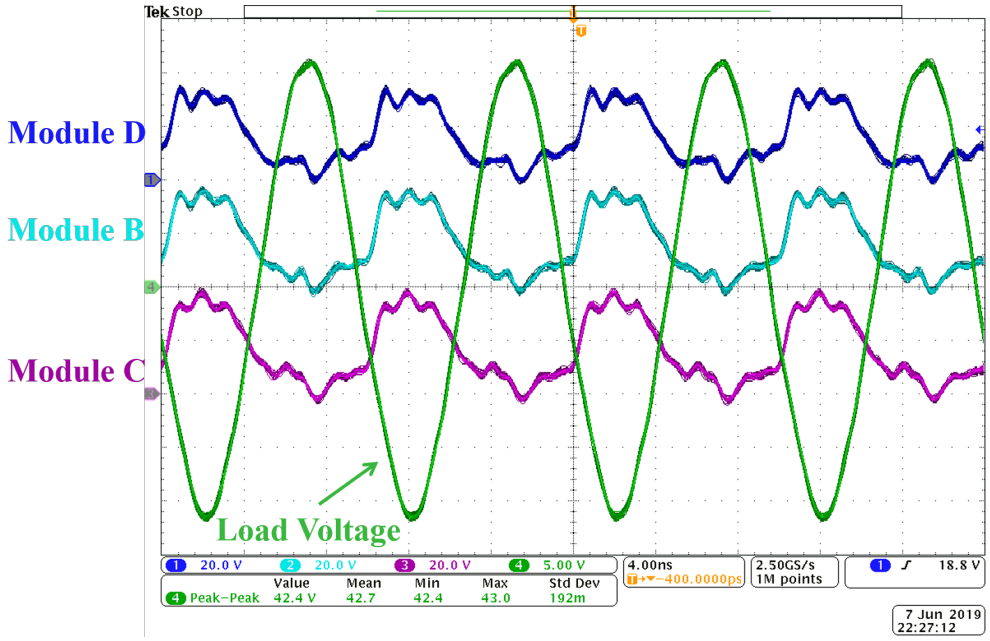

Figure 5.13: Output and drain voltages of even switches of the four active segmented CMCD primitive modules with a 20 Ω load.

CHAPTER 6

Segmentation CMCD WPT System

6.1 Introduction

Unmanned aerial vehicles (UAV) and agile robots are currently among the leading topics in research and innovation. Although control algorithms have been a vital focus, powering technology is emerging as critical to mission accomplishment. For UAVs and agile robots, which charge frequently and intensively, connector wear and unreliability is unacceptable; wireless power transfer (WPT) can eliminate cabling and power quickly, reliably, and resiliently. However, wireless power transfer is challenging for these applications. As illustrated in Fig. 6.1(a) and Fig. 6.1(b), the transfer distance between the WPTs coils can be relatively long and variable because of protrusions like skids, wheels, or propellers in UAVs and limbs on agile robots; good alignment cannot always be achieved between the transmitter coil and the receiver coil because of position and posture, resulting in poor coupling coefficient despite requiring power approaching tens to hundreds of watts. Moreover, the receiver coils need to be lightweight and placed near the fuselage or the trunk because of aerodynamics or clearance.

At higher frequencies, the power transfer through electromagnetic waves to smaller objects in-

(a) The UAV picture is from [105].

(b) The robot picture is from [106].

Figure 6.1: Wireless power transfer for UAVs and agile robots.

creases as the wavelength decreases. Increasing switching frequency also achieves lighter weight and smaller profile because passive components can be smaller at VHF [5]. Notably, bulky and fragile ferrite cores can be eliminated because air-core coils become volumetrically efficient as their quality factors increase with frequency [5], while also increasing the figure of merit of WPT systems [100, 101]. Large wireless power transfer coils increase coupling coefficient, extending transfer distance, and improving tolerance to misalignment. A significant challenge in taking advantage of high $Q \cdot k$ with large coils is that high terminal voltages are needed, often exceeding device capability or incurring unfavorable trade-offs in efficiency or power.

Conventional segmentation [44] is a method to reduce the terminal voltage in a large coil by using discrete resonant capacitors to partition the coil. This is equivalent to a series combination of primitive series resonant circuits (inductor and capacitor) so that the primitive resonance frequencies are identical to that of the aggregate resonance. However, conventional segmentation at VHF has limitations [75]. First, there is a power-frequency trade-off because of the semiconductor devices. VHF requires small parasitic capacitances from the devices which typically means correspondingly small current rating, hence severely limiting power at VHF. Second, conventional segmentation has relatively small power-frequency product because for a single switch, the power rating is limited by small current rating; for parallel switches, the operational frequency is limited by parallel combination of switch capacitances.

In this chapter, we investigate active-to-passive segmented wireless power transfer systems (APS-WPT). Compared with conventional segmentation [44], where the segmented coil is driven by only one power amplifier or power converter, active-to-passive segmented WPT additionally partitions the power conversion by driving each segment separately, while at the same time aggregating their magnetic flux. The primitive power converters in either active or passive segmentation operate simultaneously and synchronously. The primitive power converter, which is the basic module of both active and passive segmentation, can be a current-mode class D converter (CMCD), which has been demonstrated to be effective at HF-VHF [52, 57, 77], including 100 MHz [4, 75]. The investigated system employs an active segmented CMCD converter as the transmitter [4] and a passive segmented CMCD converter as the receiver. Both WPT coils are identical and segmented with discrete capacitors.

6.2 VHF Active-to-Passive Segmented WPT

VHF active-to-passive segmented wireless power transfer improves the $Q \cdot k$ product to obtain higher power, higher efficiency, better tolerance to parameter variation, and longer transfer distance. APS-WPT overcomes the challenges of high power-frequency product. Compared with singleton CMCD WPT systems at the same frequency [4], one of the biggest advantages of APS-WPT

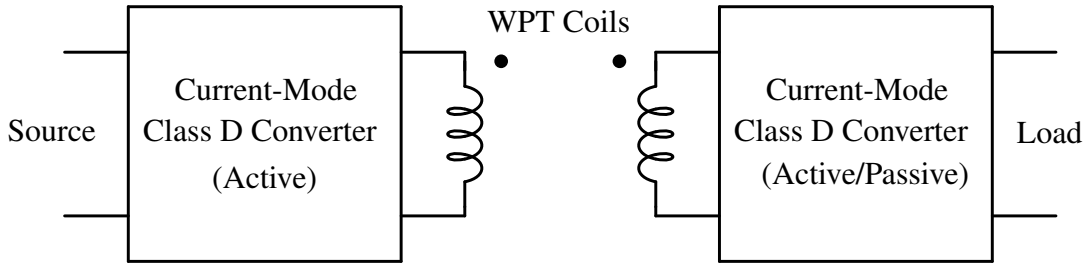

Figure 6.2: Singleton CMCD WPT systems.

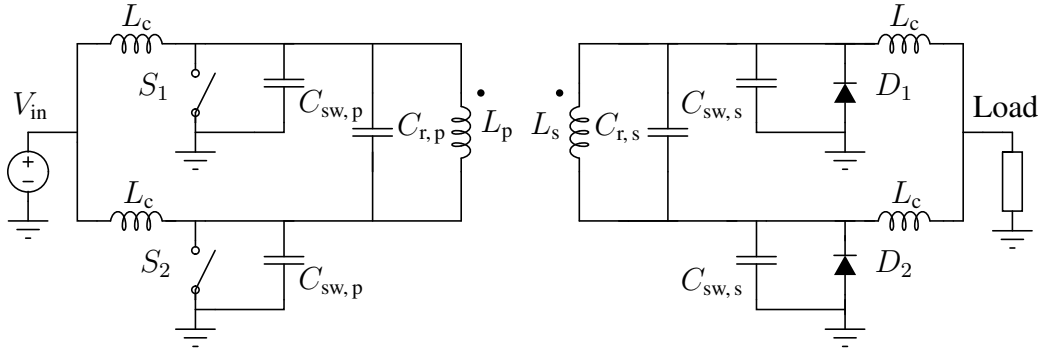

Figure 6.3: Circuits for Singleton CMCD WPT systems.

is that with N primitives one can increase the power level by a factor of $N/2$, while preserving the same efficiency as that of a singleton CMCD WPT system with the same device utilization, input voltage, resistive load, and coupling coefficient.

6.2.1 VHF Singleton CMCD WPT System

A VHF singleton CMCD WPT system, shown in Fig. 6.2, is the basic module of a VHF active-to-passive segmented WPT system. The VHF singleton CMCD WPT system employs current-mode class D (CMCD) converters for both transmitter and receiver, as shown in Fig. 6.3. Similar structure and operation of CMCD converters have been delineated in [4]. Because of 100 MHz and switch capacitances which are in parallel with the switches, the maximum WPT coil inductance is limited by

$$L_{\text{max}} = 1/\left[(1-k^2)\omega^2 C_{\text{sw}}\right], \tag{6.1}$$

which is limited by the switching frequency ω and the switch parasitic capacitance C_{sw}, where k is the coupling coefficient, indicating that limited transfer distance at a specific k or limited k at the

specific transfer distance d. The power transferred [4] in the WPT system is

$$P_{\mathrm{o}} = \frac{\pi^4 k^2 {V_{\mathrm{in}}}^2 R_{\mathrm{load}}}{4\left(1-k^2\right)} \sqrt{\frac{C_{\mathrm{p}}}{L_{\mathrm{p}}}} \sqrt{\frac{C_{\mathrm{s}}}{L_{\mathrm{s}}}}, \tag{6.2}$$

where L_{p} and L_{s} are the respective primary and secondary self-inductances, C_{p} and C_{s} are the corresponding primary and secondary capacitances where the switch capacitance have been absorbed, and V_{in} is the input voltage while R_{load} is the output resistive load. For a particular well-designed WPT system, the only way to increase the power is to increase the input voltage V_{in}, correspondingly increasing the switch voltage stress; however, the increased voltage may exceed the component voltage ratings and other safety limits. Above all, these show that VHF singleton CMCD WPT systems have limited power and transfer distance, which do not satisfy the requirement of high power and long transfer distance for lightweight UAVs and agile robots. Additionally, singleton systems can only drive smaller-sized coils, hence degrading misalignment tolerance.

6.2.2 VHF Segmentation CMCD WPT System

An idealized system that represents segmentation with eight primitive converters is shown in Fig. 6.4. The idealized transmitter uses four active CMCD converters while the CMCD converters in the idealized receiver can be either active or passive, depending on the choices of active switches or passive diodes. The idealized system can be regarded as a combination of four separate and distributed singleton CMCD WPT systems, yet gathering magnetic flux or power together through dedicated physical and electrical connections. Compared with a singleton CMCD WPT system, the power level and transfer distance can be increased. The idealized transmitter is an active segmented CMCD converter, which was first investigated in [75]. The receiver can be an active segmented CMCD converter or can be a passive segmented CMCD converter, which is investigated in this paper first time. In this paper, the segmented CMCD WPT system uses an active segmented CMCD converter as the transmitter and a passive segmented CMCD converter as the receiver for lightweight UAVs and agile robots. The implementable circuit with the delicated connections for active-to-passive segmented CMCD WPT systems is shown in Fig. 6.5.

By comparing Fig. 6.5 with Fig. 6.3, the relationship between a VHF segmented CMCD WPT system and a VHF singleton CMCD WPT system is salient. The components with the same symbol are exactly identical, including choke inductors L_{c}, resonant components L_{p}, L_{s}, C_{p}, C_{s}, switches S_1, S_2, D_1, and D_2, input V_{in}, output R_{load}, and same coupling coefficient k. Moreover, the active four primitive CMCD converters operate synchronously and simultaneously, with four identical pairs of complementary control signals. Thus, intuitively, the transfer power level is increased by a factor of 4 while the device utilization and efficiency is preserved. Transfer distance is increased

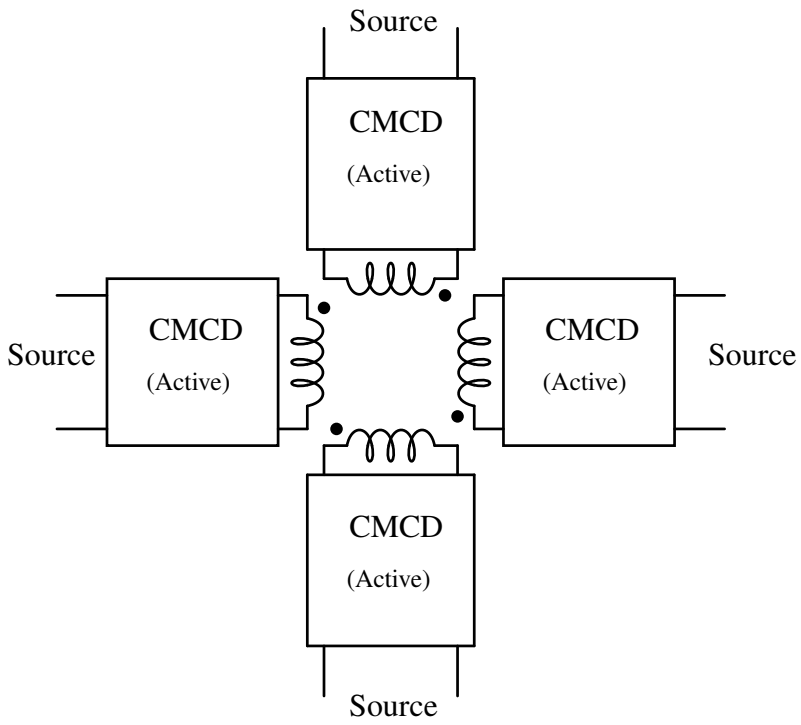

(a) Active segmented CMCD WPT transmitter.

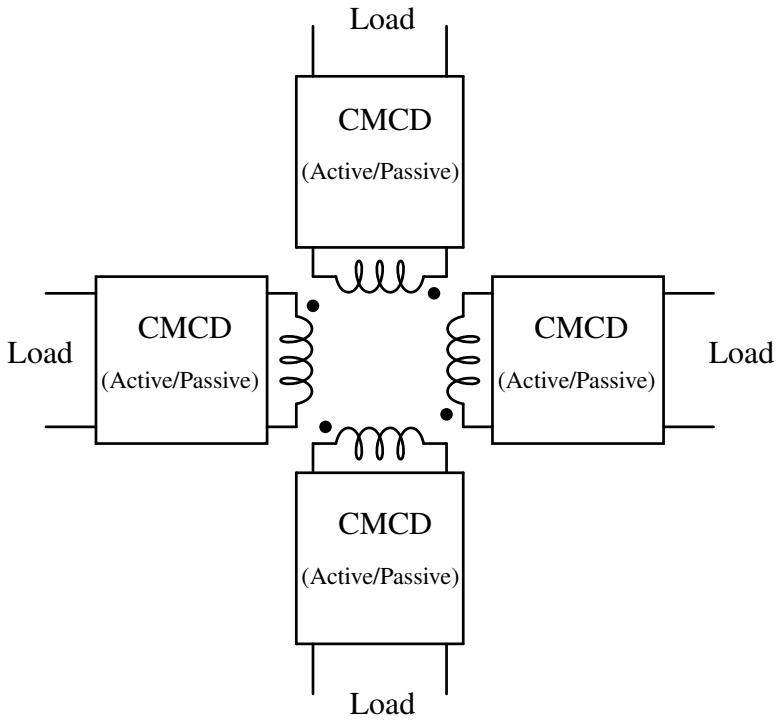

(b) Active/passive segmented CMCD WPT receiver.

Figure 6.4: An idealized representation of segmentation CMCD WPT systems.

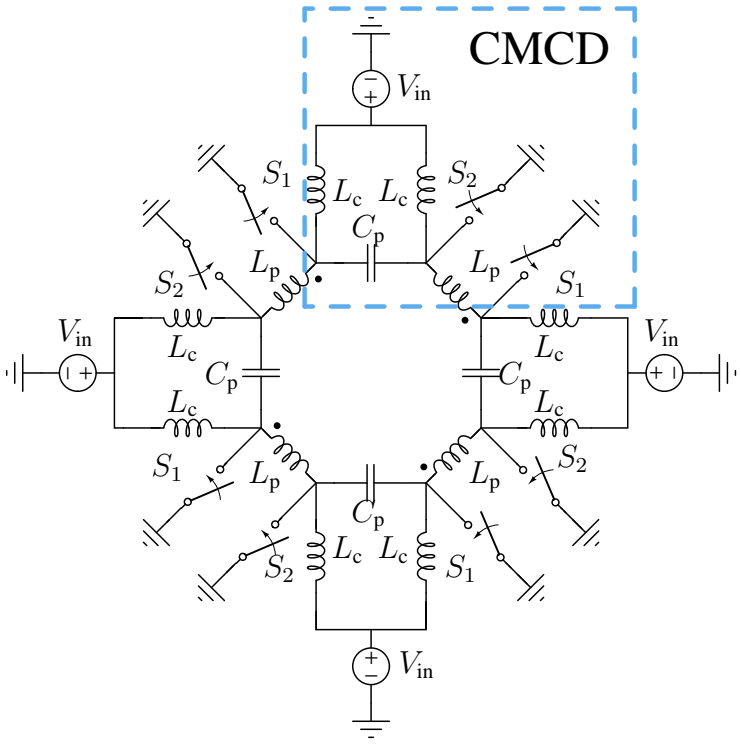

(a) Active segmented CMCD converter.

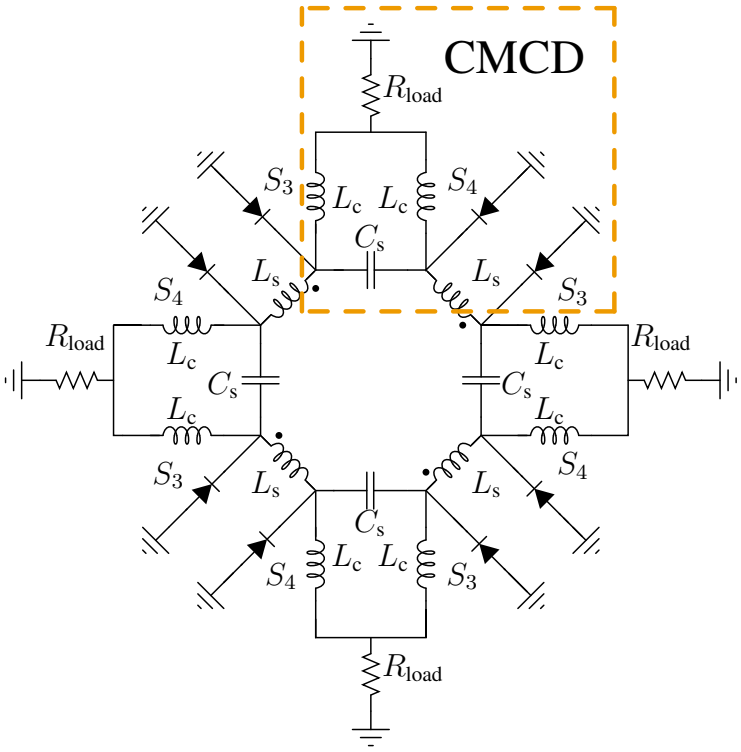

(b) Passive segmented CMCD converter.

Figure 6.5: Circuits for active-to-passive segmented CMCD WPT (APS-WPT) systems. An active segmented CMCD inverter is coupled to a passive segmented CMCD rectifier.

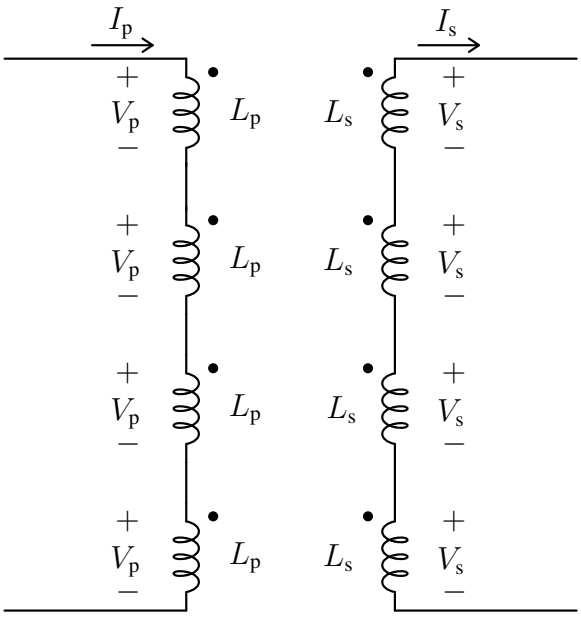

Figure 6.6: Pseudo equivalent circuit for segmentation CMCD WPT systems.

by a factor of 4 as well.

6.2.3 Comparison with Singleton WPT System

The current in each segment is identical in phase and magnitude, the magnetic flux and coil voltage are added directly in magnitude; The idealized equivalent circuit is shown in Fig. 6.6 while the simplified equivalent circuit is shown in Fig. 6.7(a). It is an air-core loosely-coupled transformer with two windings. The primary and secondary self-inductances are $4L_\mathrm{p}$ and $4L_\mathrm{s}$.

$$\begin{pmatrix} 4V_\mathrm{p} \\ 4V_\mathrm{s} \end{pmatrix} = \begin{pmatrix} j\omega \cdot 4L_\mathrm{p} & -j\omega M \\ j\omega M & -j\omega \cdot 4L_\mathrm{s} \end{pmatrix} \begin{pmatrix} I_\mathrm{p} \\ I_\mathrm{s} \end{pmatrix}, \tag{6.3}$$

where the mutual inductance is $M = k\sqrt{4L_\mathrm{p} \cdot 4L_\mathrm{s}}$. Thus, we could use the current-controlled-voltage-source model for a singleton CMCD WPT system [77]. The primary side and the coupled coils are equivalently replaced by

$$V_\mathrm{p}' = k\sqrt{\frac{4L_\mathrm{p}}{4L_\mathrm{s}}}\,(4V_\mathrm{p}) \tag{6.4}$$

and

$$L_\mathrm{eff} = (1 - k^2)\,(4L_\mathrm{s})\,. \tag{6.5}$$

The power transferred is

$$\begin{aligned} P_{\mathrm{o}} &= \frac{\left|\frac{V_{\mathrm{p}}'}{\sqrt{2}}\right|\left|\frac{4V_{\mathrm{s}}}{\sqrt{2}}\right|}{\omega L_{\text{eff}}}\sin\theta \\ &= 4\frac{k\sqrt{\frac{L_{\mathrm{s}}}{L_{\mathrm{p}}}}\,|V_{\mathrm{p}}|\,|V_{\mathrm{s}}|}{2\,\omega\,(1-k^2)\,L_{\mathrm{s}}}\sin\theta, \end{aligned} \tag{6.6}$$

where θ is the phase shift of V_{p} and V_{s}, which is the same phase shift as $4\,V_{\mathrm{p}}$ and $4\,V_{\mathrm{s}}$. Maximum power transfer is achieved at 90° [77].

With

$$\omega = 1/\sqrt{(1-k^2)\,L_{\mathrm{p}}C_{\mathrm{p}}} = 1/\sqrt{(1-k^2)\,L_{\mathrm{s}}C_{\mathrm{s}}} \tag{6.7}$$

and

$$\sqrt{\frac{C_{\mathrm{p}}}{L_{\mathrm{s}}}} = \sqrt{\frac{C_{\mathrm{s}}}{L_{\mathrm{p}}}} \tag{6.8}$$

for each primitive CMCD converter or a singleton CMCD WPT system, (6.6) can be further simplified as

$$P_{\mathrm{o}} = 4\frac{k|V_{\mathrm{p}}||V_{\mathrm{s}}|}{2\sqrt{1-k^2}}\sqrt{\frac{C_{\mathrm{p}}}{L_{\mathrm{s}}}} = 4\frac{k|V_{\mathrm{p}}||V_{\mathrm{s}}|}{2\sqrt{1-k^2}}\sqrt{\frac{C_{\mathrm{s}}}{L_{\mathrm{p}}}}. \tag{6.9}$$

With $V_{\mathrm{p}} = \pi V_{\mathrm{in}}$, (6.9) can be further simplified as

$$P_{\mathrm{o}} = 4\frac{k\pi V_{\mathrm{in}}|V_{\mathrm{s}}|}{2\sqrt{1-k^2}}\sqrt{\frac{C_{\mathrm{p}}}{L_{\mathrm{s}}}} \tag{6.10}$$

and

$$|V_{\mathrm{s}}| = |I_{\mathrm{s}}|R_{\mathrm{ac}}. \tag{6.11}$$

From [4], we know

$$R_{\mathrm{ac}} = \frac{\pi^2}{2}R_{\mathrm{load}} \tag{6.12}$$

and

$$|I_{\mathrm{s}}| = kV_{\mathrm{p}}\sqrt{\frac{C_{\mathrm{s}}}{(1-k^2)\,L_{\mathrm{p}}}} = kV_{\mathrm{p}}\sqrt{\frac{C_{\mathrm{p}}}{(1-k^2)\,L_{\mathrm{s}}}}. \tag{6.13}$$

Hence,

$$|V_{\mathrm{s}}| = \frac{k\pi^3 V_{\mathrm{in}}R_{\mathrm{load}}}{2\sqrt{1-k^2}}\sqrt{\frac{C_{\mathrm{s}}}{L_{\mathrm{p}}}} = \frac{k\pi^3 V_{\mathrm{in}}R_{\mathrm{load}}}{2\sqrt{1-k^2}}\sqrt{\frac{C_{\mathrm{p}}}{L_{\mathrm{s}}}}. \tag{6.14}$$

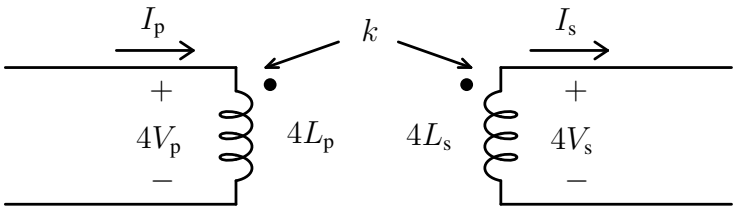

(a) Canonical representation.

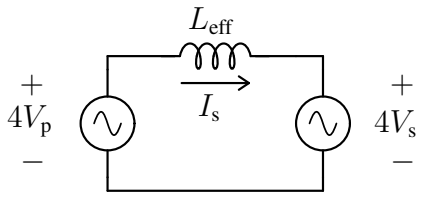

(b) One side simplified model.

Figure 6.7: Equivalent circuit for segmentation CMCD WPT systems.

Substituting (6.14) into (6.9), we have

$$\begin{aligned} P_\mathrm{o} &= 4\frac{k^2\pi^4 V_\mathrm{in}^2 R_\mathrm{load}}{4\left(1-k^2\right)}\sqrt{\frac{C_\mathrm{p}}{L_\mathrm{s}}}\sqrt{\frac{C_\mathrm{s}}{L_\mathrm{p}}} \\ &= \frac{k^2\pi^4 V_\mathrm{in}^2 R_\mathrm{load}}{\left(1-k^2\right)}\sqrt{\frac{C_\mathrm{p}}{L_\mathrm{s}}}\sqrt{\frac{C_\mathrm{s}}{L_\mathrm{p}}}, \end{aligned} \tag{6.15}$$

which is a factor of 4 in power compared to (6.2) for a singleton CMCD system.

For a segmented system, the efficiency remains the same as the power scales using identical components with identical stresses; this is not true for singleton CMCD WPT systems. The details of loss calculation are similar to [75].

Ultimately, transfer distance among near-field CMCD systems is determined by self-inductances using single turn coils. For a singleton CMCD system, the self-inductance of WPT coils are L_p and L_s; the equivalent self-inductances of WPT coils in segmentation WPT systems are $4\,L_\mathrm{p}$ and $4\,L_\mathrm{s}$. For a crude approximation using circular wire loops, a factor of four in inductance corresponds to a factor of four in radius [36]. With a factor of four increase in radius and hence self-inductance, the mutual inductance is higher by a factor of 4 for the same coupling coefficient k [37]. This demonstrates a transfer distance that increases linearly with the number of segments while maintaining k, which is important for UAVs and agile robots.

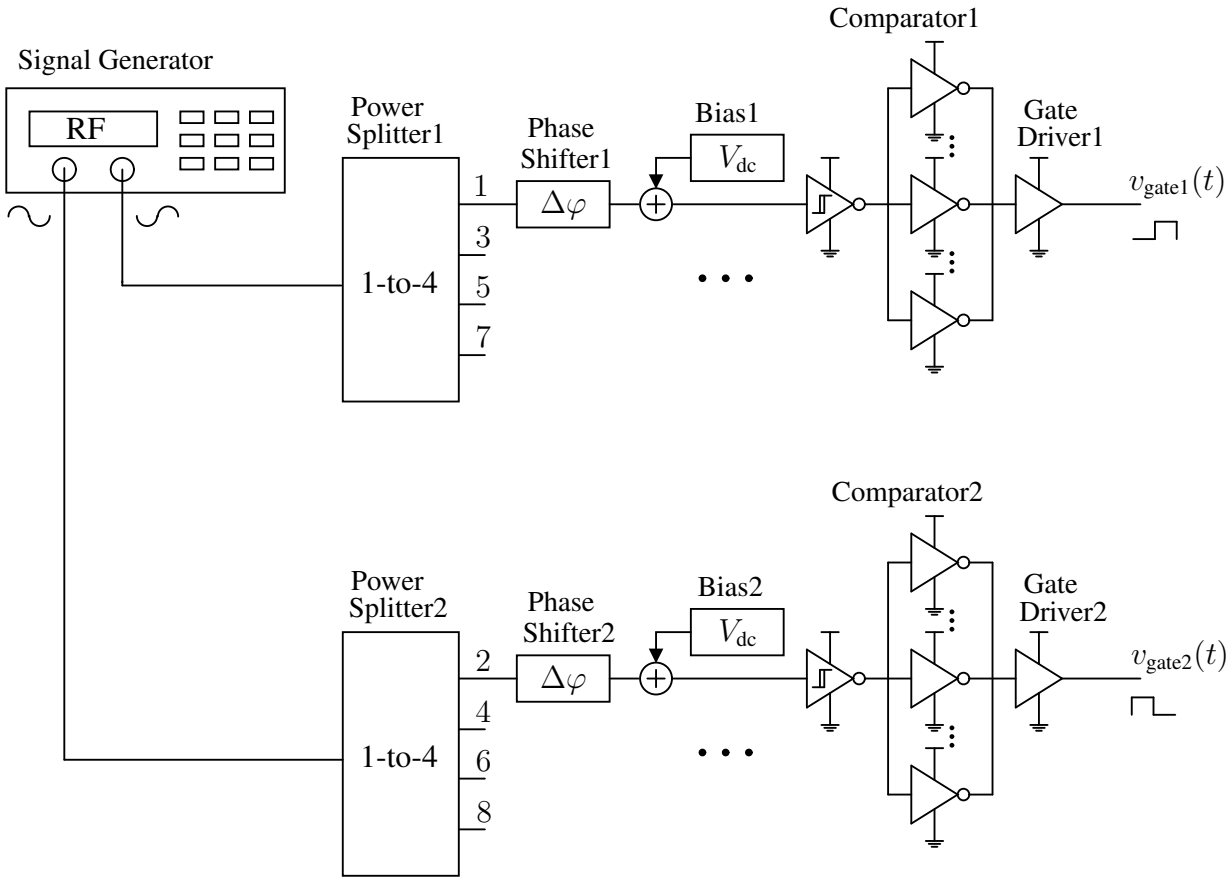

Figure 6.8: Multi-channel synchronized PWM generator and gate drivers.

6.3 Hardware Implementation and Results

6.3.1 Multi-channel Synchronized PWM Generator

Digital controllers are a prevalent and apparent choice to generate multi-channel synchronized PWM signals for modular converters, interleaving converters, and multi-phase converters. FPGA has been used in 27.12 MHz power converters [77]. Typically, commercial function generators at 100 MHz have only two channels available for generating square waves. Fortunately, sine waves can be easily split into multiple channels and converted to square waves. Fig. 6.8 shows the system structure of the multi-channel synchronized PWM generators. Two out-of-phase sine waves are expanded into four pairs of out-of-phase signals. Individual phase shifters can follow the splitter to eliminate mismatches in the signal path. Biased sine waves are fed into comparators to produce square wave with different duty ratios, which depend on the bias voltages. The Schmitt trigger in the gate driver from [57] can be effectively used as a comparator.

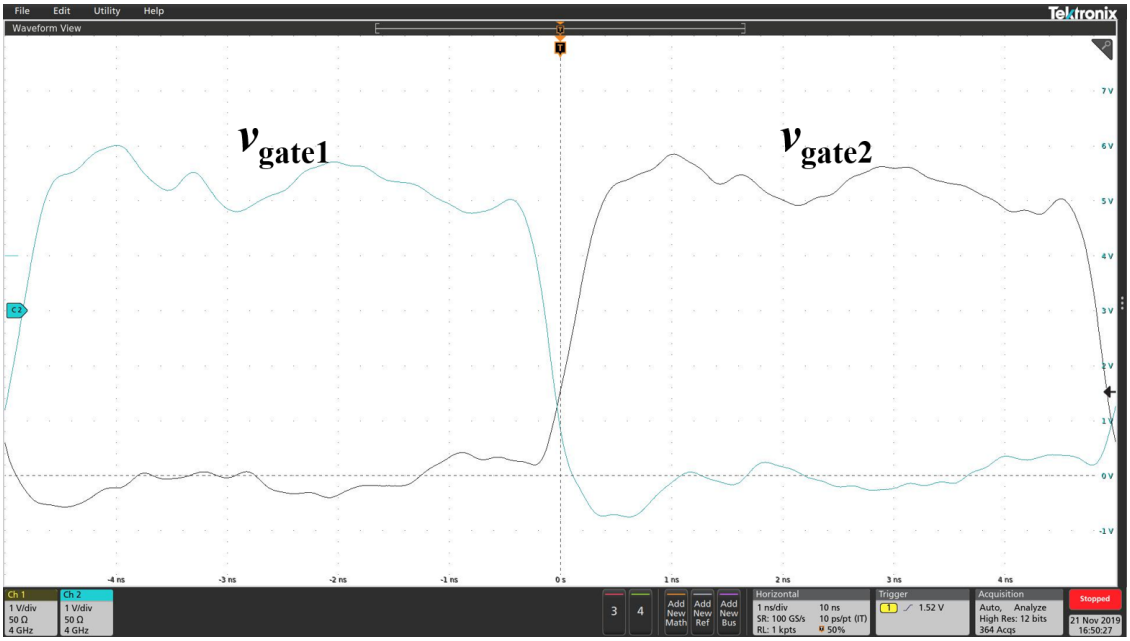

Figure 6.9: Complementary gate signals for an active primitive CMCD converter.

A pair of complementary gate signals for a primitive converter is shown in Fig. 6.9 under 4 GHz measurement bandwidth with active probe TAP400 and 4 GHz 6-series mixed-signal oscilloscope from Tektronix. The signals are out-of-phase with rising and falling times within 400 ps. The synchronization is verified in Fig. 6.10 with four 1 GHz TPP1000 from Tektronix.

6.3.2 VHF Active-to-Passive Segmentation WPT Implementation

As mentioned before, a VHF singleton CMCD WPT system is the basic module for a VHF active-to-passive segmentation WPT system. A 100 MHz CMCD WPT system had been demonstrated in [4], which had 2.734 W load power with close to 70 % end-to-end drain efficiency and close to 60 % total efficiency with gating loss of 0.607 W. A 100 MHz active segmented CMCD transmitter and a passive series RLC resonant tank as the receiver was demonstrated in [75], which had a load power of 12 W with 81 % drain efficiency and total dc-ac, ac-ac efficiency of 74 % with 1.3 W gating loss. The PCB layout and WPT coils design are the same as [75]. The choke is replaced by BCL-272JB from Coilcraft with 2.72 μH for smaller ESR. The parallel inverters for the gate drivers are replaced with SN74LVC2G04 with buffered output instead of SN74LVC2GU04 with unbuffered ones and the turn-on voltage is increased to 5 V instead of 4 V to reduce the $R_{ds,\,\mathrm{on}}$ of the GaN FETs. Other components are identical to [75]. The PCB layout of the active segmentated CMCD transmitter with its primitive module is shown in Fig. 6.11. The implementation components are enumerated in Table 6.1.

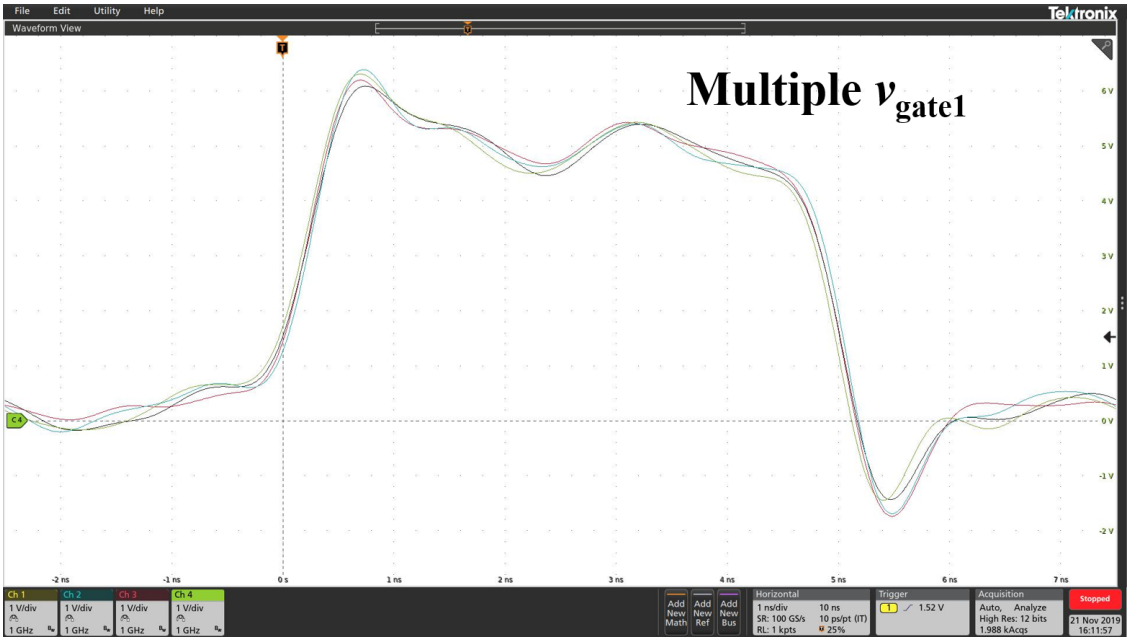

Figure 6.10: Synchronization of the gate signals.

The passive segmented CMCD rectifier is a scalable expansion of the singleton passive CMCD rectifier [4, 52]. The diode and choke inductors are identical to [4]. The corresponding PCB layout and its module design are shown in Fig. 6.12. The receiver coil is identical to the transmitter coil, which are 4 layer FR4 PCBs with 2 oz copper. The implementation components are enumerated in Table 6.1.

6.3.2.1 VHF Active-to-Passive Segmentation WPT Results

The hardware setup of the active-to-passive segmentation wireless power transfer system is shown in Fig. 6.13. The air gap for the transfer distance is 4 cm. With [37], the calculated mutual inductance is 55 nH, and the calculated coupling coefficient is around 0.2.

Reference [4] introduced a method to tune the 100 MHz singleton WPT system. The APS WPT can use the same tuning strategy with the following steps:

(1) Implementing an unloaded active segmented transmitter with zero-voltage-switching (ZVS);

(2) Tuning the distance with the designed coupling coefficient or measuring the coupling coefficient with the designed transfer distance;

(3) Loading the transmitter with the passive segmented receiver and tuning the receiver capacitance with the transmitter GaN FETs remaining ZVS and 90° phase shift between the drain and cathode voltages [52].

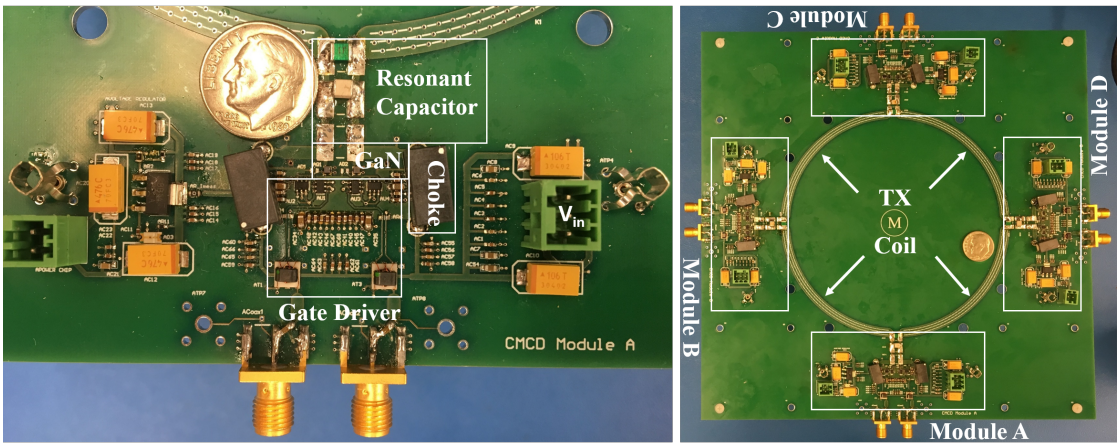

Figure 6.11: PCB layout of active segmented CMCD converter and its primitive module.

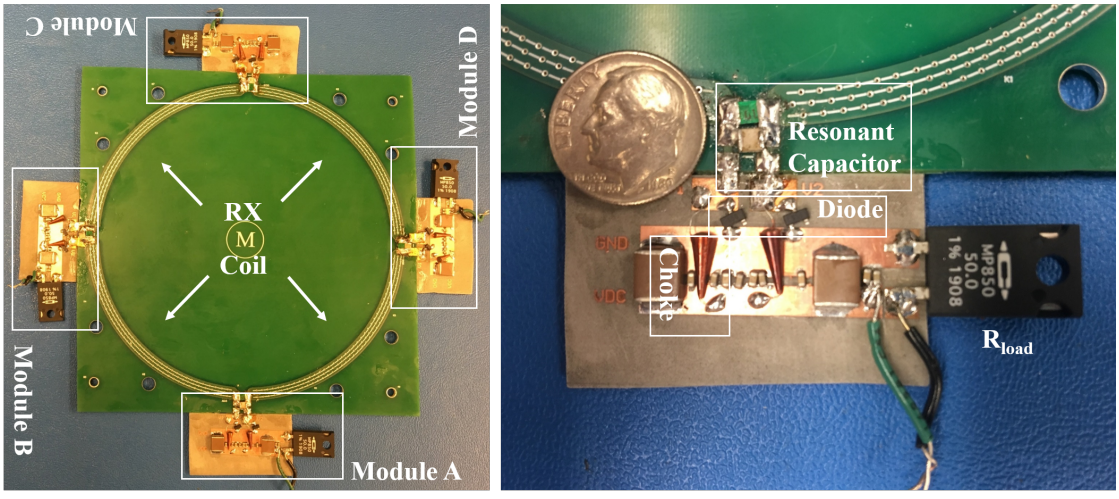

Figure 6.12: PCB layout of passive segmented CMCD converter and its primitive module.

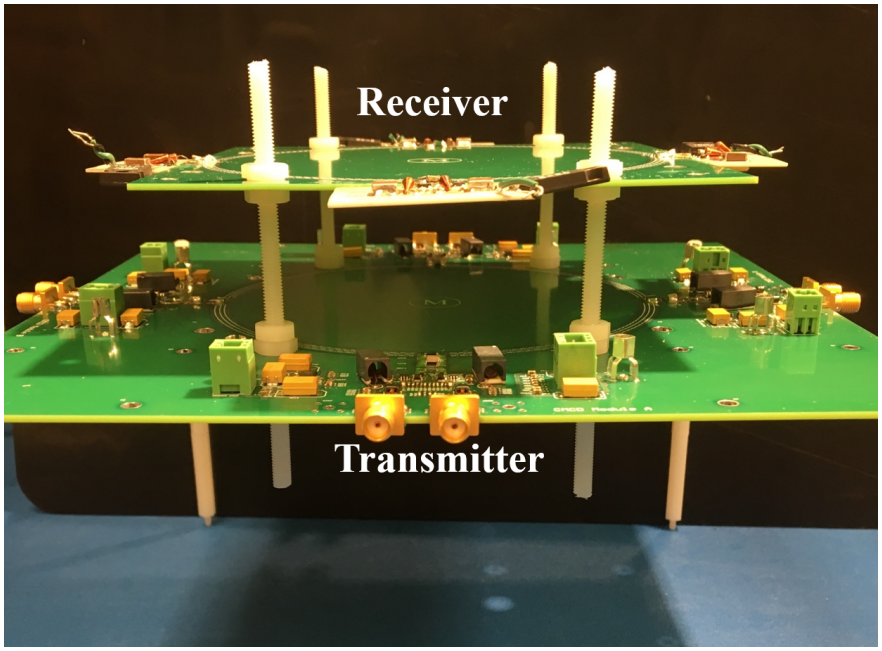

Figure 6.13: Hardware setup of the VHF ative-to-passive segmentation CMCD WPT systems.

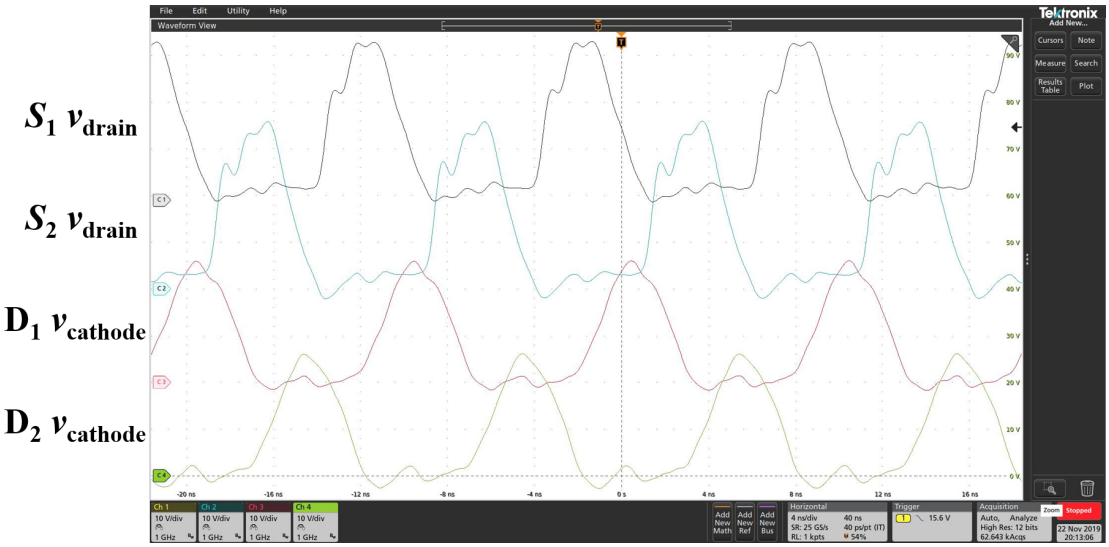

Figure 6.14: Drain and cathode voltages of a primitive CMCD WPT in the APS-WPT system when $V_{\text{in}} = 12\,\text{V}$.

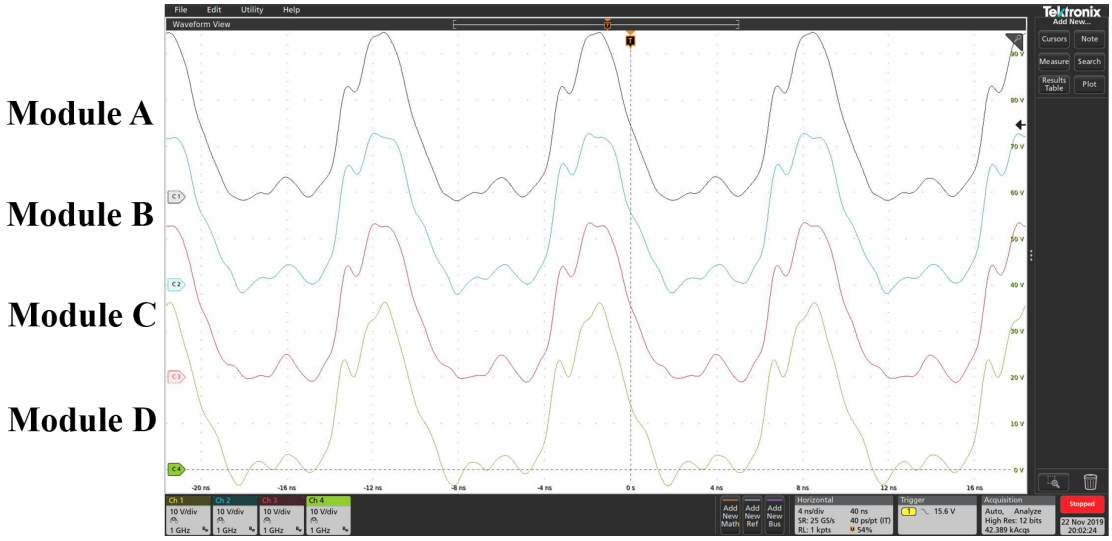

Figure 6.15: Drain voltages of even switches in the APS-WPT system when $V_{\text{in}} = 12\,\text{V}$.

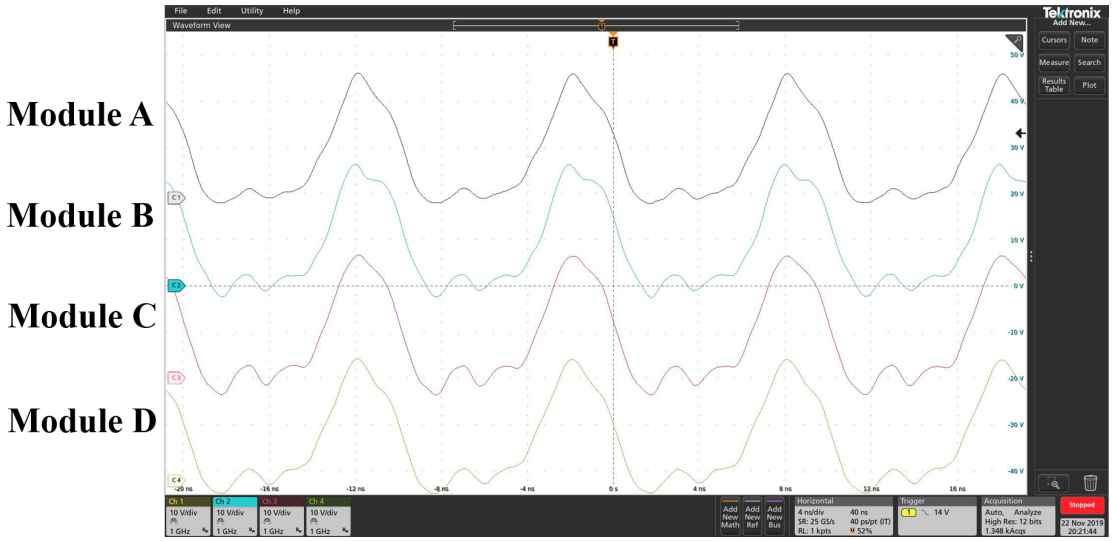

Figure 6.16: Cathode voltages of even switches in the APS-WPT system when $V_{\text{in}} = 12\,\text{V}$.

Table 6.1: Implementation of Segmentation WPT System.

Items	Components & Parameters
Choke Inductor	BCL-272 2.7 μH
Active Device	GaN FET EPC 2038
Passive Diode	ZHCS506
Gate Driver	SN74LVC2G04
Transmitter Resonant Capacitance	QUAD HIFREQ Series 25.9 pF
Receiver Resonant Capacitance	QUAD HIFREQ Series/MICA 18.5 pF
Transmitter/Receiver PCB Coil	297 nH ($R = 6.3$ cm)
Transfer Distance	4 cm

The tuning capacitances for both sides are shown in Table 6.1. The tuned systems can be verified in Fig. 6.14 with nearly 90 degree phase shift between the drain and cathode voltages of Module A. Identical switch voltages with synchronization in transmitter and receiver side are shown in Fig. 6.15 for even switches in the transmitter and in Fig. 6.16 for even diodes in the receiver. The little discrepency can be resulted from the mismatched of the components values. The load power is measured with four current meters ($6\frac{1}{2}$ digit multimeters Keysight 34465A and HP 34401A) in series with the four distributed 50 Ω loads and a voltage meter ($6\frac{1}{2}$ digit multimeter HP 34401A). The input power and gating loss are based on the calculations from the dc power supply HMP4040 from ROHDE&SCHWARZ.

The distributed loads share the received power quite equally with almost the same voltage and current. The output power is the sum of the four loads, which is 6.34 W when the input dc voltage is 12 V. Better efficiency can be achieved with more careful phasing and tuning of the segments to ensure that the power delivery from each is evenly shared. The total input power is 9.25 W. The gate driver loss is similar among the four modules with 1.76 W in total. The end-to-end drain efficiency is 68.5 % while the end-to-end total efficiency is 57.6 %. With a higher input dc voltage, the output power can as high as 9.7 W with a smaller efficiency of 65.1 %. Power and efficiency are shown in Fig. 6.17.

6.4 Summary

VHF active-to-passive segmentation can improve the performance of WPT for UAVs and agile robots by segmenting both the power conversion and the WPT coils. The demonstrated 100 MHz segmented CMCD WPT system delivers 6.34 W to the load with 69 % drain efficiency and 58 %

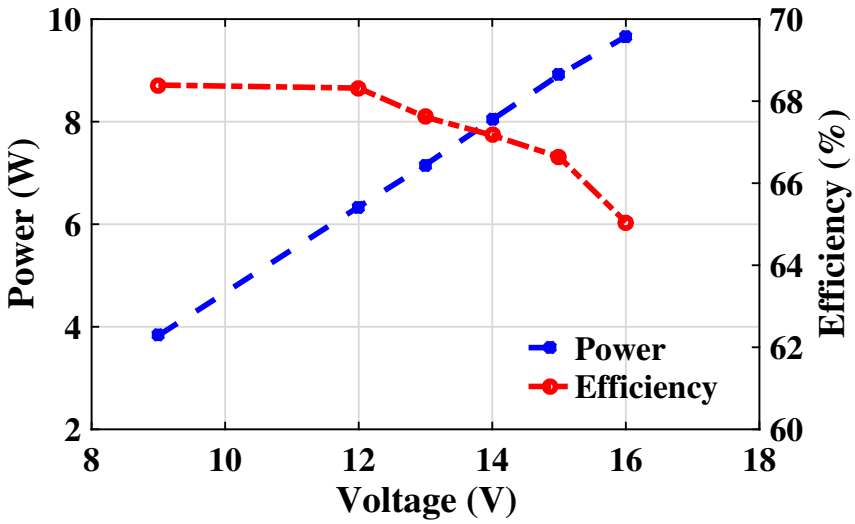

Figure 6.17: The relationship among output power, drain efficiency, and input voltage in the APS-WPT system.

total efficiency at 4 cm transfer distance. Higher power of (9.7 W) can be achieved with the higher input voltage and 65.1 % drain efficiency. Compared to a singleton CMCD WPT system, higher power and longer transfer distance can be achieved with additional partitioning with more primitive parts in the VHF active-to-passive segmentation CMCD WPT system, which are needed for lightweight UAVs and agile robots.

CHAPTER 7

Piecewise Resonant WPT System

7.1 Introduction

Artificial heart pumps [107], ventricular assist devices [108], brain-machine interfaces [109], spinal cord stimulators [110], and many other implantable medical devices [111] save lives and improve health. Currently, many devices are still powered by percutaneous wires that inevitably result in exit site infection (ESI). Wireless power transfer (WPT), first proposed by Nikola Tesla in 1899, offers a preferable solution. Much of the research in WPT for medical applications is focused on increasing power and efficiency while decreasing specific absorption rate (SAR) [1]. Furthermore, most efforts in WPT focus on circuit optimization [107]. Recently, there is a trend that waveform design helps with enhancing the performance of WPT systems [110, 112–118], especially for implantable medical devices [110, 115].

Because the WPT receiver is in vivo, there is a strong emphasis on efficiency, simplicity, reliability, and low specific absorption rate (SAR). Approaches to improve efficiency include methods that use multi-sine resonance with high peak-to-average power ratio (PAPR) to allocate power over multiple frequencies [112–118]. High peak-to-average power ratio (PAPR) means higher dc output voltage with a resulting improvement in rectifier efficiency [114–117] for the same WPT coil rms voltage and hence equivalent tissue heating level, which is related to maximum allowable input power of the WPT coils. Tissue heating is a crucial safety concern in implantable medical devices when utilizing wireless powering technology and SAR is the regulatory metric [119–121]. For these implantable receivers, passive components are preferred (the fewer the better) and series resonance is typically better because the inductor current equals the load current. To achieve high receiver efficiency in these applications, there is often a willing trade-off in transmitter efficiency and subsequent end-to-end efficiency.

In this chapter, I investigate a piecewise resonant wireless power transfer system (PR-WPT)

[1] SAR $= \frac{\sigma E^2}{\rho}$, E is the rms value of the electric field strength in the tissue (V/m), σ is the conductivity of body tissue (S/m), ρ is the density of body tissue (kg/m^3).

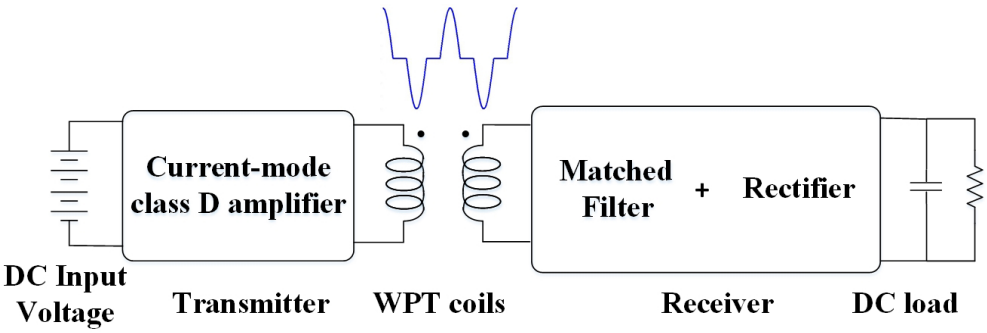

Figure 7.1: Piecewise resonant wireless power transfer system.

with a single transmitter to generate a piecewise resonant (PR) voltage waveform with PAPR and a high-efficiency receiver for implantable devices, illustrated in Fig. 7.1. The transmitter is a zero-voltage-switching (ZVS) current-mode class D (CMCD) amplifier [83], shown in Fig. 4.2. By extending the mode when both switches are ON between the half-sine waveforms, the output is differentially grounded with the inductor current remaining constant. The waveforms transferred between the coils are piecewise resonant with a fundamental frequency of 6.78 MHz. The PAPR of the piecewise resonant waveform can be adjusted by the ratio of the resonant period to the switching period D, which is incidentally the duty ratio for power conversion from the transmitter to the receiver. A judicious choice of D enables harmonic elimination to lower the order of the receiver. The resulting receiver contains a matched filter [122], which is able to receive the fundamental and third harmonic voltages that well-approximate the transmitter output PR voltage, even at this low order. The filter is a 4^{th}-order series resonance with values derived from closed-form equations. The well-approximated PR voltage is converted into dc by a full-bridge rectifier. To improve the rectifier efficiency with this preferred series resonance, a high peak transmitter voltage of 200 V trades off the transmitter efficiency to obtain the needed peak voltage at the secondary coil. The resulting rms currents which flow through the two transmitter switches and primary coil are higher than those for a simple sine-wave resonance (SR). The extended mode when the two switches are both ON, contributes to the lower efficiency because no power is transferred from the transmitter to the receiver.

Many efforts have been dedicated to WPT systems. For circuit-level optimization, the series compensation methods perform better for tissue heating than series-parallel and series-series-parallel compensation methods [107]. In optimizing waveform for WPT systems, there are many other ways to achieve high PAPR using multi-resonance. Analogies can be found in the field of microwave where multi-sine with high PAPR is generated by adding multiple sine signals with adjusted tone number, tone spacing, and amplitude [114]. There is an optimal number of tones for maximum output dc voltage [115]. A multisine signal with 0° phase relationship among tones

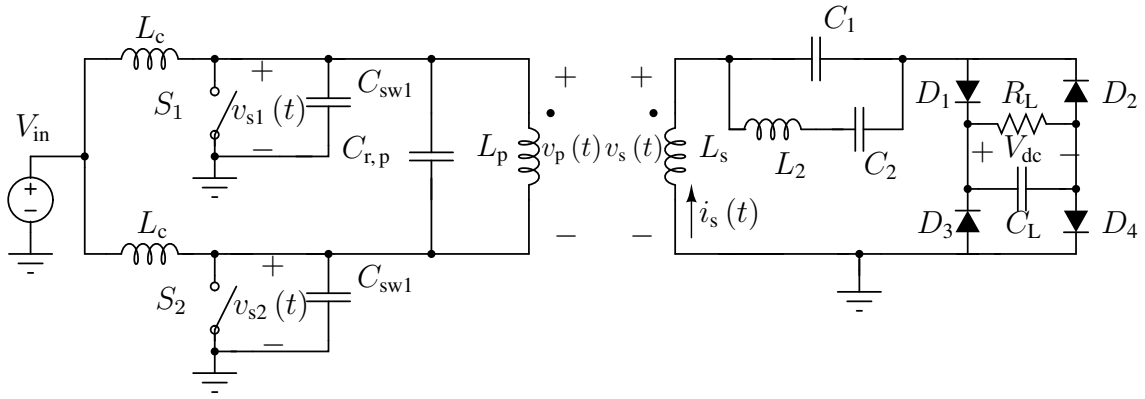

Figure 7.2: Piecewise resonant wireless power transfer circuit.

can generate the highest dc voltage [117]. By changing the pulse width or duty cycle of the signals, dc voltage can be enhanced significantly [116]. Higher dc voltage means higher rectifier efficiency [114–117]. In the field of power electronics, multiple LC networks are utilized in both primary and secondary resonant circuits to transfer equal amounts of power at 25 kHz and 75 kHz [118]. A 6.78 MHz multi-resonant WPT system with an 18 mm implant depth for powering a spinal cord stimulator can be designed with a PAPR waveform to achieve an end-to-end efficiency of 50.7 %. The PAPR is achieved by a transmitting waveform with a three-tone signal consisting of 6.55 MHz, 6.78 MHz, and 7.01 MHz [110].

7.2 Piecewise Resonant Method

PR-WPT with a high peak-to-average power ratio (PAPR) results in a higher dc output voltage and a lower receiver loss for implantable medical devices. In PR-WPT, a single current-mode class D amplifier with a parallel resonant tank, which includes the transmitter coil, generates PR voltage with high PAPR as a transmitter. ZVS is ensured to minimize the switching loss. Power has been received with a low-order passive matched filter, which includes the receiver coil, at the switching frequency of 6.78 MHz and its third harmonic frequency 20.34 MHz. A full-bridge Schottky rectifier with RC load generates dc voltage. Fig. 7.2 shows the circuit of piecewise resonant wireless power transfer (PR-WPT) systems.

7.2.1 Transmitter Design with a High PAPR Waveform

To generate a high PAPR waveform, the CMCD amplifier operates differently. Normally, the differential output of the CMCD amplifier is sine-wave resonance when the duty cycle D equals 100 % [83]. The two switches turn on and off alternately, each for 50 % of the switching period.

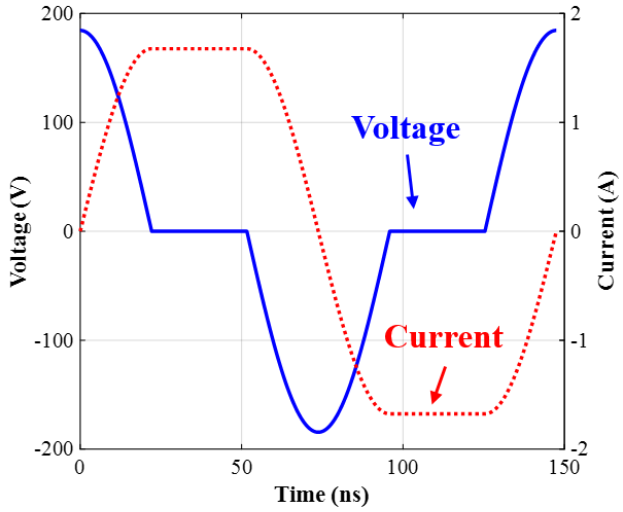

Figure 7.3: Piecewise resonant waveforms of primary coil.

The switching frequency f_{s} equals the resonant frequency f_{r}, which is calculated from

$$f_{\mathrm{s}} = f_{\mathrm{r}} \times D = \frac{D}{2\pi\sqrt{L_{\mathrm{r,p}}(C_{\mathrm{r}} + C_{\mathrm{sw}})}} \tag{7.1}$$

when D equals 100 %. To generate piecewise resonant waveforms with PAPR, shown in Fig. 7.3, the resonant frequency is chosen to be higher than the switching frequency, which is calculated from (7.1) with D less than 100%. During the zero-voltage mode, when both switches are ON, the transmitter coil current is held constant and the capacitor voltage is zero, hence pausing the resonance. When one of the two switches turns OFF, the resonance resumes. The piecewise resonant voltage and current waveforms of primary coil in Fig. 7.3 can be expressed by

$$v(t) = \begin{cases} V_{\mathrm{p}} \cos\left(\omega_{\mathrm{r}}\, t\right) & 0 \le t < \frac{1}{4}T_{\mathrm{r}} \\ 0 & \frac{1}{4}T_{\mathrm{r}} \le t < \frac{1}{2}T_{\mathrm{s}} - \frac{1}{4}T_{\mathrm{r}} \\ V_{\mathrm{p}} \cos\left(\omega_{\mathrm{r}}\, \left[t - \left(\frac{1}{2}T_{\mathrm{s}} - \frac{1}{2}T_{\mathrm{r}}\right)\right]\right) & \frac{1}{2}T_{\mathrm{s}} - \frac{1}{4}T_{\mathrm{r}} \le t < \frac{1}{2}T_{\mathrm{s}} + \frac{1}{4}T_{\mathrm{r}} \\ 0 & \frac{1}{2}T_{\mathrm{s}} + \frac{1}{4}T_{\mathrm{r}} \le t < T_{\mathrm{s}} - \frac{1}{4}T_{\mathrm{r}} \\ V_{\mathrm{p}} \cos\left(\omega_{\mathrm{r}}\, \left[t - (T_{\mathrm{s}} - T_{\mathrm{r}})\right]\right) & T_{\mathrm{s}} - \frac{1}{4}T_{\mathrm{r}} \le t < T_{\mathrm{s}} \end{cases} \tag{7.2}$$

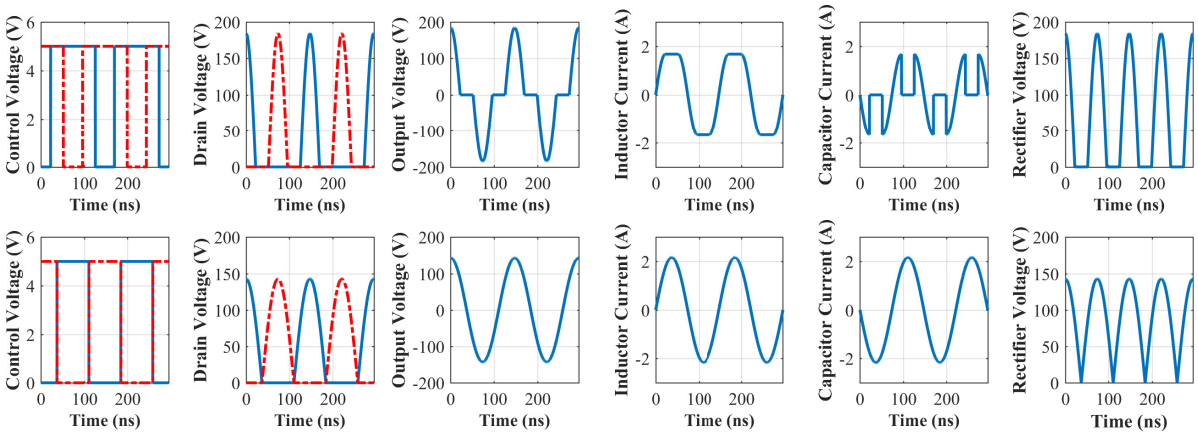

Figure 7.4: Typical waveforms in current-mode class D amplifier under two resonances.

and

$$i(t) = \begin{cases} I_{\mathrm{p}} \sin\left(\omega_{\mathrm{r}}\, t\right) & 0 \le t < \frac{1}{4}T_{\mathrm{r}} \\ I_{\mathrm{p}} & \frac{1}{4}T_{\mathrm{r}} \le t < \frac{1}{2}T_{\mathrm{s}} - \frac{1}{4}T_{\mathrm{r}} \\ I_{\mathrm{p}} \sin\left(\omega_{\mathrm{r}}\, \left[t - \left(\frac{1}{2}T_{\mathrm{s}} - \frac{1}{2}T_{\mathrm{r}}\right)\right]\right) & \frac{1}{2}T_{\mathrm{s}} - \frac{1}{4}T_{\mathrm{r}} \le t < \frac{1}{2}T_{\mathrm{s}} + \frac{1}{4}T_{\mathrm{r}}, \\ I_{\mathrm{p}} & \frac{1}{2}T_{\mathrm{s}} + \frac{1}{4}T_{\mathrm{r}} \le t < T_{\mathrm{s}} - \frac{1}{4}T_{\mathrm{r}} \\ I_{\mathrm{p}} \sin\left(\omega_{\mathrm{r}}\, \left[t - \left(T_{\mathrm{s}} - T_{\mathrm{r}}\right)\right]\right) & T_{\mathrm{s}} - \frac{1}{4}T_{\mathrm{r}} \le t < T_{\mathrm{s}} \end{cases} \tag{7.3}$$

where T_{s} is the switching period and T_{r} is the resonant period.

Table 7.1 compares parameters of piecewise resonance with those of sine-wave resonance using equivalent current-mode class D amplifier with the same switching frequency f_{s}, rms voltage V at the differential output, and primary coil inductance L_{p}. The rms, peak, and average values of voltages and currents of resonant tank for piecewise resonance can be derived by time-domain integration, similar to those for sinewave resonance. The required dc input voltage can be derived according to (4.2). The dc output voltage of sine-wave resonance after a full-bridge Schottky rectifier and RC load can be derived by a fundamental-harmonic model. Fig. 7.4 shows the typical waveforms in current-mode class D amplifier for these two types of resonances. It can be seen that sine-wave resonance is a special case of piecewise resonance when D equals 100 %. In piecewise resonance, if D varies, the peak-to-average power ratio changes. In both resonances, ZVS can be ensured by setting the frequency required by (7.1).

Table 7.1: Parameters Comparisons in Two Resonances

parameters	Sine-wave Resonance	Piecewise Resonance
Switching frequency	f_s	f_s
Resonant frequency	f_s	f_s/D
Resonant inductor	L_p	L_p
Resonant capacitor	C_r	D^2C_r
Output rms voltage	V	V
Output peak voltage	$\sqrt{2}V$	$\sqrt{2/D}V$
Peak inductor current	$\sqrt{2}V/(\omega_\mathrm{s}L_\mathrm{r})$	$\sqrt{2D}V/(\omega_\mathrm{s}L_\mathrm{r})$
Rms inductor current	$V/(\omega_\mathrm{s}L_\mathrm{r})$	$\sqrt{2D(1-D/2)}V/(\omega_\mathrm{s}L_\mathrm{r})$
Peak capacitor current	$\sqrt{2}\omega_\mathrm{s}C_\mathrm{r}V$	$\sqrt{2D}\omega_\mathrm{s}C_\mathrm{r}V$
Rms capacitor current	$\omega_\mathrm{s}C_\mathrm{r}V$	$D\omega_\mathrm{s}C_\mathrm{r}V$
DC input voltage	$\sqrt{2}V/\pi$	$\sqrt{2D}V/\pi V$
Average output voltage after rectifier	$2\sqrt{2}V/\pi$	$2\sqrt{2D}V/\pi$
Peak to average voltage ratio	$\pi/2$	$\pi/\left(2D\right)$
PAPR	$(\pi/2)^2$	$\pi^2/(2D)^2$

7.2.2 Waveform Approximation of PAPR

Since the piecewise resonant voltage with PAPR in Fig. 7.3 consists of multiple frequencies, for simplicity and reliability, we choose a low-order receiver which is able to receive the dominant frequency components. Equation (7.2) expresses the piecewise resonant voltage for one period, which as a periodic function can be expressed as a Fourier series. Since the primary output voltage is even and balanced, it can be expressed in the form of

$$v(t) = \sum_{k=1}^{\infty} a_\mathrm{k} \cos\left(k\omega_1\, t\,\right) \tag{7.4}$$

and Fourier coefficients a_k can be calculated by

$$a_\mathrm{k} = \frac{2}{T_\mathrm{s}} \int_0^{T_\mathrm{s}} v(t) \cos\left(k\omega_1\, t\right) dt = \frac{2V_\mathrm{p}}{T_\mathrm{s}} \begin{cases} \frac{4\omega_\mathrm{r}}{(\omega_\mathrm{r}-k\omega_1)(\omega_\mathrm{r}+k\omega_1)} & k \quad \text{is odd,} \\ 0 & k \quad \text{is even.} \end{cases} \tag{7.5}$$

Hence, the Fourier series expression of the piecewise resonant voltage waveform is

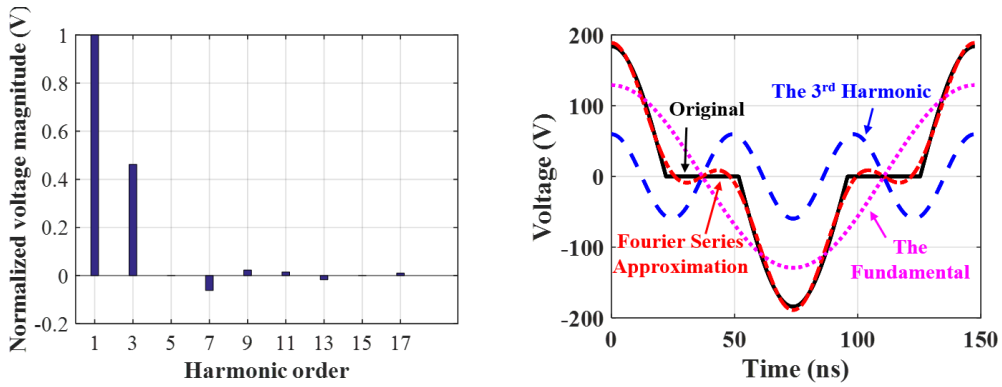

(a) Normalized voltage magnitude of fundamental and harmonics

(b) Waveform appriximation.

Figure 7.5: Resonant networks for segmentation and singleton wireless power transfer.

$$\begin{aligned} v(t) &= \frac{2V_\mathrm{p}}{T_\mathrm{s}} \sum_{k=1}^{2k+1} \left[\frac{4\omega_\mathrm{r}}{(\omega_\mathrm{r} - k\omega_1)(\omega_\mathrm{r} + k\omega_1)} \cos\left(\frac{k\omega_1 T_\mathrm{r}}{4}\right) \cos(k\omega_1 t) \right] \\ &= \frac{2V_\mathrm{p}}{T_\mathrm{s}} \sum_{k=1}^{2k+1} \left[\frac{4D}{\omega_1 (1 - kD)(1 + kD)} \cos\left(\frac{kD}{2}\pi\right) \cos(k\omega_1 t) \right]. \end{aligned} \tag{7.6}$$

Observe that if D equals 60 %, the 5^{th} harmonic and its harmonic multiples are eliminated. The piecewise resonant voltage can be well-approximated by the 1^{st} and 3^{rd} harmonic, as illustrated in

$$v(t) \approx 0.7016 V_\mathrm{p} \cos(\omega_1 t) + 0.3244 V_\mathrm{p} \cos(3\omega_1 t). \tag{7.7}$$

Fig. 7.5 shows the ratio of the amplitude of each harmonic to the fundamental when D equals 60 %. The dc output voltage is the highest when all harmonics are all in phase [117].

7.2.3 High-Efficiency Receiver Design

A receiver that is implanted in a human body has multiple design objectives: small volume, simple structure, easy design, high efficiency, and low SAR. A matched filter and a full-bridge Schottky rectifier comprise the receiver. From Section 7.1, high PAPR and series resonance are crucial to the receiver design. Because the PR voltage of the primary coil can be well-approximated by (7.7), this PR voltage can be received by a 4^{th}-order matched filter designed with the dominant fundamental and third harmonic response.

The equivalent circuit of the receiver can be shown in Fig. 7.6 with the inductance $L_1 = (1 - k^2)L_\mathrm{s}$ in (7.14) and the ac voltage $V_\mathrm{p}' = k\sqrt{L_\mathrm{s}/L_\mathrm{p}}V_\mathrm{p}$. One approximation is that the full-

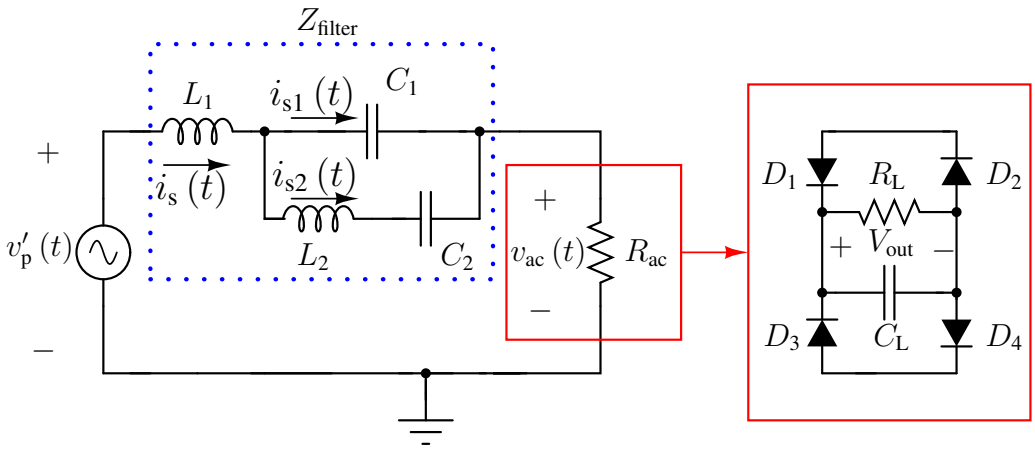

Figure 7.6: Piecewise resonant wireless power transfer matched filter.

bridge rectifier together with the RC load R_{L} and C_{L} can be regarded as an effective resistance R_{ac} considering power balance [87].

The matched filter is designed to have zero impedances, i.e, short circuit, at 6.78 MHz and 20.34 MHz. An infinite impedance frequency can be located between these two frequencies. The impedance of the matched filter is

$$Z_{\text{filter}} = sL_1 + \frac{1}{sC_1} \parallel \left(sL_2 + \frac{1}{sC_2} \right) = sL_1 + \frac{\frac{s^2}{\omega_2^2} + 1}{sC_2 + sC_1 \left(\frac{s^2}{\omega_2^2} + 1 \right)}, \tag{7.8}$$

where $\omega_2 = \frac{1}{L_2 C_2}$.

The zero impedance frequency of the matched filter can be derived from:

$$Z_{\text{filter}} = 0 \Rightarrow -\frac{\omega^2}{\omega_2^2} - \frac{\omega^2}{\omega_2^2} \left(-\frac{\omega^2}{\omega_2^2} + 1 + \alpha \right) + 1 = 0, \tag{7.9}$$

where $\omega_1^2 = \frac{1}{L_1 C_1}$,$\alpha = C_2/C_1$, $s = j\omega$, and

$$\Rightarrow \frac{u^2}{\Omega_1 \Omega_2} - \left(\frac{1+\alpha}{\Omega_1} + \frac{1}{\Omega_2} \right) u + 1 = 0, \tag{7.10}$$

where $u = \omega^2$, $\Omega_1 = \omega_1^2$, $\Omega_2 = \omega_2^2$

Let u_1 and u_2 be the solutions of the quadratic euqation (7.10), then

$$\begin{cases} \Omega_{1\pm} = & \frac{u_1+u_2 \pm \sqrt{(u_1+u_2)^2 - 4(1+\alpha)u_1 u_2}}{2} \\ \Omega_{2\pm} = & \frac{2u_1 u_2}{u_1+u_2 \pm \sqrt{(u_1+u_2)^2 - 4(1+\alpha)u_1 u_2}}. \end{cases} \tag{7.11}$$

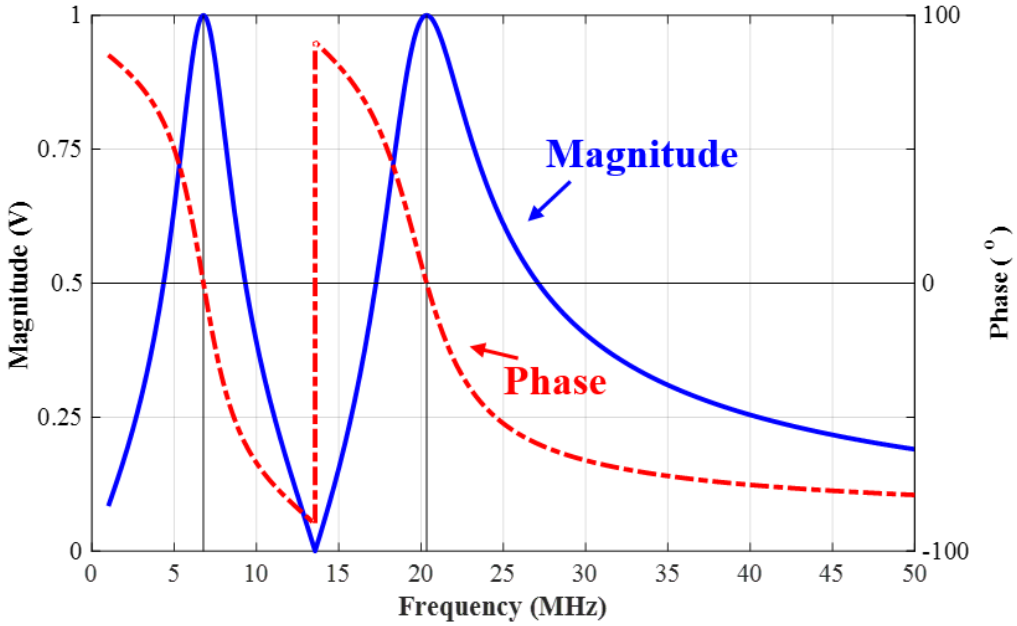

Figure 7.7: Matched filter frequency response when R_{eff} =80 Ω.

The infinite impedance frequency of the matched filter can be derived from:

$$Z_{\text{filter}} = \infty \Rightarrow \omega^2 = (1+\alpha)\omega_2^2 \tag{7.12}$$

and

$$u_{3\pm} = \frac{2(1+\alpha)u_1u_2}{u_1+u_2 \pm \sqrt{(u_1+u_2)^2 - 4(1+\alpha)u_1u_2}}. \tag{7.13}$$

$Z_{\text{filter}} = 0$ when $u = u_1$ and $u_2 = u$; $Z_{\text{filter}} = \infty$ when $u = u_3$. $u_1 = (3\omega)^2$, $u_2 = \omega_s^2$ for the filter that matches the fundamental and third harmonic voltages. u_3, which is determined by α, can be chosen between u_1 and u_2. If the four parameters (u_1, u_2, u_3, α) are pre-determined, the other three component values in the matched filter can be calculated by

$$\begin{cases} L_1 = & (1-k^2)\, L_{\text{s}}, \\ C_1 = & \frac{1}{L_1\Omega_1}, \\ C_2 = & \alpha C_1, \\ L_2 = & \frac{1}{L_2\Omega_2}. \end{cases} \tag{7.14}$$

An example of the frequency response of the matched filter is seen in Fig. 7.7.

L_1 is determined by the hardware setup. The other three components depend on α, which is related to the infinite impedance frequency, seen in Fig. 7.8. Then the relationship of component

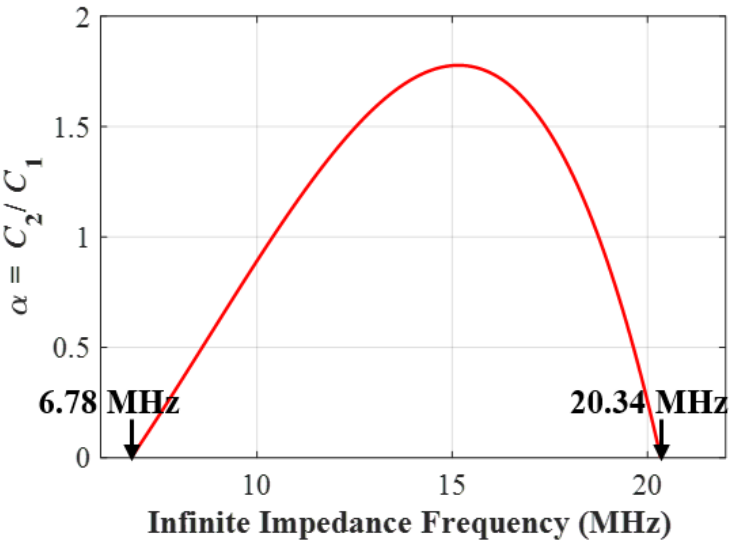

Figure 7.8: Depedence of $\alpha = C_2/C_1$ on the infinite impedance frequency.

values and the infinite impedance frequency is illustrated in Fig. 7.9.

The infinite impedance frequency is chosen to be 13.56 MHz, the second harmonic. For $R_{\text{eff}} = 80\,\Omega$, the frequency response of the matched filter is shown in Fig. 7.7. At 6.78 MHz and 20.34 MHz, the output voltage of the matched filter equals the input voltage with zero phase offset. At 13.56 MHz, the output voltage is zero.

From Fig. 7.6, based on the approximation that the full-bridge rectifier is an ac effective resistance, one can use phasor analysis for linear systems and analyze the currents and voltages in the matched filter. The peak value of the ac input voltage source for the receiver is

$$V_{\text{peak, secondary}} = k\sqrt{\frac{L_{\text{s}}}{L_{\text{p}}}}\sqrt{\frac{2}{D}}V. \tag{7.15}$$

If we assume that there is no voltage drop across the matched filter, then the peak current of the secondary coil can be expressed as

$$I_{\text{peak}} = \frac{V_{\text{peak, secondary}}}{R_{\text{eff}}}. \tag{7.16}$$

The receiver can be considered as resistive to the transmitter, which means the secondary coil current is in phase with the primary coil output voltage. The current flow through the secondary coil can be expressed as

$$i_{\text{s}}(t) \approx 0.7016 I_{\text{p}} \cos(\omega_1 t) + 0.3244 I_{\text{p}} \cos(3\omega_1 t)\,. \tag{7.17}$$

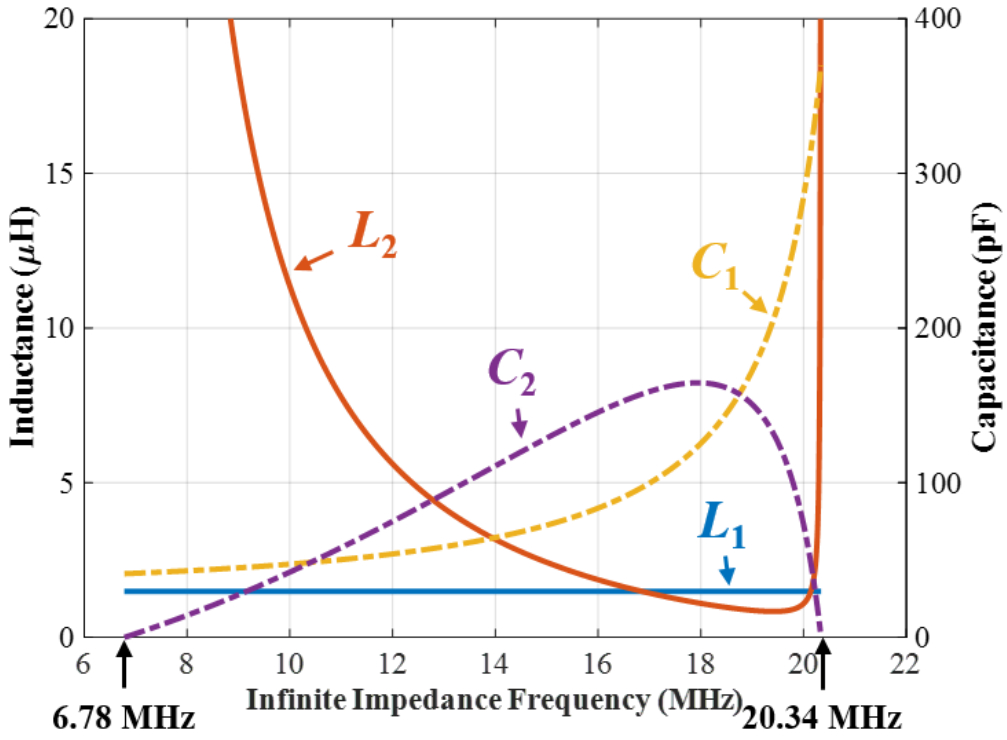

Figure 7.9: Depedence of the matched filter components on infinitie impedance frequency.

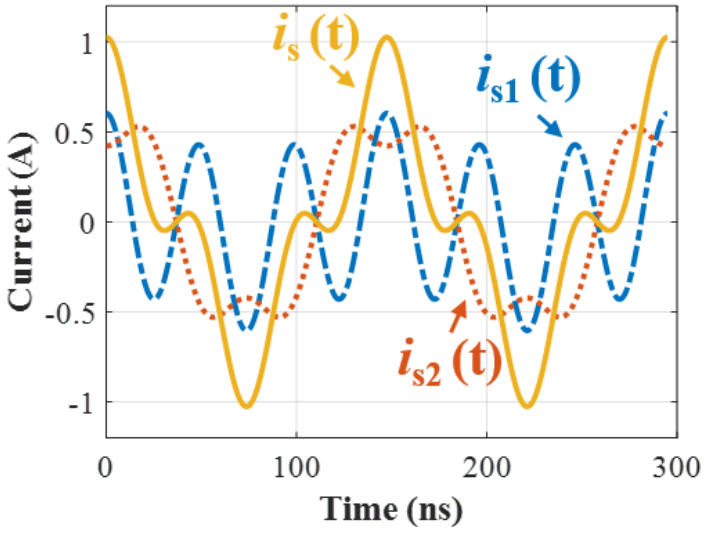

Figure 7.10: Current waveforms in the matched filter.

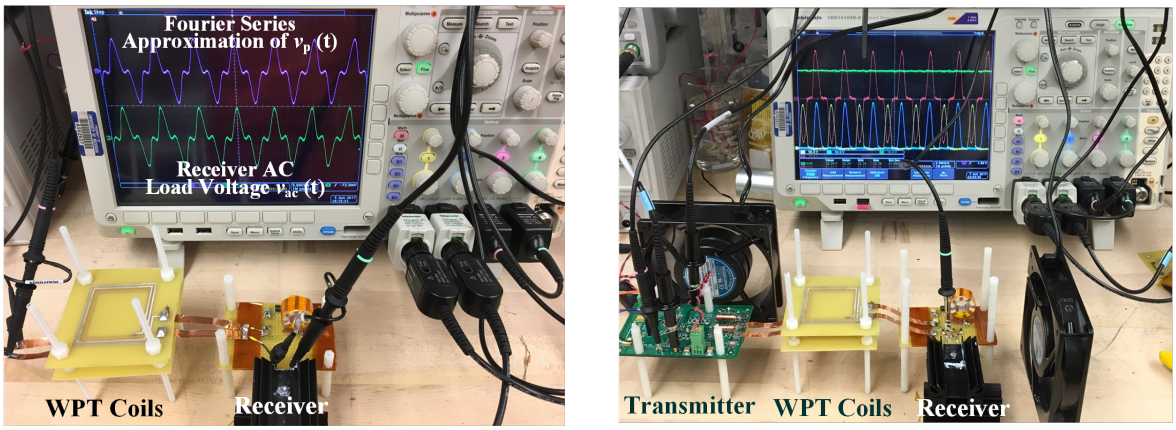

(a) Receiver with AC load.

(b) Receiver with DC load.

Figure 7.11: Demonstration of the PR-WPT system.

Through phasor analysis and superposition, the current flow through C_1, L_2 and C_2 can be calculated at both the fundamental and third harmonic separately and then added in

$$\dot{I}_{s1} = \dot{I}_{s,\,1st}\frac{\omega_s^2 L_2 C_2 - 1}{\omega_s^2 L_2 C_2 - 1 - \frac{C_2}{C_1}} + \dot{I}_{s,\,3rd}\frac{9\omega_s^2 L_2 C_2 - 1}{9\omega_s^2 L_2 C_2 - 1 - \frac{C_2}{C_1}} \tag{7.18}$$

and

$$\dot{I}_{s2} = \dot{I}_{s,\,1st}\frac{1}{1 + \frac{C_1}{C_2} - \omega_s^2 L_2 C_1} + \dot{I}_{s,\,3rd}\frac{1}{1 + \frac{C_1}{C_2} - 9\omega_s^2 L_2 C_1}. \tag{7.19}$$

Because of diodes nonlinearity, the current I_s, shown in Fig. 7.10, flows through the full-bridge rectifier and generates a higher dc output in comparison to a sine-wave resonant system.

7.3 Hardware Implementation

In this section, I present the details of the prototype design for piecewise resonant wireless power transfer (PR-WPT). The complete experimental set-up is illustrated in Fig. 7.11.

7.3.1 Transmisster Design

A relatively higher voltage transmitter switch is needed to obtain the needed peak voltage at the secondary coil for better efficiency using series resonance. The transmitter uses two 650 V E-mode GaN transistors (GS66502B) from GaN Systems. For the gate driver, we use CMOS inverters (SN74LVC2GU04DCKR). For overvoltage protection, we use a string of Zener diodes (BZX100A,115) in parallel with each FET. The series string also avoids forward conduction and

Table 7.2: PAPR Experimental Components

L_{p}	1.55 μH
L_{s}	1.55 μH
k	0.2
Coil Diagonal Dimension	70 mm
C_{r}	33 pF
C_1	53 pF
C_2	103 pF
L_2	3.57 μH

the resulting reverse recovery loss because 3.5 V drop of the Zener diodes is higher than the reverse voltage drop of the GaN FETs. The reduced parasitic capacitance from the series of Zener diodes along with the output capacitance of the GaN FETs is absorbed into $C_{\mathrm{r,p}}$. The resonant components, input choke, and WPT coils are in Table 7.2.

7.3.2 Receiver Design

Using closed-form equations for the matched filter simplifies design. The additional inductor L_2 uses a P-material from Ferronics, Inc. (11-786-P-1) and 0.125-inch wide copper foil from Bridgeport Magnetics. The resonant capacitors are high-Q, low ESR capacitors from Johanson Technology. Because of parasitic capacitances and inductances in the layout, the capacitors C_1 and C_2 in the receiver have to be tuned with a two-channel signal generator 33612A from Keysight Technologies. After the matched filter, Schottky diodes are chosen for the full-bridge rectifier because the lower voltage drops reduce loss [115–117]; also a low parasitic capacitance is required for a lower impact on the matched filter: SMD1200PL-TP from Micro Commercial Components is selected. The component values are in Table 7.2.

7.4 Results and Dissusions

In this section, we demonstrate a proof of principle for piecewise resonant methods for wireless power transfer. Also, we examine the advantages and the potential applications of piecewise resonant methods.

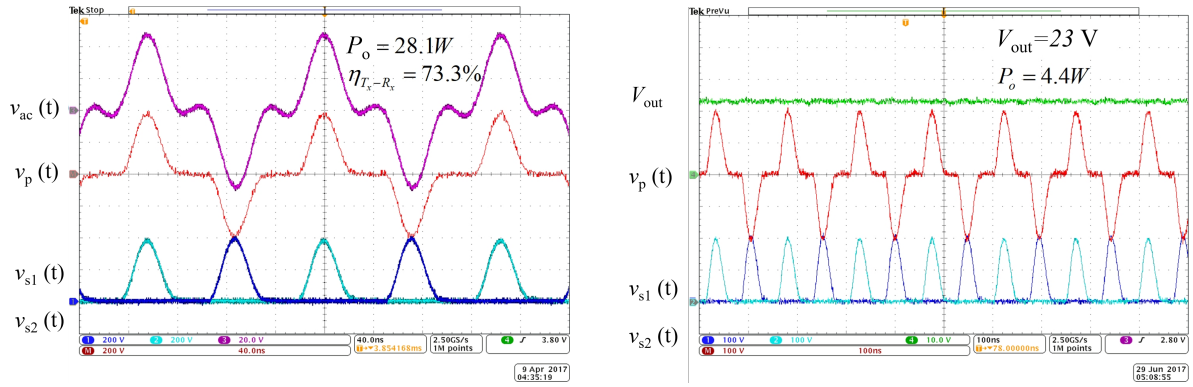

(a) PR-WPT experiment results with resistive load to the matched filter.

(b) PR-WPT experiment results with the rectifier and RC load to the matched filter.

Figure 7.12: PR-WPT experiment waveforms.

7.4.1 Experimental Results

Results in Fig. 7.12(a) show that the voltage of the resistive load in the matched filter, consisting of the fundamental and third harmonic, is in phase with the transmitter voltage, which means that the filter is matched and the receiver presents as a resistive load to the transmitter. The peak drain voltage of GaN FET equals 400 V and output power equals 28.1 W with an end-to-end efficiency (dc-ac, ac-ac) of 73.3 %. Results in Fig. 7.12(b) show that the proof of principle for PR-WPT in Fig. 7.2 when we replace the resistive load of the matched filter with the rectifier and RC load. The dc output voltage is 23 V and the output power is 4.4 W.

7.4.2 Rectifier Loss Comparison Between Piecewise Resonance and Sine-Wave Resonance

To determine the advantages of using piecewise resonance, sine-wave and piecewise resonant systems with ideal switches were compared for the same output power 16 W and primary coil rms voltage 101 V, hence equivalent SAR. The PR-WPT system is seen in Fig. 7.2 while the equivalent circuit of the SR-WPT system simply take out the L_2, C_2,making series compensation with $L_1 = (1 - k^2)\, L_s$ and C_1. Table 7.3 shows the component values in these two topologies with the same WPT coils in Table 7.2. Fig. 7.14 shows the typical waveforms comparison in piecewise and sine-wave resonance piecewise resonance.

The output dc voltage is 21 V in sine-wave resonance while it is increased to 27 V in piecewise resonance, increased by around 30 % with same rms voltage 101 V at the primary output and output power 16 W. Observe that in these two resonances, the receiver can be regarded as a pure resistance to the transmitter and the full-bridge rectifier can be regarded as resistive to the matched filter or

Table 7.3: PAPR Resonant Components in Simulation

	Sine-wave resonance	Piecewise resonance
C_r	350 pF	125 pF
C_1	350 pF	57 pF
C_2	–	102.9 pF

Table 7.4: Rectifier Loss Comparison

	Sine-wave resonance	Piecewise resonance
RMS voltage at the primary	V	V
DC output voltage	$\frac{\sqrt{2}\pi}{4}kV - 2V_\mathrm{F}$	$\frac{\sqrt{2}\pi}{4}kV \times 1.3 - 2V_\mathrm{F}$
DC load current	$\frac{P_\mathrm{o}}{\frac{\sqrt{2}\pi}{4}kV - 2V_\mathrm{F}}$	$\frac{P_\mathrm{o}}{\frac{\sqrt{2}\pi}{4}kV \times 1.3 - 2V_\mathrm{F}}$
Rectifier loss	$\frac{2V_\mathrm{F}P_\mathrm{o}}{\frac{\sqrt{2}\pi}{4}kV - 2V_\mathrm{F}}$	$\frac{2V_\mathrm{F}P_\mathrm{o}}{\frac{\sqrt{2}\pi}{4}kV \times 1.3 - 2V_\mathrm{F}}$

series compensation. The higher dc output voltage decreases the full-bridge rectifier loss. The comparison of the rectifier loss is done between these two resonances with the same rms voltage V at primary, same output power P_o and same voltage drop V_F of Schottky. The results are seen in Table 7.4.

7.4.3 Efficiency Advantage of Piecewise Resonant Receivers

The receiver for PR-WPT systems requires two additional components for the matched filter compared to a sine-wave resonant (SR) receiver, as shown in Fig. 7.13. The additional inductor L_2 results in more loss, which can be overcome by the decreased rectifier loss. Thus, there are a number of potential applications for piecewise resonant WPT systems when their total receiver loss is less than the loss of equivalent sine-wave resonant WPT systems; these include implantable medical devices.

The current flow through L_2 is derived in (7.19). When calculating I_peak in the secondary coil, effective resistance R_eff in (7.16) needs to take rectifier loss into account, calculated as

$$R_\mathrm{eff} = \frac{V^2}{P_\mathrm{o} + R_\mathrm{rec,\,loss}}. \tag{7.20}$$

Then the loss caused by L_2 can be derived in (7.21) if we could obtain the ESR of L_2, including coil resistance and winding resistance at 6.78 MHz and 20.34 MHz where we transfer power.

$$
\begin{aligned}
P_{L_2,\,\text{loss}} &= \left(\frac{0.7016 I_\text{p}/\sqrt{2}}{1+\frac{C_1}{C_2}-\omega^2 L_2 C_1}\right)^2 R_{\text{ac},\,1} + \left(\frac{0.3244 I_\text{p}/\sqrt{2}}{1+\frac{C_1}{C_2}-9\omega^2 L_2 C_1}\right)^2 R_{\text{ac},\,3} \\
&= 0.171 I_\text{p}^2 R_{\text{ac},\,1} + 0.013 I_\text{p}^2 R_{\text{ac},\,3} \\
&\approx 0.171 I_\text{p}^2 R_{\text{ac},\,1}.
\end{aligned}
\tag{7.21}
$$

From (7.21), it is known that mainly the fundamental current flows through the additional inductor, which is also indicated by Fig. 7.10. For convenience and simplicity, we only take fundamental loss in (7.21) into account. Here we utilize the principle of underdamped second-order systems to obtain the winding resistance of L_2 at 6.78 MHz and utilize Steinmetz's equation to estimate the coil resistance [123].

From our calculation, the ac resistance of the additional inductor is roughly $2\,\Omega$ at the fundamental frequency. The critical condition of the receiver loss between piecewise resonance and sine-wave resonance is

$$
P_{L_2,\,\text{loss}} + P_{\text{rectifier, PR}} = P_{\text{rectifier, SR}}. \tag{7.22}
$$

To strength the piecewise resonance, we can define a parameter β, which is the ratio between sine-wave resonant receiver loss and piecewise resonant receiver loss, as

$$
\beta = \frac{P_{\text{rectifier, SR}}}{P_{L_2,\,\text{loss}} + P_{\text{rectifier, PR}}}. \tag{7.23}
$$

Piecewise resonance targets those applications when $\beta > 1$. Fig. 7.15 shows the promising applications with specific range of rms voltage and power. Low power and relatively high voltage is the promising market for piecewise resonance. Retinal Implants, Cortical implants, peripheral nerve implants, brain-machine interfaces, and spinal cord stimulators are definitely the targets whose power consumption are less than 1 W [111].

7.5 Summary

Wireless power transfer is the pre-eminent technology in transferring power to implantable medical devices in vivo. These devices are critical to the health and prolonged life. High PAPR waveforms using piecewise resonant (PR) methods result in higher dc output voltage and less rectifier loss with an application space that includes low power and high rms voltage. A PR-WPT system includes a current-mode class D amplifier which generates a piecewise resonant voltage at 6.78 MHz and a matched filter receives the dominant fundamental and third harmonic voltages, benefiting from

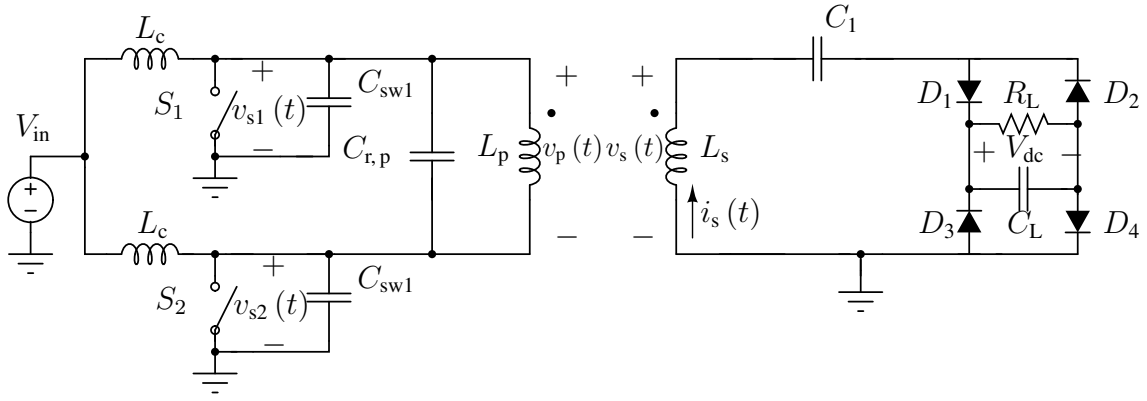

Figure 7.13: Sine resonance WPT circuit.

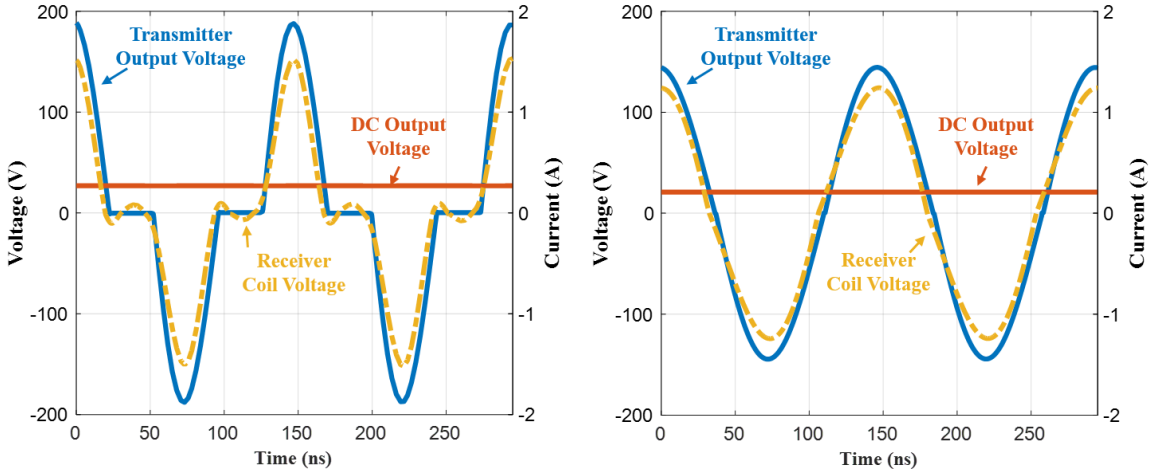

(a) (b)

Figure 7.14: Piecewise resonant receiver obtains higher dc output voltage compared with sine-wave resonant receiver with the same rms voltage in the primary coil and same outpower power.

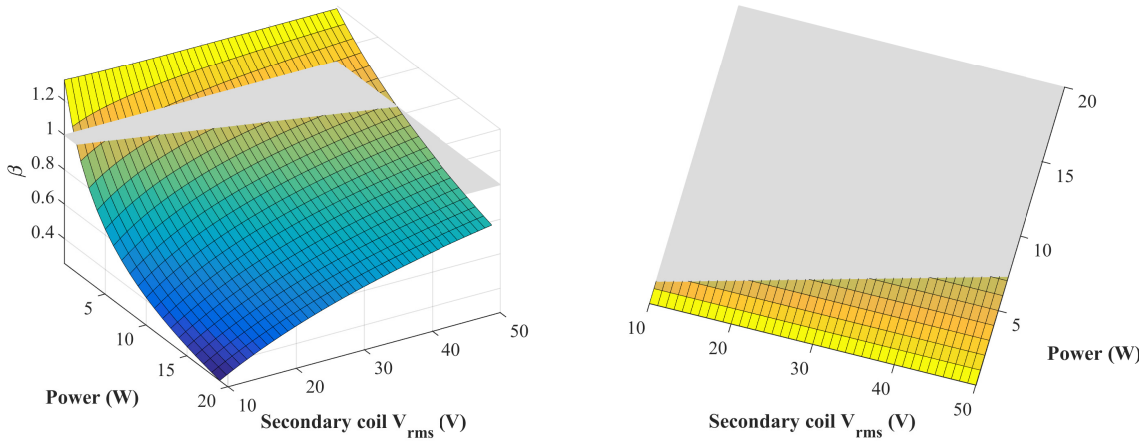

(a) (b)

Figure 7.15: (a) shows the β under different secondary coil rms voltage and output power for implantable medical devices, which is plotted for a Schottky voltage drop of 0.4 V. The application space for PR-WPT is denoted by the lighted gridded region in (b). The altitude of the solid grey plane equals 1 ,which is the critical condition (7.22).

harmonic elimination and closed-form solutions to impedance analysis. DC voltage is converted by a Schottky rectifier. These methods enhanced the total performance and design of the receiver in vivo.

CHAPTER 8

Conclusion and Future Directions

8.1 Summary

This thesis investigates scalable architectures for high frequency (HF) and very high frequency (VHF) wireless power transfer (WPT), which can scale the power level and transfer distance while maintaining the efficiency with an application range from watts for biomedical and consumer electronics to tens of watts for robots and drones, breaking the trade-offs among devices, power, frequency, and transfer distance. VHF gate drivers, electromagnetics, power amplifiers, and power architectures were introduced and investigated. Three application scenarios were illustrated for different applications in wireless powering the Internet of Things. The ultimate vision is to provide energy anytime and everywhere for electronic devices in the wireless power world.

Chapter 1 introduces the vision of the wireless power world, which requires different power levels and transfer distances for different applications, i.e., scalable architectures for WPT. It also investigates the advantages at higher operating frequencies of better passive components, faster transient response, better combination with communications, and higher receiver voltages. It also reviews the state-of-the-art of current HF and VHF WPT and two fundamental limitations at HF-VHF WPT, i.e., **Power and Frequency Trade-off** and **Transfer Distance and Frequency Trade-off**. The current WPT can only solve either **Power and Frequency Trade-off** or **Transfer Distance and Frequency Trade-off** while decreasing the efficiency. The main contribution of this thesis is that the scalable architectures can overcome the design challenges at HF and VHF power conversion and the two fundamental trade-offs. The scalable architectures for HF and VHF WPT can scale the power level and transfer distance while maintaining the efficiency.

Chapter 2 presents the design of an isolated ultrafast gate driver which can have variable frequencies, variable duty cycles, and arbitrary long pulses. It can run up to 165 MHz with rise and fall times below 270 ps. It is also scalable to different devices with different junction dimensions and input gate capacitances.

Chapter 3 investigates a field cancellation method that utilizes a single power electronics con-

verter to drive a two-coil structure to have field cancellation for the encircled circuits inside the WPT coils. The two-coil structure has opposite-phase currents with the optimized current amplitude ratio to optimize the field cancellation.

Chapter 4 demonstrates a 100 MHz wireless power transfer system that can achieve a maximum load power of 6.9 W with an end-to-end dc-dc efficiency of 79.1 % including gating loss. The system achieves greater than 80 % end-to-end dc-dc efficiency without gating loss and above 70 % total end-to-end dc-dc efficiency including gating loss for a wide power range of 1.7 W to 6.9 W. The peak total efficiency including gating loss is above 79.1 % for an output power of 4.9 W to 6.9 W. The system uses a current-mode class D (CMCD) inverter and a current-mode class D (CMCD) rectifier with straightforward design and easily tuned compensation networks, which has a wide load range, constant output current, and small input and output current ripple.

Chapter 5 introduces the segmented CMCD power converter. The segmented CMCD power converters aggregate the magnetic flux and corresponding power together from each identical and synchronous module by electrically connecting the resonance, which also physically increases the coil size at HF-VHF and extends the transfer distance and power level but maintains the efficiency of the optimized CMCD power converter.

Chapter 6 demonstrates the segmentation WPT system with a segmented CMCD inverter and a segmented CMCD rectifier. Together with Chapter 4, the scalable architectures can increase the power level and transfer distance while maintaining the system efficiency and device utilization.

Chapter 7 presents a piecewise resonant (PR) WPT system with aims to achieve high efficiency, simplicity, and reliability for the in-vivo receivers. The PR-WPT system has a CMCD inverter to generate a high peak-to-average-power ratio (PAPR) waveform and a 4^{th}-order matched filter and a full-bridge rectifier to receive the PAPR waveform and convert it to dc.

8.2 Conclusion

High frequency (HF) and very high frequency (VHF) wireless power transfer (WPT) systems can be the future of the wireless power world. Scalable architectures are needed for various applications including biomedical and consumer electronics, robots and drones, and electric vehicles for different power levels and transfer distances. Scalable architectures with current-mode class D (CMCD) power converters can easily achieve the targets for the wireless power world through singleton WPT systems, segmentation WPT systems, and piecewise resonant WPT systems by segmentation of the WPT coils, distributed power electronics converters, and waveform shaping. The main contribution of the thesis is that the scalable architectures for HF and VHF WPT can scale the power level and transfer distance while maintaining the efficiency. This thesis also investigates the HF-VHF gate drivers, field cancellation, power circuits, and power architectures.

8.3 Future Work

8.3.1 Gate Driver

The gate driver in Chapter 2 can be integrated and even co-packaged with the GaN devices, which has a high potential to become commercial products. The gate driver is suitable for both high-side and low-side switches and is also suitable for both enhancement mode and depletion mode devices.

8.3.2 Field Manipulation

The field cancellation method in Chapter 3, which uses a single power electronics converter to drive a two-coil structure with opposite-phase current and optimized current amplitude ratio, can manipulate the electromagnetic field profile. A few power electronics converters can drive a multi-coil or a multi-stack structure to optimize the electromagnetic field profile.

8.3.3 Segmented CMCD Power Converter

The segmented CMCD power converters in Chapters 5 and 6 operate at 100 MHz. The segmented CMCD power converter can operate at a lower frequency to achieve a higher power level, which can be used for electric vehicles and robots. The modules in the segmented CMCD power converters operate synchronously and identically in this thesis but other control modulation can be implemented in the segmented CMCD power converter. The sources and loads in the segmented CMCD power converter can be the different motors in electric vehicles or the different limbs in robots.

The segmented CMCD power converters can also combine with the techniques of parallel switches to optimize the power and efficiency performance.

8.3.4 Piecewise Resonant WPT System

The rectification in the piecewise resonant WPT in Chapter 7 is based on hardware demonstration. The theory of the rectification of a multi-resonant signal or a PAPR signal can be further investigated.

8.4 Future Directions

Dr. William E. Newell proposed the well-known power electronics triangular in 1974. As shown in Fig. 8.1(a), **Power Electronics** is an interdisciplinary that contains **Electronics**, **Power**, and

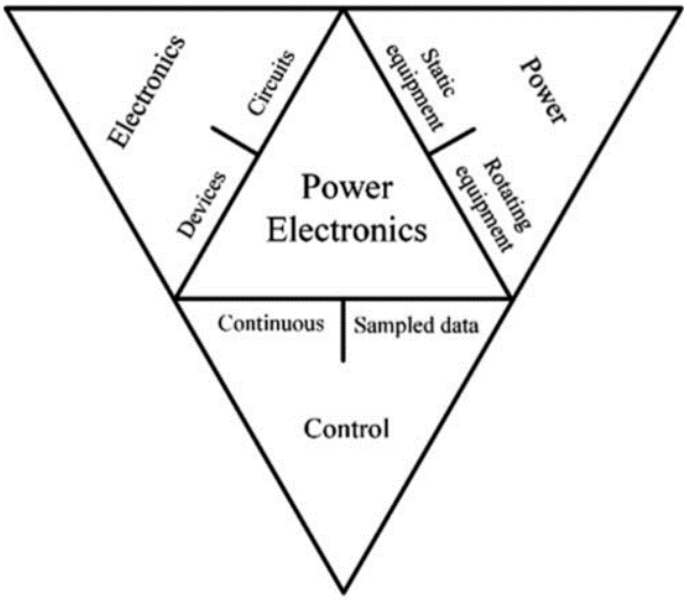

(a) William E. Newell's vision in 1974 [124].

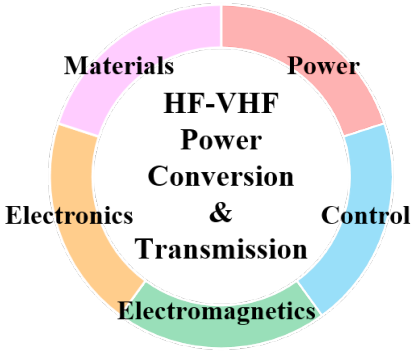

(b) Xin Zan's vision in 2022.

Figure 8.1: Vision of power electronics.

Control. In my point of view, **HF-VHF power conversion & Transmission** is an even broader interdisciplinary that contains **Materials** and **Electromagnetics** besides Dr. William E. Newell's point of view in 1974, as shown in Fig. 8.1(b).

For devices, we need new switches with new materials or new structures that work at 3-300 MHz as switches.

1. Although there are devices that can work at even higher frequencies at GHz, those microwave devices are optimized for linearity or maximum available power, which are different goals for semiconductor devices that work as switches for power conversion and transmission.

2. C_{oss} loss in HF-VHF resonant converters with ZVS is equivalent to the switching loss in

hard-switching power conversion.

3. Current switches are the bottleneck for boosting the system efficiency.

For **Control**, we need new control frameworks and algorithms at 3-300 MHz.

1. Nyquist sampling frequency is challenging or even unrealistic for hardware implementation.
2. Current sliding mode control is not accurate enough.

For **Electromagnetics**, new paradigms of power conversion and transmission can exist because the physical dimensions of the electronics systems are comparable to the operating wavelengths.

1. Waveguides and transmission lines can be adopted in power conversion and transmission.
2. Fresnel-zone WPT can achieve a balance between the energy transmission efficiency and transfer distance, taking advantages of both near-field and far-field WPT.

With the motivations and advantages of HF-VHF illustrated in Section 1.2, HF-VHF operation is attractive to the following applications.

1. Ultrafast and ultra-efficient power supplies.
2. Flexible electronics and integration.
3. RF plasma generator for semiconductor processing with switch-mode power amplifiers.
4. Anntena drivers with switch-mode power amplifiers.
5. Wireless power transfer for the Internet of Things.
6. Dynamic wireless power transfer for electric vehicles and unmanned aerial vehicles.

Currently, HF-VHF power is a blue ocean with potential fortune and treasure, waiting for navigators and divers to explore and discover them.

BIBLIOGRAPHY

[1] Sasatani, T., Sample, A. P., and Kawahara, Y., "Room-scale magnetoquasistatic wireless power transfer using a cavity-based multimode resonator," *Nature Electronics*, Vol. 4, No. 9, 2021, pp. 689–697.

[2] Hayes, M. and Zahnstecher, B., "The Virtuous Circle of 5G, IoT and Energy Harvesting," *IEEE Power Electronics Magazine*, Vol. 8, No. 3, 2021, pp. 22–29.

[3] Chu, S. Y., Cui, X., Zan, X., and Avestruz, A.-T., "Transfer-PowerMeasurement Using a Non-Contact Method For Fair and Accurate Metering ofWireless Power Transfer in Electric Vehicles," *IEEE Transactions on Power Electronics*, 2021, pp. 1–1.

[4] Zan, X., Guo, Z., and Avestruz, A., "Inductive Wireless Power Transfer at 100 MHz with Wide Load Range and Constant Output Current," *2019 IEEE Energy Conversion Congress and Exposition (ECCE)*, Sep. 2019, pp. 4967–4975.

[5] Perreault, D. J., Hu, J., Rivas, J. M., Han, Y., Leitermann, O., Pilawa-Podgurski, R. C. N., Sagneri, A., and Sullivan, C. R., "Opportunities and Challenges in Very High Frequency Power Conversion," Feb 2009, pp. 1–14.

[6] Hong, Y.-P., Mukai, K., Gheidi, H., Shinjo, S., and Asbeck, P. M., "High efficiency GaN switching converter IC with bootstrap driver for envelope tracking applications," *2013 IEEE Radio Frequency Integrated Circuits Symposium (RFIC)*, 2013, pp. 353–356.

[7] Villarruel-Parra, A. and Forsyth, A., "75 MHz discrete GaN based multi-level buck converter for envelope tracking applications," *2019 IEEE Applied Power Electronics Conference and Exposition (APEC)*, March 2019, pp. 1553–1560.

[8] He, X., Wang, R., Wu, J., and Li, W., "Nature of power electronics and integration of power conversion with communication for talkative power," *Nature Communications*, Vol. 11, May 2020.

[9] Zan, X. and Avestruz, A.-T., "100MHz Symmetric Current-Mode Class D Wireless Power Transfer," *IEEE Journal of Emerging and Selected Topics in Power Electronics*, 2022, pp. 1–1.

[10] Knott, A., Andersen, T. M., Kamby, P., Pedersen, J. A., Madsen, M. P., Kovacevic, M., and Andersen, M. A. E., "Evolution of Very High Frequency Power Supplies," *IEEE Journal of Emerging and Selected Topics in Power Electronics*, Vol. 2, No. 3, Sep. 2014, pp. 386–394.

[11] Wang, Y., Lucia, O., Zhang, Z., Guan, Y., and Xu, D., "Review of very high frequency power converters and related technologies," *IET Power Electronics*, Vol. 13, No. 9, 2020, pp. 1711–1721.

[12] Rivas, J. M., Jackson, D., Leitermann, O., Sagneri, A. D., Han, Y., and Perreault, D. J., "Design considerations for very high frequency dc-dc converters," *2006 37th IEEE Power Electronics Specialists Conference*, June 2006, pp. 1–11.

[13] Pilawa-Podgurski, R. C. N., Sagneri, A. D., Rivas, J. M., Anderson, D. I., and Perreault, D. J., "Very-High-Frequency Resonant Boost Converters," *IEEE Transactions on Power Electronics*, Vol. 24, No. 6, June 2009, pp. 1654–1665.

[14] Andersen, T. M., Christensen, S. K., Knott, A., and Andersen, M. A. E., "A VHF class E dc-dc converter with self-oscillating gate driver," *2011 Twenty-Sixth Annual IEEE Applied Power Electronics Conference and Exposition (APEC)*, March 2011, pp. 885–891.

[15] Zan, X. and Avestruz, A. T., "Isolated Ultrafast Gate Driver with Variable Duty Cycle for Pulse and VHF Power Electronics," *IEEE Transactions on Power Electronics*, Vol. 35, No. 12, 2020, pp. 12678–12685.

[16] Madsen, M. P., Pedersen, J. A., Knott, A., and Andersen, M. A. E., "Self-oscillating resonant gate drive for resonant inverters and rectifiers composed solely of passive components," *2014 IEEE Applied Power Electronics Conference and Exposition - APEC 2014*, March 2014, pp. 2029–2035.

[17] Gu, L., Tong, Z., Liang, W., and Rivas-Davila, J., "A Multi-Resonant Gate Driver for High-Frequency Resonant Converters," *IEEE Transactions on Industrial Electronics*, 2019, pp. 1–1.

[18] Gu, L., Surakitbovorn, K., Zulauf, G., Chakraborty, S., and Rivas-Davila, J., "High-Frequency Bidirectional Resonant Converter for High Conversion Ratio and Variable Load Operation," *IEEE Journal of Emerging and Selected Topics in Power Electronics*, Vol. 8, No. 3, 2020, pp. 1983–1993.

[19] Aldhaher, S., Yates, D. C., and Mitcheson, P. D., "Load-Independent Class E/EF Inverters and Rectifiers for MHz-Switching Applications," *IEEE Transactions on Power Electronics*, Vol. 33, No. 10, Oct 2018, pp. 8270–8287.

[20] Roslaniec, L., Jurkov, A. S., Bastami, A. A., and Perreault, D. J., "Design of Single-Switch Inverters for Variable Resistance/Load Modulation Operation," *IEEE Transactions on Power Electronics*, Vol. 30, No. 6, June 2015, pp. 3200–3214.

[21] Zhang, H., Shao, Y., Liu, M., and Ma, C., "A Wide-Load-Range and Compact MHz Wireless Power Transfer System Based on Novel Reactance Compression Design and Edge Inductor," *IEEE Transactions on Power Electronics*, Vol. 36, No. 10, 2021, pp. 11183–11195.

[22] Han, Y., Leitermann, O., Jackson, D. A., Rivas, J. M., and Perreault, D. J., "Resistance Compression Networks for Radio-Frequency Power Conversion," *IEEE Transactions on Power Electronics*, Vol. 22, No. 1, Jan 2007, pp. 41–53.

[23] Gu, L., Zulauf, G., Zhang, Z., Chakraborty, S., and Rivas-Davila, J., "Push–Pull Class Φ_2 RF Power Amplifier," *IEEE Transactions on Power Electronics*, Vol. 35, No. 10, 2020, pp. 10515–10531.

[24] Gu, L., Zulauf, G., Stein, A., Kyaw, P. A., Chen, T., and Davila, J. M. R., "6.78-MHz Wireless Power Transfer With Self-Resonant Coils at 95 % DC–DC Efficiency," *IEEE Transactions on Power Electronics*, Vol. 36, No. 3, 2021, pp. 2456–2460.

[25] Gu, L. and Rivas-Davila, J., "1.7 kW 6.78 MHz Wireless Power Transfer with Air-Core Coils at 95.7 % DC-DC Efficiency," *2021 IEEE Wireless Power Transfer Conference (WPTC)*, 2021, pp. 1–4.

[26] Jurkov, A. S., Radomski, A., and Perreault, D. J., "Tunable Matching Networks Based on Phase-Switched Impedance Modulation," *IEEE Transactions on Power Electronics*, Vol. 35, No. 10, 2020, pp. 10150–10167.

[27] Al Bastami, A., Jurkov, A., Otten, D., Nguyen, D. T., Radomski, A., and Perreault, D. J., "A 1.5 kW Radio-Frequency Tunable Matching Network Based on Phase-Switched Impedance Modulation," *IEEE Open Journal of Power Electronics*, Vol. 1, 2020, pp. 124–138.

[28] Tong, Z., Gu, L., and Rivas-Davila, J., "Wideband PPT Class Φ_2 Inverter using Phase-Switched Impedance Modulation and Reactance Compensation," *IEEE Transactions on Industrial Electronics*, 2021, pp. 1–1.

[29] Ramos, I., Ruiz Lavín, M. N., García, J. A., Maksimović, D., and Popović, Z., "GaN Microwave dc–dc Converters," *IEEE Transactions on Microwave Theory and Techniques*, Vol. 63, No. 12, Dec 2015, pp. 4473–4482.

[30] Hazucha, P., Schrom, G., Hahn, J., Bloechel, B., Hack, P., Dermer, G., Narendra, S., Gardner, D., Karnik, T., De, V., and Borkar, S., "A 233-MHz 80 %-87 % efficient four-phase DC-DC converter utilizing air-core inductors on package," *IEEE Journal of Solid-State Circuits*, Vol. 40, No. 4, 2005, pp. 838–845.

[31] Burton, E. A., Schrom, G., Paillet, F., Douglas, J., Lambert, W. J., Radhakrishnan, K., and Hill, M. J., "FIVR — Fully integrated voltage regulators on 4th generation Intel® Core™ SoCs," *2014 IEEE Applied Power Electronics Conference and Exposition - APEC 2014*, 2014, pp. 432–439.

[32] Zhang, Y., Rodríguez, M., and Maksimović, D., "Very High Frequency PWM Buck Converters Using Monolithic GaN Half-Bridge Power Stages With Integrated Gate Drivers," *IEEE Transactions on Power Electronics*, Vol. 31, No. 11, Nov 2016, pp. 7926–7942.

[33] Sepahvand, A., Kumar, A., Afridi, K., and Maksimović, D., "High power transfer density and high efficiency 100 MHz capacitive wireless power transfer system," *2015 IEEE 16th Workshop on Control and Modeling for Power Electronics (COMPEL)*, July 2015, pp. 1–4.

[34] Song, J., Jeong, S., Park, S., Kim, J., Cho, Y., and Kim, J., "PCB-package to chip wireless power transfer scheme using magnetic-field resonance coupling for high-density 3-D IC," *2016 IEEE Wireless Power Transfer Conference (WPTC)*, 2016, pp. 1–4.

[35] Systems, G., "GaN Transistors 650 V E-HEMT," .

[36] Lee, T. H., *The Design of CMOS Radio-Frequency Integrated Circuits*, Cambridge University Press, Cambridge UK, 2nd ed., 2003, p. 147.

[37] Babic, S., Sirois, F., Akyel, C., and Girardi, C., "Mutual Inductance Calculation Between Circular Filaments Arbitrarily Positioned in Space: Alternative to Grover's Formula," *IEEE Transactions on Magnetics*, Vol. 46, No. 9, Sep. 2010, pp. 3591–3600.

[38] Baliga, B. J., *Fundamentals of Power Semiconductor Devices*, Springer Publishing Company, Incorporated, Raleigh, NC, USA, 1st ed., 2008, p. 2.

[39] Baliga, B. J., *Fundamentals of Power Semiconductor Devices*, Springer Publishing Company, Incorporated, Raleigh, NC, USA, 1st ed., 2008, p. 15.

[40] Zulauf, G., Park, S., Liang, W., Surakitbovorn, K. N., and Rivas-Davila, J., "COSS Losses in 600 V GaN Power Semiconductors in Soft-Switched, High- and Very-High-Frequency Power Converters," *IEEE Transactions on Power Electronics*, Vol. 33, No. 12, Dec 2018, pp. 10748–10763.

[41] Aoki, I., Kee, S. D., Rutledge, D. B., and Hajimiri, A., "Fully integrated CMOS power amplifier design using the distributed active-transformer architecture," *IEEE Journal of Solid-State Circuits*, Vol. 37, No. 3, March 2002, pp. 371–383.

[42] Aoki, I., Kee, S. D., Rutledge, D. B., and Hajimiri, A., "Distributed active transformer-a new power-combining and impedance-transformation technique," *IEEE Transactions on Microwave Theory and Techniques*, Vol. 50, No. 1, Jan 2002, pp. 316–331.

[43] Surakitbovorn, K. and Rivas-Davila, J. M., "A Simple Method to Combine the Output Power from Multiple Class-E Power Amplifiers," *IEEE Journal of Emerging and Selected Topics in Power Electronics*, 2020, pp. 1–1.

[44] Tang, S. C., Lun, T. L. T., Guo, Z., Kwok, K., and McDannold, N. J., "Intermediate Range Wireless Power Transfer With Segmented Coil Transmitters for Implantable Heart Pumps," *IEEE Transactions on Power Electronics*, Vol. 32, No. 5, May 2017, pp. 3844–3857.

[45] Stoecklin, S., Yousaf, A., Gidion, G., and Reindl, L., "Efficient Wireless Power Transfer With Capacitively Segmented RF Coils," *IEEE Access*, Vol. 8, 2020, pp. 24397–24415.

[46] Glaser, J., "How GaN Power Transistors Drive High-Performance Lidar: Generating ultra-fast pulsed power with GaN FETs," *IEEE Power Electronics Magazine*, Vol. 4, No. 1, March 2017, pp. 25–35.

[47] Abramov, E., Evzelman, M., and Peretz, M. M., "Low Voltage Sub-Nanosecond Pulsed Current Driver IC for High-Speed LIDAR Applications," *IEEE Journal of Emerging and Selected Topics in Power Electronics*, 2019, pp. 1–1.

[48] Turriate, V., Witcher, B., Boroyevich, D., and Burgos, R., "Self-powered Gate Driver Design for a Gallium Nitride Based Phase Shifted Full Bridge DC-DC Converter for Space Applications," *2018 IEEE 6th Workshop on Wide Bandgap Power Devices and Applications (WiPDA)*, Oct. 2018, pp. 141–148.

[49] Wang, H., Wei, J., Xie, R., Liu, C., Tang, G., and Chen, K. J., "Maximizing the Performance of 650-V p-GaN Gate HEMTs: Dynamic RON Characterization and Circuit Design Considerations," *IEEE Transactions on Power Electronics*, Vol. 32, No. 7, July 2017, pp. 5539–5549.

[50] Li, R., Wu, X., Yang, S., and Sheng, K., "Dynamic on-State Resistance Test and Evaluation of GaN Power Devices Under Hard- and Soft-Switching Conditions by Double and Multiple Pulses," *IEEE Transactions on Power Electronics*, Vol. 34, No. 2, Feb 2019, pp. 1044–1053.

[51] Zhang, Z., Zhang, W., Wang, F., Tolbert, L. M., and Blalock, B. J., "Analysis of the switching speed limitation of wide band-gap devices in a phase-leg configuration," *2012 IEEE Energy Conversion Congress and Exposition (ECCE)*, Sep. 2012, pp. 3950–3955.

[52] Zan, X. and Avestruz, A., "Performance Comparisons of Synchronous and Uncontrolled Rectifiers for 27.12 MHz Wireless Power Transfer Using CMCD Converters," *2018 IEEE Energy Conversion Congress and Exposition (ECCE)*, Sep. 2018, pp. 2448–2455.

[53] Kaplan, Z., "Simple, fully isolated, pulse transformer," *Review of scientific instruments*, Vol. 55, No. 8, 1984, pp. 1355–1356.

[54] Balogh, L., "Design and application guide for high speed MOSFET gate drive circuits," *Power Supply Design Seminar SEM-1400, Topic*, Vol. 2, 2001.

[55] de León, F., Purushothaman, S., and Qaseer, L., "Leakage Inductance Design of Toroidal Transformers by Sector Winding," *IEEE Transactions on Power Electronics*, Vol. 29, No. 1, Jan 2014, pp. 473–480.

[56] Zhang, Z., Wang, F., Tolbert, L. M., and Blalock, B. J., "Active Gate Driver for Crosstalk Suppression of SiC Devices in a Phase-Leg Configuration," *IEEE Transactions on Power Electronics*, Vol. 29, No. 4, April 2014, pp. 1986–1997.

[57] Zan, X. and Avestruz, A., "Wireless power transfer for implantable medical devices using piecewise resonance to achieve high peak-to-average power ratio," *2017 IEEE 18th Workshop on Control and Modeling for Power Electronics (COMPEL)*, July 2017, pp. 1–8.

[58] Denison, T., Consoer, K., Santa, W., Avestruz, A.-T., Cooley, J., and Kelly, A., "A 2 μW 100 nV/rtHz Chopper-Stabilized Instrumentation Amplifier for Chronic Measurement of Neural Field Potentials," *IEEE Journal of Solid-State Circuits*, Vol. 42, No. 12, 2007, pp. 2934–2945.

[59] Liu, M., Song, J., and Ma, C., "Analysis and Design of a Self-Resonant Rectenna for Small-Size and Ultraloosely Coupled MHz Wireless Power Transfer Applications," *IEEE Journal of Emerging and Selected Topics in Industrial Electronics*, Vol. 2, No. 4, 2021, pp. 535–544.

[60] Lee, E. S., Sohn, Y. H., Choi, B. G., Han, S. H., and Rim, C. T., "A Modularized IPT With Magnetic Shielding for a Wide-Range Ubiquitous Wi-Power Zone," *IEEE Transactions on Power Electronics*, Vol. 33, No. 11, 2018, pp. 9669–9690.

[61] Apple, "MagSafe," .

[62] Shao, Y., Liu, M., Zhang, H., and Ma, C., "Dual-Band Wireless Power Transmitter with Reconfigurable Power Amplifier and "Decoupling Ring"," *IECON 2020 The 46th Annual Conference of the IEEE Industrial Electronics Society*, 2020, pp. 3889–3894.

[63] Cruciani, S., Campi, T., Maradei, F., and Feliziani, M., "Active Shielding Design for Wireless Power Transfer Systems," *IEEE Transactions on Electromagnetic Compatibility*, Vol. 61, No. 6, 2019, pp. 1953–1960.

[64] Park, J., Kim, D., Hwang, K., Park, H. H., Kwak, S. I., Kwon, J. H., and Ahn, S., "A Resonant Reactive Shielding for Planar Wireless Power Transfer System in Smartphone Application," *IEEE Transactions on Electromagnetic Compatibility*, Vol. 59, No. 2, 2017, pp. 695–703.

[65] Hong, S., Kim, Y., Lee, S., Jeong, S., Sim, B., Kim, H., Song, J., Ahn, S., and Kim, J., "A Frequency-Selective EMI Reduction Method for Tightly Coupled Wireless Power Transfer Systems Using Resonant Frequency Control of a Shielding Coil in Smartphone Application," *IEEE Transactions on Electromagnetic Compatibility*, Vol. 61, No. 6, 2019, pp. 2031–2039.

[66] Kim, J. and Ahn, S., "Dual Loop Reactive Shield Application of Wireless Power Transfer System for Leakage Magnetic Field Reduction and Efficiency Enhancement," *IEEE Access*, Vol. 9, 2021, pp. 118307–118323.

[67] Zhu, Q., Zhang, Y., Guo, Y., Liao, C., Wang, L., and Wang, L., "Null-Coupled Electromagnetic Field Canceling Coil for Wireless Power Transfer System," *IEEE Transactions on Transportation Electrification*, Vol. 3, No. 2, 2017, pp. 464–473.

[68] Mohammad, M., Wodajo, E. T., Choi, S., and Elbuluk, M. E., "Modeling and Design of Passive Shield to Limit EMF Emission and to Minimize Shield Loss in Unipolar Wireless Charging System for EV," *IEEE Transactions on Power Electronics*, Vol. 34, No. 12, 2019, pp. 12235–12245.

[69] Avestruz, A.-T., Chang, A. H., Khushrushahi, S., Banerjee, A., and Leeb, S. B., "Single-sided AC magnetic fields for induction heating," *IECON 2013 - 39th Annual Conference of the IEEE Industrial Electronics Society*, 2013, pp. 5052–5057.

[70] Simpson, J. C., Lane, J. E., Immer, C. D., and Youngquist, R. C., "Simple analytic expressions for the magnetic field of a circular current loop," Tech. rep., 2001.

[71] Griffith, J. M. and Pan, G. W., "Time Harmonic Fields Produced by Circular Current Loops," *IEEE Transactions on Magnetics*, Vol. 47, No. 8, 2011, pp. 2029–2033.

[72] Ulaby, F. and Ravaioli, U., *Fundamentals of Applied Electromagnetics*, Pearson, 8th ed., 2020.

[73] Hou, D., Lee, F. C., and Li, Q., "Very High Frequency IVR for Small Portable Electronics With High-Current Multiphase 3-D Integrated Magnetics," *IEEE Transactions on Power Electronics*, Vol. 32, No. 11, 2017, pp. 8705–8717.

[74] Liang, W., Raymond, L., and Rivas, J., "3-D-Printed Air-Core Inductors for High-Frequency Power Converters," *IEEE Transactions on Power Electronics*, Vol. 31, No. 1, Jan 2016, pp. 52–64.

[75] Zan, X. and Avestruz, A., "Active Segmentation at 100 MHz for 12 W VHF Wireless Power Transfer," *2019 20th Workshop on Control and Modeling for Power Electronics (COMPEL)*, June 2019, pp. 1–8.

[76] Zan, X. and Avestruz, A., "100 MHz Wireless Power Transfer for Lightweight UAVs and Agile Robots," *2020 IEEE Applied Power Electronics Conference and Exposition (APEC)*, 2020, pp. 1655–1661.

[77] Zan, X. and Avestruz, A., "27.12 MHz Bi-Directional Wireless Power Transfer Using Current-Mode Class D Converters with Phase-Shift Power Modulation," *2018 IEEE PELS Workshop on Emerging Technologies: Wireless Power Transfer (Wow)*, June 2018, pp. 1–6.

[78] Zhao, L., Thrimawithana, D. J., Madawala, U. K., and Hu, A. P., "A Push–Pull Parallel Resonant Converter-Based Bidirectional IPT System," *IEEE Transactions on Power Electronics*, Vol. 35, No. 3, 2020, pp. 2659–2667.

[79] Kazimierczuk, M. K., *RF Power Amplifiers*, John Wiley & Sons, 2014, pp. 164–241.

[80] Krauss, H. L., Bostian, C. W., and Raab, F. H., *Solid State Radio Engineering*, Wiley New York, 1980, pp. 432–448.

[81] Kazimierczuk, M. and Czarkowski, D., *Resonant Power Converters*, Hoboken, N.J. : Wiley, 2nd ed., 2011, pp. 290–310.

[82] Perreault, D. J., Sullivan, C. R., and Rivas, J. M., "GaN in Switched-Mode Power Amplifiers," *Gallium Nitride-enabled High Frequency and High Efficiency Power Conversion*, Springer, 2018, pp. 200–203.

[83] Kobayashi, H., Hinrichs, J. M., and Asbeck, P. M., "Current-mode class-D power amplifiers for high-efficiency RF applications," *IEEE Transactions on Microwave Theory and Techniques*, Vol. 49, No. 12, Dec 2001, pp. 2480–2485.

[84] Hamill, D., "Time reversal duality in DC-DC converters," *PESC97. Record 28th Annual IEEE Power Electronics Specialists Conference. Formerly Power Conditioning Specialists Conference 1970-71. Power Processing and Electronic Specialists Conference 1972*, Vol. 1, 1997, pp. 789–795 vol.1.

[85] Chu, S. Y., Zan, X., and Avestruz, A.-T., "Electromagnetic Model-Based Foreign Object Detection for Wireless Power Transfer," *IEEE Transactions on Power Electronics*, Vol. 37, No. 1, 2022, pp. 100–113.

[86] Bai, H., Nie, Z., and Mi, C. C., "Experimental Comparison of Traditional Phase-Shift, Dual-Phase-Shift, and Model-Based Control of Isolated Bidirectional DC–DC Converters," *IEEE Transactions on Power Electronics*, Vol. 25, No. 6, 2010, pp. 1444–1449.

[87] Steigerwald, R. L., "A comparison of half-bridge resonant converter topologies," *IEEE Transactions on Power Electronics*, Vol. 3, No. 2, April 1988, pp. 174–182.

[88] Qu, X., Chu, H., Huang, Z., Wong, S., Tse, C. K., Mi, C. C., and Chen, X., "Wide Design Range of Constant Output Current Using Double-Sided LC Compensation Circuits for Inductive-Power-Transfer Applications," *IEEE Transactions on Power Electronics*, Vol. 34, No. 3, March 2019, pp. 2364–2374.

[89] Corporation, E. P. C., "EPC 2037 Datasheet," 2020.

[90] Corporation, E. P. C., "EPC 2038 Datasheet," 2019.

[91] Corporation, D., "ZHCS506 Datasheet," 2019.

[92] CDE, "Types MC and MCN Multilayer RF Capacitors," .

[93] Vishay, "Surface Mount Multilayer Ceramic Chip Capacitors for High Frequency," 2021.

[94] Song, J., Liu, M., Kang, N., and Ma, C., "A Universal Optimal Drain–Source Voltage Tracking Scheme for Synchronous Resonant Rectifiers in Megahertz Wireless Power Transfer Applications," *IEEE Transactions on Power Electronics*, Vol. 36, No. 5, 2021, pp. 5147–5156.

[95] Berger, A., Agostinelli, M., Vesti, S., Oliver, J. A., Cobos, J. A., and Huemer, M., "A Wireless Charging System Applying Phase-Shift and Amplitude Control to Maximize Efficiency and Extractable Power," *IEEE Transactions on Power Electronics*, Vol. 30, No. 11, 2015, pp. 6338–6348.

[96] Huang, X., Dou, Y., Lin, S., Tian, Y., Ouyang, Z., and Andersen, M. A. E., "Synchronous Push–Pull Class E Rectifiers With Load-Independent Operation for Megahertz Wireless Power Transfer," *IEEE Transactions on Power Electronics*, Vol. 36, No. 6, 2021, pp. 6351–6363.

[97] Cochran, S. and Costinett, D., "Frequency Synchronization and Control for a 6.78 MHz WPT Active Rectifier," *2018 IEEE 19th Workshop on Control and Modeling for Power Electronics (COMPEL)*, 2018, pp. 1–7.

[98] Cochran, S. and Costinett, D., "Discrete Time Synchronization Modeling for Active Rectifiers in Wireless Power Transfer Systems," *2019 20th Workshop on Control and Modeling for Power Electronics (COMPEL)*, 2019, pp. 1–8.

[99] Thrimawithana, D. J., Madawala, U. K., and Neath, M., "A Synchronization Technique for Bidirectional IPT Systems," *IEEE Transactions on Industrial Electronics*, Vol. 60, No. 1, 2013, pp. 301–309.

[100] Waffenschmidt, E. and Staring, T., "Limitation of inductive power transfer for consumer applications," *2009 13th European Conference on Power Electronics and Applications*, Sep. 2009, pp. 1–10.

[101] Chen, C., Chu, T., Lin, C., and Jou, Z., "A Study of Loosely Coupled Coils for Wireless Power Transfer," *IEEE Transactions on Circuits and Systems II: Express Briefs*, Vol. 57, No. 7, July 2010, pp. 536–540.

[102] Stein, A. L. F., Kyaw, P. A., and Sullivan, C. R., "Figure of merit for resonant wireless power transfer," *2017 IEEE 18th Workshop on Control and Modeling for Power Electronics (COMPEL)*, July 2017, pp. 1–7.

[103] Lu, J. L. and Chen, D., "Paralleling GaN E-HEMTs in 10kW-100kW systems," *2017 IEEE Applied Power Electronics Conference and Exposition (APEC)*, March 2017, pp. 3049–3056.

[104] Perreault, D. J., "A New Power Combining and Outphasing Modulation System for High-Efficiency Power Amplification," *IEEE Transactions on Circuits and Systems I: Regular Papers*, Vol. 58, No. 8, Aug 2011, pp. 1713–1726.

[105] Aerospace, R., "The Most Advanced Lightweight UAV in the World," .

[106] Ackerman, E., "How MIT's Mini Cheetah Can Help Accelerate Robotics Research," .

[107] Knecht, O. and Kolar, J. W., "Comparative evaluation of IPT resonant circuit topologies for wireless power supplies of implantable mechanical circulatory support systems," *2017 IEEE Applied Power Electronics Conference and Exposition (APEC)*, 2017, pp. 3271–3278.

[108] Waters, B. H., Sample, A. P., Bonde, P., and Smith, J. R., "Powering a Ventricular Assist Device (VAD) With the Free-Range Resonant Electrical Energy Delivery (FREE-D) System," *Proceedings of the IEEE*, Vol. 100, No. 1, 2012, pp. 138–149.

[109] Wu, R., Li, W., Luo, H., Sin, J. K. O., and Yue, C. P., "Design and Characterization of Wireless Power Links for Brain–Machine Interface Applications," *IEEE Transactions on Power Electronics*, Vol. 29, No. 10, 2014, pp. 5462–5471.

[110] Liu, Z., Zhong, Z., and Guo, Y., "In Vivo High-Efficiency Wireless Power Transfer With Multisine Excitation," *IEEE Transactions on Microwave Theory and Techniques*, Vol. 65, No. 9, 2017, pp. 3530–3540.

[111] Agarwal, K., Jegadeesan, R., Guo, Y., and Thakor, N. V., "Wireless Power Transfer Strategies for Implantable Bioelectronics," *IEEE Reviews in Biomedical Engineering*, Vol. 10, 2017, pp. 136–161.

[112] Clerckx, B. and Bayguzina, E., "Waveform Design for Wireless Power Transfer," *IEEE Transactions on Signal Processing*, Vol. 64, No. 23, 2016, pp. 6313–6328.

[113] Boaventura, A., Belo, D., Fernandes, R., Collado, A., Georgiadis, A., and Carvalho, N. B., "Boosting the Efficiency: Unconventional Waveform Design for Efficient Wireless Power Transfer," *IEEE Microwave Magazine*, Vol. 16, No. 3, 2015, pp. 87–96.

[114] Pan, N., Boaventura, A. S., Rajabi, M., Schreurs, D., Carvalho, N. B., and Pollin, S., "Amplitude and frequency analysis of multi-sine wireless power transfer," *2015 Integrated Nonlinear Microwave and Millimetre-wave Circuits Workshop (INMMiC)*, 2015, pp. 1–3.

[115] Yang, C., Yang, Y., and Yang, C., "Adaptive pulse waveform modulation to enhance wireless power efficiency for biomedical applications," *2013 IEEE MTT-S International Microwave Symposium Digest (MTT)*, 2013, pp. 1–3.

[116] Lo, C., Yang, Y., Tsai, C., Lee, C., and Yang, C., "Novel wireless impulsive power transmission to enhance the conversion efficiency for low input power," *2011 IEEE MTT-S International Microwave Workshop Series on Innovative Wireless Power Transmission: Technologies, Systems, and Applications*, 2011, pp. 55–58.

[117] Boaventura, A. S. and Carvalho, N. B., "Maximizing DC power in energy harvesting circuits using multisine excitation," *2011 IEEE MTT-S International Microwave Symposium*, 2011, pp. 1–4.

[118] Pantic, Z., Lee, K., and Lukic, S., "Inductive power transfer by means of multiple frequencies in the magnetic link," *2013 IEEE Energy Conversion Congress and Exposition*, 2013, pp. 2912–2919.

[119] on Non-Ionizing Radiation Protection, I. C. et al., "Guidelines for limiting exposure to time-varying electric and magnetic fields (1 Hz to 100 kHz)," *Health physics*, Vol. 99, No. 6, 2010, pp. 818–836.

[120] "IEEE Standard for Safety Levels with Respect to Human Exposure to Radio Frequency Electromagnetic Fields, 3 kHz to 300 GHz," *IEEE Std C95.1-2005 (Revision of IEEE Std C95.1-1991)*, 2006, pp. 1–238.

[121] Xingyi Shi, Waters, B. H., and Smith, J. R., "SAR distribution for a strongly coupled resonant wireless power transfer system," *2015 IEEE Wireless Power Transfer Conference (WPTC)*, 2015, pp. 1–4.

[122] Turin, G., "An introduction to matched filters," *IRE Transactions on Information Theory*, Vol. 6, No. 3, 1960, pp. 311–329.

[123] Han, Y., Cheung, G., Li, A., Sullivan, C. R., and Perreault, D. J., "Evaluation of Magnetic Materials for Very High Frequency Power Applications," *IEEE Transactions on Power Electronics*, Vol. 27, No. 1, 2012, pp. 425–435.

[124] Wang, H., Liserre, M., Blaabjerg, F., de Place Rimmen, P., Jacobsen, J. B., Kvisgaard, T., and Landkildehus, J., "Transitioning to Physics-of-Failure as a Reliability Driver in Power Electronics," *IEEE Journal of Emerging and Selected Topics in Power Electronics*, Vol. 2, No. 1, 2014, pp. 97–114.